



TECHNICAL UNIVERSITY OF DENMARK

DTU PHYSICS | DEPARTMENT OF PHYSICS

DOCTORAL THESIS

**Merging 2D and 3D Worlds for Novel
Electronics: the case of Graphene/Ge(110)**

Author:
Miriam GALBIATI

Supervisors:
Prof. Jakob Kibsgaard
Associate Prof. Luca Camilli
Prof. Sebastian Horch (former)

Preface

The thesis is written as one of the requirements for the fulfilment of the Ph.D. degree according to rules set out by Technical University of Denmark (DTU) and the Department of Physics. All the work described here has been performed from September 2018 to November 2021 as part of my studies carried out in the Nanoscale Materials and Devices (NANOMADE) group. During this time, I have been funded by the Villum Foundation.

Large part of my Ph.D. studies have been spent at the Department of Physics of the University of Roma Tor Vergata in Italy. This period was financially supported by Otto Mønsted Fonden.

My Ph.D. project has been conducted under the supervision of Jakob Kibsgaard (main supervisor), Luca Camilli (co-supervisor) and Sebastian Horch (former main supervisor).

Acknowledgements

My first and biggest thanks goes to my family. My mum and my dad, who thought me the value of hard work, to be independent and keep my chin up. You raised the kindest person in the world, my sister. You have always supported me through all my paths, I am infinitely grateful to you three. I love you very much.

I would like to thank my co-supervisor Luca, for pairing the amount of work with an equal amount of laughter. I would like to thank all people in the NANOMADE section, for always being welcoming and helpful. I wish to thank Prof. Maurizio De Crescenzi from Rome, for his kindness, the history and art lessons and whose vast culture I deeply admire. In addition, I would like to thank Prof. Manuela Scarselli for the support and company in the lab during my stay in Rome.

I would like to thank all my friends in Copenhagen. The Spanish (-ish) gang - Dani, Guille, Rafa, Alex, Nacho, Borja and Alejandro - thank you for all the crazy fun nights and great friendship. You are my family in Denmark. Mina, Janko and Abhay for all the interesting conversations, fun dinners and support. Fra, to me, you just never really left. Andrea, for sharing my same enthusiasm for sports and making me a better cook. Andrea, for being always positive and ready for adventures. Ditte, who is always real, I love you just the way you are. Jorge, who is always sweet to me even when I don't deserve it. I want to also thank Arianna and Chiara, through the endless working days, the flights, the laughs, and craziness of those years we become adults and I cannot be happier you still in my life. Pesa, the biggest smile on earth, Distortion and I are waiting for you. Guido, thank you for the all adventures, travels and wine. To another decade of friendship. Marco, for the deep conversations and kilometers walked side by side. Gian, Vale, Ale and Giulia, you made Rome my second home. Last, thanks to the all GLAZE team, our project was the main drive to power through the end of my Ph.D. studies, and now that I am done, let's take the world.

Miriam Galbiati

*"To go wrong in one's own way is better than to go right
in someone else's."*

- Fyodor Dostoevsky, Crime and Punishment

Abstract

The advances in electronics have been achieved by downscaling the physical size of devices' components to the nanometer range. However, already in the late 1990s, it was clear that the dimensional scaling of silicon-based technologies had reached its limits. Therefore, to meet the requirements and expectations of future applications, novel materials need to be employed and integrated within the current infrastructure, which is mainly based on silicon.

In this scenario, two-dimensional (2D) materials might offer many advantages. Indeed, the integration of graphene, the first among 2D materials, with complementary metal-oxide semiconductor (CMOS) compatible platforms is expected to be the breakthrough point in the research field. In order to control the integration process, the properties of the interface between graphene and substrate need to be thoroughly investigated. However, graphene presents some fundamental weaknesses. Thus, in parallel to graphene's investigation, research on novel 2D materials beyond graphene has boosted over recent years. Therefore, this Ph.D. thesis focus on the case of graphene deposited on Ge(110) via chemical vapor deposition and potential alternatives to graphene, focusing specifically on silicene.

The thesis begins with a brief motivation for novel electronics, a background on graphene's electronic properties, and state-of-the-art graphene/Ge interface studies. The following chapter gives an overview of the main experimental techniques used in this work.

The graphene/Ge(110) interface investigation describes the system's structural, electronic, and chemical properties. The study is structured to induce modification in the interface by different thermal annealings in vacuum. Upon each annealing, the interface is systematically characterized with different techniques to correlate the various properties and offer the full picture of the system.

The last part of the thesis focuses on potential 2D materials that could overcome the lack of bandgap in graphene. In this regard, a brief overview of the opportunities

and challenges of growing X-enes is presented. Then the focus narrows on the silicene case, and the studies on suitable substrates to support its synthesis. In this scenario, the experimental work on CaF_2 grown on Si(111) is finally described.

Resumé (summary in Danish)

Fremskridtene inden for elektronik er opnået ved at nedskalere den fysiske størrelse af elektronikhedernes komponenter til nanometerområdet. Men allerede i slutningen af 1990'erne stod det klart, at den dimensionelle skalering af siliciumbaserede teknologier havde nået sin grænse. For at imødekomme kravene og forventningerne til fremtidige applikationer skal nye materialer derfor anvendes og integreres i den nuværende infrastruktur, som hovedsageligt er baseret på silicium.

I dette scenarie kan todimensionelle (2D) materialer give mange fordele. Faktisk forventes integrationen af grafen, det først fundne 2D-materiale, med komplementære metaloxid-halvleder (CMOS) kompatible platforme, at være gennembrudspunktet på forskningsområdet. For at kontrollere integrationsprocessen skal egenskaberne af grænsefladen mellem grafen og substrat undersøges grundigt. Imidlertid har grafen nogle grundlæggende svagheder. Parallelt med undersøgelsen af grafen, har forskningen i nye 2D-materialer ud over grafen således fået et løft over de seneste år. Denne ph.d. afhandling fokuserer derfor på tilfældet med grafen deponeret på Ge(110) via chemical vapor deposition og potentielle alternativer til grafen, med fokus specifikt på silicen.

Afhandlingen begynder med en kort motivering af ny elektronik, en baggrund om grafens elektroniske egenskaber og state-of-the-art grafen/Ge-grænsefladestudier. Det følgende kapitel giver et overblik over de vigtigste eksperimentelle teknikker, der anvendes i dette arbejde.

Undersøgelsen af grafen/Ge(110)-grænsefladen beskriver systemets strukturelle, elektroniske og kemiske egenskaber. Undersøgelsen er struktureret til at inducere modifikation i grænsefladen ved forskellige termiske annealing i vakuum. Ved hver annealing karakteriseres grænsefladen systematisk med forskellige teknikker til at korrelere de forskellige egenskaber og give det fulde billede af systemet.

Den sidste del af afhandlingen fokuserer på potentielle 2D-materialer, der kunne overvinde manglen på båndgab i grafen. I denne forbindelse præsenteres en kort

oversigt over mulighederne og udfordringerne ved at dyrke X-ener. Derefter indsnævres fokus på silicen-tilfældet, og undersøgelser af egnede substrater til at understøtte silicens syntese. I dette scenarie beskrives slutteligt det eksperimentelle arbejde med CaF_2 dyrket på Si(111).

List of publications

This thesis is based on the article contributions listed below and attached in Appendix A.

- **M. Galbiati**, N. Motta, M. De Crescenzi, and L. Camilli.
"Group-IV 2D materials beyond graphene on nonmetal substrates: Challenges, recent progress, and future perspectives."
Applied Physics Reviews, **6**, 2006041 (2019)
- **M. Galbiati**, L. Persichetti, P. Gori, O. Pulci, M. Bianchi, L. Di Gaspare, J. Tersoff, C. Coletti, P. Hofmann, M. De Seta, and L. Camilli.
"Tuning the Doping of Epitaxial Graphene on a Conventional Semiconductor via Substrate Surface Reconstruction."
Journal of Physical Chemistry Letters, **12**, 1262-1267 (2021)
- **M. Galbiati**, M. Scarselli, F. Arciprete, M. De Crescenzi and L. Camilli.
"Scanning tunneling microscopy study of CaF₂ on Si(111): Observation of metastable reconstructions."
Journal of Physics D: Applied Physics, **55**, 095304 (2021)

Other publications by the author (not covered in this thesis):

- D. M. A. Mackenzie, **M. Galbiati**, X. D. de Cerio, I. Y. Sahalianov, T. M. Radchenko, J. Sun, D. Peña, L. Gammelgaard, B. S. Jessen, J. D. Thomsen, P. Bøggild, A. Garcia-Lekue, L. Camilli and J. M. Caridad.
"Unraveling the electronic properties of graphene with substitutional oxygen."
2D Materials, **8**, 045035 (2021)

Contents

Preface	iii
Acknowledgements	v
Abstract	ix
Resumé (summary in Danish)	xi
List of publications	xiii
1 Introduction	1
1.1 Motivation for Novel Electronics	1
1.2 Graphene's Electronic Properties	5
1.3 Chemical Vapour Deposition Growth of Graphene	9
1.4 Ge as substrate for Graphene Growth	11
1.4.1 (100) Surface	12
1.4.2 (111) Surface	14
1.4.3 (110) Surface	16
1.5 Thesis Outline	17
2 Experimental Techniques	19
2.1 Infinity LT - UHV System	19
Preparation Chamber	20
Analysis Chamber	22
2.2 Synchrotron Radiation and Facilities	23
2.2.1 Storage Rings and Sources	23
2.2.2 Synchrotron Radiation Properties	24
2.3 Scanning Tunneling Microscopy (STM)	27
2.3.1 Principles	28
2.3.2 Imaging in constant-current mode	31

2.4	Angle Resolved Photoemission Spectroscopy (ARPES)	32
2.5	X-ray Photoelectron Spectroscopy (XPS)	37
2.6	Near Edge X-ray Absorption Fine Structure (NEXAFS) Spectroscopy	40
2.7	Raman Spectroscopy	43
3	Structural characterization of the Graphene/Ge(110) interface	47
3.1	STM Study	48
3.2	Conclusion	54
4	Electronic Properties of Graphene/Ge(110)	57
4.1	Experimental ARPES	58
4.2	Theoretical Model	61
4.3	Conclusion	66
5	Chemical Properties of Graphene/Ge(110)	69
5.1	XPS and NEXAFS	70
5.2	Conclusion	77
6	2D Materials Beyond Graphene	79
6.1	Opportunities & Challenges for Group-IV X-enes	80
6.2	Suitable Growth Substrates for Silicene	83
6.3	Suitable Substrates for Silicene: the CaF ₂ /Si(111) case	87
6.4	Conclusion	96
7	Conclusions & Outlook	101
A	Publications	105
	Bibliography	145

List of Figures

1.1	Model of a MOSFET. Cross-section of an n-channel Si MOSFET. The length of the channel is defined by the length of the gate terminal. The thickness of the channel is the depth to which the electronic properties of the semiconductor (<i>p</i> -doped Si in this model) are influenced by the gate.	2
1.2	Overview of 2D materials. Summary of different categories of 2D materials according to their composition. Adapted from [11]. . .	4
1.3	Potential applications of 2D materials and modern transistor devices. Applications of 2D materials integrated with conventional semiconductor technology mapped in time and integration complexity. The area of the circles is a rough qualitative estimate of addressable market opportunity. The position of a circle indicates the time when the first products with the 2D materials-based technology could potentially be introduced. Complexity increases when moving from back end of line to front end of line integration. Adapted from [6].	6
1.4	Graphene. On the left, schematic of a graphene monolayer. On the right, the lattice structure of graphene, made out of two interpenetrating triangular lattices. a_1 and a_2 are the lattice unit vectors (2.46 Å) and d is the nearest-neighbor vector (1.42 Å).	6
1.5	Graphene linear dispersion. Energy band diagram of graphene with a zoom-in of the energy bands close to one of the Dirac points, showing the linear dispersion. The valence π and conduction π^* bands are well separated. The Fermi level coincides with the Dirac points where the bands touch. Figure adapted from [20].	8

- 1.6 **Graphene energy dispersion around Dirac point.** Blue indicates levels filled with electrons while red indicates empty levels (holes). On the left, neutral graphene where the valence band is completely filled with electrons and the conduction band is completely empty. The Fermi level and the Dirac point coincide for this case. In the middle, some electrons are drained from the valence band. This case corresponds to hole-doped graphene where the Fermi level shifts below the Dirac point. On the right, some extra electrons are forced into the conduction band. This case corresponds to electron-doped graphene where the Fermi level shifts above the Dirac point. 9
- 1.7 **CVD process.** Schematic illustration of the main steps of graphene CVD on copper. 1) Diffusion of precursor gases, 2) surface adsorption of precursors, 3) catalytic reactions of precursors on the surface, 4) supersaturation of species and nucleation, and 5) growth of nucleated domains. 10
- 1.8 **Graphene/Ge(100).** Serie of scanning tunneling microscopy (STM) images of the different samples as a function of temperature and deposition time. The third row from the top shows a comparison of 3D topographies with the z-axis range 0 - 12 Å. The inset shows the Fast Fourier Transform of the high-quality graphene observed for the sample grown at 930 °C and deposition time of 60 min. STM images were acquired with the $V = 50$ mV and $I = 1.8$ nA. Reprinted from [50]. 13
- 1.9 **Polycrystalline monolayer graphene grown on Ge(111) surface.** a) A scanning electron microscopy (SEM) image of graphene seeds formed at the early stage of growth. b) A SEM image of flat monolayer graphene grown from the seeds in (a). c) high-resolution TEM image of polycrystalline graphene. The inset shows the Fast Fourier Transform diffraction pattern of the TEM image, indicating that the graphene obtained from the Ge(111) surface has two main orientations. d,e) Magnified TEM images at selected regions (Region I, II and Region III, IV) in (c), showing that the misorientation angle between two domains is 30 °. Adapted from [38]. 15

1.10	Single-crystal monolayer graphene grown on Ge(110) surface. a) A typical SEM image of graphene seeds at the early stage of growth. b) Picture of graphene grown on a Ge/Si (110) wafer. c) A high-resolution TEM image of the single-crystal monolayer graphene. (Inset) Four overlaid Selected Area Electron Diffraction patterns, which were measured across the four different points. The distance between each point is $\sim 2 \mu\text{m}$. d) A cross-sectional TEM image demonstrating that the as-grown graphene is monolayer. (Inset) A schematic illustration of the monolayer graphene grown on the H-terminated Ge surface. Adapted from [38].	16
2.1	The LT-UHV Infinity System. The system consists of two chambers connected. The samples are deposited in the preparation chamber and moved to the analysis chamber for scanning probe microscopy (SPM) characterization.	20
2.2	E-beam evaporator. a) Picture of the QUAD-EV-C Mini e-beam evaporator from Mantis uses in this thesis work to evaporate CaF_2 onto Si(111) substrate. b) Picture of the four-pocket of the evaporator, where the material to evaporate is loaded either in pellets within Mo crucibles or as a rod. c) Schematic of the evaporator.	21
2.3	Analysis Chamber. a) Picture of the analysis chamber containing the SPM head for structural characterization of the samples. b) Picture of a typical sample holder and c) picture showing the sample and tip acceptor stages.	22
2.4	Schematic of a Storage Ring. Simplified schematic planar view of a typical storage ring of a synchrotron facility. Adapted from [71].	24
2.5	Elements of a Storage Ring. Schematic view of a storage ring where some of the main elements are highlighted. Namely, bending magnets, focusing and de-focusing magnets (quadrupoles), insertion devices (undulator, wigglers), and the radio frequency (RF) cavity. Adapted from [71].	25
2.6	Schematic of STM principle. a) Simple illustration of quantum tunneling of electrons. b) Schematic energy diagram of the STM tunneling junction. Here, E_{vac} is the vacuum energy level, E_F is the Fermi energy level, indicated for both tip and sample, ρ_{tip} (ρ_{sample}) is the density of states of the sample and the tip, ϕ_{tip} (ϕ_{sample}) is the work function of the tip (sample) metal, V is the applied sample bias voltage, and z is the distance from the sample to the tip. Adapted from [76].	29

2.7	STM images of (7x7)-Si(111) surface. STM images of empty (a) and filled (b) states of the (7x7)-Si(111) surface. Areas of both images are 10x10 nm ² . (a) I = 1.5 nA; V = 2.0 V. (b) I = 0.5 nA; V = -2.0 V.	32
2.8	ARPES. Schematic diagram of outgoing excited electrons in an ARPES setup.	34
2.9	ARPES. Spectral function for non-interacting (left panel) and interacting (right panel) systems.	36
2.10	Electrons mean free path. The mean free path of electrons at different kinetic energies in different materials. Reprinted from [84].	37
2.11	XPS. Sketch of the photoemission process.	38
2.12	XPS spectrum. XPS survey spectrum of a Rh/Al ₂ O ₃ catalyst prepared by impregnating Al ₂ O ₃ with a solution of RhCl ₃ in water. Adapted from [84].	39
2.13	NEXAFS. a) Schematic illustration of the X-ray absorption process. b) Example of a NEXAFS spectrum at C K-edge of graphene. Adapted from [85].	42
2.14	Raman Scattering. a) Stokes. An incoming photon ω_L excites an electron - hole pair (e - h). This pair decays into a phonon Ω and another electron-hole pair (e - h'). The latter recombines, emitting a photon ω_{Sc} . b) Anti-Stokes. The phonon is absorbed by the e - h pair. c) Rayleigh and Raman scattering in resonant and non resonant conditions. Reprinted from [57].	44
2.15	Raman Graphene. Single-layer graphene Raman spectrum. The two most intense features are the G peak at 1580 cm ⁻¹ and the 2D band at 2700 cm ⁻¹ . Other slightly intense peaks are the 2D' at \sim 3200 cm ⁻¹ , the D+D'' at \sim 2450 cm ⁻¹ and the D peak at 1350 cm ⁻¹ .	45
3.1	Raman as-grown graphene/Ge(110) sample. Typical Raman spectrum of the as-grown graphene/Ge(110) samples. Spectrum acquired with excitation laser with wavelength of 532 nm.	49
3.2	STM graphene/Ge(110) as-grown sample. STM images of the as-grown sample. The inset shows the FFT of the image in (c), highlighting the six primary spots of graphene. Figures acquired with V = -1.0 V and I = 0.8 nA (a,b), V = 0.4 V and I = 1.0 nA (c). Scale bar FFT is 5 nm ⁻¹ . Adapted from [68].	50

- 3.3 **STM graphene/Ge(110) after annealing above 350 °C.** (a) The surface shows both the sample as-grown and the (6x2) reconstruction. The white arrows indicate the hydrogen nanobubbles. (b) High magnification image of the (6x2) reconstruction. In black, a and b indicate the unit cell vectors. Inset shows the FFT of (b) where the white circles highlight the six primary spots of graphene, and in the middle the rectangular pattern of the (6x2) phase is recognizable ($V = -1.5$ V and $I = 0.8$ nA in (a) and $V = -1.5$ V and $I = 0.3$ nA in (b)). Inset scale bar is 5 nm^{-1} . Adapted from [68]. 51
- 3.4 **LEED of the (6x2) reconstruction.** LEED collected on the graphene/Ge(110) sample after annealing above 350 °C showing the pattern for the (6x2) reconstruction using primary electron energy of 97 eV. A moiré pattern can be observed around the six graphene diffraction spots. The ratio between the two edges of the moiré pattern is consistent with the ratio between the lattice vectors of the (6x2) phase as measured in STM. LEED spot size 1 mm. Adapted from [68]. 52
- 3.5 **Bias Dependency of STM images.** Serie of STM images of the same surface area acquired with different bias voltages. Tunneling current in all images is 0.1 nA. Adapted from [68]. 52
- 3.6 **STM images of graphene/Ge after high temperature annealing.** STM images of the graphene/Ge(110) sample after annealing above 700 °C. Inset shows the FFT of the corresponding real space STM image in (b) and highlights the six primary spots of graphene. Inset scale bar 5 nm^{-1} ($V = -1.2$ V and $I = 0.8$ nA in (a); $V = -0.5$ V and $I = 0.8$ nA in (b)). Adapted from [68]. 53
- 3.7 **STM image of graphene/Ge(110) after high temperature annealing.** (a) Atomic-resolution of the Ge surface underneath graphene. The black arrow marks the $[\bar{1}10]$ direction. Inset shows the FFT of the corresponding STM image in panes (a) and highlights the 0.566 nm periodicity of the Ge surface. Inset scale bar is 5 nm^{-1} . (b) Line profiles taken along the Ge surface as indicated in (a). ($V = -1.2$ V and $I = 0.8$ nA). Adapted from [68]. 54

- 4.1 **ARPES of the graphene/Ge(110).** Photoemission intensity of the graphene/Ge(110) sample (a) as-grown, (b) after annealing above 350 °C, and (c) after high temperature annealing. The spectra were acquired along the direction orthogonal to the Γ - K direction ((a-c) upper panels) and along the Γ - K direction ((a-c) middle panels) in the Brillouin zone, as schematically shown in the inset in the middle panel in (a). Bottom row: sketch highlighting the evolution of graphene doping level with the annealing of the sample. Adapted from [68]. 59
- 4.2 **Bandgap in graphene/Ge(110) after high temperature annealing.** The MDCs analysis along k_x in the energy range 0.04 - 0.56 eV for the graphene/Ge(110) sample upon high temperature annealing. The diagram shows the opening of a small band gap of ≈ 120 meV marked here in grey. Reprinted from [68]. 61
- 4.3 **ARPES of graphene/Ge(110).** Constant binding energy cuts at 0.90 eV below the extrapolated Dirac point for the samples as-grown (a), after annealing above 350 °C (b), and after high temperature annealing (c). The white arrows in panel (b) point to the position of two out of four replicas. E_b values indicate the corresponding binding energy values of the cut. Adapted from [68]. 62
- 4.4 **ARPES Graphene/Ge(110) after annealing above 350 °C.** Absence of minigaps at the crossing of graphene main Dirac cone with its replica. a) ARPES intensity map. The main Dirac cone and replica (dashed red lines) dispersion bands cross at ~ 1.2 eV. b) Intensity of Dirac cone dispersion extracted by MDCs analysis. The intensity of the band does not vanish or decrease at the crossing point, as would be expected in presence of a minigap. Reprinted from [68]. 63
- 4.5 **Simulations of graphene/Ge(110) as-grown and after high temperature annealing.** 3D side-view of as-grown sample with all dangling bonds being H-terminated (a) and after high temperature annealing (b). Cyan denotes H atoms, violet Ge atoms, and yellow C atoms. The black circles mark the position of the vacancy. (c), (d) Calculated electronic band structures around K with a total k range of 0.07 \AA^{-1} for (a) and (b), respectively. Red dots represent graphene-derived states, whereas grey dots represent Ge or H states. Reprinted from [68]. 64

4.6	3D models of graphene/Ge(110) as-grown and after high temperature annealing. (Left) Side-view of the as-grown sample where all Ge dangling bonds are saturated by H atoms. (Right) Side-view of the sample after high temperature annealing. In cyan the H atoms, in violet the Ge atoms, and yellow the C atoms. The position of the vacancy in the topmost layer of Ge is highlighted in green. Reprinted from [68].	64
4.7	Hall measurements on bare Ge. Examples of Hall and resistivity measurements performed at room temperature on different Ge substrates after annealing in the atmosphere to 930 °C in H ₂ /Ar atmosphere during simulated graphene growth experiments. The measurements have been carried out with Van der Pauw configuration. Magnetic field: 0.7 T. For all the samples investigated, a p-type Hall behavior is observed with sheet carrier density in the range 0.8 - 7.0 x 10 ¹⁴ cm ⁻² . Reprinted from[68].	65
5.1	LEED pattern graphene/Ge(110) samples. LEED patterns acquired after each annealing as indicated in the pictures. Column a) corresponds to measurements acquired with energy of the primary source of 80 eV to highlight only the superficial features. Column b) represents the images acquired with a primary source of 130 eV to distinguish also the features within deeper regions of Ge substrate. .	71
5.2	C 1s XPS spectra graphene/Ge(110) samples. Core levels acquired after annealing at (a) 100 °C, (b) 500 °C and (c) 660 °C. .	72
5.3	Ge 3d XPS spectra graphene/Ge(110) samples. Core levels acquired after annealing at (a) 100 °C, (b) 500 °C and (c) 660 °C. .	73
5.4	NEXAFS C K-edge spectra graphene/Ge(110) samples. The dashed grey lines mark the resonances π^* at 285.6 eV, σ_1^* at 292 eV, and σ_2^* at 293 eV.	74
5.5	XPS graphene/Ge(110) after annealing at 800 °C. a) C 1s core level and b) Ge 3d core level.	75
5.6	STM of graphene/Ge(110) after annealing at 660 °C. STM images performed on the graphene/Ge(110) sample after annealing at 660 °C and after the XPS and NEXAFS experiments. The results shows no presence of hydrogen nanobubbles. The images reveal the coexistence of areas of (6x2) reconstruction and (1x1) phase. V = -1.6 V and I = 0.3 nA.	76

5.7	XPS and STM of graphene/Ge(110) after annealing at 500 °C. a) C 1s core level spectrum of the control sample after annealing at 500 °C. b and c) STM images of the control sample after annealing at 500°C. b) $V = -1.6$ V and $I = 0.35$ nA. c) $V = 1.6$ V and $I = 0.05$ nA.	76
5.8	Raman spectra of graphene/Ge(110). a) Raman spectra of graphene/Ge(110) sample. b) Plot of the 2D vs G-band energies. ε is the strain and n the charge density. Straight lines indicate E_{2D} vs E_G relationship for strained undoped (black line, $n = 0$) and unstrained n -doped (red line, $\varepsilon = 0$) graphene. The two lines cross at the expected 2D and G positions for suspended freestanding graphene. Raman measurements were performed before and after the XPS and NEXAFS experiments as indicated in the legends. . .	78
6.1	Group-IV X-enes atomic structure. Simple sketch of the buckled atomic structure of Group-IV X-enes. Adapted from [136]. . . .	81
6.2	STM Silicene on MoS₂. (a) STM image of clean MoS ₂ surface ($V = 1$ V, $I = 0.7$ nA); (b) MoS ₂ surface after deposition of 0.8 ML of Si ($V = 1$ V, $I = 0.7$ nA). Inset: reflection high energy electron diffraction pattern displaying the characteristic streaks. (c) Higher resolution image ($V = 0.2$ V, $I = 2$ nA) of a partially covered surface. (Below) Line profile taken across the gray arrow in the image above showing a height difference of 5 \AA between Si-covered area and clean MoS ₂ . (d) Zoom-in of the area highlighted in (c) showing a hexagonal surface pattern. The corresponding periodicity is extracted from the analysis of the self-correlation function. A sketch models the Si honeycomb structure. Adapted from [173].	84
6.3	ARPES Silicene on MoS₂. Valence band structure of clean MoS ₂ (a) and after Si deposition at 200 °C (b). Data collected with photon energy $h\nu = 100$ eV along the K- Γ -K reciprocal lattice direction. Adapted from [174].	85
6.4	Silicene on HOPG. (a) STM image of a HOPG substrate after room temperature deposition of 1ML of Si. The ball-and-stick models superimposed on the image represent Si lattice (blue and red) and HOPG lattice (black). ($V = 0.3$ V, $I = 0.3$ nA). (b) Line profile recorded along the blue dashed line in (a). (c) Line profile recorded along the solid black line in (a). (d) Normalized differential conductance $dI/dV/(I/V)$ related to the LDOS. The red dotted line is the theoretical density of states for the system. Adapted from [175]. . .	86

- 6.5 **CaF₂ as substrate for silicene.** (a) Model of silicene deposited on a clean CaF₂ (111) surface. Si, Ca and F atoms in blue, yellow and red, respectively. (b) Calculated band structure of silicene deposited on CaF₂(111). The regions of the dense slab bands represent the projected bulk CaF₂ band structures. The silicene bands are indicated by black lines. The red-dashed horizontal line represents the Fermi level. Adapted from [180]. 87
- 6.6 **CaF₂/Si(111) samples grown at low temperatures.** STM images of clean (7x7)-Si(111) surface (a), after deposition of 0.25 ML of CaF₂ deposition at room temperature with post-deposition annealing for 30 min at 400 °C (b) and after deposition of 0.30 ML of CaF₂ deposition with the substrate at 460 °C (c). Scale bars 10 nm. (a, b) V = 2.0 V and I = 0.5 nA. (c) V = -3.3 V and I = 0.3 nA. 88
- 6.7 **DAS model (7x7)-Si(111) surface.** (a) Top view of the 2x2 supercell of the DAS model. Gray, blue and green shadow represent first, second and third lattice planes. Solid dots represent Si atoms. Blue rhombus highlights the (7x7) unit cell. Yellow ellipses mark the 9 dimers of two halves of the unit cell and lies two layers below the top surface layer. The rest atoms (6 in one unit cell) are colored in pink and the adatoms (12 in one unit cell) are colored in blue. The bulk Si atoms are colored in gray. (b) and (c) The corresponding top- and side- view structure of one unit cell, respectively, labeled with lateral and vertical distance between the featured atoms. Reprinted from [196]. 89
- 6.8 **(7x7)-Si(111) reactive sites.** 7x7 nm² STM images of CaF₂ molecules adsorbed on (7x7)-Si(111). The coverage is 0.46 ML. (a) 0.25 ML of CaF₂ was deposited at room temperature and subsequently the sample was annealed at 400 °C for 30 min. (b) 0.30 ML of CaF₂ was deposited with the substrate at 460 °C (b). (a) V = 2.0 V and I = 0.8 nA. (b) V = -3.0 V and I = 0.1 nA. 90
- 6.9 **CaF₂/Si(111) samples grown at low temperatures.** STM images of the sample after deposition of 0.25 ML of CaF₂ at room temperature and post-deposition annealing at 400 °C for 30 min (a) and after deposition of 0.30 ML of CaF₂ with the substrate at 460 °C (b). Scale bar 400 nm (a), 50 nm (b). (a) V = -2.0 V and I = 0.5 nA. (b) and inset V = -3.3 V and I = 0.3 nA. Scale bar in the Inset is 20 nm. 91

- 6.10 **CaF₂/Si(111) samples grown at 460 °C.** STM images of sample after CaF₂ deposition at 460 °C. At the bottom, the line profile taken across the terraces of the surface shown in panel (a) reveals that there is no height difference within the terrace. The high-contrast image shown in panel (b) highlights a higher density of adsorbates in the region closer to the step with the lower terrace. $V = -3.3$ V and $I = 0.3$ nA. Scale bar = 20 nm. 92
- 6.11 **CaF₂/Si(111) samples grown at 570 °C.** (a-c) STM images of the sample after deposition of 0.20 ML of CaF₂ at 570 °C showing the unreacted (7x7) and reacted Si areas. (c) Blow-up of 25 x 12 nm² rectangular area marked in the top-right corner in (b). The areas highlighted in light blue and green represent patches of c(2x4) and ($\sqrt{3} \times \sqrt{3}$) reconstructions, respectively. Scale bar 200 nm (a), 10 nm (b). (d) Schematics of ($\sqrt{3} \times \sqrt{3}$) and c(2x4) unit cell reconstruction. (e) Line profiles taken on the STM image as indicated in panel (c). The periodicities of first-neighbor atoms are consistent with those expected for the c(2x4) and $\sqrt{3} \times \sqrt{3}$ reconstructions. (a) $V = 3.0$ V and $I = 0.5$ nA. (b) and (c) $V = 3.0$ V and $I = 0.6$ nA. Reprinted from [69]. 94
- 6.12 **STS measurements on CaF₂/Si(111) sample.** STS measurements recorded via lock-in technique on the three different types of regions on the sample where 0.20 ML of CaF₂ was deposited at 570 °C. Namely, the three regions are unreacted Si (black spectra), reacted Si (blue spectra), and CaF₂ island (red spectra). Three spectra were acquired on three different spots within the same type of region, as indicated by the rectangular boxes in the STM image. These spectra are vertically shifted by an arbitrary quantity for visualization purposes. Reprinted from [69]. 95
- 6.13 **CaF₂/Si(111) samples showing (3x1) reconstruction.** STM images of the samples after deposition of 0.20 ML of CaF₂ at 570 °C and post-deposition annealing at 600 °C (a,b); and after deposition of 0.60 ML of CaF₂ at 680 °C (c,d). Scale bars 200 nm (a,c) and 10 nm (b,d). $V = 3.0$ V and $I = 0.2$ nA (a,b). (c) $V = 2.5$ V, $I = 0.6$ nA and (d) $V = 2.5$ V, $I = 0.5$ nA. Reprinted from [69]. 97
- 6.14 **STM images of cleaned (7x7)-Si(111) surface.** STM image of CaF₂/Si after flash annealing at 1200 °C. The surface reveals only (7x7) areas. (a) $V = -2.5$ V and $I = 0.5$ nA. Scale bar 50 nm. (b) $V = 3.5$ V and $I = 0.15$ nA. Scale bar 10 nm. Reprinted from [69]. 98

List of Tables

4.1	Comparison between the experiments and DFT calculated position of the Dirac point with respect to the Fermi level (E_D-E_F), for the samples as-grown, ordered Ge surface after high temperature annealing and intentionally disordered Ge phase after high temperature annealing. The following notation is used: Pristine refers to the intrinsic, undoped Ge substrate; Vacancy refers to the Ge substrate with 1 vacancy in the 3x5 cell; Sb refers to the Ge substrate with 1 Sb atom segregated at the surface.	66
6.1	Predicted values of lattice parameter (a), buckling (δ) and band gap for free-standing 2D low-buckled Si, Ge and Sn.	81

List of Abbreviations

2D	Two-dimensional
3D	Three-dimensional
AFM	Atomic Force Microscopy
ARPES	Angle Resolved Photoemission Spectroscopy
CMOS	Complementary Metal Oxide Semiconductor
CVD	Chemical Vapor Deposition
DAS	Dimer Adatom Stacking fault
DFT	Density Functional Theory
DOS	Density of States
EXAFS	Extended X-ray Absorption Fine Structure
FET	Field Effect Transistor
FFT	Fast Fourier Transform
LDA	Local Density Approximation
LDOS	Local Density of States
LEED	Low Energy Electron Diffraction
LT	Low Temperature
MBE	Molecular Beam Epitaxy
MDCs	Momentum Distribution Curves

MOSFET	Metal Oxide Semiconductor Field Effect Transistor
NEXAFS	Near Edge X-ray Absorption Fine Structure
SPM	Scanning Probe Microscopy
STM	Scanning Tunneling Microscopy
STS	Scanning Tunneling Spectroscopy
TEM	Transmission Electron Microscopy
TMDs	Transition Metal Dichalcogenides Electron Microscopy
UHV	Ultra High Vacuum
XAS	X-ray Absorption Spectroscopy
XPS	X-ray Photoelectron Spectroscopy

Introduction

1.1 Motivation for Novel Electronics

The improvements of electronic components have been achieved mostly through dimensional scaling [1]. The fundamental units of modern electronic devices are the transistors, which exist in different types, including field-effect transistors (FETs). A FET is a three terminals device, with two of them (source and drain) separated by a channel region, and the third one (called gate) separated from the channel by an insulating barrier [2]. In order to operate a FET, a voltage is applied between source and gate, which induces a current flowing from the source to the drain terminal through the conducting channel.

Among the various type of FETs, the metal oxide semiconductor FET (MOSFET) is the most commonly used in electronics, a simple model of MOSFET is shown in figure 1.1. As explained by Dennard [3], in order to scale down a FET to a small size, all the physical dimensions have to be proportionally scaled down while the doping concentration of the conducting channel has to increase.

The progress in semiconductor technology is reflected in the doubling of the number of components, such as transistors, that follows the well-known Moore's law [4, 5]. Indeed, in the recent years, the semiconductor industry was able to offer silicon logic technologies at the 7-nm technology node¹ [6]. Alongside, memory technologies stopped following the common dimensional downscaling of geometry with the dynamic random access memory (DRAM) moving to the stacking of logic

¹A technology node is a generation of semiconductor manufacturing processes associated with a particular size.

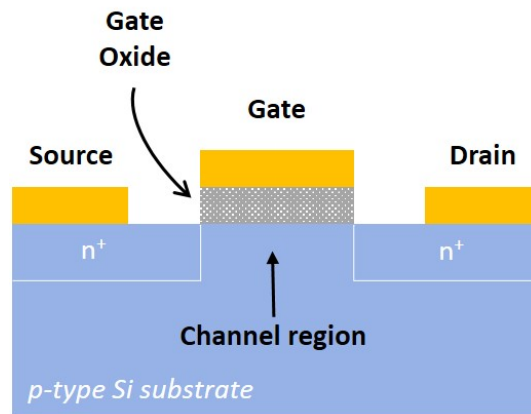


Figure 1.1 | Model of a MOSFET. Cross-section of an n-channel Si MOSFET. The length of the channel is defined by the length of the gate terminal. The thickness of the channel is the depth to which the electronic properties of the semiconductor (*p*-doped Si in this model) are influenced by the gate.

units to provide the memory capacity, decrease latency and increase bandwidth. All these features are required in order to improve computing systems.

Similarly, the flash memories, which are the main data storage devices, also stopped the dimensional downscaling in the two-dimensional (2D) plane of the chip. Indeed, both the current and future generations of flash memories offer larger storage capacity by stacking multiple layers of memory units in the third dimension.

Given the continuous increase in demand for faster and more powerful electronic components, the semiconductor industry has to face some pressing questions.

How will the future technologies provide the required efficiency of computing systems? Will future applications require novel materials and device architectures? How to integrate the novel materials with the current semiconductor infrastructure? What is the new metric to assess technological progress now that the geometric dimension of devices has ceased to be *the* suitable metric?

In order to build FETs that can quickly respond to variation of the source-gate voltage, the gate length needs to be short and the carriers in the channel fast. However, already in the 1990s, it was understood that the dimensional scaling reached its limits because of the degraded electrostatic integrity and other issues associated with short gate barriers [7]. All these problems are collectively known as short-channel effects [8].

The scaling theory predicts that a FET with a thin insulating barrier combined with a thin channel region (measured in the vertical direction in figure 1.1) will not

suffer from short-channel effects even for very short gate lengths (measured in the horizontal direction in figure 1.1) [9].

Unfortunately, for three-dimensional (3D) semiconductors, the carrier mobility and transport along a channel below 3 nm degrades considerably [10].

Therefore, to sustain the demand for higher performance of future electronic devices and processes for complementary metal-oxide-semiconductor (CMOS) technology², novel materials need to be employed for the channel. In this scenario, many advantages might be offered by 2D materials, which could in turn have a massive economic impact on semiconductor technology, as summarized in figure 1.3.

Even though within a *three dimensional* world, the term *2D material* is intrinsically faulty, it well describes the main characteristic of these materials. 2D materials are indeed only one- or few- atoms thick. Thus, the possibility of building channels with a thickness of one- or few- atoms makes 2D materials extremely attractive for FETs.

Triggered by the mechanical isolation of graphene, a single atomic layer of graphite, and motivated by their remarkable properties, the 2D materials have been intensively studied and over the last two decades the scientific community has achieved important advances in the field. An overview of different 2D materials is presented in figure 1.2.

The technological application of graphene is expected to revolutionize the electronic industry, which is still built on conventional semiconductors, mainly on silicon. For economic reasons, it is hard to think that the technology will suddenly switch from Si to graphene. Instead, a breakthrough point can be achieved if graphene is integrated with CMOS compatible platforms.

However, many are the challenges and obstacles to effective integration of graphene with current technology.

One of the major challenges is the fabrication of graphene in sufficient quantity and quality to be commercially relevant. Graphene was first produced via mechanical exfoliation³ from graphite, which is an easy method to produce good quality graphene. However, it is not a commercially viable technique [12].

²CMOS technology is the main technology for manufacturing integrated circuits. It uses both n- and p-type transistors and the signal that switches ON a transistor type, switches OFF the other one.

³Mechanical exfoliation is a top-down approach where graphene is prepared by exfoliating graphite. In the ideal case, graphene can be peeled from the bulk graphite layer by layer. This method usually leads to graphene flakes of different sizes and thicknesses.

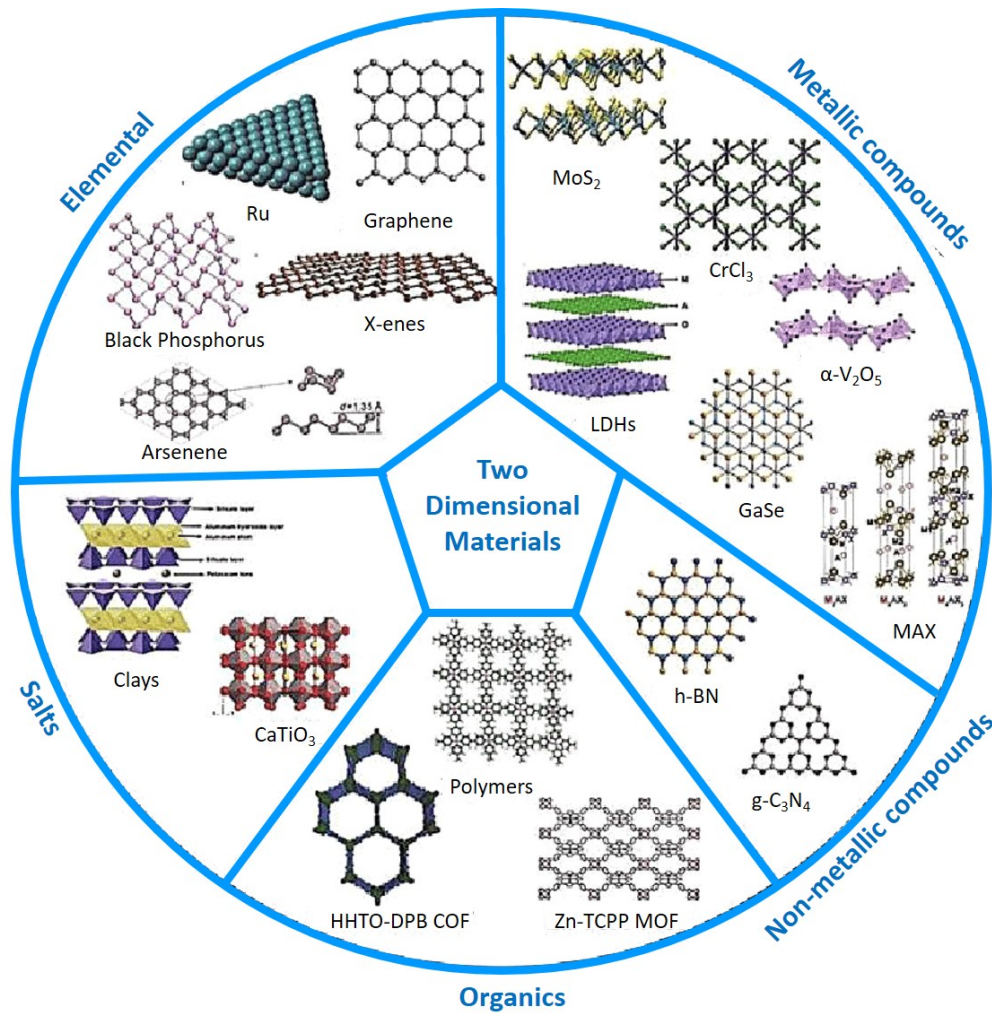


Figure 1.2 | Overview of 2D materials. Summary of different categories of 2D materials according to their composition. Adapted from [11].

Therefore, various alternative methods have been developed to support an eventual large scale production. Among those, chemical vapor deposition (CVD) [13] has been remarked as the most promising graphene production method because of the relatively high sample quality and scalability.

As previously stated, the emergence of graphene also boosted the research for novel 2D materials, which are heavily studied and display outstanding properties that could (i) improve existing applications, (ii) create new structures consisting of their combinations and (iii) overcome the challenges and limitations of graphene itself. Indeed, graphene presents also some fundamental weaknesses, above all the lack of bandgap that, so far, has hampered its effective integration in digital logic devices.

Current silicon MOSFETs have the capability to switch-off, meaning that at steady state no current flows through the gate⁴. Thus, current silicon CMOS offers very low power dissipation thanks to the excellent switching capability, which in conventional FETs requires channels made of semiconducting materials with sizeable bandgaps.

Therefore, because of the absence of energy bandgap, a graphene device could not be switched off, which would lead to both high leakage currents and high energy dissipation.

However, it is important to note that this problem is not unsolvable and many research groups are working on different strategies to overcome this limitation, for example via the application of an electric field [14], quantum confinement of carriers in nanometer-scale ribbons [15], surface functionalization with various atoms [16, 17], interaction with the substrate [18], and strain engineering [19].

For all these reasons, the development of synthesis, characterization, and device fabrication processes for graphene has acted as a platform to study and develop all the other 2D materials.

1.2 Graphene's Electronic Properties

Graphene is a monolayer of sp^2 hybridized carbon atoms, arranged in a hexagonal structure called honeycomb lattice [20], as shown in figure 1.4.

Graphene was first isolated in 2004 via mechanical exfoliation by Geim and Novoselov [21] and it has attracted interest for its ultrahigh carrier mobility ($>10000 \text{ cm}^2/\text{Vs}$)

⁴In this context, within the terminology of digital logic, *gate* does not refer to the gate terminal of a transistor. It refers to a combination of at least two transistors able to perform a logic operation.

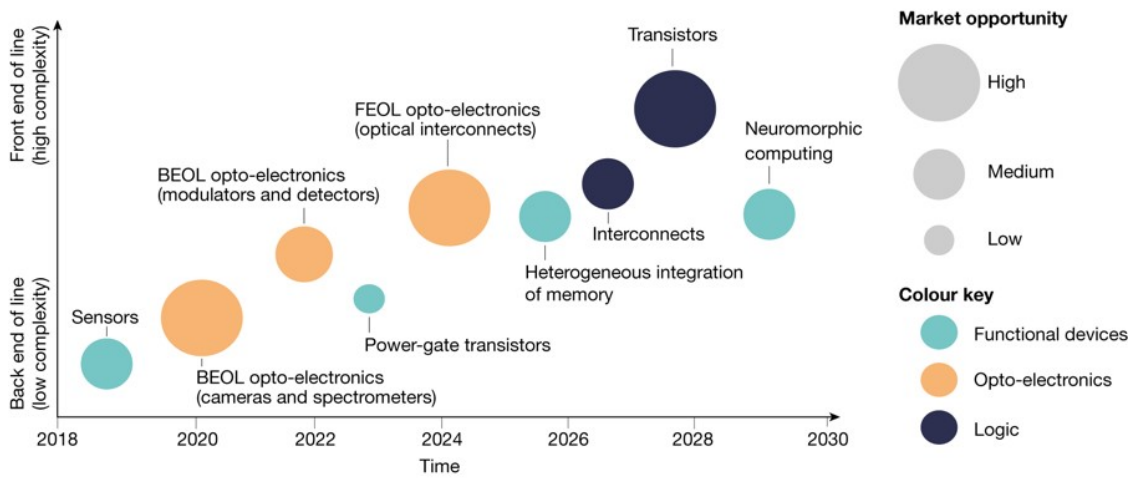


Figure 1.3 | Potential applications of 2D materials and modern transistor devices. Applications of 2D materials integrated with conventional semiconductor technology mapped in time and integration complexity. The area of the circles is a rough qualitative estimate of addressable market opportunity. The position of a circle indicates the time when the first products with the 2D materials-based technology could potentially be introduced. Complexity increases when moving from back end of line to front end of line integration. Adapted from [6].

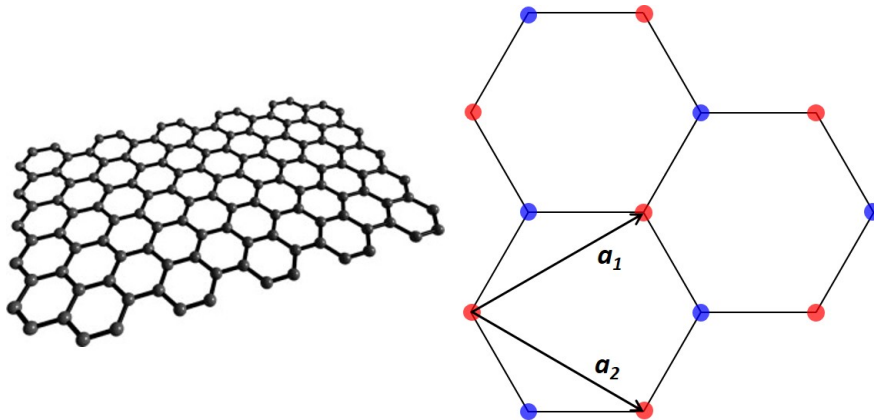


Figure 1.4 | Graphene. On the left, schematic of a graphene monolayer. On the right, the lattice structure of graphene, made out of two interpenetrating triangular lattices. a_1 and a_2 are the lattice unit vectors (2.46 Å) and d is the nearest-neighbor vector (1.42 Å).

[20], optical transparency [22], high thermal conductivity [23], and impressive mechanical properties [24].

In-plane σ bonds result from the sp^2 hybridization of the s , $2p_x$ and $2p_y$ orbitals and connect each atom with its three nearest neighbors, with a bond length of 1.42 Å [20]. The σ bonds account for the robustness of the lattice structure in graphene and all its derivatives. Due to the Pauli principle, these electronic bands have a filled shell and thus form a deep valence band. The fourth carbon valence electron is in the $2p_z$ orbital. The $2p_z$ orbitals are orthogonal to the graphene plane and form the π bonds, which account for a delocalized electron cloud. Since each p_z orbital has one extra electron, the band is half filled [20]. Graphene's electronic structure is rather unique and can be described using a tight-binding Hamiltonian [25].

The p_z electrons, which form the π bonds, can be treated independently from the other valence electrons. Within this π -band approximation, the dispersion relation restricted to the first nearest neighbor interaction brings to the formation of two non-interacting bands π and π^* .

The π states form the valence band and the π^* states the conduction band. These two bands touch at six points called the Dirac points. The symmetry of the system allows these six to be reduced to a pair of independent points, denoted as K and K'. In 3D materials, the electrons at band edges follow a quadratic energy-momentum relation. Instead, in graphene, the bands have a linear dispersion and their structure can be seen as two cones touching at the Dirac points, as described in figure 1.5.

The crossing of the bands is allowed because the orthogonal π and π^* states do not interact. The fact that the two bands touch at the Dirac points indicates that graphene has zero bandgap, and it is therefore described as a zero-gap semiconductor. Since the band structure is symmetric around the Dirac points, electrons and holes in pure, free-standing graphene should have the same properties [25]. The full derivation of the electronic band structure is omitted here, but a detailed description can be found in [20].

Graphene's charge carriers exhibit very high carrier mobility, up to $\sim 10^6$ cm²/Vs in suspended devices [26]. When graphene is deposited on a substrate, mobility is reduced due to scattering caused by surface roughness, charged traps, defects, etc. On the most commonly used substrate, oxidized silicon wafers, graphene shows charge carrier mobility up to a few thousand cm²/Vs at room temperature [20] due to scattering and charge inhomogeneity.

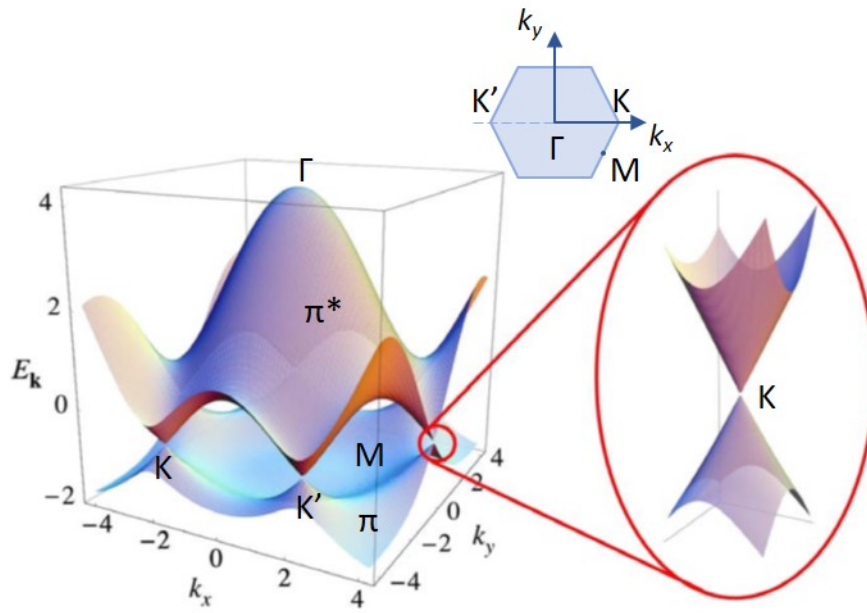


Figure 1.5 | Graphene linear dispersion. Energy band diagram of graphene with a zoom-in of the energy bands close to one of the Dirac points, showing the linear dispersion. The valence π and conduction π^* bands are well separated. The Fermi level coincides with the Dirac points where the bands touch. Figure adapted from [20].

Because of the linear dispersion, charge carrier transport in graphene is ambipolar [25], meaning that the majority of charge carriers can be continuously tuned between electrons and holes by applying an electric field by a suitable gate [27]. Gate bias shifts the Fermi level E_F either above or below the Dirac point, resulting in electron or hole transport, respectively [25]. As the Fermi level is shifted by the gate, the density of states (DOS) and thus the carrier density is changed [25]. The Fermi energy can be shifted away from the Dirac point, either by applying a gate voltage or by doping, as schematically reported in figure 1.6.

The resistance is determined by the response of electrons to the electric fields. Theoretically, the resistance in pristine graphene can reach values around few hundreds of Ω/sq , but can be highly increased (up to $10^5 \Omega/\text{sq}$) in presence of defects such as interflake junction or grain boundaries, which act as tunneling barriers and obstruct the movement of the electrons [28]. Graphene's resistance is related to the DOS of its substrate, thus, since the DOS of graphene can be tuned by doping, the resistance can slightly change depending on the interaction with the substrate [28].

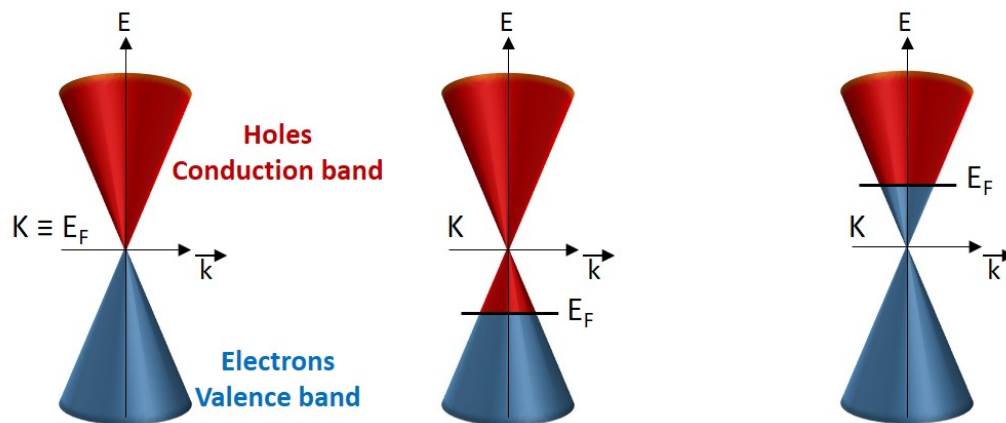


Figure 1.6 | Graphene energy dispersion around Dirac point. Blue indicates levels filled with electrons while red indicates empty levels (holes). On the left, neutral graphene where the valence band is completely filled with electrons and the conduction band is completely empty. The Fermi level and the Dirac point coincide for this case. In the middle, some electrons are drained from the valence band. This case corresponds to hole-doped graphene where the Fermi level shifts below the Dirac point. On the right, some extra electrons are forced into the conduction band. This case corresponds to electron-doped graphene where the Fermi level shifts above the Dirac point.

1.3 Chemical Vapour Deposition Growth of Graphene

CVD is a process used both in research and industry to deposit thin films of various materials [29] by feeding a source gas at a suitable temperature. The process parameters such as temperature, pressure, and source gas flow, have a key role in the resulting structure of the film deposited in terms of thickness (from one layer to few layers) and defects. The fundamental five steps of a CVD process (illustrated in figure 1.7) are:

- Diffusion of precursors to the substrate surface
- Adsorption of precursors onto the substrate surface
- Catalytic reactions of precursors on the substrate surface
- Supersaturation of species on the surface leading to nucleation
- Growth and expansion of nucleated domains

The layer grown by CVD usually shows several domains, with different orientations separated by grain boundaries. The dimension of the domains depends mainly on the growth conditions. Graphene is now commonly grown via CVD and its electronic properties are highly influenced by the final structure of the layer. Indeed, a high concentration of grain boundaries leads to low mobility because the movement

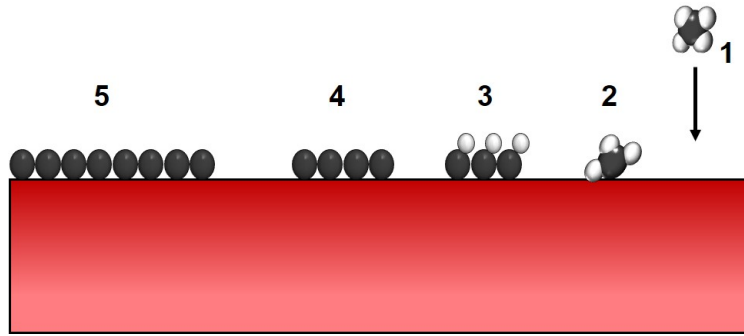


Figure 1.7 | CVD process. Schematic illustration of the main steps of graphene CVD on copper. 1) Diffusion of precursor gases, 2) surface adsorption of precursors, 3) catalytic reactions of precursors on the surface, 4) supersaturation of species and nucleation, and 5) growth of nucleated domains.

of the electrons is obstructed by the presence of defects in the honeycomb lattice [30].

From a technological point of view, graphene synthesis on metals have great potential [31, 32] and it was shown that huge monolayer graphene sheets with size up to 30 inches can be synthesized on polycrystalline Cu foil and then transferred onto a final substrate for further processing. However, the technological adaptation of such synthesized graphene on metals followed by the transfer onto the desired substrate has several drawbacks.

The first one is the low scalability of this method, which does not allow the controllable production of graphene of the desired shape and edge configuration. The second is connected to the chemical reagents and polymers used in the transfer process. Together with the contaminants that are unavoidably present in the chosen substrate, these two factors lead to the fabrication of the contaminated graphene–substrate interface, which can drastically modify graphene’s transport properties. The third main drawback after the metal-based graphene synthesis is connected with the residual metal contamination (Cu, in most cases, as a widely used substrate for mass production) of a graphene layer [33, 34]. It was found that even small amounts of metals ($\sim 10^{13}$ - 10^{14} atoms/cm²) may be relevant during front-end-of-line integration approaches and can lead to the contamination of Si-based devices and cross-contamination of fabrication tools.

Therefore the search for graphene synthesis methods directly on semiconductor surfaces was very active in the last decade. In such a way, synthesized graphene layers, either after their transfer onto the desired semiconductor support or directly grown on semiconductors, can be used in different attractive applications [35, 36].

Further progress in the search for appropriate methods and semiconductor substrates led to the discovery of the direct graphene CVD synthesis on Ge surfaces in 2013 [37], followed by the successful implementation of this approach for wafer-scale graphene preparation [38].

1.4 Ge as substrate for Graphene Growth

Among conventional semiconductors, germanium proved itself to be an excellent substrate to grow graphene [38] in contrast to silicon, in which carbon atoms have high solubility. The catalytic activity of Ge for growing graphene has stimulated interest in the graphene/Ge system in the field of device physics [39–41] and material science [42–45].

The first experiments reporting the direct growth of graphene on Ge substrates using CVD [37, 38, 44, 46] showed that all main surfaces of Ge – (001), (110), and (111) – are suitable for growing graphene. Although the choice of the surface affects both the quality of graphene and the morphology of the interface. The successful deposition is possible thanks to the catalytic activity of Ge and because C has an extremely low solubility in Ge ($<0.1\%$) [37]. Graphene growth on Ge via CVD is a self-limiting and surface-mediated process, similar to the growth on Cu substrate, and a crucial role is played by the deposition temperature, which affects the alignment of graphene grains on the substrate.

After a few promising works on the (110), most of the attention has been focused on the Ge(001) surface. However, the experiments concerning the Ge(100) surface have shown that the surface under the graphene flakes or ribbons is severely faceted along $\{1,0,L\}$ orientations [39, 47]. The formation of these nanofacets questions the suitability of this interface for further technological processing, and has led to renewed interest in graphene/Ge(110) for which the underlying Ge surface not only remains flat but also promotes the formation of large graphene domains.

On the other hand, surprisingly little attention has been paid to the graphene/Ge(111) system so far. Indeed, the Ge(111) surface could be expected to be the best choice for a high-quality heteroepitaxial graphene film from a symmetry point of view, similar to numerous cases of (111) metal substrates. However, it has been demonstrated that graphene tends to be polycrystalline and the domains do not show a preferential alignment [38].

Despite quite a few studies have been published on the graphene/Ge system, there is still confusion about the structure and potential of this promising interface.

1.4.1 (100) Surface

Wang et al. [37] developed a synthesis method for large-scale and high-quality graphene directly on Ge substrates by atmospheric pressure CVD. The study highlighted the catalytic properties of Ge for growing graphene. Based on the results, the authors proposed a self-limiting mechanism for graphene growth on Ge substrate, which is an analog of graphene on Cu foil. The obtained graphene on Ge substrate is scalable and compatible with the mainstream microelectronics technology.

Notably, a study by Scaparro et al. [48] suggested a layer-by-layer growth regime, a model similar to that proposed in [32] for Cu substrates. The growth proceeds in a layer-by-layer regime when, under the specific process conditions, the concentration of C species before the nucleation is just above the critical super-saturation level. The nucleation and growth of graphene grains deplete the adsorbed carbon species, reducing their concentration so that the nucleation rate becomes negligible and only monolayer domains can grow and coalesce. The uniformity and structural quality of graphene are influenced by the $\text{H}_2:\text{CH}_4$ flow ratio during the CVD process [49] and graphene's roughness depends on the Ge substrate [49], and the rough morphology of Ge can be directly related to the presence of defects and strains [48].

Interestingly, the quality of the graphene deposited on Ge(100) abruptly changes when it is grown around 930 °C - thus, very close to Ge melting point - due to the combination of two effects [50]. Indeed, on the one hand, Ge surface corrugates at the nanometer-scale below 930 °C while the graphene bulks-up to form nano-wrinkles and ripples and develops a larger density short-wavelength corrugations on the Ge. On the other hand, at 930 °C the absence of facets results in a high-quality layer, flat on the scale of the facet size.

The abovementioned faceting phenomena on Ge(100) was first reported by Jacobberger et al. [39] and later investigated by McElhinny et al. [47]. The Ge facets form at high temperatures during the deposition of graphene and are stable after cooling at room temperature. Moreover, the facets are highly selective and belong to the $\{1,0,L\}$ family [39], in particular tending towards the $\{1,0,7\}$ [47].

It is worth noticing that the dramatic changes in the Ge topography occur only within an extremely narrow temperature range, as shown in figure 1.8, in which the catalytic properties of Ge and the graphene formation are not altered. The quasi-liquid adlayer of Ge is stable only within a few degrees to the Ge melting point [51, 52]. The weakening of the in-plane bonds in the melted layer results in

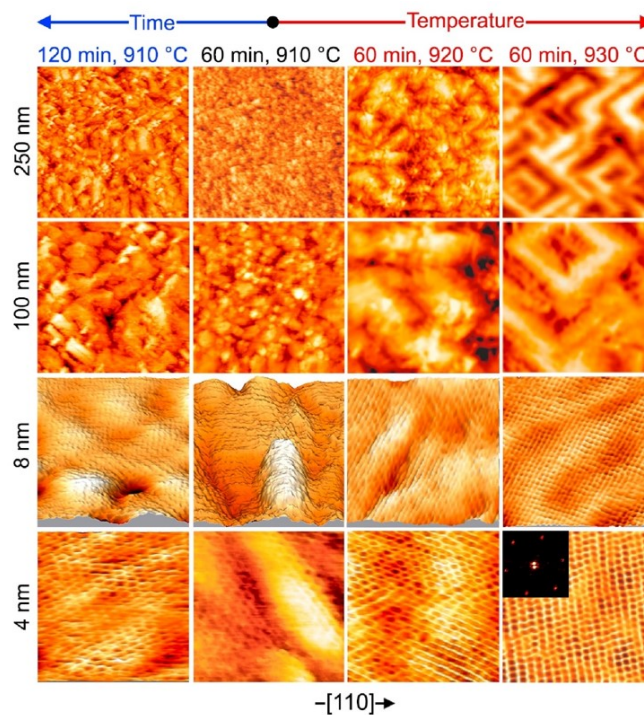


Figure 1.8 | Graphene/Ge(100). Serie of scanning tunneling microscopy (STM) images of the different samples as a function of temperature and deposition time. The third row from the top shows a comparison of 3D topographies with the z-axis range 0 - 12 Å. The inset shows the Fast Fourier Transform of the high-quality graphene observed for the sample grown at 930 °C and deposition time of 60 min. STM images were acquired with the $V = 50$ mV and $I = 1.8$ nA. Reprinted from [50].

a higher diffusivity and sublimation rate for the surface atoms of the substrate, which affects the graphene films [53, 54]. The graphene domains growing on the quasi-liquid Ge layer lead to local asymmetry in the sublimation rate, resulting in the formation of height instabilities in the areas covered by graphene [55].

Distortions in the graphene structure indicate the presence of strong interactions between graphene and Ge, which results in the parabolic tunneling conductance probed by scanning tunneling spectroscopy (STS) [56].

On the other hand, at 930 °C the quasi-liquid Ge layer has high mobility and thus it can smoothen out the local corrugations of the surface, preventing the curvature in graphene. At the scale of the facet size (i.e. several tens of nanometers), the Ge substrate provides atomically flat and electronically homogeneous support that allows the graphene layer to reduce the interaction with the substrate as confirmed by the linear behavior of the tunneling conductance [56].

1.4.2 (111) Surface

From a symmetry point of view, Ge(111) is theoretically the best choice to grow high-quality heteroepitaxial graphene. However, in practice, graphene tends to grow polycrystalline on this surface with no preferential domains alignment. This is the major reason for few reported studies on the graphene/Ge(111) system.

The successful CVD growth of monolayer graphene on the isotropic Ge(111) surface was first reported by Lee et al. [38]. However, low-energy electron diffraction (LEED) measurements and transmission electron microscopy (TEM) images revealed that the deposited graphene was, as said before, polycrystalline and with no preferential domain orientations, as reported in figure 1.9. Moreover, Raman spectroscopy confirmed the presence of monolayer graphene although the intensity ratio between D and G peaks was high [57], suggesting the presence of extended grain boundaries in the polycrystalline graphene grown on Ge(111).

There is no doubt that CVD is a successful method to deposit high-quality graphene onto Ge substrate under the right growth conditions, however, it is a complicated multi-step process. An alternative could be C deposition from e-beam evaporation, a simpler method to grow graphene. Indeed, further investigations used this technique with Ge(111) surface kept close to the melting point (~ 938 °C) [58]. The results of the study highlight how the surface morphology of the samples changed with the deposition time and the root mean square roughness of the surface increases with longer deposition times, as longer C exposure leads to the formation of wrinkles.

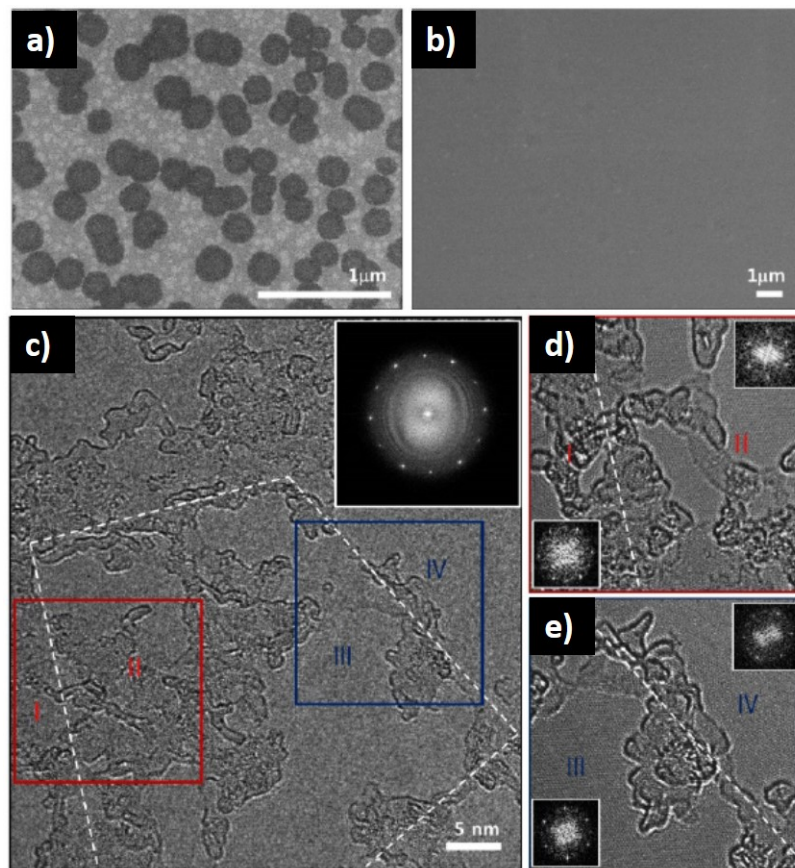


Figure 1.9 | Polycrystalline monolayer graphene grown on Ge(111) surface. a) A scanning electron microscopy (SEM) image of graphene seeds formed at the early stage of growth. b) A SEM image of flat monolayer graphene grown from the seeds in (a). c) high-resolution TEM image of polycrystalline graphene. The inset shows the Fast Fourier Transform diffraction pattern of the TEM image, indicating that the graphene obtained from the Ge(111) surface has two main orientations. d,e) Magnified TEM images at selected regions (Region I, II and Region III, IV) in (c), showing that the misorientation angle between two domains is 30° . Adapted from [38].

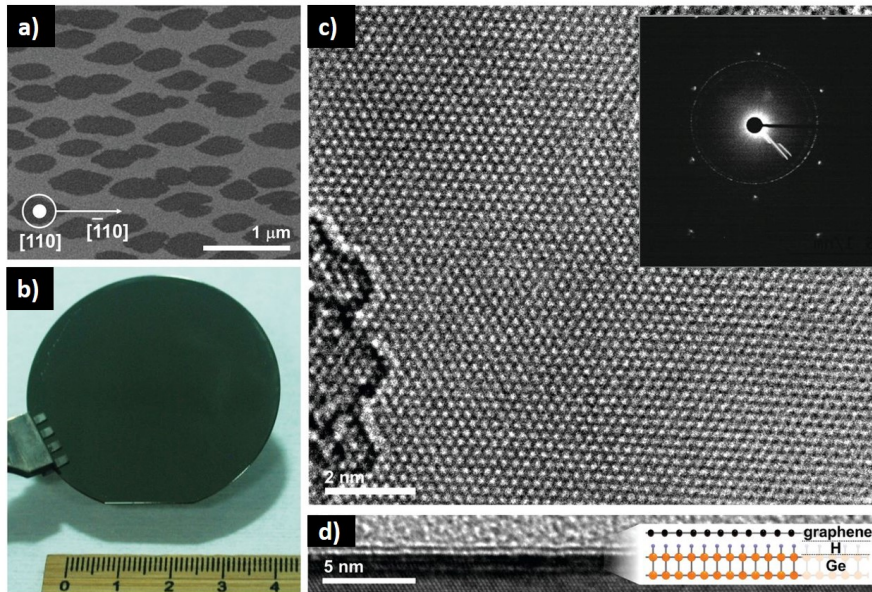


Figure 1.10 | Single-crystal monolayer graphene grown on Ge(110) surface. a) A typical SEM image of graphene seeds at the early stage of growth. b) Picture of graphene grown on a Ge/Si (110) wafer. c) A high-resolution TEM image of the single-crystal monolayer graphene. (Inset) Four overlaid Selected Area Electron Diffraction patterns, which were measured across the four different points. The distance between each point is $\sim 2 \mu\text{m}$. d) A cross-sectional TEM image demonstrating that the as-grown graphene is monolayer. (Inset) A schematic illustration of the monolayer graphene grown on the H-terminated Ge surface. Adapted from [38].

On the other hand, the roughness of the surface remained comparable with that of the bare Ge surface and Raman data suggests that the more C is deposited, the smaller the average crystal size of graphene domains. It should be noted that the structural nature and morphology of graphene layers grown in this way still need to be fully understood.

1.4.3 (110) Surface

The (110) surface of Ge has attracted a lot of interest as it can support the growth of single-crystal graphene on a wafer-scale [38, 59–62]. Moreover, the faceting phenomenon does not occur on this surface [63, 64]. Indeed, the two-fold in-plane surface symmetry of the Ge(110) surface supports single-crystal graphene growth, the early stage islands in the deposition process are uniaxially aligned along the $[\bar{1}10]$ direction of the surface substrate and then grow to form the high quality graphene monolayer on an entire substrate [38], as shown in figure 1.10. At present, the understanding of the graphene/Ge(110) interface is largely limited to its morphology, while still little is known about the electronic properties. Attention has been focused on the interfacial structure of graphene with the Ge(110)

surface. Indeed, when graphene is synthesized via CVD, the Ge substrate features a hydrogen-passivated surface [65]. Upon annealing in vacuum above 300 °C, the hydrogen atoms on the surface start to desorb and the Ge surface reconstructs into the (6x2) phase [65–67], which has never been observed on bare Ge. It has also been shown that further in-vacuum annealing to temperatures closer to the Ge melting point leads to additional structural modifications of the Ge surface, and possibly to the formation of stronger bonds between graphene and Ge [67]. Yet, despite the few morphological studies, little is known about whether and how these structural changes affect the system’s electronic properties.

1.5 Thesis Outline

This thesis revolves around the two main projects I have worked on during the last three years. Namely, (i) the characterization of the structure, electronic and chemical properties of the graphene/Ge(110) interface and (ii) the growth and characterization of CaF₂ deposited on Si(111). CaF₂ could be a potential substrate to grow a novel 2D material, called silicene, which is the Si-based counterpart of graphene as the name suggests. The two studies have been published in the Journal of Physical Chemistry Letters [68] and in the Journal of Physics D: Applied Physics [69], respectively. In addition, a review article regarding group-IV X-enes, which include silicene, was published in Applied Physics Reviews [70]. These three publications constitute the core of this thesis. Here, I briefly outline the contents of the chapters.

Chapter 2: consists of a summary of the experimental equipment and main experimental techniques used throughout the thesis. This chapter does not give a full comprehensive review of the methods but rather aims to give the reader the information necessary to understand the following chapters.

Chapter 3: describes the structure of the graphene/Ge(110) interface using scanning tunneling microscopy (STM). Specifically, the study here presented describes how the structure of the interface changes upon annealing in vacuum above 350 °C and after high temperature annealing in vacuum above 700 °C. The results presented have been published in ref. [68].

Chapter 4: describes the electronic properties of graphene grown on Ge(110) surface using angle resolved photoemission spectroscopy (ARPES). Supported by a theoretical model, the experimental findings in this chapter links the electronic properties to the structural modification of the interface described in chapter 2. The experiments presented have been performed at the SGM-3 beamline of the

synchrotron radiation source ASTRID-2 (Aarhus, Denmark). The results presented have been published in ref. [68].

Chapter 5: contains the investigation of the chemical properties of graphene on Ge(110) by means of X-ray photoelectron spectroscopy (XPS) and near-edge X-ray absorption fine structure spectroscopy (NEXAFS). This chapter complements the the previous two. The experimental measurements have been performed at the BACH beamline of the synchrotron facility ELETTRA (Trieste, Italy). The results presented are currently been drafted into a manuscripts.

Chapter 6: briefly introduces a novel class of 2D materials known as group-IV X-enes, focusing on the opportunities and challenges of these materials, which could constitute powerful alternatives to graphene. In particular, the emphasis is put on silicene and the importance of finding a suitable substrates for its epitaxial growth. To this end, the last section presents the case of $\text{CaF}_2/\text{Si}(111)$ substrate. The chapter is based on the results published in ref. [70] and in ref. [69].

Chapter 7: provides a brief summary of the main results presented in the previous chapters.

Experimental Techniques

This chapter describes the equipment used to grow the $\text{CaF}_2/\text{Si}(111)$ samples and to perform STM characterization. In addition, it introduces the working principles of the major experimental techniques used throughout this work.

2.1 Infinity LT - UHV System

The main part of the experimental work during my project has been performed using the low-temperature (LT) ultra high vacuum (UHV) system called Infinity from Scienta Omicron, which I helped to install at the beginning of the project. Working in UHV conditions is necessary for the experiments within the field of surface science, as ambient conditions contaminate the samples surface immediately. A picture of the system is provided in figure 2.1. The setup consists of two main parts: the preparation chamber and the analysis chamber, which are separated by a gate valve.

The base pressure in the Infinity system is on the order of 10^{-10} mbar and the preserved by a combination of ion getter pumps and titanium sublimation pumps (TSP), and a turbo pump. The pressure is continuously monitored by two ion gauges, one in each chamber. Additionally, a load lock chamber is attached to the preparation chamber and the two are separated by a gate valve. The samples are loaded into the preparation chamber through the load lock, which can store multiple samples at the same time. Approximately, after pumping down the load lock for one hour, the samples can be transferred into the preparation chamber without ruining its base pressure.

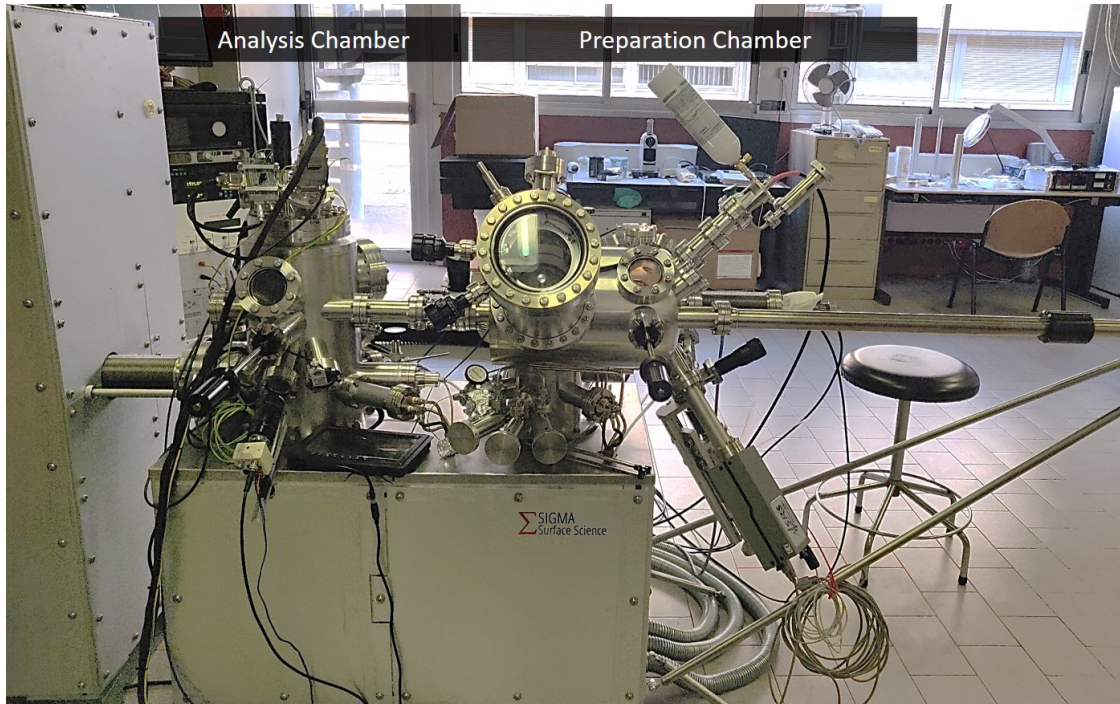


Figure 2.1 | The LT-UHV Infinity System. The system consists of two chambers connected. The samples are deposited in the preparation chamber and moved to the analysis chamber for scanning probe microscopy (SPM) characterization.

Preparation Chamber

Once the sample is loaded into the preparation chamber, it can be placed on the heating stage for annealing and/or sputtered by Argon ions using the dedicated ion gun, if needed. The preparation chamber is equipped with a combined low energy electron diffraction (LEED)-Auger system provided by SPECS for sample characterization and with an electron beam (e-beam) evaporator, specifically the QUAD-EV-C Mini e-beam evaporator provided by Mantis. A picture of the evaporator is shown in figure 2.2.

E-beam evaporation is a form of physical vapor deposition in which the target material to be deposited is bombarded with a beam of electrons from a charged tungsten filament. This technique is commonly used when the materials to deposit are difficult to evaporate with standard thermal methods and when the applications require high purity samples.

The evaporation head is made of copper and cooled with flowing water during operation. This ensures that all parts of the evaporator stay close to room temperature except for the emission filament and the source material, so that the outgassing during evaporation is negligible. The evaporator head has four different pockets, as shown in figure 2.2b. Thus, up to four different materials can be loaded at

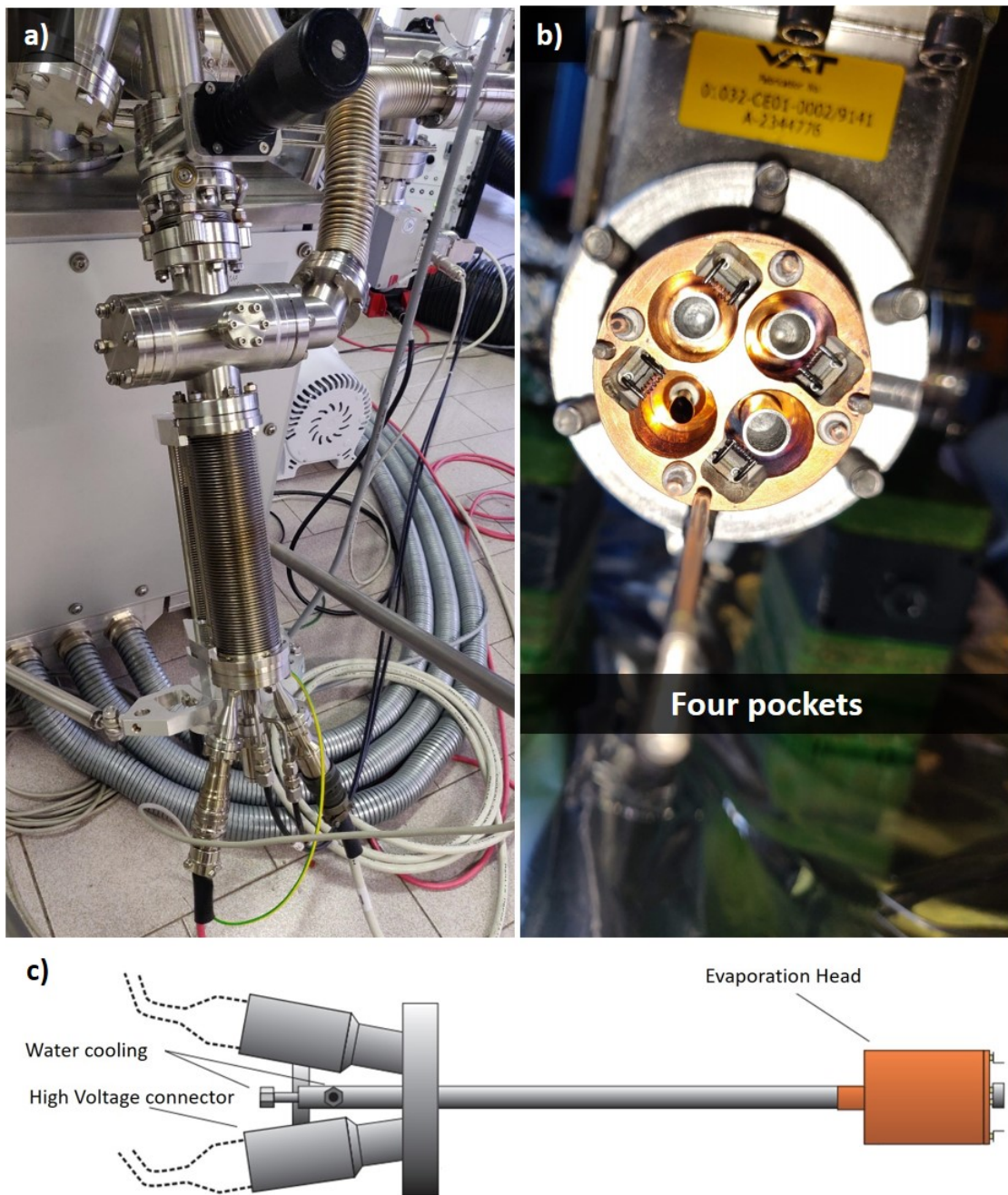


Figure 2.2 | E-beam evaporator. a) Picture of the QUAD-EV-C Mini e-beam evaporator from Mantis uses in this thesis work to evaporate CaF_2 onto Si(111) substrate. b) Picture of the four-pocket of the evaporator, where the material to evaporate is loaded either in pellets within Mo crucibles or as a rod. c) Schematic of the evaporator.

the same time, and each pocket has its own independent filament, flux, and high-voltage channels. The pockets can be equipped either with rods or with crucibles. We use rods to evaporate Si and crucibles in Mo to load and evaporate CaF_2 pellets.

Analysis Chamber

The analysis chamber used for characterization of the samples consists of a scanning probe microscopy (SPM) that works as both high-resolution STM and non-contact atomic force microscope (AFM). The analysis chamber is designed to work at both room- and low- temperature (around 10K). All the STM measurements presented in this thesis are performed at $\sim 10\text{K}$. The LT condition is ensured by a pulse tube cooler that relies on liquid-He closed cycle.

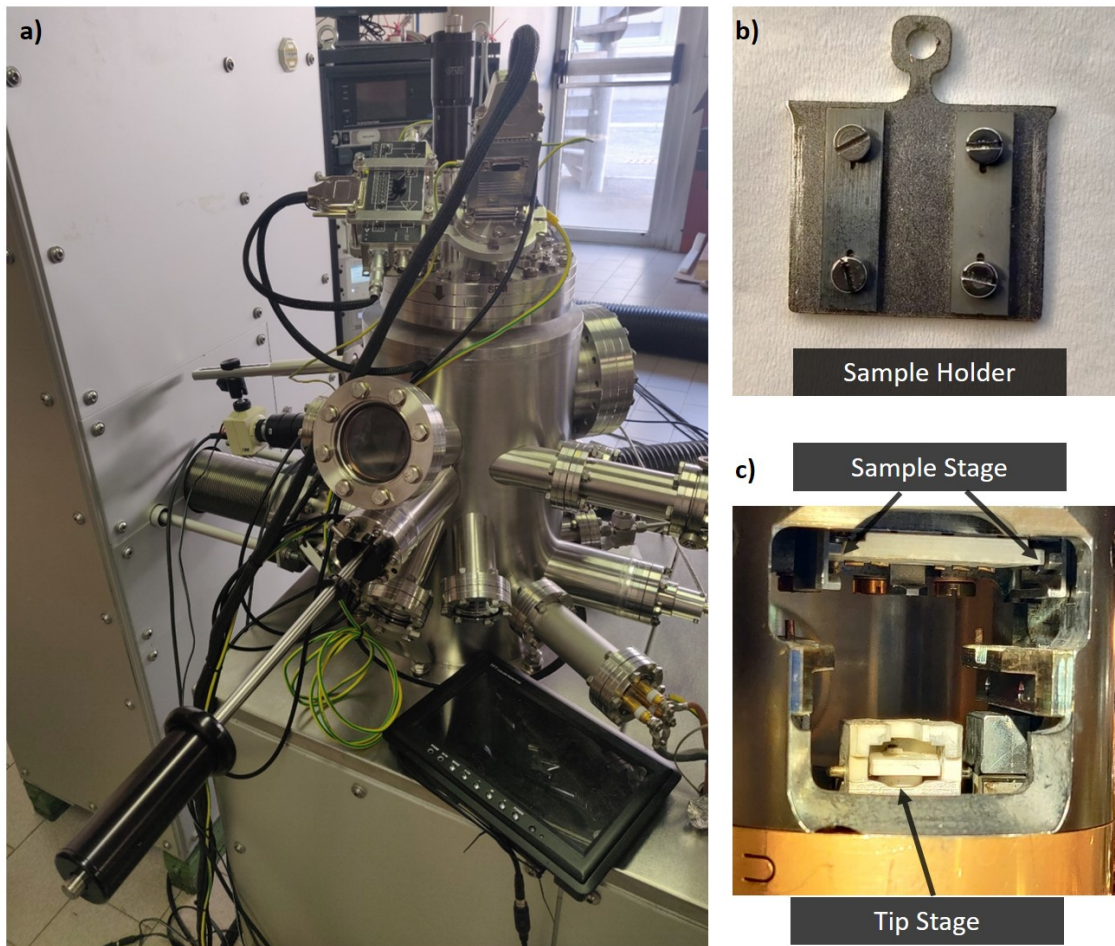


Figure 2.3 | Analysis Chamber. a) Picture of the analysis chamber containing the SPM head for structural characterization of the samples. b) Picture of a typical sample holder and c) picture showing the sample and tip acceptor stages.

The SPM head in the analysis chamber is enclosed by a thermal radiation shield with different view-ports allowing for easy exchange of tip and samples, as can be seen in figure 2.3a. Two main parts constitute the SPM head: (i) the sample

acceptor stage and (ii) the lower building block. The former is where the sample on its holder (shown in figure 2.3b) is placed during the measurements and it also includes the lateral coarse motors for the sample movement (figure 2.3c). The latter contains the tip acceptor stage (figure 2.3c), the vertical coarse motor and the piezoelectric tube scanner (for fine positioning and scanning).

In order to reach atomic resolution during measurements, the SPM head has to be decoupled both from the UHV system and the floor. For this reason, three springs suspend the SPM head and an eddy current damping mechanism is integrated into the system to damp any potential oscillations of the SPM head. During the exchange of tip and/or sample, a clamping mechanism locks the head to protect the piezoelectric tubes responsible for scanning and motion of samples. When no measurements is performed, the same mechanism moves the head to the rapid cooldown position, as it clamps the head against the cold finger responsible for the LT.

2.2 Synchrotron Radiation and Facilities

Synchrotron radiation refers to the electromagnetic radiation emitted when charged particles travel in curved paths. It can be found in nature, as, for example, it is emitted by cosmic sources. It can also be produced in particle accelerators, such as storage rings, usually by electrons.

It is an extremely intense type of radiation and extends in energy from the infrared to the hard X-ray regions of the electromagnetic spectrum. It represents the major source of energy loss in high-energy particle accelerators. Thus, synchrotron radiation was first considered a problem. However, in the late sixties, it was realized that synchrotron radiation could be very useful for the study of condensed matter and that it represents a unique tool in many research fields. Indeed, synchrotron radiation is now used to investigate many different aspects of the structure of matter at atomic and molecular scale, surface properties of solids, and the structure of proteins. The following discussions on the properties of the radiation emitted by storage rings facilities are based on [71] unless otherwise stated.

2.2.1 Storage Rings and Sources

Synchrotron radiation is produced in high-energy electron (or positron) circular accelerators, like storage rings, consisting of circular pipes with magnets (called bending magnets) placed along the circumference and that force the particles to

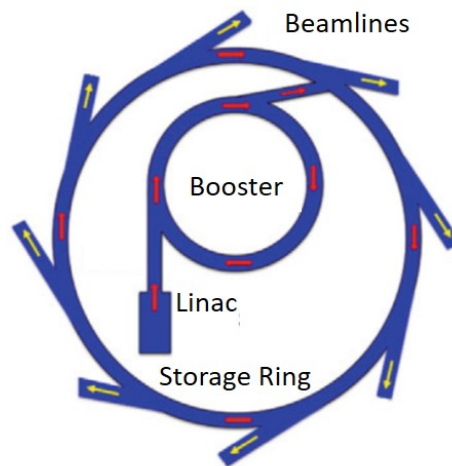


Figure 2.4 | Schematic of a Storage Ring. Simplified schematic planar view of a typical storage ring of a synchrotron facility. Adapted from [71].

follow the designed path. Before entering into the storage ring, the electrons are accelerated by a linear accelerator, called Linac, until their energy reaches the MeV range. From the Linac, the electrons enter into the booster ring, where they reach the GeV range in energy and then can enter into the final storage ring. A simplified model of a synchrotron is illustrated in figure 2.4.

The storage ring consists of an array of focusing and bending magnets connected by linear sections where the radio frequencies cavities are installed to accelerate the particles. A simple model of a typical storage ring is provided in figure 2.5. Once in the storage ring, the electrons can be further accelerated by radio frequency electric fields. At this point, the electrons are in a quasi-stationary situation. The bending magnets ensure the electrons follow circular paths, thus losing part of their energy and emitting synchrotron light. The energy lost in this process is collected passing through the radio frequencies cavities.

One of the main properties of interest for synchrotron radiation is the spectral brightness or flux per unit source area and unit solid angle. Good sources of high brightness radiation are the undulators, characteristic of the third generation sources of synchrotron light, that allowed for an increase of many orders of magnitude in brightness.

2.2.2 Synchrotron Radiation Properties

The main properties of synchrotron radiation are the following:

1. High intensity

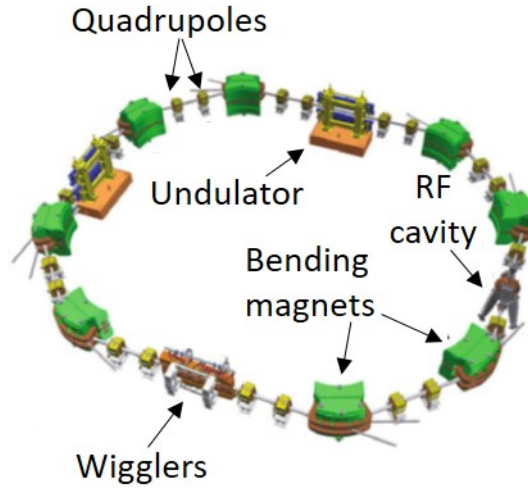


Figure 2.5 | Elements of a Storage Ring. Schematic view of a storage ring where some of the main elements are highlighted. Namely, bending magnets, focusing and de-focusing magnets (quadrupoles), insertion devices (undulator, wigglers), and the radio frequency (RF) cavity. Adapted from [71].

2. Continuous spectral range from infrared up to the hard X-ray region
3. Narrow angular collimation
4. Pulsed time structure
5. High brightness of the source due to small cross-section of the electron beam and high degree of collimation of the radiation
6. High beam stability

In a storage ring, bending magnets keep electrons moving in a closed trajectory applying a magnetic field perpendicular to their velocity. The acceleration of such particles is given by the Lorentz equation:

$$\frac{d\mathbf{p}}{dt} = e \left(\mathbf{E} + \frac{\mathbf{v} \times \mathbf{B}}{c} \right) \quad (2.1)$$

where \mathbf{p} , e and \mathbf{v} are the particle momentum, charge, and velocity respectively. \mathbf{E} and \mathbf{B} are the electric and magnetic fields. The power radiated by a relativistic electron forced to move along a circular orbit, with a radius of curvature R , is given by Schwinger's formula:

$$P_e = \iint P(\lambda, \psi) d\lambda d\psi = \frac{2}{3} \frac{e^2 c}{R^2} \left[\frac{E}{mc^2} \right]^4 \quad (2.2)$$

where λ is the wavelength of the emitted radiation, ψ is the azimuthal angle perpendicular to the orbital plane. $P(\lambda, \psi)$, the power radiated by an electron in a unit wavelength interval centered at λ and in a unit azimuthal angular aperture centered at ψ . E is the electron energy, m its mass, c is the speed of light and mc^2 is the electron rest mass energy (0.511 MeV). In Equation 2.2, the dependence of the radiated power on E^4 must be noted; this implies that to keep the radiated power at reasonable values, it is necessary to increase also their radius R . The energy lost per turn by the charged particle, taking into account a revolution time, $2\pi R/c$, is given by equation 2.3.

$$\Delta E_e = \frac{4\pi}{3} \frac{e^2}{R} \left[\frac{E}{mc^2} \right]^4 \quad (2.3)$$

In a storage ring, radio frequency cavities are used to maintain the energy of the electron beam, by compensating for losses due to the emission of synchrotron radiation. Indeed, the electrons receive energy from longitudinal electric fields present in the radio frequency cavities.

Assuming a situation in which there are no losses of energy, the frequency of the field would be such that an electron traveling at the exact desired orbit would cross the cavity when the electric field is zero. If an electron crosses the cavity earlier than the optimal point, the electric field will have a non-zero value, which will accelerate the electron, giving it energy. The added energy increases the relativistic mass of the electron and thus, its angular velocity decreases. After each revolution, the electron's phase will become closer to the desired one, until it crosses the cavity at zero electric field. However, this particle will still have energy higher than the needed to cross the cavity at the zero field and it will tend to arrive at a time after the optimal electron in later revolutions.

The electric field, in this case, will act to decrease the electron's energy towards the synchronous value. Thus, the particles oscillate in phase and energy around the constant synchronous values generating the so-called synchrotron oscillations. If the goal is to increase the energy of the particles at each turn, one must increase the synchronous value, which, in synchrotron facilities, is done by increasing the magnetic field of the magnets, while the frequency of the electric field remains constant.

The stability of the beam is achieved by applying strict conditions which result in only 5-10% of the radio frequency period being used to restore the electron energy. Those electrons that do not arrive within this interval are lost as they do

not belong to the same stable orbit. This is the reason why the electron beam in synchrotron facilities travels in bunches with time lengths of 5-10% of the radio frequency period.

The total current depends on the number of filled bunches, as the time length of the bunches is limited, so is the number of electrons in each bunch. Therefore, the more bunches injected in the ring, the higher the beam current.

The quality of a photon source must be assessed based on how effective it is for practical applications. A high flux is certainly important as it results in high signal-to-noise ratio. However, it is not sufficient alone to define the "quality" of the source. For many experiments, it is necessary to focus as many photons as possible in a small area. Therefore, a suitable focusing system is needed to achieve this result and the relevant parameter becomes the *spectral brightness*, defined as the number of photons emitted per second, in a spectral bandwidth $\Delta E/E = 0.1\%$ in a unit source area and per unit of solid angle. From Liouville's theorem [72], it follows that the brightness of the source equals the brightness of the beam when it is focused on the sample. The brightness depends on the size of the source and on the angular spread of the radiation, which is given by the size of the electron beam and by the convolution of the angular distribution of synchrotron radiation ($\Delta\psi$) with the angular divergence of the electron beam, respectively. Therefore, the characteristics of the electron beam source are essential in order to determine the brightness of the photon source. In a storage ring, the product of the electron beam transverse size and angular divergence is constant along the ring and is called *emittance*. In order to get high brightness, small emittance machines must be used.

Synchrotron facilities provide radiation with high brightness, meaning that samples can be analyzed with great resolution in a relatively short amount of time. Synchrotron radiation can be used in many characterization techniques, among them, ARPES, XPS and NEXAFS are relevant for this thesis.

2.3 Scanning Tunneling Microscopy (STM)

The demonstration of the feasibility of experiments based on vacuum tunneling in 1981 by Binnig, Rohrer, Gerber, and Weibel [73], opened the door to a new powerful tool for surface characterization: the STM. Furthermore, STM boosted the development of multiple similar techniques, such as, for example, AFM [74] and the magnetic force microscopy (MFM) [75]. These methods have in common that they use a probe to locally observe physical properties down to atomic lateral resolution. The information from the sample is thereby obtained by scanning a probe on the

surface and combining the detected physical properties into an image. Because of the common scanning mechanism, these techniques are collectively known as SPM techniques.

The purpose of this section is to give a short introduction on the STM method, which represents the major characterization technique I used during the project.

2.3.1 Principles

The STM uses the tunneling effect to establish a current between a sharp tip and the sample by applying a voltage between them. The effect is classically forbidden yet allowed by quantum mechanics. The probability of electrons tunneling through a potential barrier (classically forbidden) depends exponentially on the width of the barrier. In vacuum, the distance between tip and sample acts as the potential barrier.

From quantum mechanics, the wavefunction of an electron at the surface of an electrode does not become zero at the potential barrier but it decays exponentially within it, as simply illustrated in figure 2.6a. This means, that when two electrodes (i.e. tip and sample in an STM experiment) are close enough to each other, the wavefunction of an electron can overlap with the electronic states of the opposite electrode, establishing a tunneling current through the barrier.

The working principle can be explained using a one-dimensional simplification, where the sample and the tip are described by ideal metals for which the electron states are filled up to the Fermi energy E_F . The two electrodes are separated by a small vacuum gap z_0 . An applied voltage V_T shifts the Fermi energies of tip and sample by eV_T . Here, as convention, a positive voltage V_T increases the energy in the tip. The distance z , the two work functions Φ_s and Φ_t for sample and tip, and eV_T represent a trapezoidal tunnel barrier for the electrons (figure 2.6b).

From quantum mechanics, an electron in the tip ($z = 0$) at Fermi energy, represented by its wavefunction $\psi(z)$, has a finite probability of being localized in the sample at the position z . Such probability is given by the equation 2.4:

$$|\psi(z)|^2 = |\psi(0)|^2 e^{-2\kappa z}; \kappa = \sqrt{\frac{m_0}{\hbar^2} (\Phi_t + \Phi_s - eV_T)} \quad (2.4)$$

Using the free electron mass m_0 , and realistic values for the work functions ($\Phi \approx 4\text{-}5\text{ eV}$), 2κ becomes of the order of 20 nm^{-1} , i.e. a variation in z of 0.1 nm results in an order of magnitude difference in the tunneling probability. This sensitivity

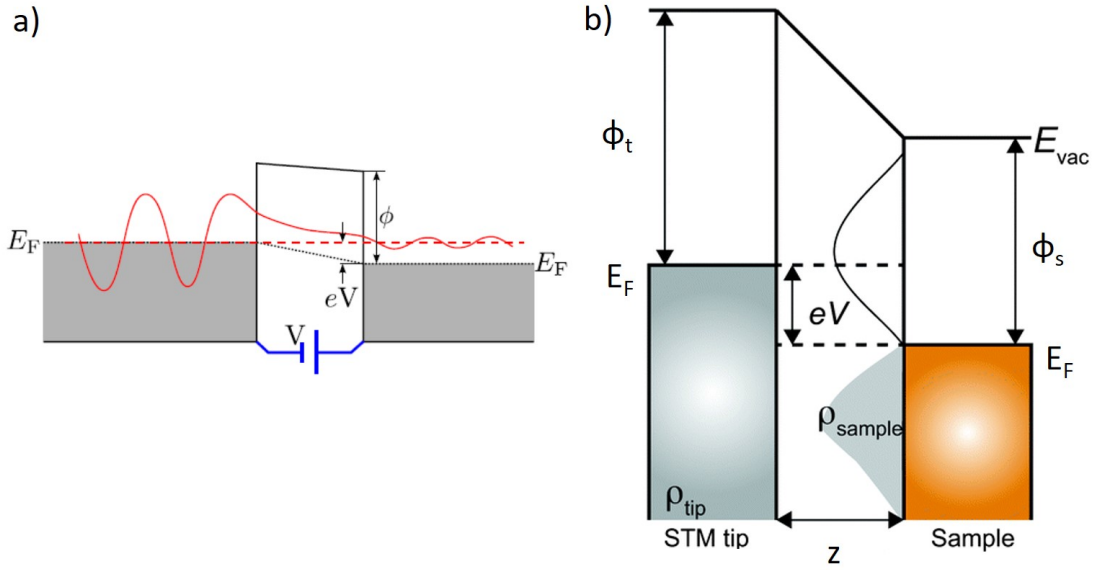


Figure 2.6 | Schematic of STM principle. a) Simple illustration of quantum tunneling of electrons. b) Schematic energy diagram of the STM tunneling junction. Here, E_{vac} is the vacuum energy level, E_F is the Fermi energy level, indicated for both tip and sample, ρ_{tip} (ρ_{sample}) is the density of states of the sample and the tip, ϕ_{tip} (ϕ_{sample}) is the work function of the tip (sample) metal, V is the applied sample bias voltage, and z is the distance from the sample to the tip. Adapted from [76].

in the tip-sample distance is the reason for the extremely high vertical resolution of the STM, which can reach the sub-picometer regime.

When no voltage is applied between the tip and sample, no net current flows between them. However, when a voltage is applied, a net current can be established.

Introducing the concept of the *local density of states* (LDOS), i.e. the density of states per energy interval at a specific position, it is possible to express the tunneling current flowing from tip to sample as 2.5:

$$I_{t \rightarrow s} = \frac{4\pi e}{\hbar} \int_{-\infty}^{\infty} \rho_t(\epsilon - eV_T) \rho_s(\epsilon) f_t(\epsilon - eV_T) (1 - f_s(\epsilon)) |M(\epsilon - eV_T, \epsilon)|^2 d\epsilon \quad (2.5)$$

where $f(\epsilon)$ represents the electrons Fermi-Dirac distributions, ρ_s and ρ_t are the LDOS respectively for sample and tip, and M is the tunneling matrix element, which represents the overlap of the wavefunctions of tip and sample. In the one-dimensional simplification $|M|^2$ is given by:

$$|M(\epsilon - eV_T, \epsilon)|^2 = \exp \left[-2z \sqrt{\frac{m_e}{\hbar^2} (\Phi_t + \Phi_s - eV_T + 2\epsilon)} \right] \quad (2.6)$$

The tunneling current depends on the LDOS of the tip and the sample, and the Fermi-Dirac distributions ensure that only occupied states in the tip ($f_t(\epsilon - eV_T)$) and unoccupied states in the sample ($1 - f_s(\epsilon)$) are counted for the tunneling from tip to sample. The whole tunneling current I_T is given by the current flows in both directions (from tip to sample and vice versa), leading to the result:

$$I_T = \frac{4\pi e}{\hbar} \int_{-\infty}^{\infty} \rho_t(\epsilon - eV_T) \rho_s(\epsilon) f_t(\epsilon - eV_T) - f_s(\epsilon) |M(\epsilon - eV_T, \epsilon)|^2 d\epsilon \quad (2.7)$$

Due to equation 2.6, the major contribution to the total current comes from the electronic states close to the Fermi energies of the tip ($V_T > 0$) or the sample ($V_T < 0$). The main challenge is the determination of the tunneling matrix element M , as the one-dimensional approximation is not really a realistic model. M depends on the geometric arrangements of the surface atoms in the sample and in the tip, and on the electron wavefunctions at given energies. The scope of STM is to produce an image of the sample surface therefore, the ideal configuration is the one where the tip DOS can be neglected. However, in most cases, the geometric and chemical structure of the tip is unknown, leading to unknown tip DOS.

J. Tersoff and D. R. Hamann proposed a representation for the STM based on first-order perturbation theory [77] and gave an analytical result for M in a simplified tunneling system [78, 79]. In particular, they solved the problem for an atomically sharp tip, meaning that only the atom at the very apex of the tip contributes to the tunneling process.

The wavefunction of the interacting atom is thus represented by a spherical, s-like orbital. The DOS over the energy interval of interest is assumed to be constant, and only elastic tunneling processes are taken into account. Under these assumptions,

M depends only on the position of the outermost atom of the tip and not on the wavefunction of the tip. From equation 2.7, for temperature $T \rightarrow 0$ and considering only voltages $|V| \ll \Phi/e$, it follows that:

$$I = \frac{4\pi e}{\hbar} |M|^2 \rho_t(E_F) \int_0^{eV_T} \rho_s(\epsilon) d\epsilon \quad (2.8)$$

Within these strong approximations, the tunneling current is proportional to the surface's LDOS at the Fermi energy and thus, an STM image can be considered as the map of LDOS of the sample's surface.

2.3.2 Imaging in constant-current mode

The tunneling current depends exponentially on the tip-sample distance. Thus, scanning the tip over the sample results in a modulation of the current, corresponding to the surface corrugation. With a tip-sample distance of usually ≤ 1 nm even small instabilities in the STM or steps on the surface would result in a crash of the tip into the sample surface. Therefore, the a common mode of operation is the so-called constant-current mode.

In this mode, the tip-sample distance z changes to keep the tunneling current at a constant value and the changes in z reflect the surface in real space. The appearance of the image depends, therefore, on the applied tunneling voltage V_T and the set tunneling current I_T and represents the LDOS of the sample integrated over the energy $E_F \leq E \leq E_F + eV_T$ according to equation 2.8. The bias voltage V_T and the tunneling current I_T are independent parameters in the experiment. Depending on the polarity of V_T , occupied ($V_T < 0$) or unoccupied states ($V_T > 0$) in the sample are imaged [80], while I_T for constant V_T determines the tip height with respect to the sample surface. On metallic samples, as their DOS around V_T is approximately constant, the obtained images correspond to the geometric surface topography [81]. However, the analysis of the STM image is not always trivial even on well-known clean surfaces. Indeed, the LDOS can be affected by many different factors. Moreover, the Tersoff-Hamann approximations might fail as the tip could change during the experiment in such a way that not only the last atom contributes to the tunneling current.

Figure 2.7 shows a typical STM image of the (7x7)-Si(111) surface. This specific example is chosen to show how the STM images can drastically change depending on the polarity of the voltage applied and the electronic structure of the sample. Indeed, a positive voltage leads to the imaging of empty states of the surface (figure 2.7a), while a negative voltage provides the image of the filled states of the surface (figure 2.7b).

To conclude, even if the beauty of STM images lies in the direct observation of the atomic structure of the sample, it has to be remembered that the underlying physical description is rather complex and even to date is not accessible in all of its details.

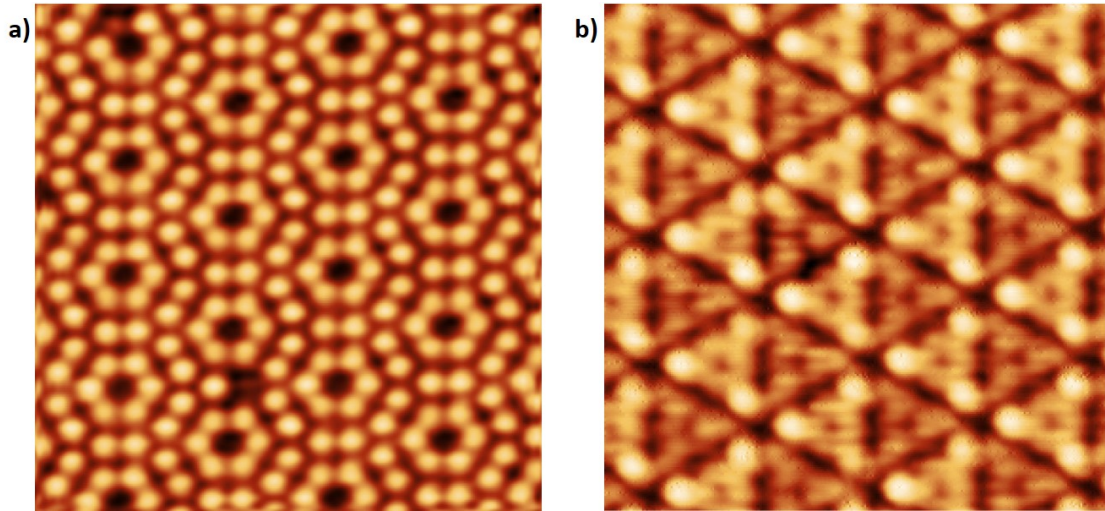


Figure 2.7 | STM images of (7x7)-Si(111) surface. STM images of empty (a) and filled (b) states of the (7x7)-Si(111) surface. Areas of both images are $10 \times 10 \text{ nm}^2$. (a) $I = 1.5 \text{ nA}$; $V = 2.0 \text{ V}$. (b) $I = 0.5 \text{ nA}$; $V = -2.0 \text{ V}$.

2.4 Angle Resolved Photoemission Spectroscopy (ARPES)

The principle of angle resolved photoemission spectroscopy (ARPES) is based on the photoemission process, where matters emit electrons as they absorb energy from electromagnetic radiation. The photoelectric effect was first observed by Hertz [82] and later explained by Einstein [83] with the quantum mechanical nature of light. Einstein recognized that photons can be absorbed by the electrons in a solid and the resulting photo-electrons can be then emitted from the solid with kinetic energy:

$$E_{kin} = h\nu - \phi \quad (2.9)$$

where ν is the photon frequency, h is the Plank's constant, and ϕ is the work function of the solid¹. The following discussions on ARPES are based on [71] unless otherwise stated. When a beam of monochromatic photons with an energy greater than ϕ interacts with a sample's electrons, the electrons can absorb the photons and gain sufficient energy to escape from the sample. By measuring the energy and momentum of the escaped photoelectron and using conservation laws, it is possible to retrieve the original properties of the electron. This information can then be used to reconstruct the band structure (energy-momentum dispersion

¹The minimum energy required to remove the electron from the solid

relationship). The momentum of the photo-electron in the vacuum (K) is related to the energy of the photo-electron, E_{kin} , by the following equation:

$$K = \frac{\sqrt{2mE_{kin}}}{\hbar} \quad (2.10)$$

where m is the mass of the free electron. The momentum of the electron can be written as the sum of two components, parallel and perpendicular to the sample's surface:

$$\vec{K}_{\parallel} = \vec{K}_x + \vec{K}_y \quad (2.11)$$

$$\vec{K}_{\perp} = \vec{K}_z \quad (2.12)$$

According to their emission angles and using spherical coordinates, the momentum and energy relation for each component of the emitted electron can be written as:

$$K_x = \frac{\sqrt{2mE_{kin}} \sin \theta \cos \varphi}{\hbar} \quad (2.13)$$

$$K_y = \frac{\sqrt{2mE_{kin}} \sin \theta \sin \varphi}{\hbar} \quad (2.14)$$

$$K_z = \frac{\sqrt{2mE_{kin}} \cos \theta}{\hbar} \quad (2.15)$$

The two angles are defined in Figure 2.8. Using simple considerations, one can derive the energy-momentum relationships for the electron before the photoemission process. Note that lower case " k " refers to the electron in the sample, and the upper case " K " refers to the vacuum electron.

Due to the translational symmetry in the x-y plane and the absence of potentials in the same plane, the k_{\parallel} component is conserved:

$$k_{\parallel} = K_{\parallel} = \left(\frac{2m}{\hbar^2} E_{kin} \right)^{\frac{1}{2}} \sin \theta = \left(\frac{2m}{\hbar^2} [E_b + h\nu - \phi] \right)^{\frac{1}{2}} \sin \theta \quad (2.16)$$

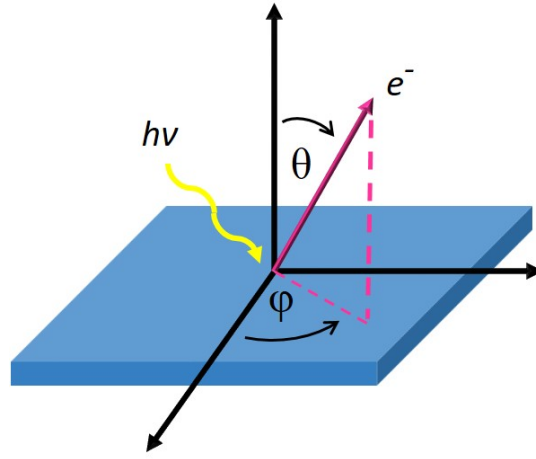


Figure 2.8 | ARPES. Schematic diagram of outgoing excited electrons in an ARPES setup.

Where E_b stands for the original binding energy of the electron. Regarding k_{\perp} , it has to be taken into account the surface potential V_0 , which results from the energy difference from the bottom of the valence band to the vacuum level.

$$k_{\perp} = \left(\frac{2m}{\hbar^2} (E_{kin} + V_0) \right)^{\frac{1}{2}} \cos \theta \quad (2.17)$$

For a 2D material, such as graphene, there is no dispersion along the sample's normal direction. Therefore, the electronic dispersion is determined only by k_{\parallel} and k_{\perp} can be neglected in our considerations.

The intensity of the photoelectrons is proportional to the transition probability ω_{fi} for an excitation between the N-electron ground state ψ_i^N and one of the possible final states ψ_f^N , which can be approximated by the Fermi's golden rule:

$$I \propto \omega_{fi} = \frac{2\pi}{\hbar} |\langle \psi_f^N | H_{int} | \psi_i^N \rangle|^2 \delta(E_f^N - E_i^N - h\nu) \quad (2.18)$$

where $E_i^N = E_i^{N-1} - E_B^k$ and $E_f^N = E_f^{N-1} + E_{kin}$ are the initial and final state energies of the N-electrons system and E_B^k is the binding energy of the photoelectron emitted with kinetic energy E_{kin} . The interaction is treated as a perturbation and is described by the Hamiltonian:

$$H_{int} = -\frac{e}{2mc} (\mathbf{A} \cdot \mathbf{p} + \mathbf{p} \cdot \mathbf{A}) = -\frac{e}{mc} \mathbf{A} \cdot \mathbf{p} \quad (2.19)$$

where \mathbf{p} is the electronic momentum operator and \mathbf{A} is the electromagnetic vector potential.

The rigorous approach to the photoemission process is a model where, photon adsorption, electron removal, and electron detection are all included in the Hamiltonian of interaction and these three steps are treated as a single coherent process. However, this approach is rather complex and thus, photoemission processes are commonly discussed with the three-step model, namely:

1. Photoexcitation of electrons in the solid
2. Propagation of the photoelectrons to the surface
3. Escape of photoelectrons from the solid into the vacuum

The total photoemission intensity is given by the product of three independent terms: the total probability of the optical transition, the scattering probability for the photoelectrons, and the transmission probability through the surface potential.

The first step contains information about the intrinsic electronic structure. To evaluate the photoelectron intensity as transition probability, the sudden approximation is applied. The approximation assumes that the electron removal is sudden and the potential of the system changes abruptly at that moment. In this way, it is possible to separate the initial and final state of the N electron system and the wavefunctions can be factorized into the photoelectron and the remaining N-1 electron. The final state is then described as:

$$\psi_f^N = A\phi_f^{\mathbf{k}}\psi_f^{N-1} \quad (2.20)$$

where A is an antisymmetric operator so that the N-electron wavefunction satisfies the Pauli principle. $\phi_f^{\mathbf{k}}$ is the wavefunction of the photoelectron with momentum \mathbf{k} and ψ_f^{N-1} is the final state wavefunction of the N-1 electron system, which can be chosen as an excited state with eigenfunction ψ_m^{N-1} . On the other hand, the initial state is described as:

$$\psi_i^N = A\phi_i^{\mathbf{k}}\psi_i^{N-1} \quad (2.21)$$

where $\phi_i^{\mathbf{k}}$ is the one electron orbital and $\psi_i^{N-1} = c_{\mathbf{k}} \psi_i^N$, with $c_{\mathbf{k}}$ as annihilation operator of an electron with momentum \mathbf{k} in the initial N-1 electron system. Thanks to the above approximation, the interaction matrix becomes:

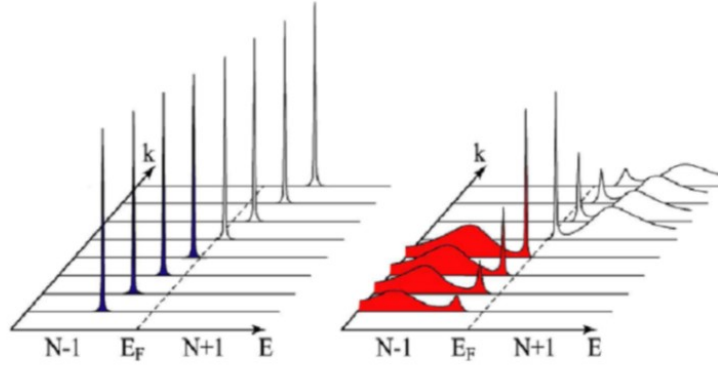


Figure 2.9 | ARPES. Spectral function for non-interacting (left panel) and interacting (right panel) systems.

$$\langle \psi_f^N | H_{int} | \psi_i^N \rangle = \langle \phi_f^{\mathbf{k}} | H_{int} | \phi_i^{\mathbf{k}} \rangle \langle \psi_m^{N-1} | \psi_i^{N-1} \rangle \quad (2.22)$$

where $\langle \phi_f^{\mathbf{k}} | H_{int} | \phi_i^{\mathbf{k}} \rangle \equiv M_{f,i}^{\mathbf{k}}$ is the dipole matrix element, which is responsible for the enhancement or the suppression of the photoemission intensity. The total photoemission intensity $I(\mathbf{k}, E_{kin})$ is then described as:

$$I(\mathbf{k}, E_{kin}) = \sum_{f,i} \omega_{f,i} \propto \sum_{f,i} |M_{f,i}^{\mathbf{k}}|^2 \sum_{f,i} |c_{m,i}|^2 \delta(E_{kin} + E_m^{N-1} - E_i^N - h\nu) \quad (2.23)$$

where $|c_{m,i}|^2 = \langle \psi_m^{N-1} | \psi_i^{N-1} \rangle$ accounts for the probability that the emission of an electron from state i will create the (N-1) electron system in the excited state m . In non-interacting system, $|c_{m,i}|^2$ will be either 1 for only specific m or 0 for all the others. This means that ARPES spectra will be described by a delta function centered at the electrons' binding energy. In a strongly correlated system, ψ_i^{N-1} will overlap with many eigenstates ψ_m^{N-1} and the ARPES spectra will be given by a convolution between delta functions and interacting states. A comparison of the two cases can be seen in figure 2.9.

The interpretation of the ARPES data is based on Green's function formalism. The spectral function is given by the imaginary part of the Green's function $G(\mathbf{k}, E)$:

$$A(\mathbf{k}, E) = -\frac{1}{\pi} \text{Im}G(\mathbf{k}, E) \quad (2.24)$$

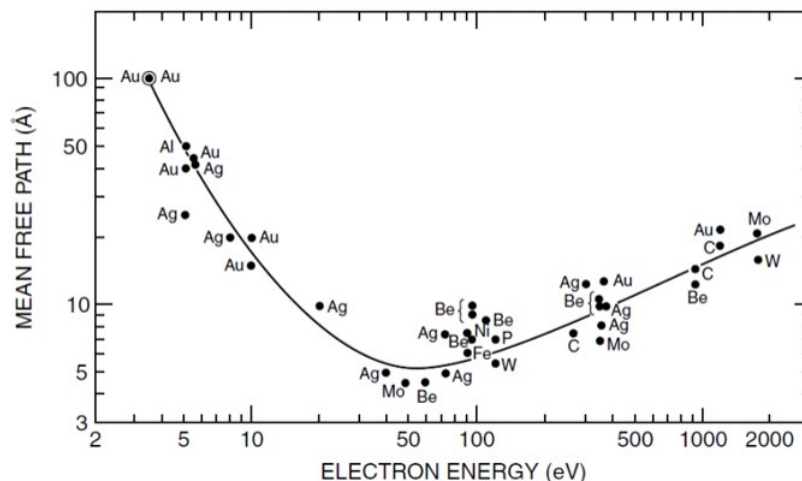


Figure 2.10 | Electrons mean free path. The mean free path of electrons at different kinetic energies in different materials. Reprinted from [84].

and for a non-interacting system the spectral function reduces to the delta function $A_0(\mathbf{k}, E) = \delta(E - E_{\mathbf{k}}^0)$. For interacting system, the correlation between electrons is given in terms of electron self-energy $\Sigma(\mathbf{k}, E) = \Sigma'(\mathbf{k}, E) + i\Sigma''(\mathbf{k}, E)$. The real part provides information about the energy normalization while the imaginary term gives information about the lifetime of an electron with energy $E_{\mathbf{k}}^0$ and momentum \mathbf{k} propagating in the system. For interacting system, the spectral function is described as:

$$A(\mathbf{k}, E) = -\frac{1}{\pi} \frac{\Sigma''(\mathbf{k}, E)}{(E - E_{\mathbf{k}}^0 - \Sigma'(\mathbf{k}, E))^2 + (\Sigma''(\mathbf{k}, E))^2} \quad (2.25)$$

The probability for electrons to escape from the solid into the vacuum is strongly related to the electron mean free path. Figure 2.10 shows the universal electron mean free path λ as a function of the electron kinetic energy for a range of metals. Between a few eV and 2000 eV, the mean free path is only 5 Å to 20 Å, meaning that only electrons on a few Å from the surface will be able to escape from the solids and be detected in ARPES experiments.

2.5 X-ray Photoelectron Spectroscopy (XPS)

X-ray photoelectron spectroscopy (XPS) is a surface sensitive technique that measures photoelectrons emitted with X-ray (50-2000eV) to obtain both qualitative and quantitative analyses of the sample. In the XPS process, the photon is absorbed by an atom in a molecule or on a surface and the resulting emitted photo-electron is a

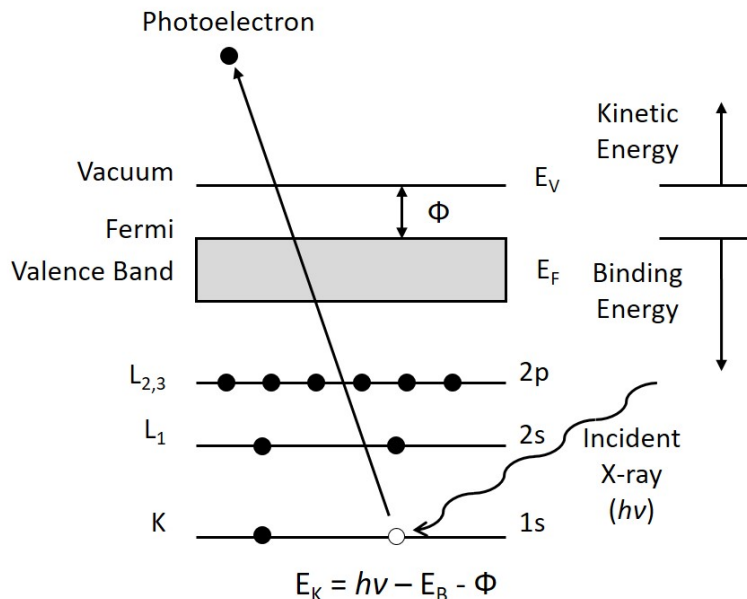


Figure 2.11 | XPS. Sketch of the photoemission process.

core electron. The following discussions on XPS are based on [71] unless otherwise stated. When a surface is irradiated by X-rays, the core level electrons of surface atoms absorb the X-ray photon energy $h\nu$, overcome their binding energy (E_B), and are emitted out of the surface with certain kinetic energy (E_{kin}). This process is described by equation 2.26 and sketched in figure 2.11.

$$E_{kin} = h\nu - E_B - \Phi \quad (2.26)$$

In this equation, $h\nu$ is the energy of the X-ray source.

Φ is the work function of the instrument. E_{kin} of the emitted electron is measured by an analyzer and thus, the binding energy E_B of the core level electron can be determined.

A typical XPS spectrum records the number of photoelectrons detected as a function of the binding energy, as shown in figure 2.12. The energy of the photoelectrons is characteristic of the probed element and the configuration of electrons inside the atom. The different electron densities in the vicinity of the atoms can also result in a shift of the energy of the characteristic peaks, which can provide information about the particular chemical environment of the atoms on the surface.

Chemical bond between atoms reflects the rearrangement of the spatial distribution

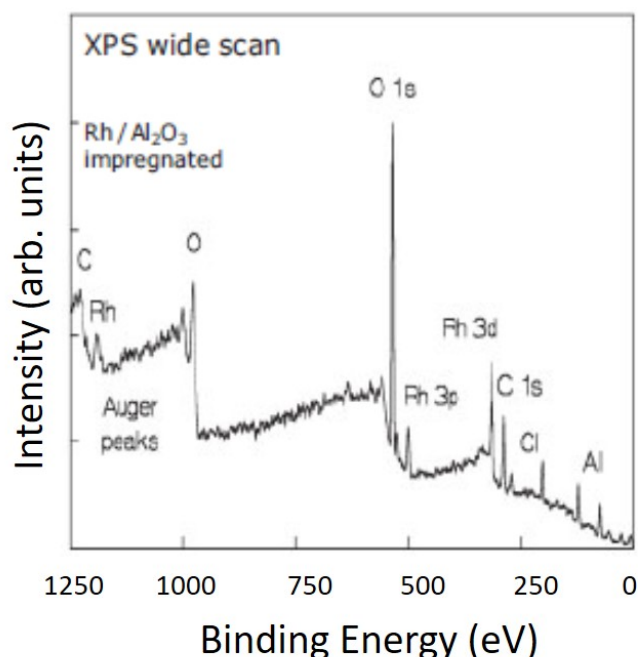


Figure 2.12 | XPS spectrum. XPS survey spectrum of a Rh/Al₂O₃ catalyst prepared by impregnating Al₂O₃ with a solution of RhCl₃ in water. Adapted from [84].

of one or more of the valence electrons. Any change in the bonding state of an atom results in modifications of binding energy, peak shape and width. The change in the core electron binding energy is called chemical shift. As a rule of thumb, an atom bonded to another with higher (lower) electronegativity have electrons with higher (lower) binding energies. This is because it occurs a charge transfer towards the atom with higher electronegativity and thus, the effective charge of the other atom becomes positive, which increase the binding energy. Using modern synchrotron facilities, chemical shifts can be detected with a resolution of 50 meV or better. Moreover, synchrotron radiation provides a continuous source of photons in the energy range 10eV - 10keV. This allows the radiation to be tuned and to reach the ideal photoionization cross-section for the specific core levels of interest.

A doublet peak structure is typical for electron transitions from levels with total angular momentum higher than s, for which $l=0$. Thus, all s peaks singlets while all other levels are doublets with the two peaks at slightly different binding energies. The energy difference results from the spin-orbit coupling, as the electron left after the photoemission process has either a parallel or an antiparallel orientation to the orbital momentum. The energy separation of the doublet increases with atomic number and decreases for the same energy level n with higher l values.

The intensity of the characteristic peaks is directly related to the amount of the

specific element within the area or volume probed. Thus, XPS can yield quantitative information about the elemental composition of the surface in the surface and within the probed depth, usually within $\sim 10\text{nm}$ from the surface.

The quantitative interpretation of XPS intensities requires taking into account the properties of the excitation source, sample, electron analyzer, and detection system. In general, the XPS peak intensity dN_k associated with the atomic subshell k is determined by the products of X-ray flux (I_0), the number of atoms ($\rho dx dy dz$), the differential cross-section for subshell k ($\frac{d\sigma_k}{d\Omega}$), acceptance solid angle of electron analyzer ($\Omega(E_{kin}, x, y, z)$), probability of electrons to escape from the sample ($\exp[-l/\Lambda_e(E_{kin})]$), and instrumental detection efficiency ($D_0(E_{kin})$):

$$dN_k = I_0 \cdot \rho dx dy dz \cdot \frac{d\sigma_k}{d\Omega} \cdot \Omega(E_{kin}, x, y, z) \cdot \exp[-l/\Lambda_e(E_{kin})] \cdot D_0(E_{kin}) \quad (2.27)$$

where l is the traveling distance for electrons to escape from the sample surface into the vacuum and Λ_e is the mean free path. The dependence of dN_k on the path length l can be used to obtain a quantitative analysis of the thickness of a film grown on a substrate.

2.6 Near Edge X-ray Absorption Fine Structure (NEXAFS) Spectroscopy

Photoabsorption spectroscopy relies on a process in which the system remains neutral, as opposed to the photoemission process in which photoelectrons are ejected from the system. The term photoabsorption spectroscopy refers to many techniques, depending on the photon energy of the incoming light, the detection method, and the type of information one wants to retrieve from the absorption process. The following discussions on X-ray absorption spectroscopy (XAS) techniques are based on [71] unless otherwise stated. In XAS, the incoming photon excites a core electron to an unoccupied valence orbital and the system will then decay in the femtosecond range. The intensity of the adsorption depends on the incoming photon energy.

Unlike photoemission processes that probes the occupied electronic structure, the absorbed X-rays excite core electrons, inducing their transition into unoccupied states.

The absorption spectrum is usually separated into two parts: (i) near-edge X-ray absorption fine structure (NEXAFS) or X-ray absorption near edge structure (XANES), for the absorption fine structures up to ~ 30 eV above the absorption edge and (ii) extended X-ray absorption fine structure (EXAFS), which extends up to 1000 eV above the absorption edge.

Figure 2.13a describes a general absorption of a photon by a core level and its excitation into an unoccupied state.

NEXAFS probes the unoccupied atomic or molecular valence electronic states in the presence of a core-hole. The excitation in the X-ray absorption process follows the dipole selection rule, meaning that the excitation can occur only for:

$$\Delta l = \pm 1, \Delta j = \pm 1, \Delta s = 0 \quad (2.28)$$

with l the angular momentum quantum number, j the total momentum quantum number and s equal to the spin quantum number.

The dipole selection rules give rise to the absorption edges in the NEXAFS spectrum and are classified according to the origin of the excited electron. This work concerns the K-edge excitations, which means that the dipole selection rule $\Delta l = 1$ allows the transitions to final states having an atomic p orbital component. Figure 2.13b shows a typical NEXAFS spectrum of graphene.

Generally, the width of NEXAFS features depends on (i) the lifetime of the core-hole (Lorentzian lineshape), (ii) the resolution of the instrument (Gaussian lineshape), and (iii) the vibrational motion of molecules, often leading to an asymmetrical broadening.

The X-ray absorption cross-section describes the probability for absorption of a photon by an atom. When the photon energy, $h\nu$, matches the energy required for a transition, the X-ray absorption spectrum shows a maximum and the intensity decreases monotonically after the core edge.

The absorption cross-section (σ_x) is defined as the number of electrons excited per unit time divided by the number of incident photons per unit time per unit area. Within the dipole approximation:

$$\sigma_x = \frac{4\pi^2 \hbar^2}{m^2} \cdot \frac{e^2}{\hbar c} \cdot \frac{1}{h\nu} \cdot \langle \Psi_f | \mathbf{E} \cdot \boldsymbol{\mu} | \Psi_i \rangle^2 \rho_f(E) \quad (2.29)$$

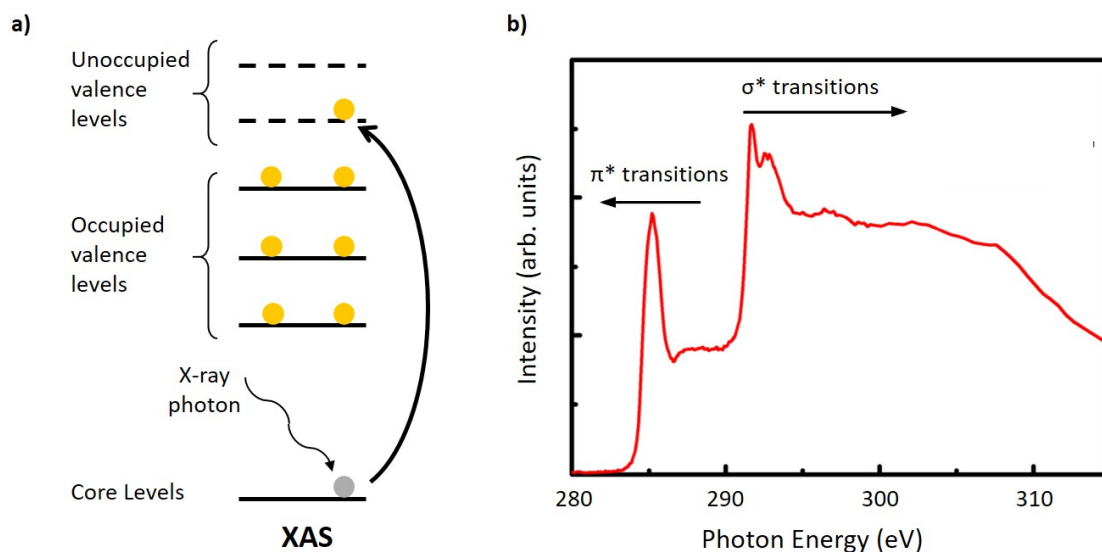


Figure 2.13 | NEXAFS. a) Schematic illustration of the X-ray absorption process. b) Example of a NEXAFS spectrum at C K-edge of graphene. Adapted from [85].

with \mathbf{E} the electric field vector, μ the electric dipole operator, Ψ_f the wavefunction of the final state, Ψ_i the wavefunction of the initial state and $\rho_f(E)$ the density of final states. The absorption edges of elements have characteristic energies thus, NEXAFS is element-specific and the spectrum reflects the bonding environment.

In the NEXAFS region of the absorption spectrum, the photoelectron energy is low and the mean free path long, meaning that multiple scattering effects are much more dominant than in the EXAFS region. Usually, the strong features in the NEXAFS spectra are related to transitions to atomic-like or unoccupied DOS in solid state systems. Therefore, NEXAFS is sensitive to the local electronic structure of the element absorbing the radiation, its oxidation state, ligands of functional groups, and the coordination geometry. However, the processes involved are complex and this means that the analysis of NEXAFS spectra is not trivial and especially difficult to calculate theoretically. Indeed, NEXAFS analysis is often performed by comparing the differences between the obtained results and reference spectra.

NEXAFS and XPS measurements presented in this thesis were performed at the BACH beamline at the ELETTRA synchrotron facility in Trieste, Italy. This beamline is located at a bending magnet which provides radiation in the energy range between 3-1600 eV, with a final spot size of 30 μm - 100 μm . The beamline features a rotatable analysis chamber, optimized for X-ray absorption measurements.

2.7 Raman Spectroscopy

Raman spectroscopy is a non-destructive characterization method that uses inelastic light scattering to probe the vibrational and electronic properties of materials. This technique is particularly useful for organic materials in general and especially valuable for carbon allotropes, including graphene. Unlike other characterization techniques, Raman spectroscopy does not require any sample preparation or specific substrates and can be performed on functional electronic devices, even during their operation [86].

The term Raman scattering denotes the inelastic scattering of photons by phonons [87]. When a photon impinges on a sample, it creates a time-dependent perturbation in the Hamiltonian of the system. Due to the photon fast changing electric field, only electrons respond to the perturbation. The perturbation introduced by a photon of energy $\hbar\omega_L$ increases the total energy to $E_{GS} + \hbar\omega_L$, where E_{GS} is the ground state energy. In general, $E_{GS} + \hbar\omega_L$ does not correspond to a stationary state, therefore the system is said to be in a virtual level. In classical language, a virtual level corresponds to a forced oscillation of the electrons with a frequency ω_L . After a short interval, the system tends to exit from the non-stationary energy state $E_{GS} + \hbar\omega_L$ and moves back to a stable state. One can formally consider the photon as being emitted by the perturbed system, which jumps back to one of its stationary states [87].

The photon scattering process can be either elastic or inelastic. In the first case, called Rayleigh scattering, the frequency of the emitted photon is the same as the incident one and the main effect is that the photon changes its propagation direction. Instead in a Raman process, the scattering is inelastic and the photon can either reduce or increase its energy. Raman scattering happens always with a much lower probability than Rayleigh scattering [87].

When the photon loses part of its energy in the interaction process, it exits the sample with a lower energy $\hbar\omega_{Sc}$. This corresponds to the Stokes (S) process. Since the sample has to return to a stationary state, the energy loss must correspond to a phonon energy $\hbar\omega_L$ $\hbar\omega_{Sc} = \hbar\Omega$. If the incoming photon finds the sample in an excited vibrational state, and after the interaction the system returns to its ground level, the photon can leave the sample with increased energy $\hbar\omega_{Sc} = \hbar\omega_L + \hbar\Omega$. This corresponds to the Anti-Stokes (AS) process [57]. Figure 2.14 shows a sketch of the process.

Given that S is the most probable, the vast majority of Raman spectra in literature

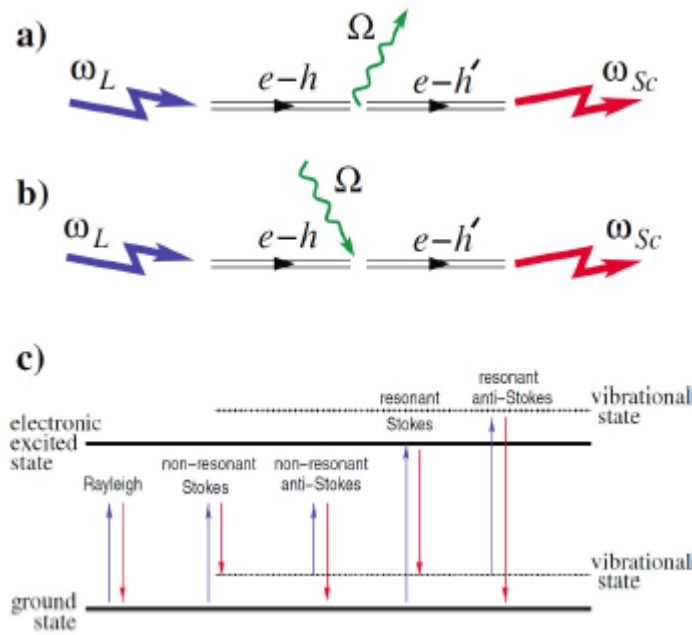


Figure 2.14 | Raman Scattering. a) Stokes. An incoming photon ω_L excites an electron - hole pair ($e - h$). This pair decays into a phonon Ω and another electron-hole pair ($e - h'$). The latter recombines, emitting a photon ω_{Sc} . b) Anti-Stokes. The phonon is absorbed by the $e - h$ pair. c) Rayleigh and Raman scattering in resonant and non resonant conditions. Reprinted from [57].

are S measurements plotting the intensity of the scattered light as a function of the difference between incident and scattered photon energy, called Raman shift [87]. Even though the Raman shift units should be those of energy, it is historically plotted in cm^{-1} . This can be converted in meV using the relation $1\text{meV} = 8.0655 \text{ cm}^{-1}$. When $E_{GS} + \hbar\omega_L$ does not correspond to a stationary state the Raman scattering is called non-resonant. If the excitation is selected to match a specific energy level, then the process is called resonant, and the intensities are strongly enhanced, as a result of the greater perturbation efficiency [57, 87].

The peculiar band structure of graphene, in the absence of a bandgap, makes all wavelengths of incident radiation resonant, thus the intensity of the Raman spectrum is enhanced and contains information about both atomic structure and electronic properties [57]. The Raman spectrum of graphene, similar to other carbon-based materials, consists of only a few prominent features. It is the shape, position, and intensity of these peaks that contain the information (e.g. doping, defects, strain, disorder, chemical modifications, edges) and therefore accurate data interpretation is essential [57, 88].

The typical spectrum of single-layer graphene looks like figure 2.15.

The two most intense features are the G peak at $\sim 1580 \text{ cm}^{-1}$ and the 2D band at

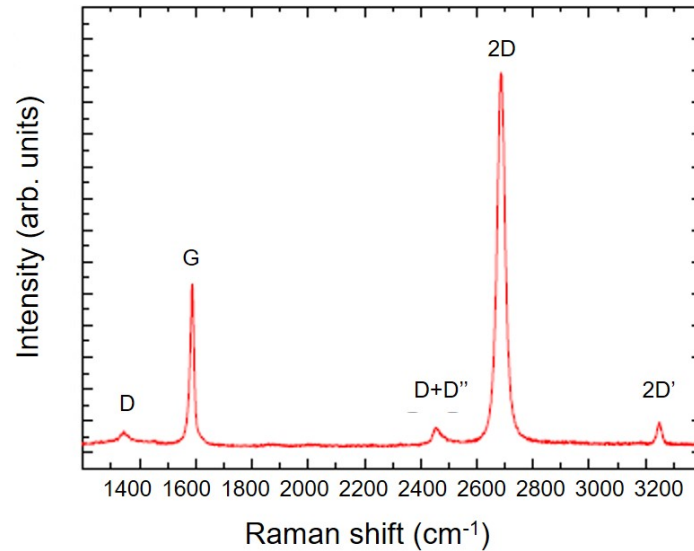


Figure 2.15 | Raman Graphene. Single-layer graphene Raman spectrum. The two most intense features are the G peak at 1580 cm^{-1} and the 2D band at 2700 cm^{-1} . Other slightly intense peaks are the 2D' at $\sim 3200\text{ cm}^{-1}$, the D+D'' at $\sim 2450\text{ cm}^{-1}$ and the D peak at 1350 cm^{-1} .

$\sim 2700\text{ cm}^{-1}$ [88]. In monolayer, not doped graphene the 2D peak is a sharp peak roughly four times more intense than the G peak. Other slightly intense peaks are present: the 2D' at $\sim 3200\text{ cm}^{-1}$, the D+D' at $\sim 2450\text{ cm}^{-1}$, and the D peak at $\sim 1350\text{ cm}^{-1}$. This last peak originates from the intervalley resonant scattering due to the presence of defects and edges in the structure, thus it is an index of the homogeneity of the structure. The position and the intensity of the G and the 2D peaks are also influenced by the doping level of graphene. The G peak sharpens for both electron and hole doping, while the 2D peak shows a different response to holes and blue-shifting of electrons, thus G and 2D peaks have different doping dependence and the 2D/G height ratio can be a sensitive parameter to monitor it [86].

Structural characterization of the Graphene/Ge(110) interface

The reinvestigation of germanium as a promising alternative to silicon has stimulated broad research in both industry and academia with the aim of overcoming the challenges preventing the full application of Ge in material science, device physics, and semiconductor processing.

This entails, among others, an extensive investigation of its surface properties. The stability of the surface is a requirement as the interface between the GeO₂ native oxide and Ge will result in a high density of electronic defects. Therefore, the Ge surface should be protected by a passivating layer to allow the on-top deposition of a suitable gate dielectric layer. Graphene either grown or transferred on Ge exhibits an effective protection against oxidation [89]. However, it should be remembered that defects in the graphene layer represent the access point for oxidizing species to the interface with Ge. The realization of single-crystal graphene free of grain boundaries and defects would provide an effective protection for Ge from oxidation potentially indefinitely.

The graphene/Ge(110) interface has sparked particular interest in the very recent years, probably since the discovery of a novel reconstruction of the Ge surface, namely the (6x2) phase. This reconstruction is induced upon annealing in vacuum above 300 °C [65–67] and is peculiar of the graphene/Ge(110) system. Indeed, it has never been observed on bare Ge [66]. This recent finding indicates that the topic is not exhausted yet. Moreover, it shows that graphene/Ge(110) is a dynamic system and that its properties can be modified by post-growth thermal annealing. Thus, making it worth further investigations.

Herein, this chapter presents the characterization of the structure of the graphene/Ge(110) interface. The study is based on STM. In order to follow the evolution of the interface, the STM measurements have been performed on samples as-grown, after annealing above 350 °C and after annealing above 700 °C in vacuum. The results and discussion here presented have been published by The Journal of Physical Chemistry Letters in the article titled "Tuning the Doping of Epitaxial Graphene on a Conventional Semiconductor via Substrate Surface Reconstruction" [68]. I performed the STM measurements and the analysis here presented, supported by my co-supervisor Luca Camilli and Ph.D. Luca Persichetti (University of Roma Tre). I would like to thank both for the interesting discussions.

3.1 STM Study

Graphene deposition was performed via CVD process on *n*-type, Sb doped ($n = 10^{16} \text{ cm}^{-3}$) Ge(110) substrates, using a commercially available CVD reactor (Aixtron BM). Before the deposition of graphene, the Ge substrates were first cleaned ex-situ by several rinsing and drying cycles using isopropyl alcohol and de-ionized water followed by in-situ annealing to 930 °C in H₂/Ar atmosphere (200/800 sccm) without methane. The growth chamber was first heated up to 800 °C at a rate of 4 °C/s. Then the ramp rate was decreased to 1 °C/s to reach 860 °C. Lastly, the rate ramp was slowed down to 0.125 °C/s to reach 930 °C, temperature which was kept constant for 5 minutes. Finally, it followed the actual growth of graphene by the addition of 2 sccm of methane to the gas mixture, keeping 100 mbar of total pressure. The samples were then cooled down to room temperature in a protective atmosphere of H₂ and Ar.

This growth procedure leads to the deposition of monolayer graphene. Raman spectroscopy of the as-grown samples shows as main feature the G and 2D peaks. The sharpness and intensity of the latter indicate the growth of monolayer graphene. Additionally, a small D peak is also present, indicating a little amount of defects in graphene structure. A characteristic Raman spectrum of the as-grown samples is shown in figure 3.1.

After Raman characterization, the as-grown sample was transferred (ex-situ) into the UHV setup described in chapter 2 for further characterization. Before performing the STM measurements, the as-grown graphene/Ge(110) was annealed in the preparation chamber at ~ 180 °C until the pressure in the chamber would drop back to the initial base value ($< 3 \times 10^{-10}$ mbar). This mild annealing was

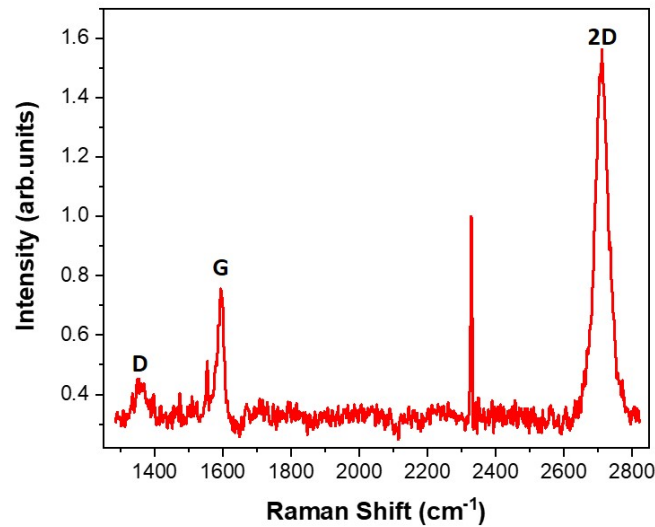


Figure 3.1 | Raman as-grown graphene/Ge(110) sample. Typical Raman spectrum of the as-grown graphene/Ge(110) samples. Spectrum acquired with excitation laser with wavelength of 532 nm.

performed to remove any potential contamination due to the exposure to ambient conditions during transfer of the sample. Thus, after this initial degas, the sample was transferred into the analysis chamber for characterization with STM. The measurements were performed with etched-W tips at a temperature of 9-10 K. Pressure in the analysis chamber was $< 2 \times 10^{-10}$ mbar.

Figure 3.2 reports the characteristic STM images of the as-grown sample. Specifically, in figure 3.2a, it is possible to observe the terraces and monoatomic steps of the Ge substrate and notice that the surface does not show either long- or short-range order. Figure 3.2b,c are higher magnification images. The image in figure 3.2b is acquired with a voltage of -1.0 V, allowing to recognize both the graphene honeycomb lattice and some features of the underneath Ge surface. Instead, in figure 3.2c, only the graphene lattice is recognizable due to the low voltage (0.4 V) applied to record this image.

Indeed, the applied voltage can be tuned to selectively show either the graphene or the underlying Ge substrate. The honeycomb lattice of graphene is usually better imaged by applying small bias voltages, while higher voltages can be used to resolve the features of the underneath Ge surface, as also explained in ref. [90]. The inset in figure 3.2c shows the Fast Fourier Transform (FFT) corresponding to the real space surface, revealing the typical graphene hexagon, as expected.

From STM, the graphene layer in the as-grown sample appears to be rippled, with

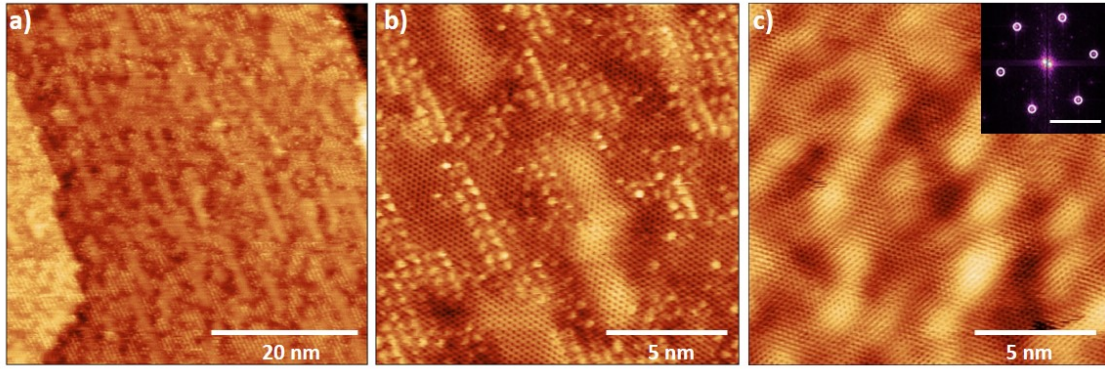


Figure 3.2 | STM graphene/Ge(110) as-grown sample. STM images of the as-grown sample. The inset shows the FFT of the image in (c), highlighting the six primary spots of graphene. Figures acquired with $V = -1.0$ V and $I = 0.8$ nA (a,b), $V = 0.4$ V and $I = 1.0$ nA (c). Scale bar FFT is 5 nm^{-1} . Adapted from [68].

height difference in the range of 300-400 pm, which could result from the presence of hydrogen between graphene and Ge surface. Indeed, the presence of H_2 in the CVD process typically results in a hydrogen-passivated Ge surface [38, 65].

The sample was then annealed above 350°C in vacuum in the preparation chamber. Typical STM images after annealing are shown in figure 3.3. The difference with the surface of the as-grown sample is striking and the changes in the topography are related to the rupture of the H-Ge bonds. Indeed, previous works have reported that above 300°C the hydrogen atoms leave the Ge surface [65–67] and thus, the outermost atoms of the substrate have to rearrange on the surface. This process leads to the formation of the (6×2) reconstruction [66]. Figure 3.3b shows the atomically-resolved STM image of the (6×2) reconstruction and its unit cell with the corresponding lattice vectors ($a = 2.06$ nm and $b = 1.30$ nm).

The surface area covered by the (6×2) phase depends directly on the duration of the annealing. Therefore, areas of (6×2) reconstruction can coexist with areas that have not yet transitioned into the (6×2) phase, as shown in the STM image reported in figure 3.3a. The few protrusions marked with white arrows in figure 3.3a are nanobubbles formed by hydrogen molecules upon rupture of the H-Ge bonds during the annealing [91]. Usually, the nanobubbles are located either at the edges of Ge steps or at the boundaries between the areas of the two different phases.

Moreover, the LEED pattern of the (6×2) phase is reported in figure 3.4, revealing, as expected, the primary six graphene diffraction spots and also the presence of a rectangular moiré pattern around graphene’s spots. This moiré is induced by the symmetry of the (6×2) reconstruction of the Ge surface underneath the graphene layer. The ratio between the two edges of the moiré pattern is indeed consistent

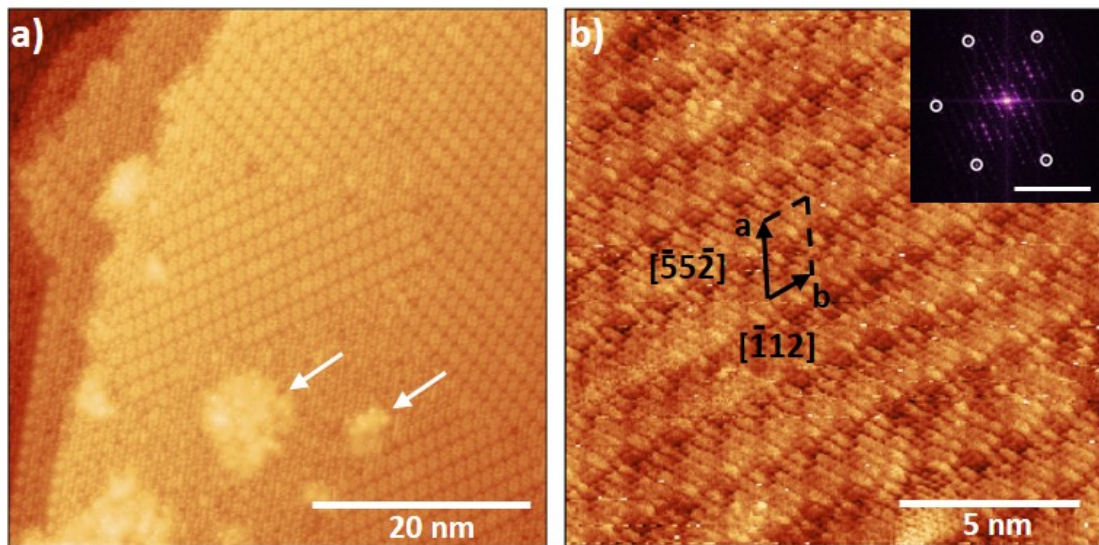


Figure 3.3 | STM graphene/Ge(110) after annealing above 350 °C. (a) The surface shows both the sample as-grown and the (6x2) reconstruction. The white arrows indicate the hydrogen nanobubbles. (b) High magnification image of the (6x2) reconstruction. In black, a and b indicate the unit cell vectors. Inset shows the FFT of (b) where the white circles highlight the six primary spots of graphene, and in the middle the rectangular pattern of the (6x2) phase is recognizable ($V = -1.5$ V and $I = 0.8$ nA in (a) and $V = -1.5$ V and $I = 0.3$ nA in (b)). Inset scale bar is 5 nm^{-1} . Adapted from [68].

with the ratio between the two lattice vectors of the (6x2) unit cell. LEED is a surface sensitive technique used to characterize the long-range order of single crystal surfaces.

It is worth reminding that the (6x2) reconstruction has never been observed on bare germanium but it is peculiar of the graphene/Ge(110) system. This is a clear example of how interfacing a 2D material with a conventional 3D semiconductor can introduce novel physical properties, which are not intrinsic to the individual materials but are the unique result of their integration.

It is interesting to see how the appearance of the surface changes with the bias voltage applied to image the surface by means of STM measurements. Figure 3.5 shows a series of images of the same area of the surface after annealing in UHV above 350 °C acquired at different bias voltages. The STM images show areas of (6x2) reconstruction, as-grown surface -i.e. areas where hydrogen has not desorbed from the Ge surface yet - and a hydrogen nanobubble in the middle. At low bias voltages (± 0.2 V), the graphene lattice is easily imaged, while the Ge surface is not clearly visible. At higher bias voltages (± 0.6 V), both the graphene lattice and the Ge surface are recognizable. At even higher bias voltages (± 1.0 V), graphene

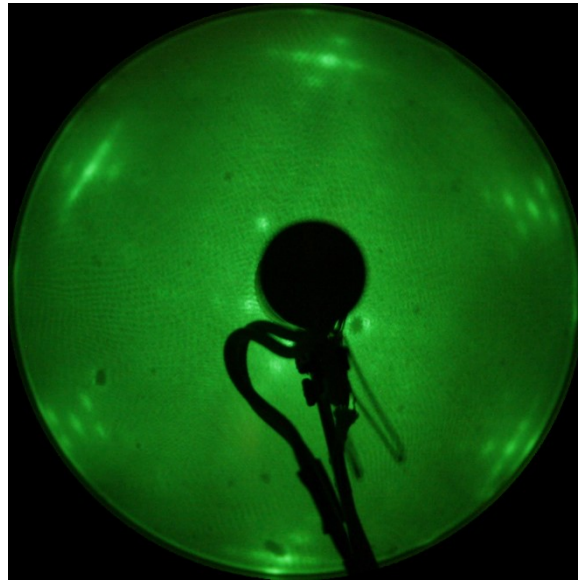


Figure 3.4 | LEED of the (6x2) reconstruction. LEED collected on the graphene/Ge(110) sample after annealing above 350 °C showing the pattern for the (6x2) reconstruction using primary electron energy of 97 eV. A moiré pattern can be observed around the six graphene diffraction spots. The ratio between the two edges of the moiré pattern is consistent with the ratio between the lattice vectors of the (6x2) phase as measured in STM. LEED spot size 1 mm. Adapted from [68].

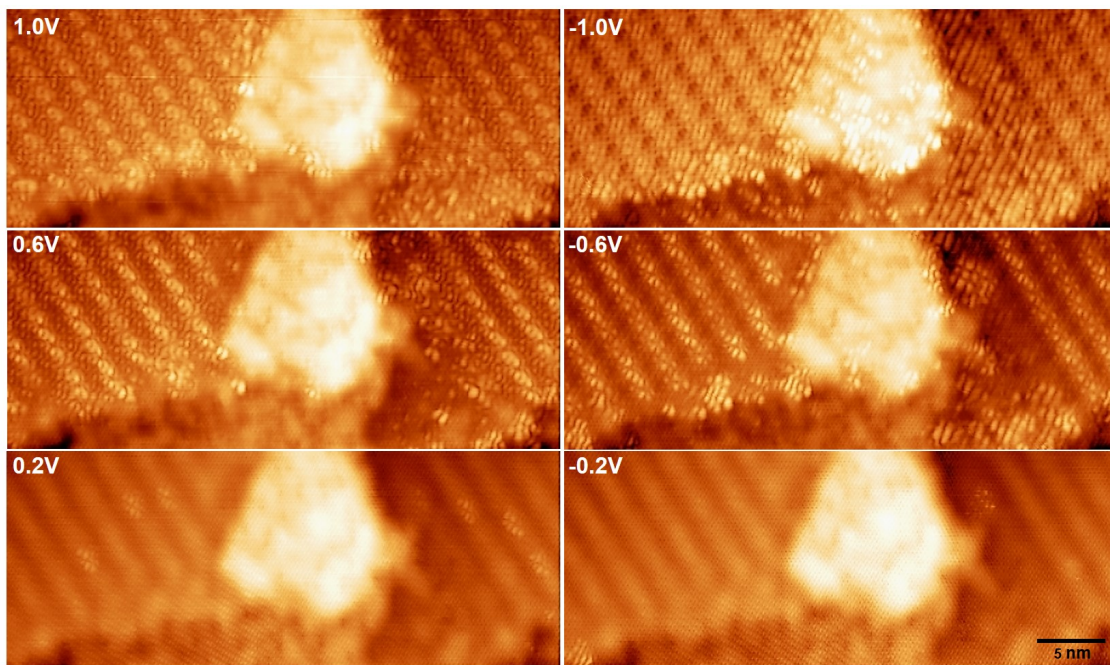


Figure 3.5 | Bias Dependency of STM images. Serie of STM images of the same surface area acquired with different bias voltages. Tunneling current in all images is 0.1 nA. Adapted from [68].

becomes transparent to the tunneling electrons and only the underneath Ge surface is observable.

Therefore, figure 3.5 highlights how the topography of a surface can depend on the chosen bias voltage used in an STM experiment. It is also interesting to point out how the Ge surface changes appearance depending on the polarity of the applied bias voltage, regardless if it is hydrogen-passivated as in the as-grown samples or if it has reconstructed into the (6x2) phase. Notably, where hydrogen has not yet desorbed, the surface looks completely disordered at positive voltages (0.6 V and 1.0 V). On the other hand, the Ge atoms of the surface appear to be aligned along the $[\bar{1}10]$ direction at negative biases (-0.6 V and -1.0 V).

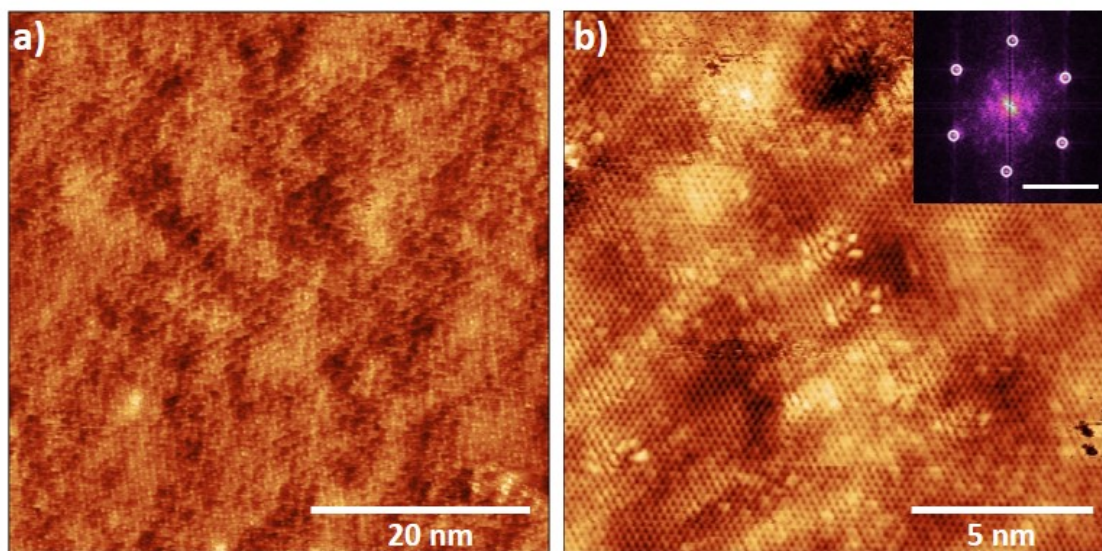


Figure 3.6 | STM images of graphene/Ge after high temperature annealing. STM images of the graphene/Ge(110) sample after annealing above 700 °C. Inset shows the FFT of the corresponding real space STM image in (b) and highlights the six primary spots of graphene. Inset scale bar 5 nm⁻¹ (V = -1.2 V and I = 0.8 nA in (a); V = -0.5 V and I = 0.8 nA in (b)). Adapted from [68].

Finally, figure 3.6 reports typical STM images of the sample surface upon annealing above 700 °C in UHV conditions. After this high temperature annealing the topography of the surface changes once again. Indeed, the (6x2) reconstruction disappears to be replaced by a rather disordered surface (figure 3.6a). By applying an appropriate bias voltage, the honeycomb lattice becomes clearly visible, confirming that the graphene layer has not been affected by the high temperature annealing, as shown in figure 3.6b. On the other hand, when the tunneling bias is high enough, graphene becomes transparent and the underneath Ge surface is easily imaged, as in figure 3.7. In particular, the STM image in figure 3.7 reveals that the surface exhibits a two-fold symmetry with a linear periodicity of 0.381 nm and 0.563 nm,

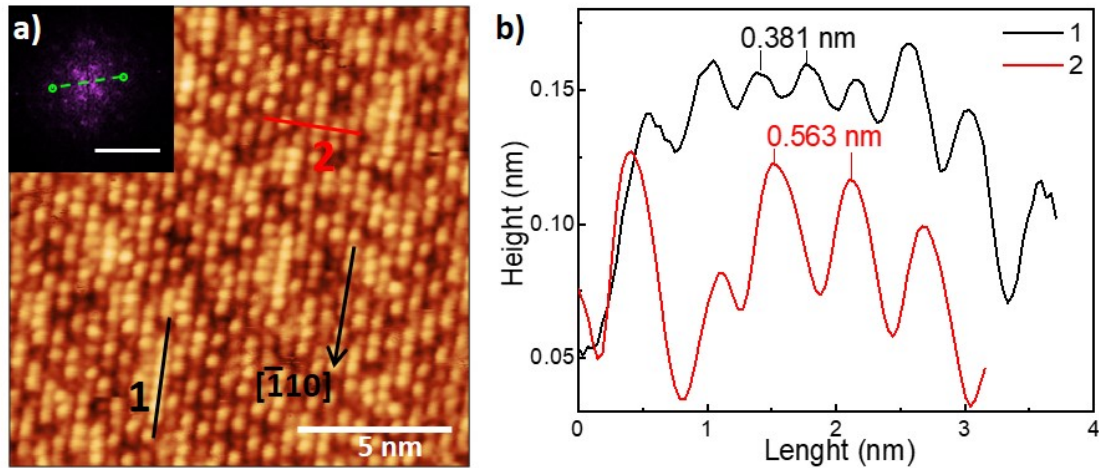


Figure 3.7 | STM image of graphene/Ge(110) after high temperature annealing. (a) Atomic-resolution of the Ge surface underneath graphene. The black arrow marks the $[\bar{1}10]$ direction. Inset shows the FFT of the corresponding STM image in panes (a) and highlights the 0.566 nm periodicity of the Ge surface. Inset scale bar is 5 nm^{-1} . (b) Line profiles taken along the Ge surface as indicated in (a). ($V = -1.2 \text{ V}$ and $I = 0.8 \text{ nA}$). Adapted from [68].

as indicated on the image itself and shown in the line profiles reported in figure 3.7b. Such periodicity values are consistent with the (1x1) phase of Ge and are furthermore confirmed by the FFT of figure 3.7a, reported in the inset. Indeed, the FFT shows only the periodicity of Ge, marked in green, and reveals a periodicity of 0.566 nm. Despite, the Ge atoms being overall aligned along the $[\bar{1}10]$ direction, as marked by the black arrow in figure 3.7, many of the atoms appear to be displaced from the expected lattice site either in the in-plane or out-of-plane direction. Moreover, the surface exhibits the presence of several defects, many of which are vacancies. It should be noted that after the high temperature annealing, we do not record the presence of hydrogen nanobubbles.

3.2 Conclusion

In conclusion, we have used STM to systematically investigate the structural modification of the interface between graphene and Ge(110) upon thermal annealing.

The as-grown sample features a H-passivated Ge surface, resulting from the graphene deposition via CVD. Upon annealing above $350 \text{ }^\circ\text{C}$ in vacuum, the H-Ge bonds break and the atoms at the Ge surface reconstruct into the (6x2) phase, peculiar of the graphene/Ge(110) system. Residual hydrogen remains trapped between graphene and the substrate to form nanobubbles, which can be found preferentially in the boundary regions between the (6x2) phase and Ge area that are still

H-passivated. Upon annealing at high temperature, above 700 °C, the hydrogen nanobubbles disappear and the Ge surface reconstructs again. Indeed, the (6x2) phase disappears and the Ge surface homogeneously exhibits a symmetry consistent with the (1x1) phase of Ge. Moreover, the surface of Ge shows several defects, such as vacancies.

Integrating graphene into conventional semiconductor technology could pave the way for the realization of novel device architectures. Therefore, in order to gain a complete control over the full integration process, the properties of the interface between graphene and substrate need to be fully investigated. To this end, this chapter presented the structural characterization of the graphene/Ge(110) interface, which constitutes the background to understand the electronic and chemical properties that will be presented in the next chapters.

Electronic Properties of Graphene/Ge(110)

This chapter presents the electronic properties of the graphene/Ge(110) system investigated by means of ARPES measurements. The experimental results are successfully supported by the theoretical model presented at the end of the chapter. In principle scanning tunneling spectroscopy (STS) can be used to determine the position of the Dirac point of graphene with respect to the Fermi level and thus measuring locally graphene's doping level. However, when it comes to the graphene/Ge(110) system, it has been shown that pinpointing the Dirac cone of graphene and determining its doping level from STS is not straightforward [92]. Indeed, in this case the spectra are largely dominated by features of the Ge substrate, thus hindering features associated to graphene. Moreover, STS provides very local information. Thus, we chose to use the ARPES in order to obtain information on the band structure of the whole system on a large scale.

The ARPES study systematically complements the STM characterization described in the previous chapter. Therefore, ARPES measurements were performed on the graphene/Ge(110) samples as-grown, after annealing above 350 °C and after annealing above 700 °C.

The results and discussion herein presented have been published by The Journal of Physical Chemistry Letters in the article titled "Tuning the Doping of Epitaxial Graphene on a Conventional Semiconductor via Substrate Surface Reconstruction" [68]. I would like to thank Ph.D. Marco Bianchi for the help with ARPES measurements and analysis. The theoretical model was built by Prof. Olivia Pulci (University of Roma Tor Vergata) and Ph.D. Paola Gori (University of Roma Tre)

4.1 Experimental ARPES

The experiments were carried out at the SGM-3 beamline of the synchrotron radiation source ASTRID-2 (Aarhus, Denmark) with the sample temperature kept at 66 K [93]. The photon energy used was 47 eV to probe the as-grown sample and after annealing above 350 °C. While photon energy of 100 eV was used to probe the sample after high temperature annealing. The combined energy and k resolution were better than 34 meV and 0.01 \AA^{-1} , respectively. The thermal annealings were performed *is-situ* in the ARPES chamber.

It should be noted that if more than one phase is present in the surface area probed by the beam, ARPES is not selective to one or the other. Thus, *in-situ* STM measurements at room temperature and LEED patterns (1 mm spot size) were collected before the ARPES measurements in order to make sure that only one phase was present before ARPES experiments. Furthermore, ARPES spot size is in the order of 1 mm^2 thus several orders of magnitude larger than the areas imaged with STM (in the order of hundreds of nm^2). This means that STM images might not be representative of the whole sample. For this reason, the STM images were complemented with LEED measurements, which probe an area comparable in size with the one investigated by ARPES. In light of the STM results in the previous chapter, where it was shown the coexistence of two different phases, it is important to stress the above point. Indeed, as we will see, the presence of one phase or the other affects the electronic properties of the system.

The overview of the experimental ARPES results, meaning the dispersion shown as photoemission intensity as a function of binding energy and momentum \mathbf{k} of the electrons, is shown in figure 4.1.

The top panels of figure 4.1 show the data collected perpendicular to the $\Gamma - K$ direction of the graphene Brillouin zone. The middle panels of the figures show the data collected parallel direction instead. The crossing point of the linearly dispersing π - band branches defines the position of the graphene's Dirac point in energy. To estimate the Dirac point binding energy (E_D), the momentum distribution curves (MDCs) corresponding to the branches of the π - band are fitted with a Lorentzian function and two peaks positions are used for linearly extrapolate the Dirac point considering a range of binding energies from 0.3 to 0.6 eV below the Fermi level. The analyses of MDCs fix the energy at a particular value, and studies the intensity as a function of momentum. The MDCs analyses eliminate the effect of the Fermi function and the energy-dependent background. As discussed previously in chapter 2, the measured intensity in ARPES is proportional to the

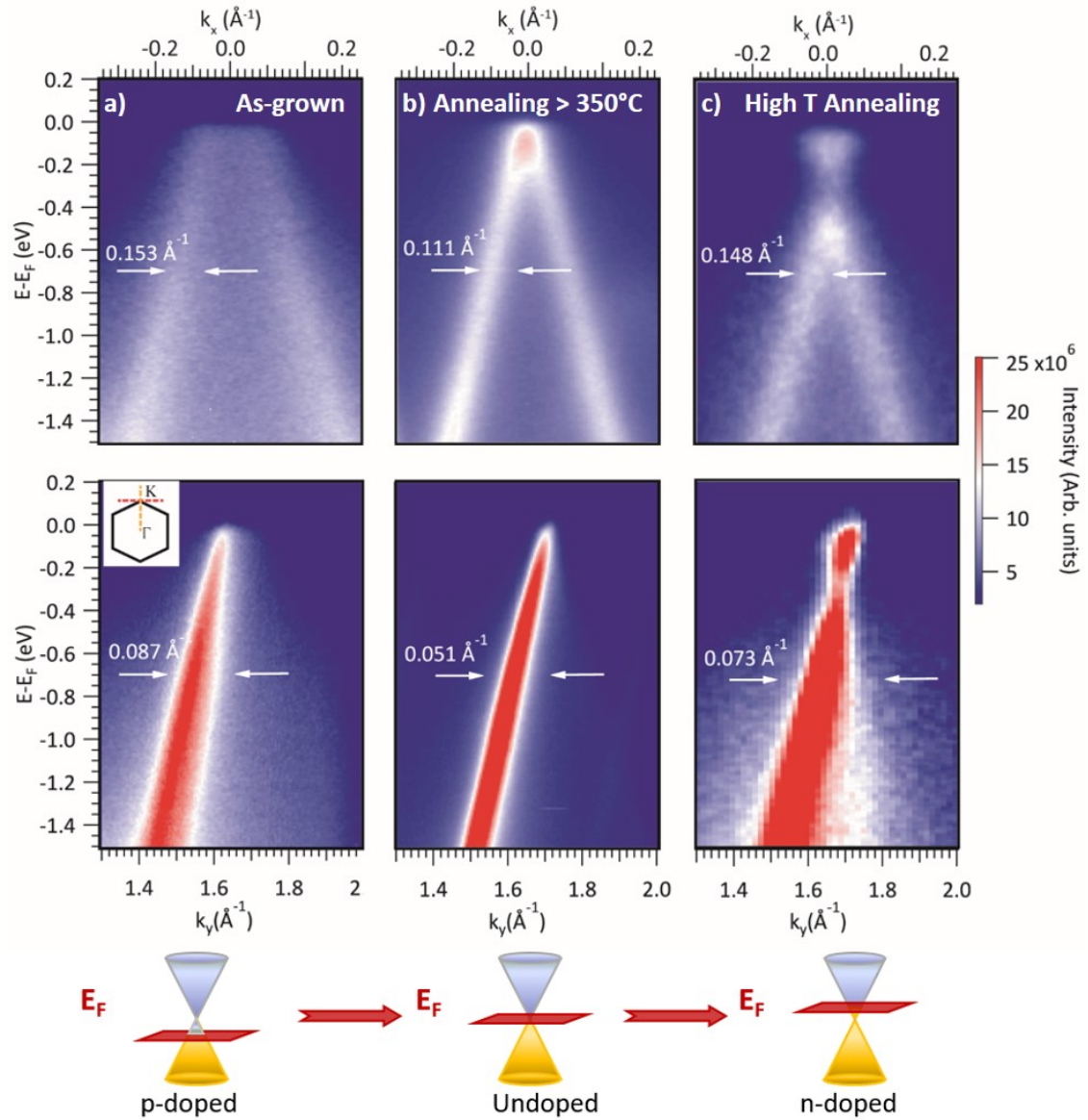


Figure 4.1 | ARPES of the graphene/Ge(110). Photoemission intensity of the graphene/Ge(110) sample (a) as-grown, (b) after annealing above 350 °C, and (c) after high temperature annealing. The spectra were acquired along the direction orthogonal to the Γ - K direction ((a-c) upper panels) and along the Γ - K direction ((a-c) middle panels) in the Brillouin zone, as schematically shown in the inset in the middle panel in (a). Bottom row: sketch highlighting the evolution of graphene doping level with the annealing of the sample. Adapted from [68].

single particle spectra function $A(\mathbf{k}, E)$. The peak positions from the MDCs fit give direct information on the renormalized band dispersion and the MDCs line width is directly related to the imaginary part of the self-energy.

Using the linear extrapolation, the ARPES measurements place E_D at a binding energy of 0.376 ± 0.018 eV above the Fermi energy (E_F) for the sample as-grown (figure 4.1a), indicating that graphene is *p*-doped. Furthermore, from the MDCs line width, it is possible to retrieve information about graphene's integrity and its interaction with the Ge substrate. Thus, the MDCs line width value orthogonal to the Γ - K direction taken at 0.70 eV below the Fermi level measures 0.153 ± 0.002 \AA^{-1} for the as-grown sample.

Upon annealing in vacuum above 350 °C, when the Ge surface reconstructs into the (6x2) phase, the doping level of graphene decreases, as shown in figure 4.1b. Indeed, the linear extrapolation shows that E_D is now very close to E_F , at a binding energy of 0.045 ± 0.005 eV. Thus, we can conclude that graphene is close to an undoped state, which suggests very little charge transfer with the Ge underneath. Moreover, the MDCs line width value is 0.111 \AA^{-1} , thus almost 30% smaller than the value for the as-grown sample, supporting the conclusion of a weaker interaction between graphene and Ge when the surface of the substrate has largely reconstructed into the (6x2) phase.

Furthermore, after the high temperature annealing (i.e. above 700 °C), following the same analysis, the E_D is found at 0.478 ± 0.007 eV below E_F . Thus, graphene is *n*-doped upon high temperature annealing. Moreover, the MDCs line width is 0.148 ± 0.002 \AA^{-1} , a value consistent with the one for the as-grown sample and therefore, larger than that of the sample after annealing above 350 °C.

These findings suggest that upon high temperature annealing, the interaction between graphene and Ge becomes stronger in comparison to the interaction when the Ge surface rearranges into the (6x2) phase. However, the integrity of the graphene layer is not affected by the annealing processes, as a poorer structural quality would reflect in the broadening of the MDCs line width with respect to the as-grown sample. In addition, for the sample after high temperature annealing, the MDCs taken along k_x close to the Dirac point in the range 0.04 - 0.56 eV shows the opening of a small band gap of ≈ 120 meV, as can be seen in the middle panel of figure 3.6c) and in figure 4.2, which again suggests a stronger interaction between graphene and the substrate.

The experimental ARPES results are quite interesting, as they point out how it is possible to change the graphene doping and eventually one can envision to control

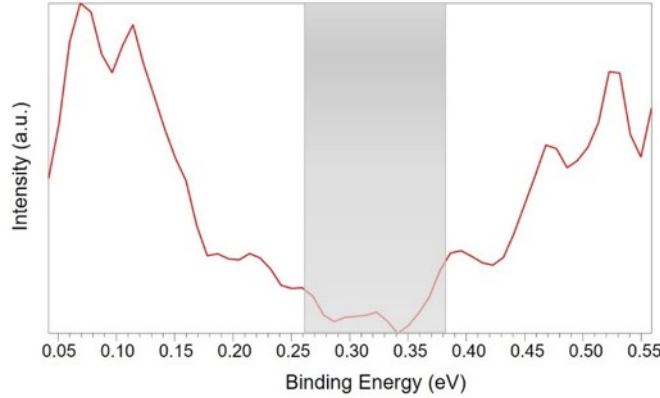


Figure 4.2 | Bandgap in graphene/Ge(110) after high temperature annealing. The MDCs analysis along k_x in the energy range 0.04 - 0.56 eV for the graphene/Ge(110) sample upon high temperature annealing. The diagram shows the opening of a small band gap of ≈ 120 meV marked here in grey. Reprinted from [68].

its interaction with the substrate using the appropriate processing.

Lastly, figure 4.3 shows the k -dependent photoemission intensity at constant energy of 0.90 eV below E_D for the sample as-grown, after annealing above 350 °C and after the high temperature annealing. Figure 4.3b refers to the sample after annealing above 350 °C and it stands out in comparison to the other two, as in this case four replicas are visible around the main Dirac cone at the K point (two of them marked by white arrows in the figure). The replicas result from the super periodic potential created by the moiré of graphene and the (6x2) symmetry of Ge. Indeed, the patterns of the replicas and the corresponding LEED (figure 3.4) are consistent with each other. The presence of replicas is not uncommon. Indeed, for example, similar replicas have been observed in the graphene/Ir(111) system, which also creates a moiré pattern [94, 95]. In contrast, graphene/Ir(111) samples show also minigaps at the crossing points of the replicas with graphene main cone [94, 95]. Such minigaps are not detected in the measurements on our graphene/Ge(110) sample. Indeed, close to the crossing points of the replicas and the main cone, the intensity of the spectral function does not vanish or decrease as expected in the case of a minigap, as shown in figure 4.4. For the as-grown sample or after high temperature annealing, the photoemission intensities at constant binding energy cut do not show any replicas (4.3a,c), as expected.

4.2 Theoretical Model

To gain more insights into the graphene/Ge(110) system and finally correlate the experimental results on the structure and electronic properties of this interface, we

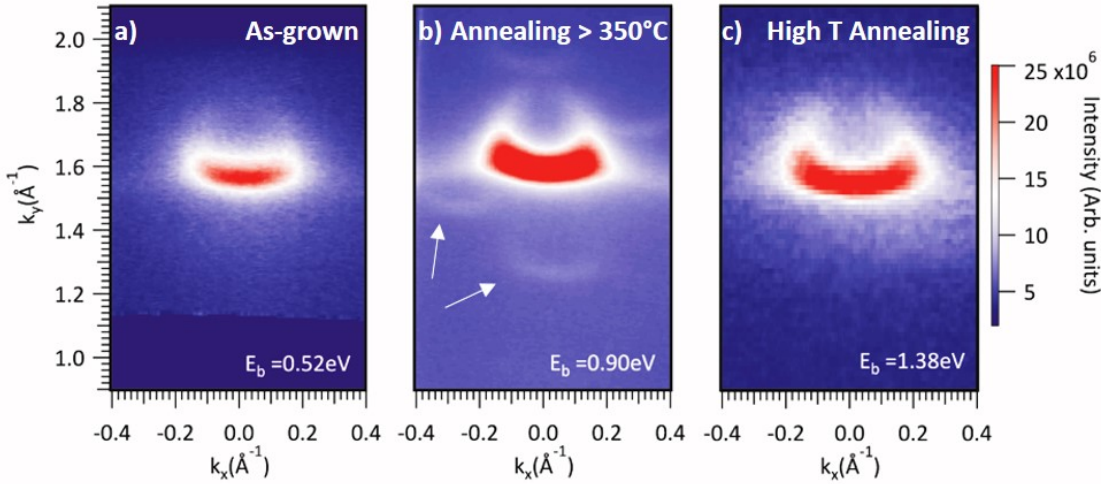


Figure 4.3 | ARPES of graphene/Ge(110). Constant binding energy cuts at 0.90 eV below the extrapolated Dirac point for the samples as-grown (a), after annealing above 350 °C (b), and after high temperature annealing (c). The white arrows in panel (b) point to the position of two out of four replicas. E_b values indicate the corresponding binding energy values of the cut. Adapted from [68].

also built a theoretical model based on ab-initio calculations to describe the sample as-grown and after high temperature annealing, which represent the two cases with opposite doping of graphene.

The simulations herein presented are performed using density functional theory - local density approximation (DFT-LDA) calculations for the geometries and the electronic band structures, using the Quantum Espresso package [96].

The Ge(110) surface was simulated by a 5-layer slab with a 3x5 rectangular geometry which contains 150 Ge atoms. The bottom of the slab was passivated by hydrogen atoms. The graphene layer was modeled by a 4x8 rectangular cell containing 128 C atoms and an angle of 30° between the $[\bar{1}10]$ direction of Ge(110) and the armchair direction of graphene accounts for a commensurate matching of the two with a strain of less than 2%. A vacuum layer of about 15 Å was used to decouple periodic images of the slabs along the direction perpendicular to the surface. We employed norm-conserving pseudopotentials and a kinetic energy cutoff of 45 Ry. Tests with ultrasoft pseudopotentials explicitly containing the semicore d states of Ge were performed, leading to no significant differences. Dipole corrections were added. Van der Waals interactions were introduced following the schemes described in refs. [97, 98]. Equilibrium geometries were obtained by relaxing the atoms until the forces were below 10^{-3} a.u. and the total energy changed less than 10^{-5} a.u. A mesh of 4x4x1 k-points in the Brillouin zone was used.

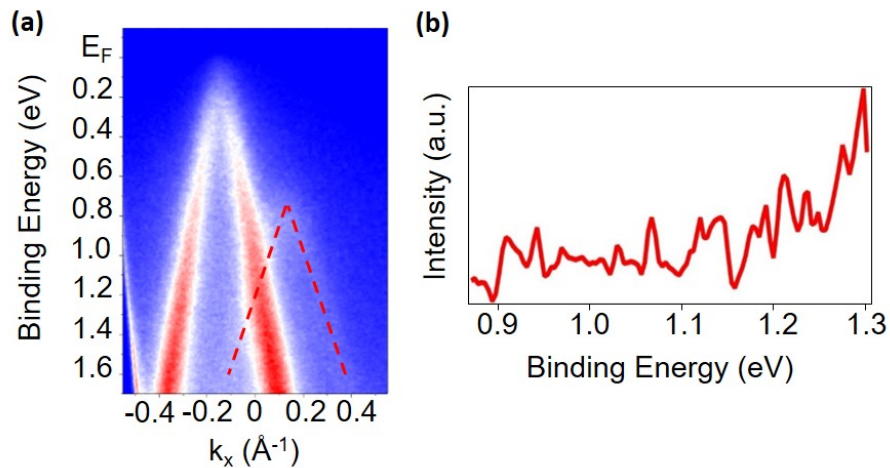


Figure 4.4 | ARPES Graphene/Ge(110) after annealing above 350 °C. Absence of minigaps at the crossing of graphene main Dirac cone with its replica. a) ARPES intensity map. The main Dirac cone and replica (dashed red lines) dispersion bands cross at ~ 1.2 eV. b) Intensity of Dirac cone dispersion extracted by MDCs analysis. The intensity of the band does not vanish or decrease at the crossing point, as would be expected in presence of a minigap. Reprinted from [68].

The sample as-grown and after high temperature annealing are modeled by the same supercell but in the latter case, the Ge surface is not passivated by H atoms, as depicted in figure 4.5. The key feature in these models is the presence of a vacancy in the surface layer of the Ge substrate (one vacancy in the 3×5 cell). The position of the vacancy is marked by the black circle in the 3D models presented in figure 4.5 and highlighted as a green atom in figure 4.6.

The vacancy in the Ge surface is introduced in the models as, from literature, it is known that when Ge is brought to high temperature, such as that used during graphene growth, occurs a spontaneous formation of vacancies, which starts from the surface and then spreads throughout the bulk [41, 99–102]. This process gives to the Ge wafer a p -doping character regardless of the initial nominal doping. Indeed, several samples of bare Ge nominally n -doped, such as those used in the experiments above presented, have been annealed in H_2/Ar atmosphere to the same temperature used for graphene growth. We performed Hall measurements on these substrate samples and they revealed that the samples were p -doped, as explained in figure 4.7.

The electronic band structure obtained for the as-grown sample shows that the Fermi level lies below the Dirac point, giving rise to p -doping of graphene (figure 4.5c). Qualitatively, this result is in agreement with the ARPES experiment reported in figure 4.1a. To support and justify the presence of vacancies in the Ge

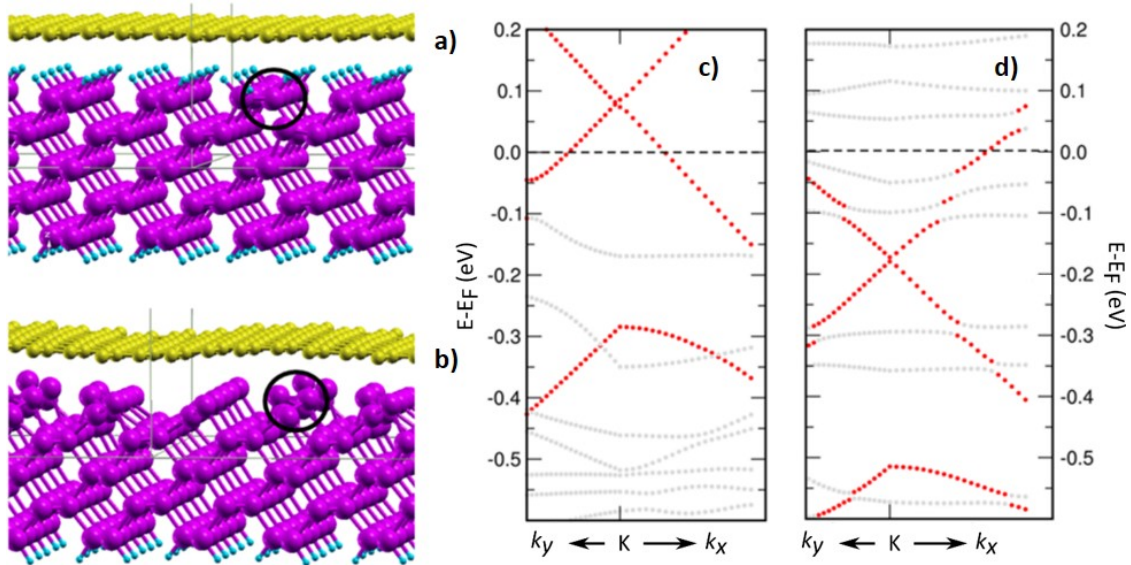


Figure 4.5 | Simulations of graphene/Ge(110) as-grown and after high temperature annealing. 3D side-view of as-grown sample with all dangling bonds being H-terminated (a) and after high temperature annealing (b). Cyan denotes H atoms, violet Ge atoms, and yellow C atoms. The black circles mark the position of the vacancy. (c), (d) Calculated electronic band structures around K with a total k range of 0.07 \AA^{-1} for (a) and (b), respectively. Red dots represent graphene-derived states, whereas grey dots represent Ge or H states. Reprinted from [68].

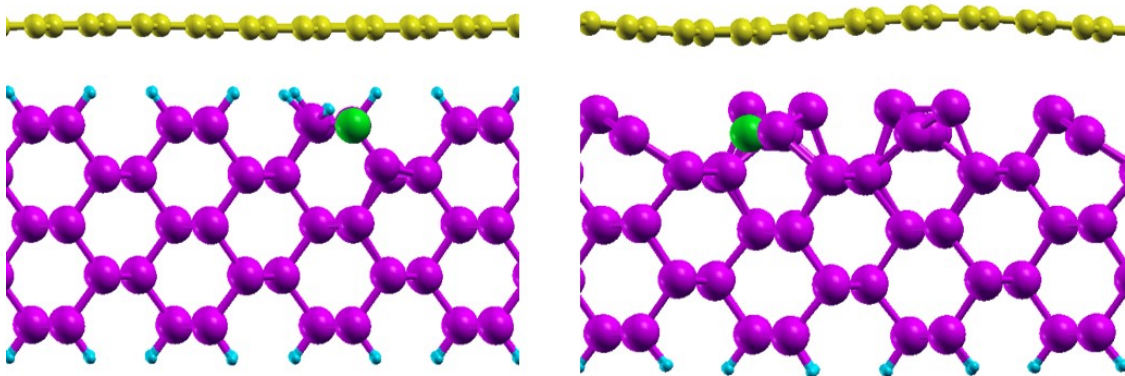


Figure 4.6 | 3D models of graphene/Ge(110) as-grown and after high temperature annealing. (Left) Side-view of the as-grown sample where all Ge dangling bonds are saturated by H atoms. (Right) Side-view of the sample after high temperature annealing. In cyan the H atoms, in violet the Ge atoms, and yellow the C atoms. The position of the vacancy in the topmost layer of Ge is highlighted in green. Reprinted from [68].

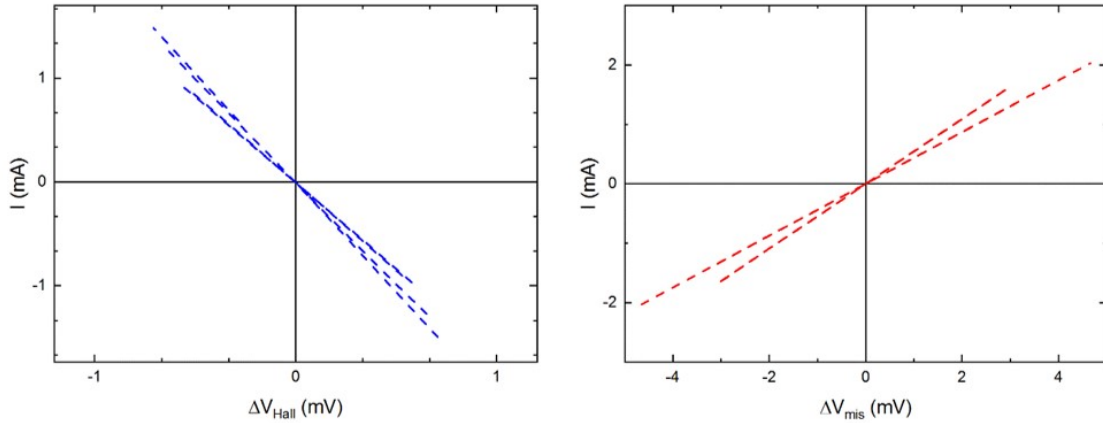


Figure 4.7 | Hall measurements on bare Ge. Examples of Hall and resistivity measurements performed at room temperature on different Ge substrates after annealing in the atmosphere to 930 °C in H₂/Ar atmosphere during simulated graphene growth experiments. The measurements have been carried out with Van der Pauw configuration. Magnetic field: 0.7 T. For all the samples investigated, a p-type Hall behavior is observed with sheet carrier density in the range 0.8 - 7.0 x 10¹⁴ cm⁻². Reprinted from[68].

substrate of the model, additional simulations were performed. Namely, we simulate a Ge surface with no vacancy and one with an Sb atom replacing the vacancy (Sb is the dopant nominally present in the Ge substrate used in the experimental work). Both the calculations result in a Fermi level above the Dirac point, corresponding to *n*-doped graphene, and therefore in contrast with the experiments, as reported in Table 4.1.

The simulation with an Sb dopant atom in the Ge surface was performed because a previous study reported the *n*-doping of graphene after high temperature annealing of the sample at 800 °C [103]. In that case, the authors ascribed the *n*-doping character to a massive surface segregation of dopants (Sb atoms also in that case) present in the bulk Ge substrate, as a result of the high temperature annealing. However, this explanation was not convincing completely despite the similar Ge substrates used in both ref. [103] and in this present work. Bright patches are visible in our STM images in figure 3.6 and could appear as areas of segregated dopants. However, a closer look at figure 3.2 reveals that similar bright patches are seen also in the as-grown sample.

Therefore, supported by the theoretical simulation, we believe that thermally induced vacancies and not Sb segregation plays a key role in determining the graphene doping as reported in the experiments performed on the as-grown sample.

The sample after high temperature annealing was simulated by removing the H atoms passivating the Ge(110) surface. In this case, the simulations reveal several

Table 4.1 | Comparison between the experiments and DFT calculated position of the Dirac point with respect to the Fermi level ($E_D - E_F$), for the samples as-grown, ordered Ge surface after high temperature annealing and intentionally disordered Ge phase after high temperature annealing. The following notation is used: Pristine refers to the intrinsic, undoped Ge substrate; Vacancy refers to the Ge substrate with 1 vacancy in the 3x5 cell; Sb refers to the Ge substrate with 1 Sb atom segregated at the surface.

	$E_D - E_F$ (eV)			Experiment
	Pristine	Vacancy	Sb	
As-grown	-0.22	+0.08	-0.49	+0.376
High T annealing (ordered)	+0.08	+0.05	+0.02	—
High T annealing (disordered)	-0.13	-0.18	-0.23	-0.478

local minima in energy after geometrical relaxation, in contrast to the single energy minimum observed for the as-grown sample. While the most stable structure is an ordered Ge(110) surface, the other minima correspond to slightly disordered Ge surfaces (figure 4.5b), with total energy within a few meV/(C atom) from the ordered one. The presence of a disordered surface is confirmed and supported by the STM images displayed in figure 3.6 and figure 3.7. The electronic band structure of the disordered surface is reported in figure 4.5d and it shows that the Fermi level lies above the Dirac point. Therefore, graphene is *n*-doped and the results are coherent with the experimental ARPES data (figure 4.1c). Furthermore, it should be noted that a similar result - meaning, *n*-doped graphene - is achieved when a second intentionally disordered Ge surface is simulated. On the other hand, when simulating an ordered Ge surface, no agreement with the experiment is found. In conclusion, the thermally induced disorder in the Ge surface and not dopant segregation is the main factor that determines the doping character of graphene.

4.3 Conclusion

In conclusion, by means of ARPES measurements, we have investigated the electronic properties of the graphene/Ge(110) system, following the same cycle of thermal annealings used for the STM investigation presented in the previous chapter.

The experimental ARPES results show that the as-grown sample features a p -doped graphene. Upon annealing above 350 °C in vacuum, thus when the Ge surface reconstructs into the (6x2) phase, graphene is nearly intrinsic (undoped). Finally, upon annealing at high temperature, above 700 °C, graphene is n -doped. Starting from the characterization of the structure with STM, we build a theoretical model that qualitatively mimics the experimental ARPES trend.

This chapter provides a contribution towards the integration of graphene with conventional semiconductors, as understanding the electronic properties of the interface between graphene and semiconductor is crucial when it comes to applications.

Chemical Properties of Graphene/Ge(110)

The published structural investigations [65, 67, 103] and the results presented in the previous chapters reveal a complex scenario in which the surface termination of Ge(110) and graphene properties can be modified by in-vacuum thermal annealing. It was found that the as-grown samples, where graphene is deposited by CVD and cooled in H₂ atmosphere, feature a Ge surface stabilized by the presence of interfacial H atoms [59, 65]. For thermal annealing above 350 °C, the Ge(110) surface reconstructs into the novel (6x2) phase after losing the H termination [44, 65–67]. At even higher temperatures, above 700 °C, further structural changes occur, leading to the formation of another phase showing a symmetry approaching that of the previous unreconstructed (110) surface but without the H passivation [67].

The results of the ARPES investigation reported in chapter 4 showed a clear correlation between graphene electronic properties and the specific surface structure and termination of the Ge(110) substrate. In particular, after the high temperature annealing, ARPES measurements show a small gap opening in graphene's Dirac cone. This finding indicates a strong interaction between graphene and substrate.

The study in ref. [67] suggests that the high temperature annealing leads to the formation of chemical bonds between graphene and Ge. This conclusion follows the observation of defect centers in graphene identified with STM and Raman spectroscopy [67]. However, these two techniques are not element-specific and thus cannot identify the elements involved in the sp³ bonding.

To this end, this chapter presents the investigation of the chemical state of the graphene/Ge(110) interface as a function of thermal annealing. The study is based on XPS and NEXAFS measurements and is supported by Raman spectroscopy and STM. The XPS and NEXAFS experiments were performed at the BACH beamline at the ELETTRA synchrotron facility in Trieste, Italy. We should point out that since only a small fraction of the Ge surface atoms is expected to be bonded to C, the magnitude of related spectral fingerprints would be too low to detect with standard laboratory equipment. Therefore, access to a synchrotron source, enabling enhanced cross-section and surface sensitivity, was needed to perform such investigation. I would like to thank Federica Bondino (scientist in charge at the beamline) and Igor Pis (scientist) for the help in setting up the measurements. The measurements and analysis presented in this chapter have been performed together with my co-supervisor Luca Camilli, Ph.D. Luca Persichetti and master student Antonio Caporale. The analysis of the measurements is currently being finalized. However, a discussion of the interesting preliminary results is presented here.

5.1 XPS and NEXAFS

The XPS and NEXAFS measurements on graphene/Ge(110) samples were performed sequentially after in-vacuum annealing at 100 °C, 450 °C, and 650 °C.

After each annealing, LEED measurements were performed to characterize the long-range order of the surface, and an overview of the measurements is reported in figure 5.1.

The brightest features in all LEED patterns correspond to the primary spots of graphene. The spots rotated of 30° with respect to the primary ones indicate the presence of a second graphene's domain [44]. In addition to graphene's features, the LEED pattern of the surface after annealing at 500 °C shows the rectangular moiré pattern around the primary spots of graphene. This indicates the presence of the (6x2) reconstruction of Ge surface and it is consistent with the results reported in chapter 3 in figure 3.4. The annealing in the current study was performed at a higher temperature than that used for STM and ARPES investigations (i.e. 500 °C instead of 350 °C). This is because LEED measurements revealed that the annealing at a nominal temperature of 350 °C was not sufficient to induce the Ge reconstruction into the (6x2) phase in the setup available for the experiments. Therefore, to build a study consistent with the STM and ARPES investigation and

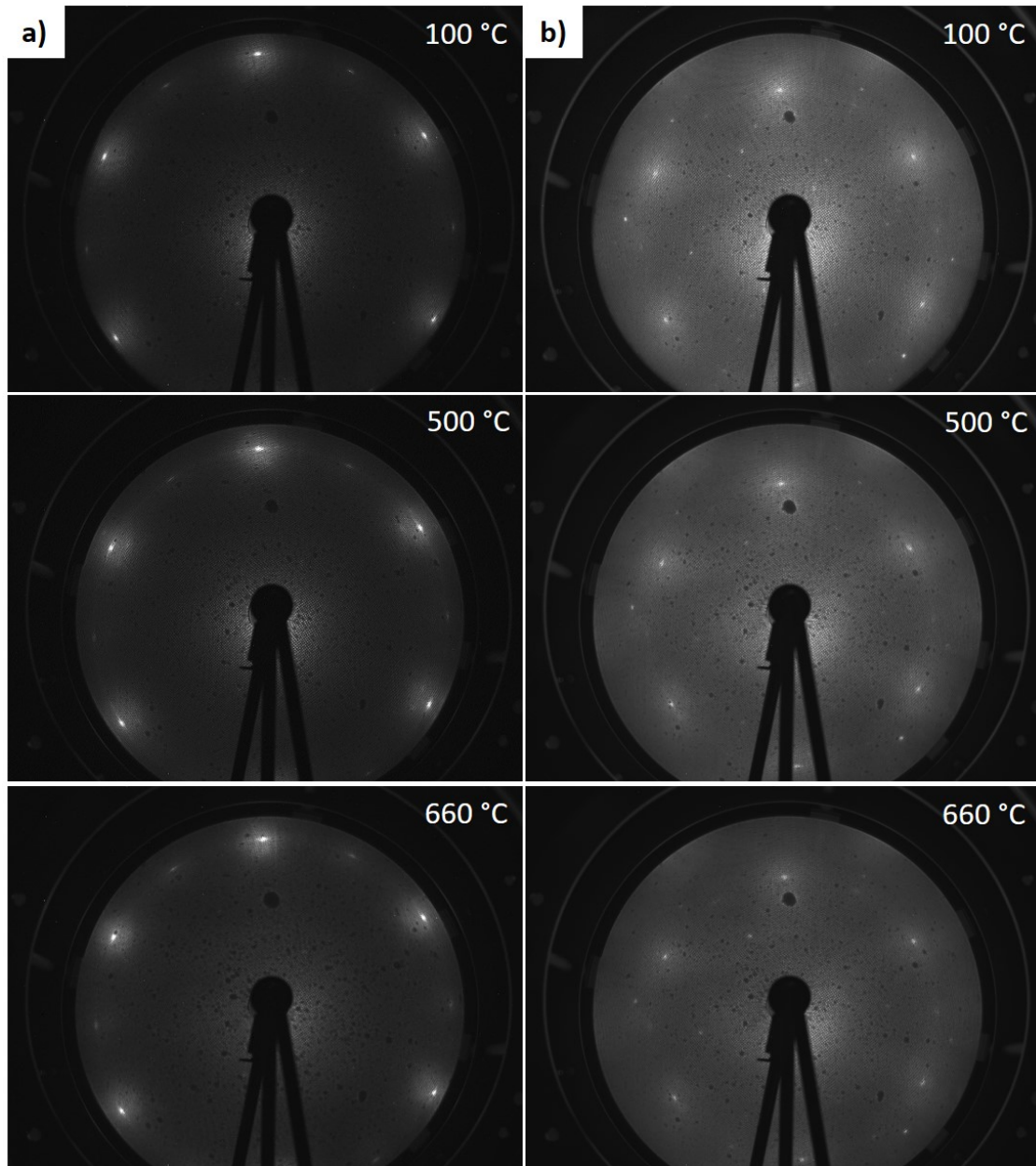


Figure 5.1 | LEED pattern graphene/Ge(110) samples. LEED patterns acquired after each annealing as indicated in the pictures. Column a) corresponds to measurements acquired with energy of the primary source of 80 eV to highlight only the superficial features. Column b) represents the images acquired with a primary source of 130 eV to distinguish also the features within deeper regions of Ge substrate.

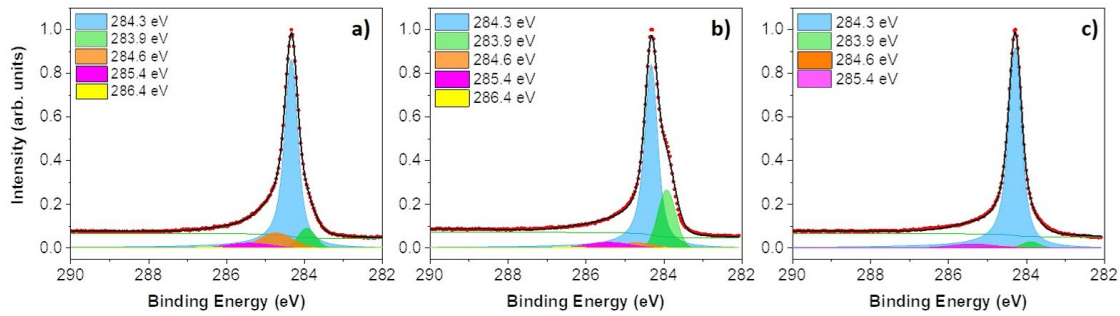


Figure 5.2 | C 1s XPS spectra graphene/Ge(110) samples. Core levels acquired after annealing at (a) 100 °C, (b) 500 °C and (c) 660 °C.

induce the reconstruction of the Ge surface, we annealed the sample at a nominally higher temperature of 500 °C.

On the other hand, the last annealing was performed at 660 °C, thus, at a slightly lower temperature than that used for STM and ARPES studies (i.e. 700 °C), due to limitations of the current setup available for the experiments.

After LEED measurements, the XPS experiments were performed focusing on C 1s and Ge 3d core levels. Figure 5.2 shows the overview of the C 1s core levels acquired after each annealing. Among the different spectra, the major difference is found in the spectrum acquired after the annealing at 500 °C, which shows a shoulder towards the low binding energies. Such a feature is not observed after the two annealings at 100 °C and 660 °C.

The deconvolution of the XPS spectra shows the different C 1s components. The main one is at a binding energy of 284.3 eV and corresponds to the sp^2 -hybridized carbon atoms [104]. In addition to the graphene peak, a few other components are observed. Towards higher binding energies, the component at 284.6 eV accounts for disordered C, which is intermediate between sp^2 and sp^3 states [104] and is related to defects of different nature such as boundaries of the graphene domains [105], C-H bonds, or C atoms close to those bonded to oxygen groups [106]. Indeed, the components at 285.4 eV and 286.4 eV correspond to C-OH or COOH groups, assigned to adventitious contaminations [107]. In the region of lower binding energy with respect to the main graphene peak, we find a component at 283.9 eV, which has been previously observed for H-intercalated graphene on Ir(111) [108–110]. Therefore, from the analysis of the C 1s spectra, we do not observe the presence of sp^3 Ge-C bonds, which would result in a component at even lower binding energy [111].

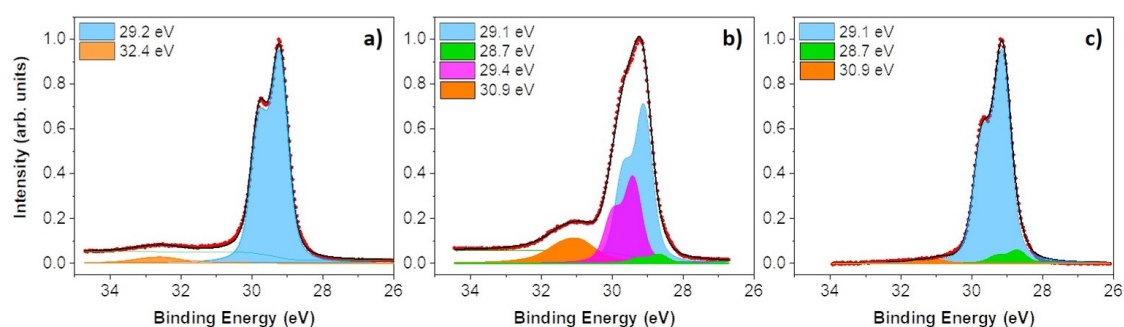


Figure 5.3 | Ge 3d XPS spectra graphene/Ge(110) samples. Core levels acquired after annealing at (a) 100 °C, (b) 500 °C and (c) 660 °C.

Upon annealing at 660 °C, the component of the adventitious carbon (286.4 eV) disappears and the intensity of the one related to disordered C (284.6 eV) significantly decreases, indicating the desorption of functional groups (figure 5.2c) bonded to graphene. At the same time, the peak's intensity at 283.9 eV significantly reduces (figure 5.2c), suggesting the desorption of the intercalated hydrogen.

The overview of Ge 3d core levels spectra is reported in figure 5.3. The measurements after the annealing at 100 °C reveal the presence of two components (figure 5.3a). The main one shows the characteristic spin-orbit doublet with $3d_{5/2}$ binding energy of 29.2 eV and the $3d_{5/2} - 3d_{3/2}$ energy splitting of ~ 0.6 eV. This peak is assigned to Ge-Ge bonds. The second component corresponds to the native oxide GeO_2 , centered at a binding energy of 32.4 eV [112].

Upon annealing at 500 °C, the Ge 3d spectrum changes. Two extra components are observed, both with the characteristic lineshape of the Ge-Ge peak and account for the differences between bulk-Ge and reconstructed surface [113–115]. Upon thermal annealing, GeO_2 decomposes to form GeO [116, 117], as confirmed by the peak at 30.9 eV and the disappearance of the GeO_2 peak at 32.4 eV. After the high temperature annealing, the components do not shift with respect to the previous annealing. However, the GeO peak's intensity reduces as result of the desorption of the oxide species [116, 117].

Therefore, also the Ge 3d core levels spectra do not indicate the formation of Ge-C bonds [111], as it was instead suggested in earlier works [67].

Moreover, the presence of chemical bonds between graphene and Ge would have been detected by NEXAFS in the C K-edge spectra. However, the performed measurements do not indicate the formation of Ge-C bonds, as shown in figure 5.4. Indeed, the only features clearly recognizable in the spectra are the transitions

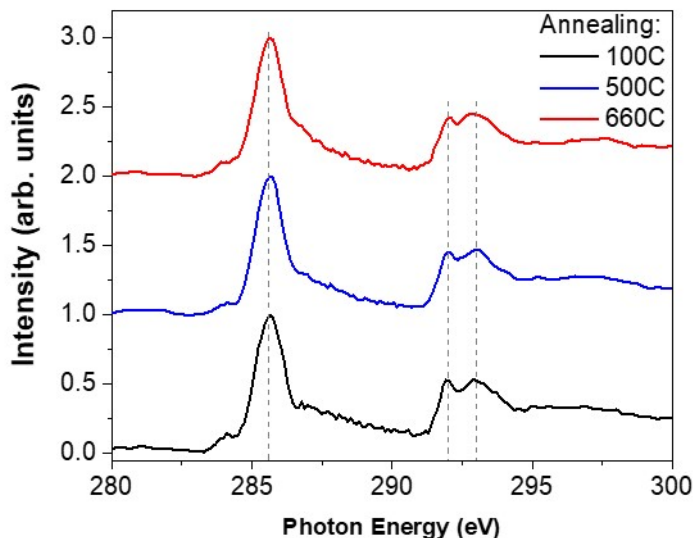


Figure 5.4 | NEXAFS C K-edge spectra graphene/Ge(110) samples. The dashed grey lines mark the resonances π^* at 285.6 eV, σ_1^* at 292 eV, and σ_2^* at 293 eV.

from C 1s core levels to the partially occupied or empty π - and σ - states, namely the π^* resonance at 285.6 eV and the σ^* resonances at 292 eV and 293 eV [118].

The $1s \rightarrow \sigma^*$ transitions feature a double peak structure. The first peak, called σ_1^* , is assigned to excitonic states and the second peak, called σ_2^* , is assigned to band-like contributions. Splitting of the σ^* resonances indicates highly crystalline graphene [119]. The intensity, shape, and position of a π^* resonance are sensitive to the π -bond order and chemical environment. If a C atom is double bonded to an atom with higher (lower) electronegativity, it will make the C atom more electropositive (electronegative) than a C=C. The different bonding affects the orbital energy and thus, the π^* transition in the spectrum will be shifted to higher (lower) binding energies.

Looking at the region below the π^* resonance, one can notice a small shoulder centered at 284 eV. In graphene, there should be only one π^* peak. Thus, a variation in the spectrum suggests the presence of a perturbation in the ideal 2D structure which can be given by defects such as pinholes and edges [120]. However, among the NEXAFS spectra collected after different annealings (and normalized to the π^* resonance intensity), there is no significant difference in the intensity of the shoulder at 284 eV.

Therefore, neither XPS or NEXAFS measurements indicate the formation of chemical bonds between graphene and Ge substrate and thus, we rule out this hypothesis.

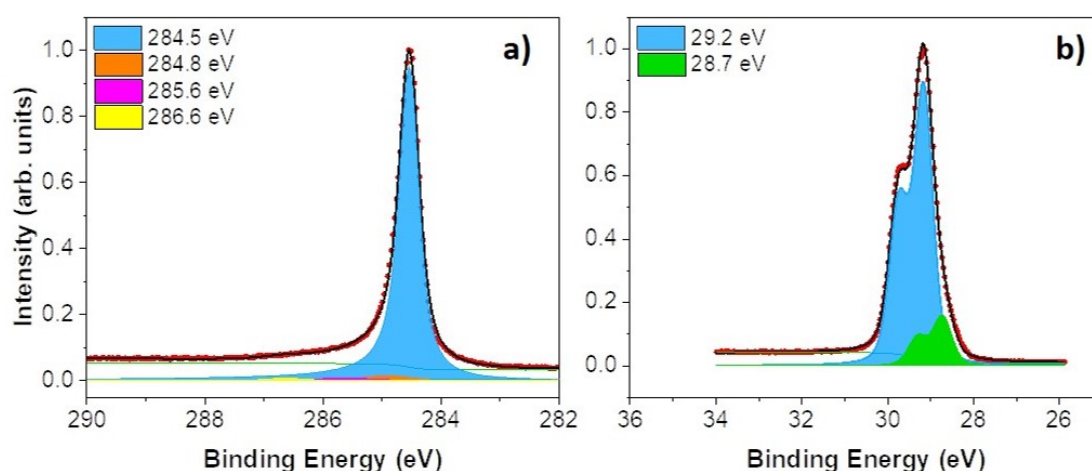


Figure 5.5 | XPS graphene/Ge(110) after annealing at 800 °C. a) C 1s core level and b) Ge 3d core level.

One could speculate that the annealing at 660 °C is not sufficient to induce the formation of C-Ge bonds. To address this point, we performed a series of annealing up to 800 °C on a second sample, as shown in figure 5.5. The XPS measurements of C 1s and Ge 3d core levels do not display any particular feature to indicate a bond between Ge and graphene or other differences with respect to the sample annealed at 660 °C.

The peculiar shape of the C 1s core level after annealing at 500 °C calls for some more considerations. The shoulder at lower binding energy results from the presence of the component at 283.9 eV. Interestingly, the intensity of this component increases after the annealing at 500 °C to then decrease after annealing at 660 °C. The STM study in chapter 3 found that upon rupture of Ge-H bonds (above 350 °C), part of the H atoms remains trapped between the Ge surface and graphene, forming hydrogen nanobubbles [91]. Thus, the increased intensity of this component could be related to the amount of intercalated hydrogen, which upon formation of nanobubbles enhances the decoupling between graphene and Ge substrate. Upon high temperature annealing, hydrogen atoms finally desorb from defects and grain boundaries in graphene and thus, the intensity of the corresponding component in the XPS measurements decreases.

Indeed, figure 5.6 shows the STM measurements performed on the sample after the annealing at 660 °C and the XPS and NEXAFS experiments. The images reveal no presence of hydrogen nanobubbles and they also reveal the coexistence of areas showing the (6x2) reconstruction and (1x1) phase. The latter one is typical of the surface after high temperature, as seen in chapter 3 (figure 3.7). Thus, the shoulder at lower binding energy in the C 1s core level is not peculiar of one reconstruction

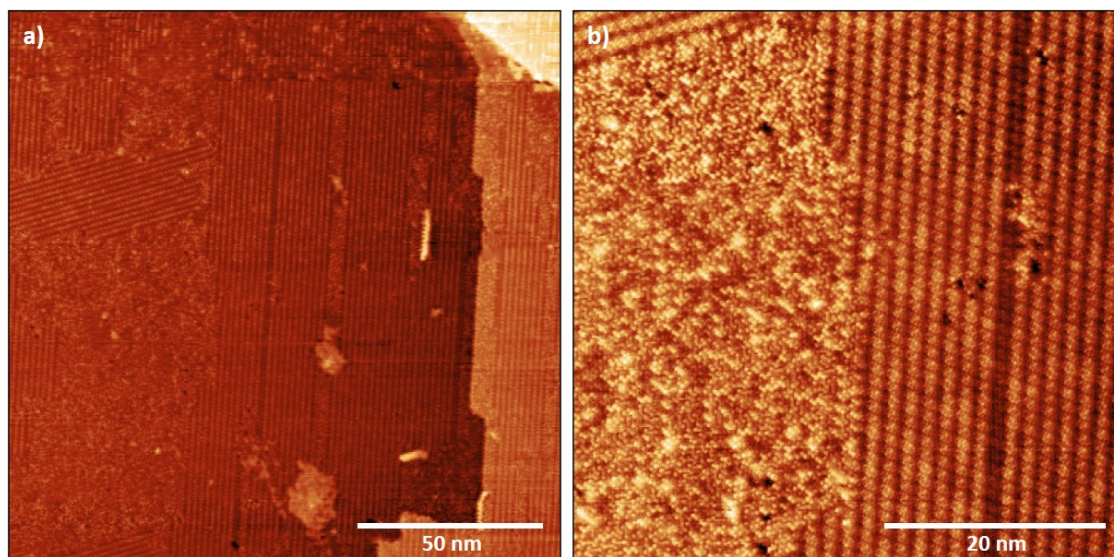


Figure 5.6 | STM of graphene/Ge(110) after annealing at 660 °C. STM images performed on the graphene/Ge(110) sample after annealing at 660 °C and after the XPS and NEXAFS experiments. The results shows no presence of hydrogen nanobubbles. The images reveal the coexistence of areas of (6x2) reconstruction and (1x1) phase. $V = -1.6$ V and $I = 0.3$ nA.

or the other.

In order to confirm the hypothesis that the shoulder in the C 1s core level is related to the presence of hydrogen nanobubbles, XPS and STM measurements were performed on a control sample after annealing at 500 °C. The C 1s core level spectrum shows the shoulder at lower binding energy (figure 5.7a), similarly to the other sample. The corresponding STM images are shown in figure 5.7b,c and highlight the presence of hydrogen nanobubbles.

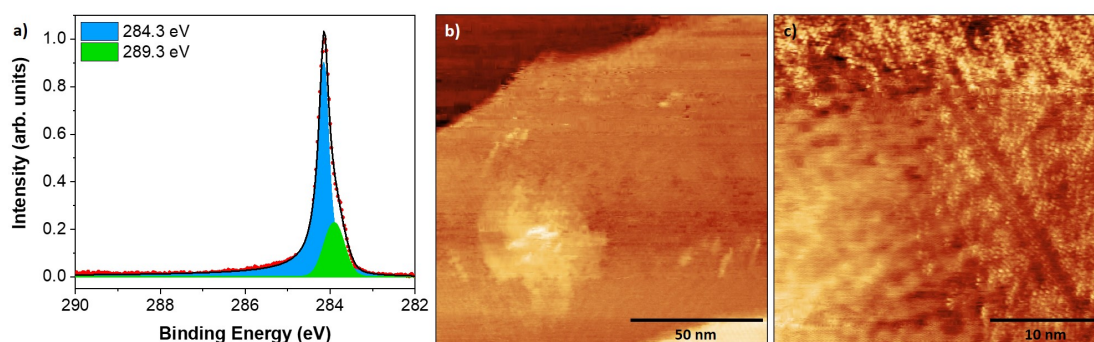


Figure 5.7 | XPS and STM of graphene/Ge(110) after annealing at 500 °C. a) C 1s core level spectrum of the control sample after annealing at 500 °C. b and c) STM images of the control sample after annealing at 500 °C. b) $V = -1.6$ V and $I = 0.35$ nA. c) $V = 1.6$ V and $I = 0.05$ nA.

Perhaps, one could think that the component at 283.9 eV in the C 1s spectrum

should instead be assigned to the nearest neighbor to the C atoms involved in the C-H bonds, as indicated in previous studies [108]. This second hypothesis is not unreasonable per se. However, this explanation does not fit with our results as the sp^3 component at 284.6 eV reduces after annealing at 500 °C. This observation indicates that after the annealing, fewer carbon atoms are involved in C-H bonds. Thus, in this case, one would expect the component at 283.9 eV to decrease as well.

Moreover, hydrogen functionalization induces n -type doping in graphene [121], which leads to a shift towards the higher binding energy of the sp^2 components of the C 1s spectrum. However, these components do not shift throughout the annealing cycle, thus ruling out the hydrogenation process. In addition, the region between the π^* and σ^* transitions in the NEXAFS spectra do not show any particular peaks, indicating a negligible amount of functional groups bonded to the graphene layer [119].

Interestingly, upon annealing at 660 °C, the σ_2^* resonance peak slightly moves towards lower energies. This shift is the only difference among the NEXAFS spectra and it might indicate the presence of defects in the graphene structure [107, 120]. We can speculate that such defects are caused by hydrogen desorption through graphene defects and grain boundaries. This hypothesis is supported by Raman measurements performed before and after the XPS and NEXAFS experiments, as shown in figure 5.8.

Indeed, the measurements before the experiments show a D peak substantially smaller than those recorded after the annealing cycle and the XPS and NEXAFS experiments. Moreover, after the experiments, the ratio of the intensity I_{2D}/I_G drastically decreases (figure 5.8a), suggesting higher doping of graphene with respect to the as-grown sample [86]. Lastly, from the position of the 2D and G peaks, it is also possible to estimate the level of stress or strain in graphene [122]. Raman measurements acquired on the samples and shown in figure 5.8b also indicate an enhanced level of stress in the graphene monolayer.

5.2 Conclusion

In conclusion, we have investigated the chemical state of the graphene/Ge(110) interface by means of XPS and NEXAFS measurements. The experiments were performed after annealing in vacuum at 100 °C, 500 °C and 660 °C.

Initially, the motivation for this study was to prove the presence of chemical bonds between graphene and Ge, which were thought to form after the annealing at high

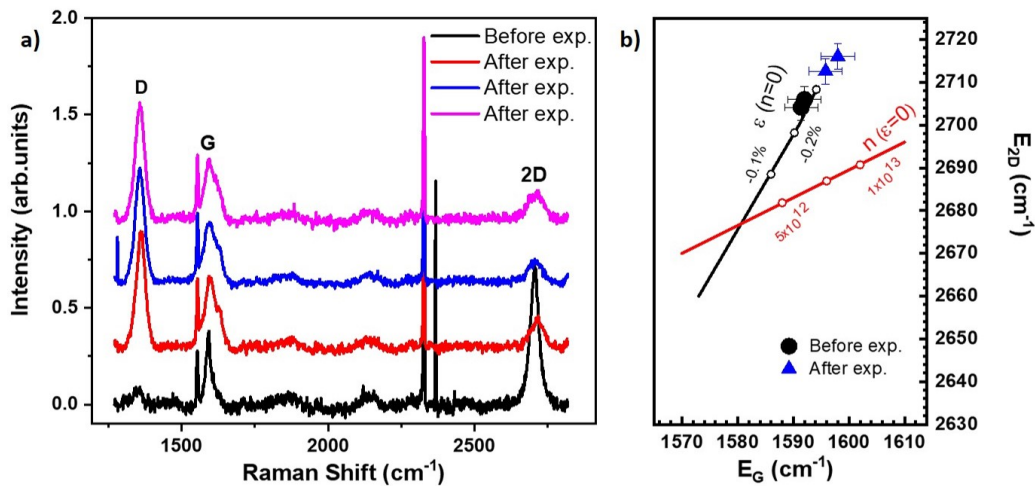


Figure 5.8 | Raman spectra of graphene/Ge(110). a) Raman spectra of graphene/Ge(110) sample. b) Plot of the 2D vs G-band energies. ε is the strain and n the charge density. Straight lines indicate E_{2D} vs E_G relationship for strained undoped (black line, $n = 0$) and unstrained n -doped ($\varepsilon = 0$) graphene. The two lines cross at the expected 2D and G positions for suspended freestanding graphene. Raman measurements were performed before and after the XPS and NEXAFS experiments as indicated in the legends.

temperature. However, the experimental results rejected this assumption to instead reveal that the presence of hydrogen nanobubbles affected the chemical state of graphene after the annealing at 500 °C. Indeed, the presence of nanobubbles reflects in the XPS measurements of the C 1s core level and gives rise to a shoulder towards lower binding energies with respect to the main graphene peak. Complementary STM measurements confirmed the presence of such nanobubbles.

The analyses of the experimental results presented in this chapter have yet to be finalized. In particular, the experimental results from NEXAFS measurements should be further analyzed and possibly compared by theoretical simulations.

2D Materials Beyond Graphene

Since the isolation of graphene in 2004, the family or for better say families of 2D-materials have grown tremendously. The research efforts are inspired by graphene's exceptional properties but also aim to overcome the challenges of the first 2D material. Above all, graphene's lack of bandgap makes difficult to integrate graphene in electronic applications.

In this scenario, silicene, germanene and stanene, which are collectively called group-IV X-enes, stand out in the landscape of 2D materials thanks to their compatibility with the existing semiconductor technology, especially for silicene and germanene. These materials, as the names suggest, are formed by a single atomic layer of one of the element of group-IV. In recent years, they have been synthesized on different metallic surfaces. However, the interaction with metals strongly affects the desired electronic properties of these materials.

In this chapter, the structures and properties of group-IV X-enes are briefly introduced along with the challenges related to their synthesis. Successively, the focus is narrowed on silicene and suitable non-interacting substrates potentially able to support its synthesis. In this regard, among the different candidates, CaF_2 have attracted our interest. For this reason, the last section of this chapter revolves around the experiments on the growth of CaF_2 on Si(111) performed during this project.

The overview on group-IV X-enes here presented have been published by Applied Physics Reviews in the article titled "Group-IV 2D materials beyond graphene on nonmetal substrates: Challenges, recent progress, and future perspectives" [70]. The results and discussion on the epitaxial growth of CaF_2 on Si(111) produced the

manuscript "Scanning tunneling microscopy study of CaF₂ on Si(111): Observation of metastable reconstructions", which has been submitted and accepted by Journal of Physics D: Applied Physics [69]. I would like to thank Prof. Maurizio De Crescenzi, Prof. Manuela Scarselli and Prof. Fabrizio Arciprete (University of Roma Tor vergata) for the helpful discussions.

6.1 Opportunities & Challenges for Group-IV X-enes

The 2D family called group-IV X-enes, formed by silicene [123, 124], germanene [123, 125, 126], and stanene [127, 128], has been proposed as a potential alternative to graphene [129–135]. These materials have an atomic structure very similar to graphene but also a fundamental distinction. Indeed, from an energetic point of view, at ambient conditions, carbon's most stable atoms arrangement is the honeycomb lattice. Thus, the most favorable structures are graphene and its bulk analog graphite. In both these configurations, the C atoms adopt a pure sp² hybridization which results in an atomically flat structure.

On the other hand, group-IV X-enes do not allow for stable flat structures, especially for Si and Ge. Considering planar structures, the phonon modes of both Si and Ge have imaginary frequencies in the Brillouin zone [123]. Specifically, a flat Si structure results in the hybridization of the optical and acoustical branches. This leads to the lowering of one optical branch into the acoustical frequencies, with imaginary frequencies along the Γ - K direction. The flat structure of Ge results in both one acoustical and one optical branch having imaginary frequencies.

Moreover, the Si-Si and Ge-Ge bond lengths are larger than the C-C one (1.42 Å in graphene), preventing a pure sp² hybridization in Si and Ge. From this consideration, it follows that silicene and germanene necessarily have a mixed sp²-sp³ hybridization, which in turn results in a buckled structure and not a flat one. A simple sketch of X-enes structure is shown in figure 6.1.

This is the key difference compared to graphene. Buckled atomic structures mean that the atoms are displaced in the out-of-plane direction. Theoretical studies predict that stable free-standing silicene, germanene, and stanene have buckling values of ~ 0.44 Å [123], 0.64 Å [123], and 0.85 Å [137] respectively, as reported in Table 6.1.

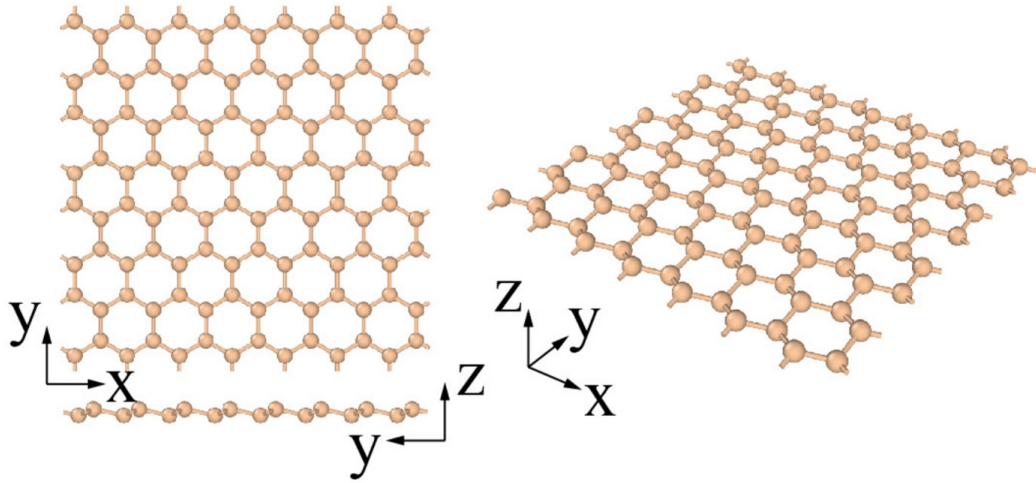


Figure 6.1 | Group-IV X-enes atomic structure. Simple sketch of the buckled atomic structure of Group-IV X-enes. Adapted from [136].

Furthermore, group-IV X-enes have enhanced spin-orbit coupling. The combination of spin-orbit coupling and buckled structures makes these materials topological insulator with bandgaps of ~ 1.5 meV [138], 23.9 meV [138], and 100 meV [139], respectively for silicene, germanene, and stanene. Interestingly, the non-trivial topological states could lead to the fabrication of devices able to preserve quantum information [140–142].

In addition, the buckled structures allow for tuning the bandgaps with different methods, namely:

- (i) applying an electric field perpendicular to the plane [140]

Table 6.1 | Predicted values of lattice parameter (a), buckling (δ) and band gap for free-standing 2D low-buckled Si, Ge and Sn.

	a (Å)	δ (Å)	Band gap (meV)
Si	3.83	0.44	1.55
Ge	3.97	0.64	23.9
Sn	4.62	0.85	100

(ii) changing the level of buckling by changing the interaction with the substrate [143–145]

(iii) introducing either chemical [146] or structural modifications by applying mechanical strain [147–149]

Therefore, the buckled structure represents a powerful feature of group-IV X-enes, as it makes them an alternative to graphene, whose lack of band gap is a significant obstacle to its integration in FETs due to the poor switching capabilities [2].

On the other hand, in contrast to graphene, group-IV X-enes are much less stable in air and above all, they do not have a bulk counterpart from which they can be easily exfoliated. Therefore, the major drawback and challenge for group-IV X-enes is their actual fabrication. So far, the main synthesis method has been via epitaxial growth on a template substrate in UHV conditions. Thus, it follows that the choice of the substrate is itself an important step prior to the actual deposition of any of the X-enes. Ideally, the growth substrate has to satisfy two main criteria: have a hexagonal symmetry and a small lattice mismatch (Δa) with the 2D overlayer.

In light of the two criteria, the majority of the of experimental syntheses has been so far performed on metallic substrates. Indeed, silicene was first successfully synthesized on Ag(111) [124, 150–152], case in which the lattice mismatch is 0.94 Å. Later, it was synthesized on Ru(0001) [153] and Ir(111) [154] surfaces and formed on top of ZrBr₂/Si(111) via segregation [155, 156].

Regarding germanene, it was first synthesized on Au(111) [129] and Pt(111) [157]. At a later stage, it was deposited on Al(111) [158] and on semimetallic Sb(111) [159]. Ultra-flat – i.e., *non*-buckled - stanene was grown on Cu(111) [144] and on Ag(111) [160].

It is worth a special mention to the study reported in ref. [144], as it is an example of how it is possible to change the electronic properties of X-enes (stanene in this case) by tuning the interaction with the substrate underneath. Indeed, when the growth takes place at room or higher temperature, stanene on Cu(111) exhibits a buckled structure. However, if stanene is deposited at a lower temperature, it tends to grow with an ultra-flat structure that reflects in the modification of its electronic properties.

Metals have proved themselves effective substrates to grow X-enes from a structural point of view. However, the strong hybridization between metals and X-enes bands results in the disruption of the electronic properties desired in these 2D materials. Specifically, the predicted Dirac cone for free-standing X-enes is missing

when they are deposited on metals [161], with the exceptions of Ca [162] and Pb [163] substrates. An additional complication is the possible formation of alloys with the metallic atoms of the substrates. This is still an open and crucial discussion that produced some controversial reports that question the successful synthesis on metal substrates [157–162].

Furthermore, the use of conductive substrates jeopardizes X-enes integration into microelectronic devices as it prevents the modulation of the Fermi level by electric gating. Due to these last-mentioned reasons and the little stability of group-IV X-enes in air, very few studies have been reported on actual electronic devices.

Indeed, the first and only example of FET made of silicene monolayer was produced few years ago and it showed the Dirac-like ambipolar charge transport at room temperature in ambient conditions [164]. However, it had a short lifetime. Nevertheless, the realization of this device [164] marks an important milestone, demonstrating the possibility of realizing working devices with group-IV X-enes, and their potential to overcome graphene’s limitations. Later on, in order to decrease the sensitivity to air, the realization of FETs based on multilayer silicene was reported as well [165].

As a last remark, it is important to stress that silicene and germanene, in contrast to graphene and other classes of 2D materials, allow for full compatibility with the existing semiconductor technology. Meaning that the existing technology infrastructure, based almost entirely on Si and to a lesser extent on Ge, could be integrated with the devices based on silicene or germanene.

6.2 Suitable Growth Substrates for Silicene

As stated in the previous section, for the evolution and development of silicene nano-electronics it is important to identify suitable non-conductive substrates that can act as a template for its synthesis. Different classes of materials have been proposed as promising candidates and preliminary experiments have been reported in recent years. For instance, hexagonal layered surfaces terminate with no dangling bonds, and thus they are expected to interact weakly with the silicene overlayer [164, 166–168]. Furthermore, some of these substrate materials have bandgaps in the range 1-6 eV, which is desirable for the direct realization of FETs. However, layered substrates bring many challenges, mainly due to the possible intercalation of group-IV atoms under the substrate top layer(s) during deposition. This has led to an interesting yet unsettled debate, with publications showing similar results

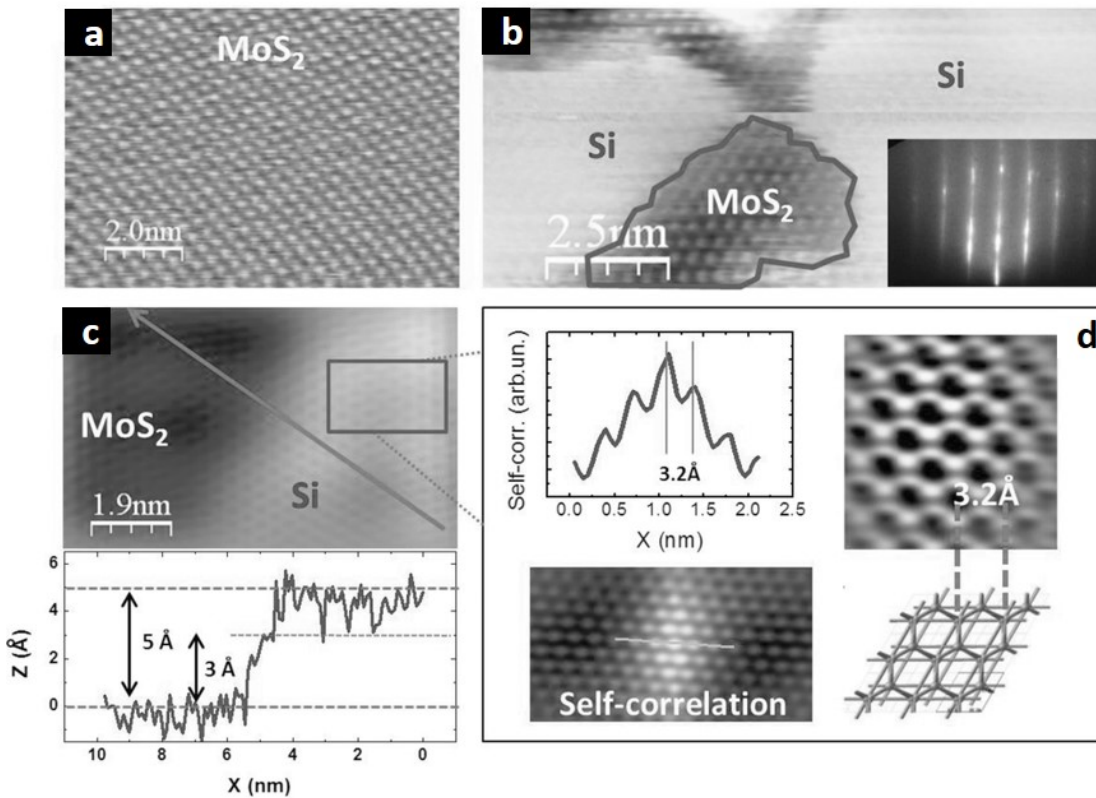


Figure 6.2 | STM Silicene on MoS₂. (a) STM image of clean MoS₂ surface ($V = 1$ V, $I = 0.7$ nA); (b) MoS₂ surface after deposition of 0.8 ML of Si ($V = 1$ V, $I = 0.7$ nA). Inset: reflection high energy electron diffraction pattern displaying the characteristic streaks. (c) Higher resolution image ($V = 0.2$ V, $I = 2$ nA) of a partially covered surface. (Below) Line profile taken across the gray arrow in the image above showing a height difference of 5 Å between Si-covered area and clean MoS₂. (d) Zoom-in of the area highlighted in (c) showing a hexagonal surface pattern. The corresponding periodicity is extracted from the analysis of the self-correlation function. A sketch models the Si honeycomb structure. Adapted from [173].

but different interpretations. Within the hexagonal layered surfaces, the first experimental syntheses of silicene have been reported on MoS₂ and HOPG (highly oriented pyrolytic graphite).

MoS₂ is a semiconducting material and the most noted compound among the transition metal dichalcogenides (TMDs) [165, 169]. Despite the small lattice parameter (3.16 Å), it fulfills the requirement of hexagonal symmetry and lack of dangling bonds on the surface required to preserve silicene electronic properties [170–172]. Bulk MoS₂ is composed of stable S-Mo-S layers interacting with each other via Van der Waals forces. The experimental results on the deposition of silicene on MoS₂ substrate using molecular beam epitaxy (MBE) at 200 °C [173] are summarized in figure 6.2.

The lattice mismatch between free-standing silicene and substrate is about 20%,

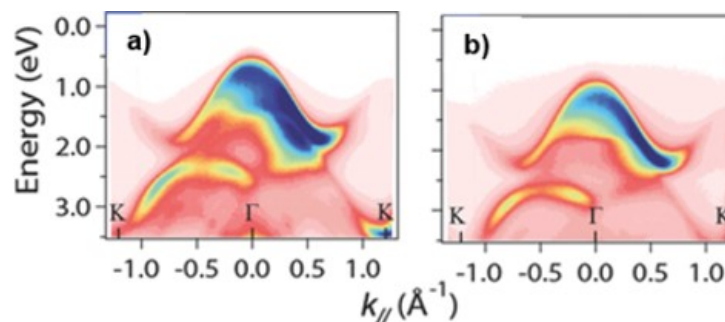


Figure 6.3 | ARPES Silicene on MoS₂. Valence band structure of clean MoS₂ (a) and after Si deposition at 200 °C (b). Data collected with photon energy $h\nu = 100$ eV along the K- Γ -K reciprocal lattice direction. Adapted from [174].

which is not a negligible value. However, the authors claim to observe Si domains with the same lattice constant of the MoS₂ substrate. DFT calculations predicted a buckling in the silicene grown on MoS₂ of about 2 Å, which is consistent with the experimental STM findings. It is a quite larger value compared to those theoretically predicted for low-buckled silicene [123], which might result from the shrinking of the Si lattice induced by the MoS₂ underneath. As the magnitude of the buckling affects the electronic band structure of silicene, ARPES measurements were also performed and are here reported in figure 6.3. ARPES measurements revealed that silicene/MoS₂ has a metallic character due to the accumulation of electrons at their interface.

As mentioned above, similar results from different studies have been interpreted in different ways. Indeed, the investigation reported in ref. [173] concludes that upon low rate deposition at room temperature, Si intercalates between MoS₂ layers rather than growing on top of the substrate to form silicene. This conclusion was supported, among other reasons, by the continuous hills-and-valley appearance of the surface with the lattice constant consistent with the one of pristine MoS₂. Indeed, for epitaxial islands of silicene grown on top of MoS₂, a step-like appearance of the surface is expected.

Another potentially suitable substrate to grow silicene is HOPG, as it features hexagonal symmetry, no dangling bonds on the surface, and it is chemically inert and no alloys are expected to form with Si atoms. Indeed, Si atoms deposited at room temperature in UHV conditions on HOPG resulted in both 3D clusters and 2D silicene islands either on-top-of or intercalated under HOPG topmost layers [175, 176]. The 2D islands exhibit a small buckling of 0.5 Å and lattice parameter close to the one predicted for free-standing silicene (3.83 Å) [123].

Thus, buckling and lattice parameters are close to the theoretically predicted values

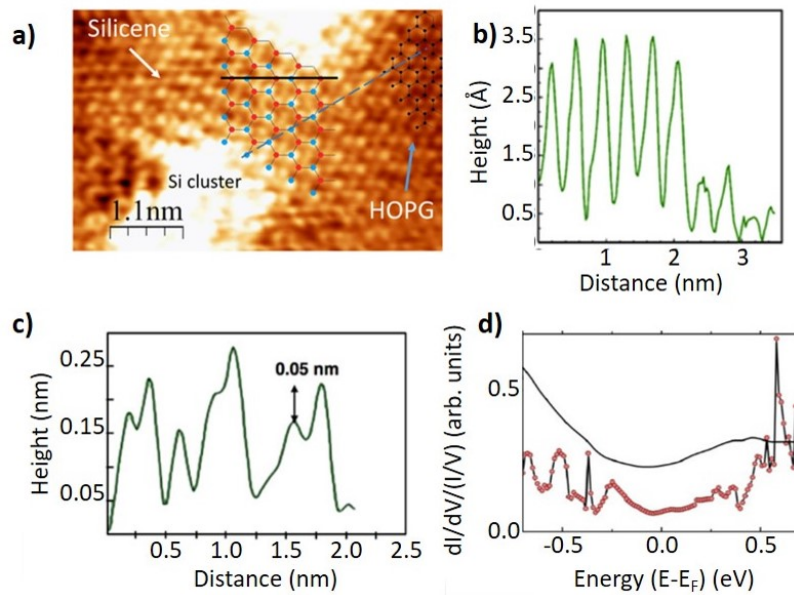


Figure 6.4 | Silicene on HOPG. (a) STM image of a HOPG substrate after room temperature deposition of 1ML of Si. The ball-and-stick models superimposed on the image represent Si lattice (blue and red) and HOPG lattice (black). ($V = 0.3$ V, $I = 0.3$ nA). (b) Line profile recorded along the blue dashed line in (a). (c) Line profile recorded along the solid black line in (a). (d) Normalized differential conductance $dI/dV/(I/V)$ related to the LDOS. The red dotted line is the theoretical density of states for the system. Adapted from [175].

and support the desired electronic properties of silicene (figure 6.4a-c), as confirmed by STS measurements that revealed a metallic behavior and finite DOS at the Fermi level (figure 6.4d).

However, the conclusions of the study in ref. [175] have been recently questioned [177]. Once again, the transition from the island to the clean substrate areas is continuous and not step-like [177]. Moreover, the 2D islands were always located at step edges of the substrate or around the 3D clusters, breaking the HOPG lattice periodicity. Therefore, authors in ref. [177] suggest that the superstructures observed are not 2D islands but rather long-range perturbations of the charge density resulting from the interference between surface and scattered waves from the clusters.

These studies and their often opposite interpretations highlight how the topic is still in its infancy, and the need for more conclusive investigations and compelling results.

In addition to the layered substrates discussed above, other possible suitable substrates for epitaxial growth of silicene have been discussed theoretically. However, no conclusive structural characterization has yet been reported.

Among those, the insulating calcium difluoride (CaF_2) resulted to be particularly interesting. Indeed, the cleaved $\text{CaF}_2(111)$ surface terminates with F^- ions arranged in a triangular symmetry with a spacing of 3.88 \AA [178]. For this reason, the lattice mismatch with silicene is only 0.5% thus, it follows a small tensile strain that should not affect the Dirac cone in silicene. Moreover, CaF_2 features a completely filled valence shell making its surface inert [179] and supporting Van der Waals epitaxy [166, 172] and growth of silicene with buckling of 0.43 \AA , which opens up a small bandgap of 52 meV, as reported in figure 6.5.

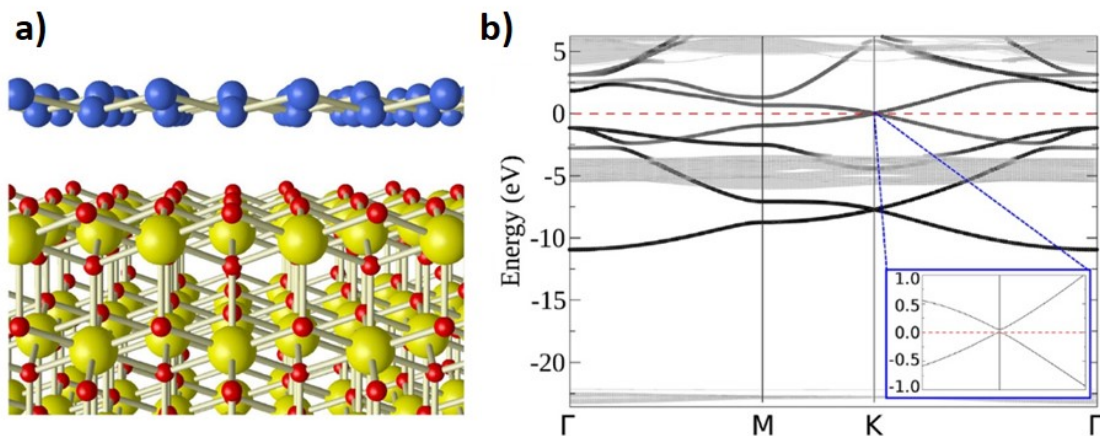


Figure 6.5 | CaF_2 as substrate for silicene. (a) Model of silicene deposited on a clean $\text{CaF}_2(111)$ surface. Si, Ca and F atoms in blue, yellow and red, respectively. (b) Calculated band structure of silicene deposited on $\text{CaF}_2(111)$. The regions of the dense slab bands represent the projected bulk CaF_2 band structures. The silicene bands are indicated by black lines. The red-dashed horizontal line represents the Fermi level. Adapted from [180].

However, before studying the growth of silicene on such substrate it is important to have a complete understanding of the growth of CaF_2 itself, which will be discussed more in detail in the next section.

6.3 Suitable Substrates for Silicene: the $\text{CaF}_2/\text{Si}(111)$ case

The epitaxial growth of CaF_2 on Si has received a great deal of attention during the last decades [181–183]. Indeed, owing to the large CaF_2 bandgap and its ability to grow homogeneously on Si, CaF_2/Si represents a promising platform for semiconductor-on-insulator devices and has been studied, for example, in the context of resonant tunneling diodes [184–186]. Furthermore, due to the small lattice mismatch of 0.6% at room temperature, the $\text{CaF}_2/\text{Si}(111)$ system is also of importance when it comes to advancing our fundamental understanding of heteroepitaxial

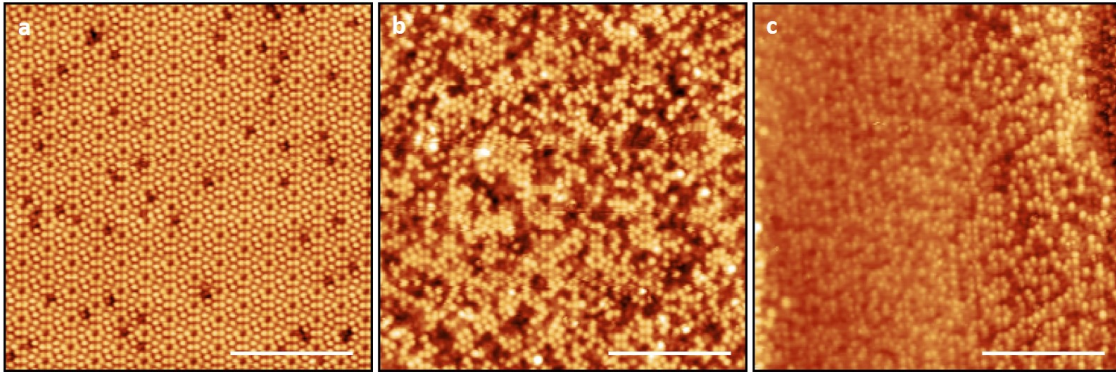


Figure 6.6 | CaF₂/Si(111) samples grown at low temperatures. STM images of clean (7x7)-Si(111) surface (a), after deposition of 0.25 ML of CaF₂ deposition at room temperature with post-deposition annealing for 30 min at 400 °C (b) and after deposition of 0.30 ML of CaF₂ deposition with the substrate at 460 °C (c). Scale bars 10 nm. (a, b) $V = 2.0$ V and $I = 0.5$ nA. (c) $V = -3.3$ V and $I = 0.3$ nA.

processes. However, despite the numerous studies already available in literature, this topic is not exhausted yet. For example, it is still unclear if preferential absorption sites for CaF₂ molecules exist on the (7x7)-Si(111) surface. In addition, another issue that is still debated is the nature of the point-like defects that are often observed with STM on the epitaxially grown CaF₂ islands. When CaF₂ grows on (7x7)-Si(111) at high temperature, the silicon surface loses its reconstruction and turns into a (1x1) phase. Earlier studies have concluded that the excess Si atoms that are produced during this transformation remain at the CaF/Si interface and eventually form the characteristic point-like defects [187, 188]. A recent study that combines STM and non-contact AFM experiments has instead proposed a new explanation based on Si atoms leaving the surface as SiF_x, at least partially, at high temperature [189]. The CaF₂ nucleation and growth can vary significantly depending on the substrate temperature during deposition [189–193].

Starting with the investigation of the deposition of CaF₂ molecules on (7x7)-Si(111) at temperatures up to 460 °C, figure 6.6a displays an empty-state STM image of a clean Si substrate, showing the well-known (7x7) reconstruction.

Figures 6.6b,c show instead STM images of Si(111) surfaces after CaF₂ deposition. In one case, 0.25 ML of CaF₂ was deposited at room temperature with subsequent post-deposition annealing at 400 °C (figure 6.6b), whereas in the other case 0.30 ML of CaF₂ was deposited on the substrate at 460 °C (figure 6.6c). In neither case CaF₂ islands are formed. Rather, CaF₂ molecules dissociate homogeneously on the (7x7)-Si(111) surface, the pattern of which is somewhat still visible. These

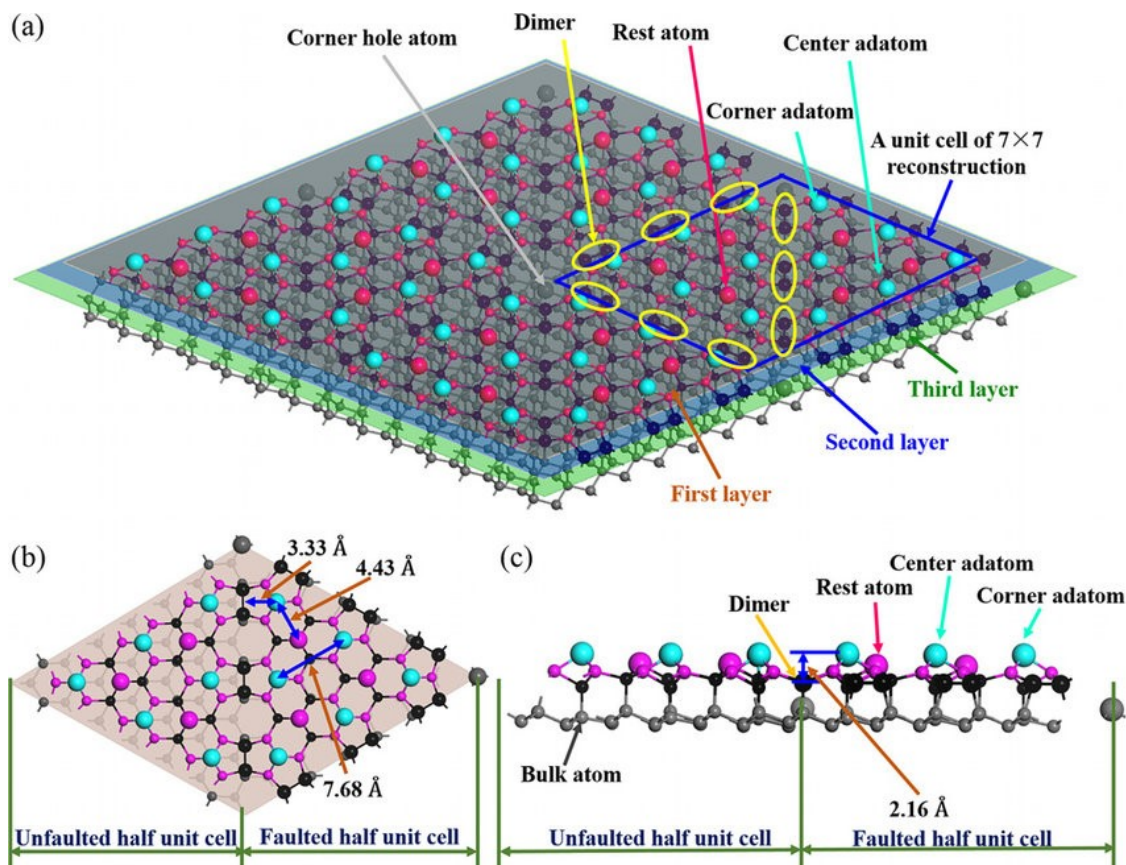


Figure 6.7 | DAS model (7×7)-Si(111) surface. (a) Top view of the 2×2 supercell of the DAS model. Gray, blue and green shadow represent first, second and third lattice planes. Solid dots represent Si atoms. Blue rhombus highlights the (7×7) unit cell. Yellow ellipses mark the 9 dimers of two halves of the unit cell and lies two layers below the top surface layer. The rest atoms (6 in one unit cell) are colored in pink and the adatoms (12 in one unit cell) are colored in blue. The bulk Si atoms are colored in gray. (b) and (c) The corresponding top- and side- view structure of one unit cell, respectively, labeled with lateral and vertical distance between the featured atoms. Reprinted from [196].

observations are in agreement with previous reflection high-energy electron diffraction measurements [194] and STM studies [190], showing that the (7×7)-Si(111) surface is maintained after CaF_2 deposition at low temperature. Hence, in these conditions, there is not enough energy for the molecules to diffuse, aggregate and form stable CaF_2 nuclei. We now focus on getting more insights into the adsorption of CaF_2 molecules on Si, looking for preferential adsorption sites with respect to the dimer adatom stacking fault (DAS) model of the (7×7)-Si(111) reconstruction [195].

In figure 6.8, two atomically resolved STM images are presented. Specifically, panel a shows the sample after deposition at room temperature and subsequent annealing at 400°C for 30 min, while panel b shows the surface after deposition with the

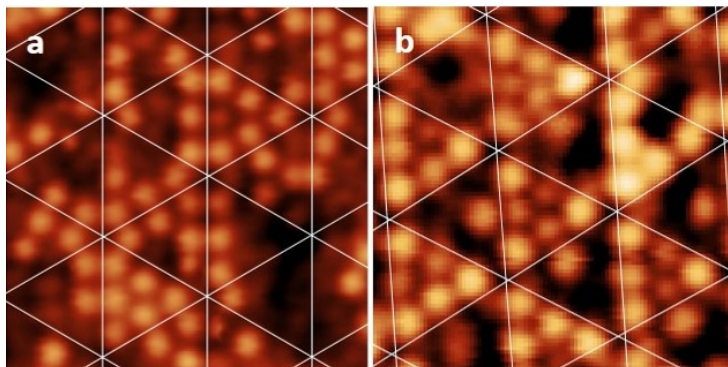


Figure 6.8 | (7x7)-Si(111) reactive sites. $7 \times 7 \text{ nm}^2$ STM images of CaF_2 molecules adsorbed on (7x7)-Si(111). The coverage is 0.46 ML. (a) 0.25 ML of CaF_2 was deposited at room temperature and subsequently the sample was annealed at $400 \text{ }^\circ\text{C}$ for 30 min. (b) 0.30 ML of CaF_2 was deposited with the substrate at $460 \text{ }^\circ\text{C}$ (b). (a) $V = 2.0 \text{ V}$ and $I = 0.8 \text{ nA}$. (b) $V = -3.0 \text{ V}$ and $I = 0.1 \text{ nA}$.

substrate kept at $460 \text{ }^\circ\text{C}$. According to the DAS model, a whole unit cell is composed of two half-unit cells, only one of them with a stacking fault. Each half-unit has nine Si atoms, composed of three corner adatoms, three center adatoms, and three rest atoms [195]. The electron density on a corner adatom is slightly higher than that on a center adatom [197–199]. It is also known that the LDOS is higher on the faulted half-unit than on the unfaulted half [198]. When the adsorption takes place at a specific site, the related LDOS changes due to the saturation of the Si dangling bonds. This leads to a modification of the contrast in the STM images, which therefore can be used to reveal the spatial distribution of the reacted sites.

Earlier studies have reported dissociative reactions on Si(111) when the surface is exposed to H_2O , NH_3 , ethanol, ethylene, and NO. They all show STM images, which are very similar to ours [197, 200–202]. In such dissociative reactions, take for example the case of H_2O , the molecule approaching Si surface dissociates leading to the formation of Si-H and Si-OH bonds [197]. Interestingly, it was found that center adatoms react much faster than corner adatoms. The reason is that a pair of two close dangling bonds is needed to split a water molecule. On the (7x7) surface, these are the adatom-rest atom dangling-bonds. As in the DAS model of the (7x7) surface, each rest atom has two center adatom neighbors but only one corner adatom, this explains the observed preferential adatom reactivity. From 6.8, we can also observe that the center adatoms are indeed more reactive than the corner adatoms, in agreement with the abovementioned studies. In particular, in the sample with CaF_2 for deposition at room temperature and subsequent annealing at $400 \text{ }^\circ\text{C}$ almost 55% of the reacted sites are center adatoms, while in the sample with CaF_2 for deposition at $460 \text{ }^\circ\text{C}$ this percentage increase to about 65%, probably due

to the increased mobility in this latter case given the higher temperature during deposition. Because of the similarities between the presented STM observations and previous studies [197, 200–202], and because earlier core levels spectroscopy measurements have reported the formation of both Si-F and Si-Ca bonds [189, 203], we conclude that CaF_2 on Si reacts by dissociation rather than etching.

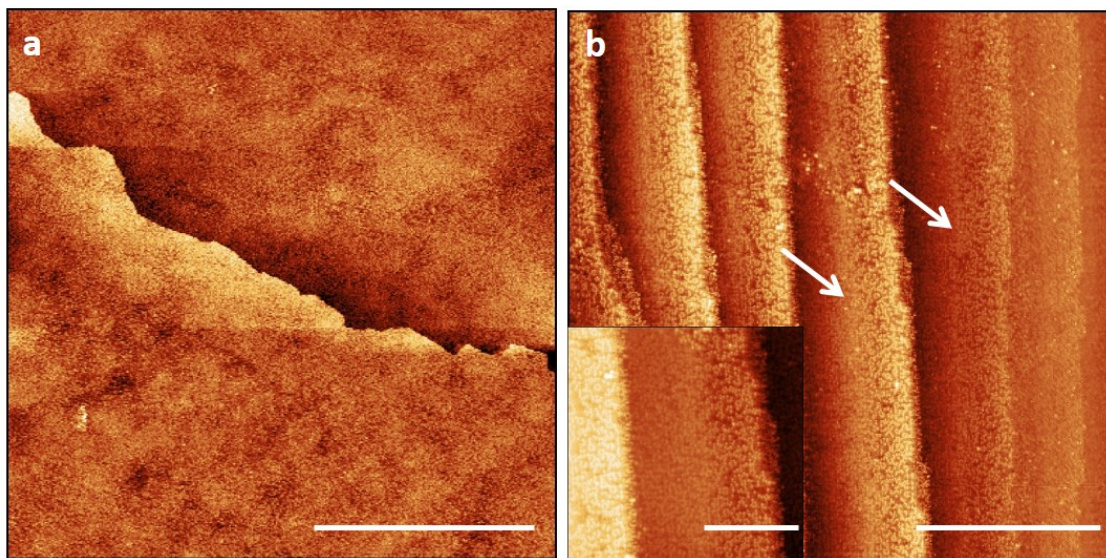


Figure 6.9 | $\text{CaF}_2/\text{Si}(111)$ samples grown at low temperatures. STM images of the sample after deposition of 0.25 ML of CaF_2 at room temperature and post-deposition annealing at 400 °C for 30 min (a) and after deposition of 0.30 ML of CaF_2 with the substrate at 460 °C (b). Scale bar 400 nm (a), 50 nm (b). (a) $V = -2.0$ V and $I = 0.5$ nA. (b) and inset $V = -3.3$ V and $I = 0.3$ nA. Scale bar in the Inset is 20 nm.

Since steps and other imperfections at the surface are preferential absorption sites, it is interesting to investigate whether the substrate surface topography affects the result of CaF_2 molecule adsorption. For example, it is known that when it comes to the formation of CaF_2 islands, substrate morphology can largely influence film growth at given temperatures, switching from island nucleation in the case of large terraces to step-flow for stepped surface [183]. Figure 6.9a reports an STM image of a sample after CaF_2 deposition at room temperature and subsequent annealing at 400 °C. This sample exhibits very large terraces (> 500 nm). Figure 6.9b instead displays an STM image of a sample after CaF_2 deposition at 460 °C; this sample features narrow terraces, with an average width of about 30 nm. In both cases, CaF_2 molecules seem to be rather homogeneously distributed on the Si surface. Yet, in figure 6.9b it is possible to see that any terrace seems to be formed by two areas that are divided by a boundary located approximately in the middle of the terrace (see arrows in figure 6.9b). The first area goes from the boundary to the step with the lower terrace, while the second area goes from the boundary to the step with the upper terrace. The difference between the two areas is the density of

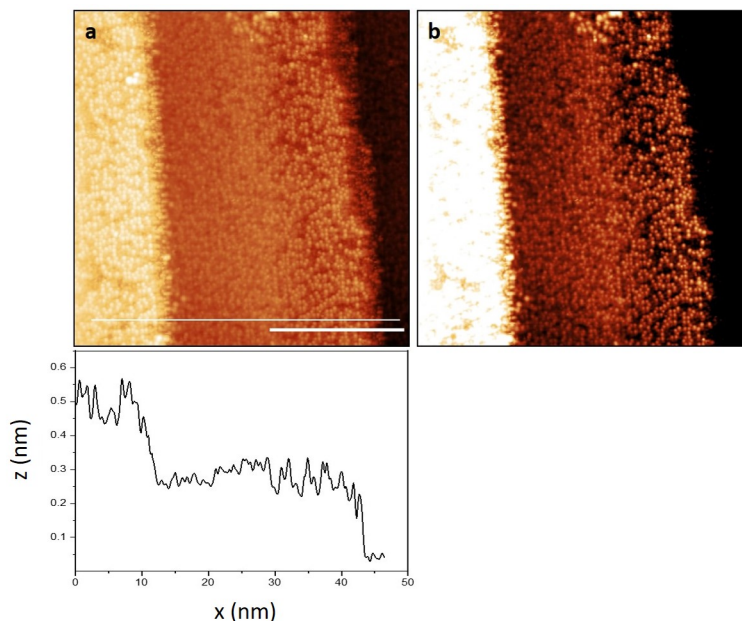


Figure 6.10 | $\text{CaF}_2/\text{Si}(111)$ samples grown at 460 °C. STM images of sample after CaF_2 deposition at 460 °C. At the bottom, the line profile taken across the terraces of the surface shown in panel (a) reveals that there is no height difference within the terrace. The high-contrast image shown in panel (b) highlights a higher density of adsorbates in the region closer to the step with the lower terrace. $V = -3.3$ V and $I = 0.3$ nA. Scale bar = 20 nm.

dark-contrast spots corresponding to adsorbed molecules, and the border is nothing but just an optical illusion due to the density difference (see inset in figure 6.9b and figure 6.10). Thus, molecules adsorb preferentially on the upper step side of the terraces.

If CaF_2/Si is annealed after deposition or if CaF_2 is deposited at higher substrate temperatures, structural and chemical modifications can occur at the interface with Si and the morphology of the deposited films change [191, 192, 204–207]. Indeed, an F:Ca ratio of 2:1 has been reported when CaF_2 is deposited at room temperature [204], whereas it changes to 1:1 for temperatures above 550 °C [204–206, 208], indicating desorption of fluorinated species.

Figure 6.11 shows the surface after 0.20 ML of CaF_2 deposition with substrate kept at a temperature of 570 °C. The topography of the surface is interesting. Unreacted areas of (7×7) -Si(111) surface are still present, but we can now also observe triangular-shaped islands of CaF_2 along with extended reacted areas that look different from ones observed at lower deposition temperatures. Concerning the islands, they can nucleate on three different types of sites on the surface, namely on terraces, at steps and along the phase domain boundaries of the (7×7) reconstruction [183]. In the present work, the nucleation of the islands happened on

terraces and along the phase boundaries, as observed in figure 6.11a. Regarding the extended reacted area, clearly visible in figure 6.11b,c, we can pinpoint the presence of small areas with $(\sqrt{3}\times\sqrt{3})$ and $c(2\times 4)$ metastable reconstructions (figure 6.11c,d), which are known to have a higher atom density than the (7×7) reconstruction [199, 209–213].

Since the surface shows three different types of regions, it is interesting to highlight the differences with STS measurements. Indeed, figure 6.12 reports STS measurements on the sample grown at 570 °C. First of all, it should be pointed out that it is known that at room temperature the (7×7) -Si(111) surface is metallic. However, for measurements performed at low temperature, the opening of a bandgap is expected, as reported in [214] and it is consistent with the experimental STS measurements here presented, which are performed at temperatures below 10 K. Moreover, it is useful to note that the local density of states depends on which type of atom (adatom or rest atom) the measurement is performed.

The spectra acquired on the same type of region are consistent with each other, while among the different regions the spectra show some differences. Both reacted and unreacted Si areas show a small feature centered at 1.5 V (marked with dashed line), already observed for (7×7) -Si(111) [214]. This feature is absent in the CaF_2 island. Qualitatively, the STS measurements performed on CaF_2 islands are similar to the ones shown in ref. [215], as both show an abrupt rise at about +2.0 eV in the empty states. Additionally, the spectra reported in figure 6.12 have a flat curve in the filled states with a rise at around -2.0 eV. The flat part is also reported in the spectrum in ref. [215] while concerning the peak at around -2.0 eV, it is difficult to compare with the mentioned literature as the spectrum, in that case, terminates around that voltage value, but it seems they also observe a somewhat increase in the DOS. It should be noted that in ref. [215] it is reported also the STS spectrum of CaF bilayer which displays a peak at 0.4 eV below the Fermi level. That peak is instead suppressed in the spectrum of CaF_2 island. Such a peak is not observed in our reported results, as there is no extended CaF layer in the reacted Si area in our samples.

Given the different appearance of the reacted areas observed in figure 6.11 and those observed in figure 6.9 and figure 6.6, it is reasonable to assume that at higher temperatures something happens that makes the reacted (7×7) areas unstable. For example, it is known that above 550 °C part of the F atoms starts combining with the substrate to form volatile SiF_x species that desorb from the surface [189, 204, 205, 208, 216]. The removal of Si atoms would induce tensile strain in the surface that thus has to rearrange into the above-mentioned reconstructions, as it was

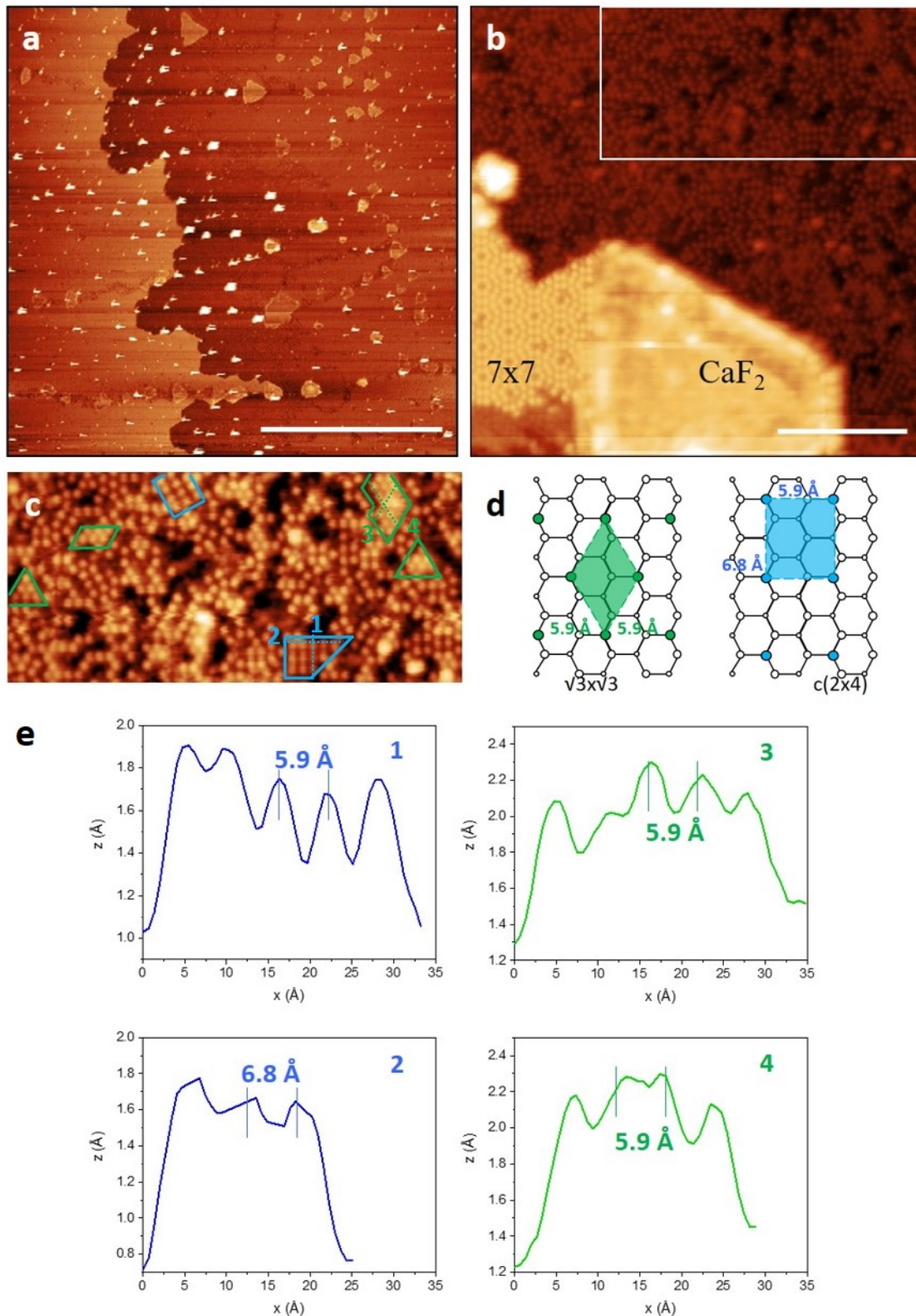


Figure 6.11 | $\text{CaF}_2/\text{Si}(111)$ samples grown at 570°C . (a-c) STM images of the sample after deposition of 0.20 ML of CaF_2 at 570°C showing the unreacted (7×7) and reacted Si areas. (c) Blow-up of $25 \times 12 \text{ nm}^2$ rectangular area marked in the top-right corner in (b). The areas highlighted in light blue and green represent patches of $c(2 \times 4)$ and $(\sqrt{3} \times \sqrt{3})$ reconstructions, respectively. Scale bar 200 nm (a), 10 nm (b). (d) Schematics of $(\sqrt{3} \times \sqrt{3})$ and $c(2 \times 4)$ unit cell reconstruction. (e) Line profiles taken on the STM image as indicated in panel (c). The periodicities of first-neighbor atoms are consistent with those expected for the $c(2 \times 4)$ and $\sqrt{3} \times \sqrt{3}$ reconstructions. (a) $V = 3.0 \text{ V}$ and $I = 0.5 \text{ nA}$. (b) and (c) $V = 3.0 \text{ V}$ and $I = 0.6 \text{ nA}$. Reprinted from [69].

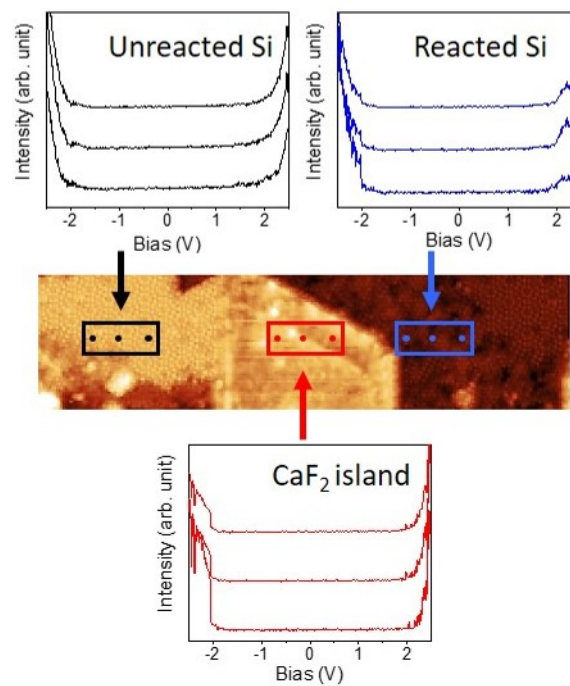


Figure 6.12 | STS measurements on $\text{CaF}_2/\text{Si}(111)$ sample. STS measurements recorded via lock-in technique on the three different types of regions on the sample where 0.20 ML of CaF_2 was deposited at 570 °C. Namely, the three regions are unreacted Si (black spectra), reacted Si (blue spectra), and CaF_2 island (red spectra). Three spectra were acquired on three different spots within the same type of region, as indicated by the rectangular boxes in the STM image. These spectra are vertically shifted by an arbitrary quantity for visualization purposes. Reprinted from [69].

observed for example for stepped Si surfaces or in the case of Si/Ge [217, 218]. In any case, the appearance of the metastable phases represents the onset of radical structural changes of the substrate that will eventually lead to the formation of the stable (3x1) reconstruction at higher temperatures.

It is known that the higher the temperature, the higher the probability of desorption of fluorine, F, and fluorinated species, SiF_x . Consequently, it was found that the F:Ca ratio decreases as a function of temperature, since Ca resides on the Si surface up to higher temperatures [189]. This, in turn, leads to different ($n \times 1$) surface reconstructions [208, 219] that finally become the (3x1) reconstruction when fluorine is completely desorbed [203]. Indeed, the (3x1) reconstruction has been observed to form also upon deposition of pure Ca atoms and identified as a mixture of (3x2) and c(6x2) reconstructions [218]. As seen in figures 6.13a,b, upon annealing at 600 °C the sample where CaF_2 was deposited at 570 °C, the areas previously covered by c(2x4) and $(\sqrt{3} \times \sqrt{3})$ metastable reconstructions have now turned into the stable (3x1) phase. The triangular-shaped CaF_2 islands, on the other hand, are not affected by the annealing and are still visible on the surface (marked with white arrows in figure 6.13a). Similarly, the unreacted (7x7)-Si(111) areas are also unaffected by the annealing. These observations suggest that in the reacted areas F or SiF_x desorbed during the annealing and consequently the remaining Ca atoms on the surface transformed the $(\sqrt{3} \times \sqrt{3})$ and c(2x4) metastable reconstructions into the stable (3x1) reconstruction. The CaF_2 islands are instead stable at 600 °C. On the other hand, at 680 °C, STM reveals the presence of large areas of clean (7x7)-Si(111) and large areas of (3x1) reconstruction, whereas the CaF_2 islands are not visible anymore (figure 6.13c,d).

Here, it is worth noting that the (3x1) areas show several point-like defects that could possibly be ascribed to Si atoms [187]. At even higher temperatures, for temperatures above 700 °C, even Ca start to desorb from the surface, and the (7x7)-Si(111) surface can be restored [208]. Figure 6.14 shows the sample in figure 6.11 after flash annealing at 1200 °C. Indeed, only (7x7) areas can be observed on the surface.

6.4 Conclusion

In conclusion, this chapter presented an overview of group-IV X-enes, which are examples of synthetic elemental 2D materials. These materials do not have bulk counterparts from which they can be easily derived, but they have to be synthesized with methods that often require high technical skills and specialized equipment.

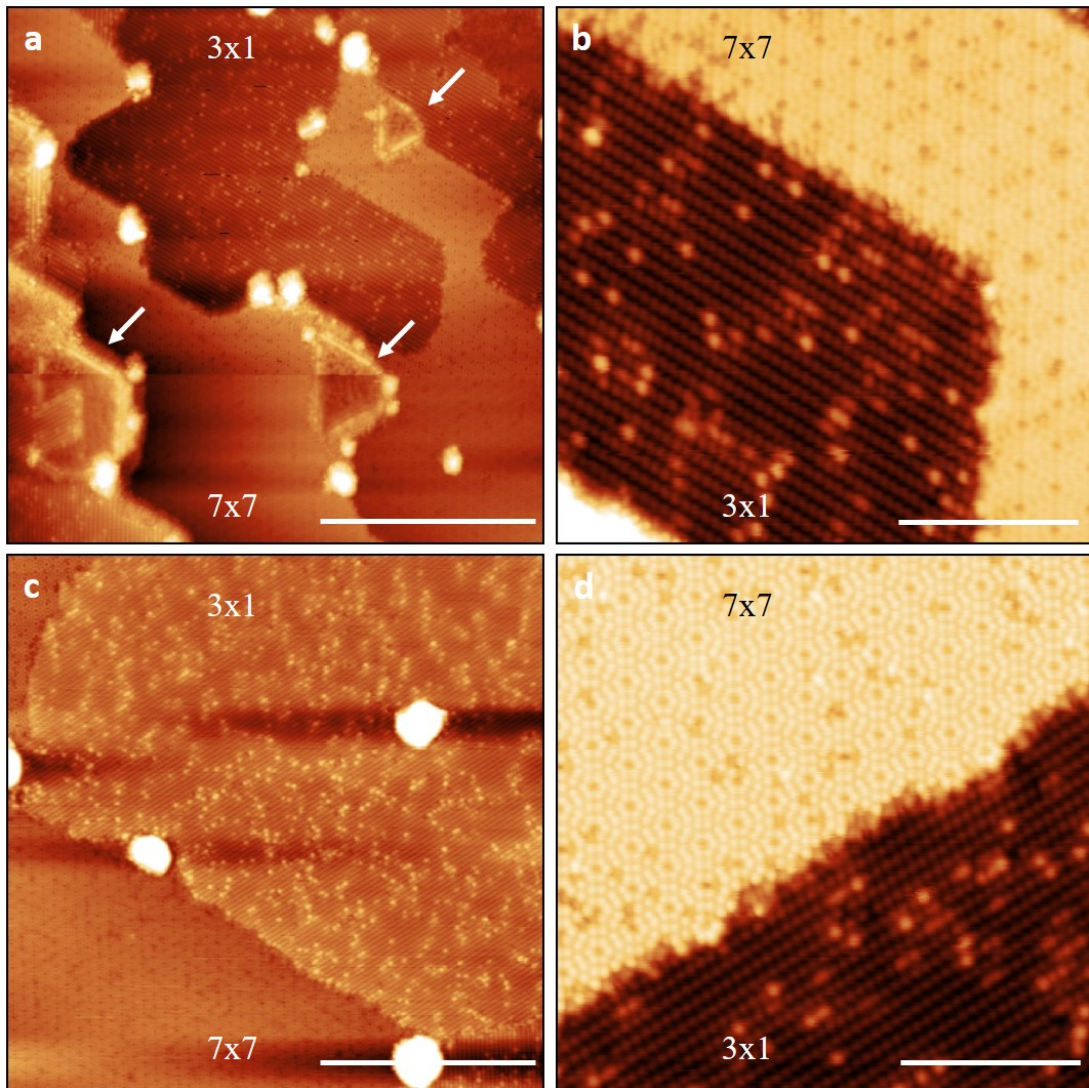


Figure 6.13 | $\text{CaF}_2/\text{Si}(111)$ samples showing (3×1) reconstruction. STM images of the samples after deposition of 0.20 ML of CaF_2 at 570 °C and post-deposition annealing at 600 °C (a,b); and after deposition of 0.60 ML of CaF_2 at 680 °C (c,d). Scale bars 200 nm (a,c) and 10 nm (b,d). $V = 3.0$ V and $I = 0.2$ nA (a,b). (c) $V = 2.5$ V, $I = 0.6$ nA and (d) $V = 2.5$ V, $I = 0.5$ nA. Reprinted from [69].

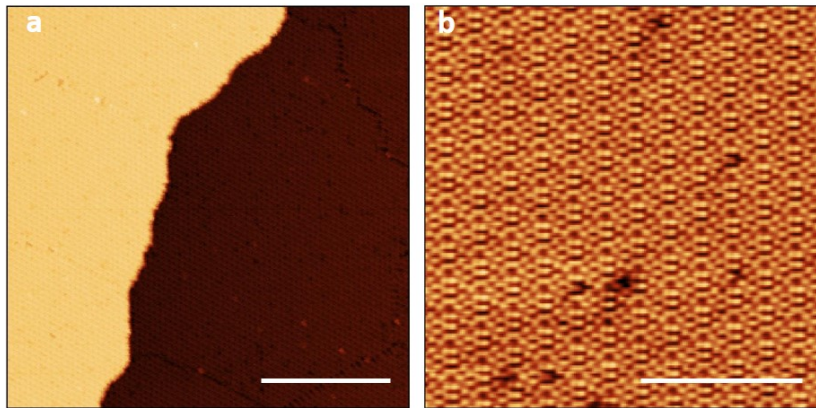


Figure 6.14 | STM images of cleaned (7x7)-Si(111) surface. STM image of CaF_2/Si after flash annealing at $1200\text{ }^\circ\text{C}$. The surface reveals only (7x7) areas. (a) $V = -2.5\text{ V}$ and $I = 0.5\text{ nA}$. Scale bar 50 nm. (b) $V = 3.5\text{ V}$ and $I = 0.15\text{ nA}$. Scale bar 10 nm. Reprinted from [69].

For this reason, the progression rate of X-enes is much slower than that of graphene or other 2D materials. Furthermore, the electronic properties of these materials are hampered by the metals usually used as growth substrates due to strong interaction. Moreover, metallic substrates do not allow for direct integration in electronic devices. Thus, the synthesis of these 2D materials on non-metals would be preferable and highly beneficial for future applications. Therefore, this chapter first reported on the properties that non-interactive substrate should have to support the growth of group-IV X-enes, focusing in particular on silicene. The chapter continues with the report of the few experimental results on the silicene synthesis on non-interacting substrates, and it then highlights the potential growth substrates so far only theoretically suggested.

The last section of the chapter presents the results of the experimental study on the growth and characterization of CaF_2 films deposited on Si(111). CaF_2 is expected to be a suitable substrate to support the epitaxial growth of silicene. However, before attempting to grow silicene, it is important to understand and control the synthesis of CaF_2 itself. Therefore, the study presents the modification of the morphology of the deposited CaF_2 films via e-beam evaporation as a function of deposition temperature. First, we have described the initial absorption of CaF_2 molecules on (7x7)-Si(111) in the low temperature (i.e. up to $460\text{ }^\circ\text{C}$), demonstrating that the center adatoms act as preferential absorption sites for the dissociation of CaF_2 molecules. Next, we have shown that when CaF_2 is deposited at $570\text{ }^\circ\text{C}$, triangular islands appear, along with the formation of the metastable $(\sqrt{3}\times\sqrt{3})$ and $c(2\times 4)$ Si reconstructions. Finally, we have shown that when the sample is annealed at higher temperatures, the metastable $(\sqrt{3}\times\sqrt{3})$ and $c(2\times 4)$ phases turn

into the stable (3x1), while the CaF₂ islands can still be observed. For deposition of CaF₂ in the high temperature regime (i.e. 680 °C), most of F atoms desorb from the surface and only areas of (3x1) or (7x7) can be seen. CaF₂ islands are not stable at these high temperatures.

Conclusions & Outlook

This thesis is motivated by the need for novel electronics and inspired by the future possibilities offered by the integration of 2D materials with conventional semiconductors. The work presented here focuses on two main projects. Namely, the investigation of graphene/Ge(110) interface and the synthesis and characterization of CaF₂ epitaxially grown on Si(111).

Chapter 3 presents the structural properties of the CVD-grown graphene/Ge(110) interface. The investigation is based on STM measurements and aims to describe the modifications induced on the interface by thermal annealing. Indeed, the samples are studied as-grown, after annealing in vacuum above 350 °C and after annealing above 700 °C in-vacuum. The STM study revealed that the as-grown sample features a rippled graphene layer and a Ge surface passivated by H-atoms, resulting from the graphene deposition via CVD process. Upon annealing above 350 °C in vacuum, H atoms leave the Ge surface, which then reconstructs into the (6x2) phase, peculiar of the graphene/Ge(110) system. Residual hydrogen can remain trapped between graphene and the substrate to form nanobubbles. Upon annealing at high temperature, above 700 °C, the hydrogen nanobubbles disappears and the Ge surface reconstructs again into a phase with symmetry consistent with the (1x1) phase of Ge. Moreover, the surface of Ge shows several defects, such as vacancies.

In chapter 4, we investigate the electronic properties of the graphene/Ge(110) system with ARPES measurements. The aim is to complement the investigation of the interface structure and its modification. Therefore, the experiments were performed on the as-grown sample and after performing in-vacuum annealings, similarly to chapter 3. The ARPES results show that the as-grown sample features a *p*-doped graphene. Upon annealing above 350 °C in vacuum, graphene is almost undoped

and last, after annealing above 700 °C, graphene is *n*-doped. Starting from the characterization of the structure with STM, we also build a theoretical model that, qualitatively in agreement with ARPES measurements, reveals that it is the thermally induced disorder in the Ge surface the key factor that determines the doping character of graphene.

In chapter 5, we finally conclude the investigation of the graphene/Ge(110) system. After characterization of the structure and electronic properties of the interface, the next logical step is to study the chemical state of the interface. Specifically, using XPS and NEXAFS measurements and supported by STM and Raman spectroscopy, we discover that the presence of hydrogen nanobubbles affects graphene's chemical state after the annealing at 500 °C. While, contrary to first assumptions, no chemical bonds between graphene and Ge substrate are formed upon annealing at high temperature.

Chapter 6 describes the second main project of this work. It briefly gives an overview of group-IV X-enes, which represents a family of 2D materials very similar to graphene and yet with a key difference. Group-IV X-enes have a buckled atomic structure that induces the opening of a small bandgap. Thus, this property overcomes the intrinsic weakness of graphene when it comes to application in electronic devices. Therefore, group-IV X-enes represents a potential powerful alternative to graphene, especially germanene and silicene, which can be directly integrated into the current technological infrastructure. However, to synthesize these materials while retaining their intrinsic electronic properties is extremely challenging. Thus, finding the appropriate growth substrate is of paramount importance. In this scenario, the last section of the chapter describes the growth and characterization of CaF₂/Si(111), which is predicted to be a suitable non-conducting substrate to grow silicene. The study presents the modification of the morphology of the deposited CaF₂ films via e-beam evaporation as a function of the deposition temperature. Thus, this study is a starting point to understand how to tune the growth parameters to obtain the desired surface morphology of CaF₂ able to support the epitaxial growth of silicene.

Outlook

To conclude, I would like to add that the enthusiasm around 2D materials is not (and should not) motivated by only the possibility of improving the current device and applications. I think it should be seen as a necessity. We have entered the era of machine learning and big data analytics, which require processing a massive volume of data at greater speed and it is possible by increasing the density of

logic and memory devices. This scenario involves not only a purely technological challenge but also the energy consumption issue. There is no clear strategy to increase energy efficiency and with the circuitry becoming more densely packed, the energy lost as heat also increases. To this end, 2D materials, particularly 2D semiconductors, might play a key role in realizing ultra low-power devices.

APPENDIX **A**

Publications

Paper I

M. Galbiati, N. Motta, M. De Crescenzi, L. Camilli.

**Group-IV 2D materials beyond graphene on
nonmetal substrates: Challenges, recent progress,
and future perspectives.**

Applied Physics Reviews, **6**, 2006041 (2019)

Group-IV 2D materials beyond graphene on nonmetal substrates: Challenges, recent progress, and future perspectives

Cite as: Appl. Phys. Rev. 6, 041310 (2019); <https://doi.org/10.1063/1.5121276>

Submitted: 23 July 2019 • Accepted: 18 October 2019 • Published Online: 15 November 2019

 Miriam Galbiati,  Nunzio Motta,  Maurizio De Crescenzi, et al.

COLLECTIONS

 This paper was selected as Featured



View Online



Export Citation



CrossMark

ARTICLES YOU MAY BE INTERESTED IN

[Synthesis and emerging properties of 2D layered III-VI metal chalcogenides](#)

Applied Physics Reviews **6**, 041312 (2019); <https://doi.org/10.1063/1.5123487>

[The properties and prospects of chemically exfoliated nanosheets for quantum materials in two dimensions](#)

Applied Physics Reviews **8**, 011312 (2021); <https://doi.org/10.1063/5.0038644>

[Catalytically mediated epitaxy of 3D semiconductors on van der Waals substrates](#)

Applied Physics Reviews **7**, 031402 (2020); <https://doi.org/10.1063/5.0006300>



Applied Physics
Reviews

Read. Cite. Publish. Repeat.

19.162

2020 IMPACT FACTOR*



Group-IV 2D materials beyond graphene on nonmetal substrates: Challenges, recent progress, and future perspectives

Cite as: Appl. Phys. Rev. 6, 041310 (2019); doi: 10.1063/1.5121276

Submitted: 23 July 2019 · Accepted: 18 October 2019 ·

Published Online: 15 November 2019



Miriam Galbiati,¹  Nunzio Motta,²  Maurizio De Crescenzi,³  and Luca Camilli^{1,a)} 

AFFILIATIONS

¹Department of Physics, Technical University of Denmark, 2800 Kgs. Lyngby, Denmark

²CPME School, Queensland University of Technology, 2 George St., Brisbane 4001, Queensland, Australia

³Dipartimento di Fisica, Università di Roma "Tor Vergata", 00133 Roma, Italy

^{a)}Author to whom correspondence should be addressed: lcam@dtu.dk

ABSTRACT

The family of two-dimensional materials has been expanding rapidly over the last few years. Within it, a special place is occupied by silicene, germanene, and stanene due to their inherent compatibility with the existing semiconductor technology (notably for the case of silicene and germanene). Although obtaining them is not trivial due to the lack of layered bulk counterparts from which they could be mechanically exfoliated, they have been recently synthesized on a number of metallic substrates. The remarkable interaction between metals and these puckered materials, however, strongly modifies their intrinsic electronic properties, and also jeopardizes their integration into functional devices. In this context, first experimental efforts are now being devoted to the synthesis of silicene, germanene, and stanene on nonmetal substrates. Here, we review these pioneering works, present the ongoing debate, analyze, and discuss the major technical challenges and finally suggest possible novel solutions worth exploring.

© 2019 Author(s). All article content, except where otherwise noted, is licensed under a Creative Commons Attribution (CC BY) license (<http://creativecommons.org/licenses/by/4.0/>). <https://doi.org/10.1063/1.5121276>

TABLE OF CONTENTS

I. INTRODUCTION	1
II. RECENT PROGRESS	3
A. Si and Ge on MoS ₂	3
B. Si and Ge on Highly Oriented Pyrolytic Graphite (HOPG)	6
C. Sn on InSb, Bi ₂ Te ₃ , and PbTe	8
III. OTHER POTENTIAL SUBSTRATES FOR GROUP-IV X-ENES GROWTH	11
A. InSe	11
B. CaF ₂	12
C. Oxides	12
1. LaAlO ₃	12
2. Al ₂ O ₃ (0001)	13
D. Epitaxial graphene/SiC	13
IV. ADDITIONAL SYNTHESIS ROUTES BEYOND EPITAXY	14
V. OUTLOOK AND CONCLUSIONS	15

I. INTRODUCTION

Since its isolation in 2004, graphene—a single atomic layer of carbon atoms bonded in a hexagonal lattice—has attracted enormous attention both in academia and industry owing to its outstanding properties.^{1,2} Notably, due to its superior charge carrier mobility and monoatomic thickness, graphene has been proposed as a viable option that could push performance of current information technology beyond its traditional boundaries.³ However, the lack of a bandgap is a significant problem that has so far hampered its integration in, for instance, digital logic devices. Indeed, field effect transistors (FETs) with a graphene-based channel exhibit poor switching capabilities or, in other words, a low on-off current ratio, which in turn gives rise to huge power consumption.⁴

In this scenario, graphene-like elemental group-IV materials (also called group-IV X-enes), such as silicene,^{5,6} germanene,^{5,7,8} and stanene,^{9,10} have been recently proposed as a potentially powerful alternative^{11–17} (Fig. 1). Here, it is worth discussing from the onset the

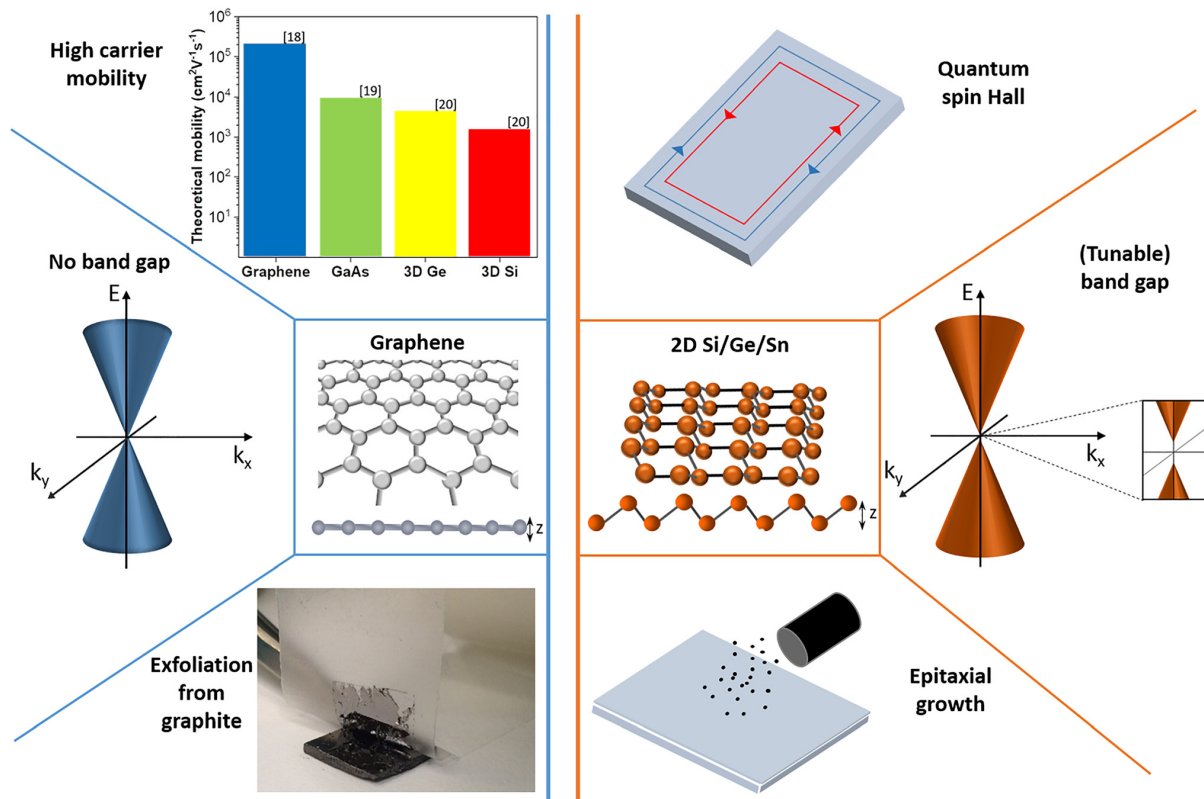


FIG. 1. Overview of graphene (left side) and group-IV X-enes (right side) main properties as reported in the text. Carrier mobility values are taken from Refs. 18–20.

fundamental difference between graphene and the other group-IV elemental two-dimensional (2D) materials. At ambient conditions (i.e., room temperature and pressure of 1 atm), the energetically most favorable structure for C is the honeycomb structure (i.e., graphene or graphite), where C atoms exhibit pure sp^2 hybridization. As a consequence, this structure is atomically flat. On the other hand, diamond, with C atoms showing a sp^3 character, is thermodynamically stable only at very high pressures.²¹ When it comes to single layers of the other group-IV elements, completely planar structures are not stable, as they would suffer from imaginary phonon modes in a large part of the Brillouin zone.⁵ The larger Si-Si or Ge-Ge bond lengths indeed prevent Si or Ge to hybridize in a purely sp^2 fashion. As a consequence, in these single layers, Si or Ge has a mixed sp^2 - sp^3 hybridization that leads to a small buckling—i.e., a displacement of the atoms in the out-of-plane direction. Theoretical calculations predict this buckling to be of about 0.44 Å,⁵ 0.64 Å,⁵ and 0.85 Å²² for free-standing silicene, germanene, and stanene, respectively, as reported in Table I.

Interestingly, the buckled structure and the enhanced spin-orbit coupling make this class of 2D materials topological insulators with energy gaps of approximately 1.5 meV,²³ 23.9 meV,²³ and 100 meV,²⁴ respectively for silicene, germanene, and stanene. The presence of topologically nontrivial electronic states^{25–27} introduces a rich physics and would possibly allow devices based on these materials to preserve

quantum information. Silicene-based spin-filters have also been suggested.²⁸ Furthermore, their structural buckling enables the bandgap to be modulated when (i) applying an electric field perpendicular to the plane,²⁵ (ii) changing the degree of buckling by tuning the interaction with the substrate,^{29–31} and (iii) introducing chemical³² or structural modifications (i.e., applying mechanical strain).^{33–35} However, X-enes are much less stable in air than graphene and moreover do not have a bulk counterpart from which they can be mechanically exfoliated. Therefore, it is more challenging to fabricate them, and the major synthesis approach has been epitaxial growth on solid surfaces in ultrahigh vacuum (UHV) chambers. Suitable growth substrates will act as a template, and thus will generally satisfy two criteria, that is, hexagonal symmetry and a small lattice mismatch (Δa) with the 2D

TABLE I. Predicted values of lattice parameter (a), buckling (δ), and bandgap for free-standing 2D low-buckled Si, Ge, and Sn.

	a (Å)	δ (Å)	Band gap (meV)
Si	3.83 ⁵	0.44 ⁵	1.5 ²³
Ge	3.97 ⁵	0.64 ⁵	23.9 ²³
Sn	4.62 ²⁴	0.85 ²²	100 ²⁴

overlayer. Thus far, the majority of experiments on the growth of group-IV X-enes have been performed on metallic substrates. For instance, silicene was first successfully synthesized by depositing silicon onto Ag(111),^{6,36–38} where the lattice mismatch is 0.94 Å. Later, it was also synthesized through a similar process on Ru(0001)³⁹ and Ir(111)⁴⁰ surfaces, or via segregation on top of ZrB₂ thin films grown on a Si(111) substrate.^{41,42} In the case of germanene, the condition of lattice match with Ag(111) does not hold anymore, and besides, it is known that Ge and Ag tend to form an Ag₂Ge alloy on the surface.⁴³ Therefore, following the considerations above regarding substrate selection, germanene was first synthesized on Au(111)⁴⁴ and Pt(111)⁴⁵ and later on Al(111).⁴⁶ More recently, germanene has been also successfully synthesized on semimetallic Sb(111).⁴⁷ When it comes to stanene, ultraflat—i.e., “nonbuckled”—stanene has been grown on Cu(111)³⁰ and on Ag(111).⁴⁸ The study reported in Ref. 30 is particularly interesting, because it is an excellent example of how it is possible to modify X-enes’ electronic properties by tuning the interaction with the growth substrate. Indeed, when grown at room or higher temperature, stanene on copper exhibits a buckled structure; however, if deposited at low temperature, it grows as an ultraflat sheet that consequently modifies profoundly the electronic properties and gives rise to topological states.

Although metallic surfaces are normally used as growth substrates, the strong hybridization between metal’s and 2D layer’s electronic bands greatly affects both structural and electronic properties of the 2D overlayer. For instance, the Dirac cone predicted for free-standing X-enes is commonly absent when they are grown on metals,⁴⁹ with Ca⁵⁰ and Pb⁵¹ substrates being theoretically predicted to be exceptions. More importantly, ruling out completely the formation of alloys between metals and Si/Ge/Sn is not trivial, and controversial reports indeed question the successful synthesis on metal substrates.^{45–50} In addition, conductive substrates jeopardize integration into microelectronic devices as they do not allow modulating the 2D material’s Fermi level by electric gating. For this reason, and because of their instability in air, there are presently only a few reports on electric devices based on this class of materials. The only example so far of FET with a single layer of silicene as the channel was fabricated in 2015 and showed Dirac-like ambipolar charge transport at room temperature in ambient conditions.⁵² Despite its short lifetime, the realization of this device represents a milestone in the research field, as it demonstrated the feasibility of fabricating working devices with group-IV X-enes, and their potential to overcome graphene’s limitations. The carrier mobility was $\sim 100 \text{ cm}^2 \text{ V}^{-1} \text{ s}^{-1}$ and, more importantly, the opening of a small bandgap was discussed. Later, FETs based on less air-sensitive multilayer silicene were reported as well,⁵³ providing an interesting pathway to stabilize the quickly degradable single-layer silicene-FET.⁵² In this scenario, it is also worth noting that silicene and germanene, differently from graphene and other classes of 2D materials, offer the prospect of full compatibility with the existing semiconductor technology. Therefore, if high performance devices were to be realized, the existing technology infrastructure, based almost entirely on the processing of Si and to a lesser extent of Ge, could easily be applied. Nevertheless, the study on X-enes is still in its infancy, and if there are only a few studies on silicene-based devices, the ones on germanene or stanene are even more rare.⁵⁴

Therefore, growing X-enes on nonmetal and inert substrates is of paramount importance in order to (i) gain more insights into their

intrinsic electronic properties and (ii) make easier the realization of electronic devices. At this aim, the first important issue becomes to identify the properties that such inert substrates should possess to enable successful growth of X-enes. With these premises, here we first review the state of the art of the recent progress achieved in the deposition of Si, Ge, and Sn on nonmetal substrates, with special attention to the most compelling experimental findings that are supported by atomic-scale structural characterization of the grown 2D sheet. In particular, we start focusing on hexagonal layered surfaces. These are very promising growth substrates because their surface terminates with no dangling bonds, and they are therefore expected to interact only weakly with the ad-layer on top (i.e., van der Waals epitaxy).^{55–58} In addition, some of them have considerable band gaps (1–6 eV), which would enable direct realization of electrical devices without the need of a postgrowth transfer step. As we will see however, layered substrates bring many challenges, mainly due to possible intercalation of group-IV atoms under the substrate top layer(s) during deposition. This has led to an interesting yet unsettled debate, and to publications showing similar results but with different interpretations. Next, we discuss those nonmetal substrates that, although not layered, are still expected to interact weakly with the growing 2D overlayer. Examples of this class of materials are calcium difluoride (CaF₂), lanthanum aluminate oxide (LaAlO₃, LAO), and sapphire (Al₂O₃). Theoretical predictions involving these substrates have been already reported, and some promising preliminary experiments have been carried out as well. Yet, convincing and thorough characterization of the structural and electronic properties of the grown 2D layers is still missing. In addition, we also look at an alternative yet promising route for the synthesis of X-enes via chemical modification of X-ene-based composites.

II. RECENT PROGRESS

A. Si and Ge on MoS₂

Molybdenum disulfide (MoS₂) is a semiconducting layered material and probably the most noted compound among the family of transition metal dichalcogenides.^{59,60} It has also been one of the first substrates used to grow silicene,⁶¹ because, despite a smaller lattice parameter (3.16 Å), it fulfills the requirement of hexagonal symmetry and lack of dangling bonds on the surface that would be required to preserve silicene electronic properties.^{61–63} MoS₂ in its bulk form is composed of stable S-Mo-S layers interacting with each other via van der Waals forces. A first experimental result on silicene epitaxy on a MoS₂ substrate was reported by Chiappe *et al.*,⁶¹ where Si was deposited through molecular beam epitaxy (MBE) at 200 °C. Figure 2 summarizes the main findings of that study. In particular, scanning tunneling microscopy (STM) data revealed that Si atoms are indeed arranged in graphene-like nanodomains with threefold symmetry. Surprisingly, despite a mismatch as large as 20% between free-standing silicene and MoS₂ and the expected weak interaction between the substrate and ad-layer in the van der Waals epitaxy growth mode, the authors claim to observe Si domains having the same lattice constant of the MoS₂ underneath. Density functional theory (DFT) calculations were used to supplement the experimental results, and revealed a remarkable buckling of the Si layer of about 2 Å, which is indeed in good agreement with line profiles extracted from the STM data. Such a value, quite large compared to those previously experimentally measured⁵ and theoretically predicted⁵ for low-buckled silicene structures,

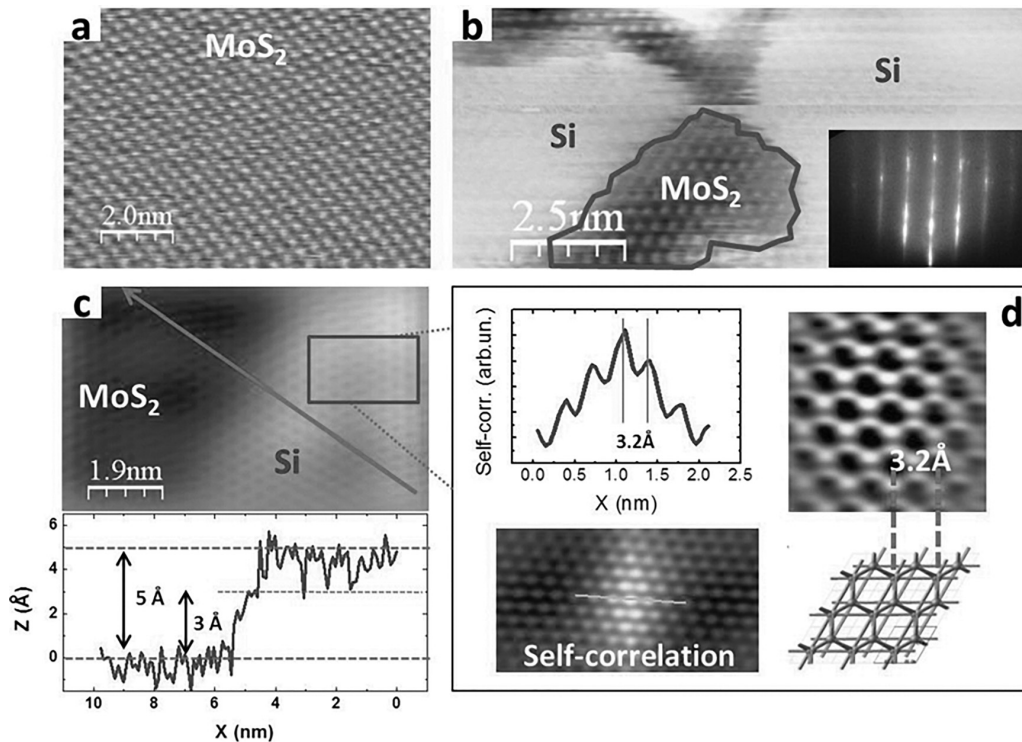


FIG. 2. Scanning tunneling microscopy characterization of Si nanosheets epitaxially grown on MoS₂. (a) Clean MoS₂ surface ($V = 1$ V, $I = 0.7$ nA); (b) MoS₂ surface after deposition of 0.8 ML of Si ($V = 1$ V, $I = 0.7$ nA). The contour delimits an uncovered portion of the MoS₂ surface. Inset: Reflection high energy electron diffraction pattern displaying the characteristic streaks. (c) Higher resolution image ($V = 0.2$ V, $I = 2$ nA) of a partially covered surface. (Below) Line profile taken across the gray arrow in the image above showing a height difference of 5 Å. (d) Magnified topography of the area highlighted by the gray rectangle in (c) showing a hexagonal surface pattern, the periodicity of which is extracted from the analysis of the self-correlation function. A sketch models the Si honeycomb structure. Reproduced with permission from Chiappe *et al.*, *Adv. Mater.* **26**, 2096 (2014). Copyright 2014 John Wiley and Sons.

might have been the result of the remarkable shrinking of the Si lattice induced by the substrate. Because the magnitude of buckling largely influences the electronic band structure of silicene, the authors performed scanning tunneling spectroscopy (STS) measurements to gain insights into the electronic properties of the highly strained silicene. Although some differences could be appreciated when STS was performed on bare MoS₂ or on Si-coated MoS₂, unfortunately STS experiments are very sensitive to tip-substrate interaction in the case of layered materials and thus compelling conclusions could not be drawn at that stage.⁶¹ To shed light onto the electronic properties of the system, the same group later carried out also *in situ* angle-resolved photoemission spectroscopy (ARPES) experiments [Figs. 3(a)–3(d)]. A comparison of the valence band structure along the high-symmetry K- Γ -K direction for the MoS₂ substrate before and after Si deposition illustrates that the silicene/MoS₂ system is metallic in character due to an accumulation of electrons at the interface.⁶⁴ It is worth pointing out that the information gained by the ARPES data is relative to the topmost MoS₂ layer because the inelastic mean free path of electrons with the photon energy used for the experiments (100 eV) was almost comparable to the thickness of a single MoS₂ layer.

Further experimental efforts were devoted to the fabrication of a back-gated FET.⁶⁴ A monolayer of silicon was deposited in vacuum onto few layers of MoS₂ previously exfoliated on a SiO₂/Si⁺⁺ substrate and already contacted by Au/Ti electrodes. Afterward, a 5 nm-thick film of Al₂O₃ was used as a capping layer to protect the 2D Si nanosheets against oxidation [Fig. 3(e)]. To better characterize the device described above, its electrical behavior was compared with that of the MoS₂ FET. First, the admittance was measured. From the data collected, the channel in the Si/MoS₂ heterosheet FET started accumulating charges at lower bias with respect to the MoS₂ FET taken as reference. Furthermore, the capacitance curves exhibited a bias-modulated stretch-out that could be explained as the interplay of the two active interfaces (i.e., Si/MoS₂ and MoS₂/SiO₂). The electrical characteristics of the two devices are shown in Fig. 3(f). The two devices showed different back gate voltage (V_{bg}) dependence in the drain-source I-V (I_{ds} - V_{ds}) curves, indicating that the two devices had different threshold voltage. The heterosheet FET showed a rigid back-shift of threshold voltage at V_{ds} values and an extra bias modulation. Looking more into details, from the linear I_{ds} - V_{bg} curve emerged a double threshold. The physical meaning of this last feature is elucidated by the transconductance (g_m) plot in Fig. 3(g). In the case of

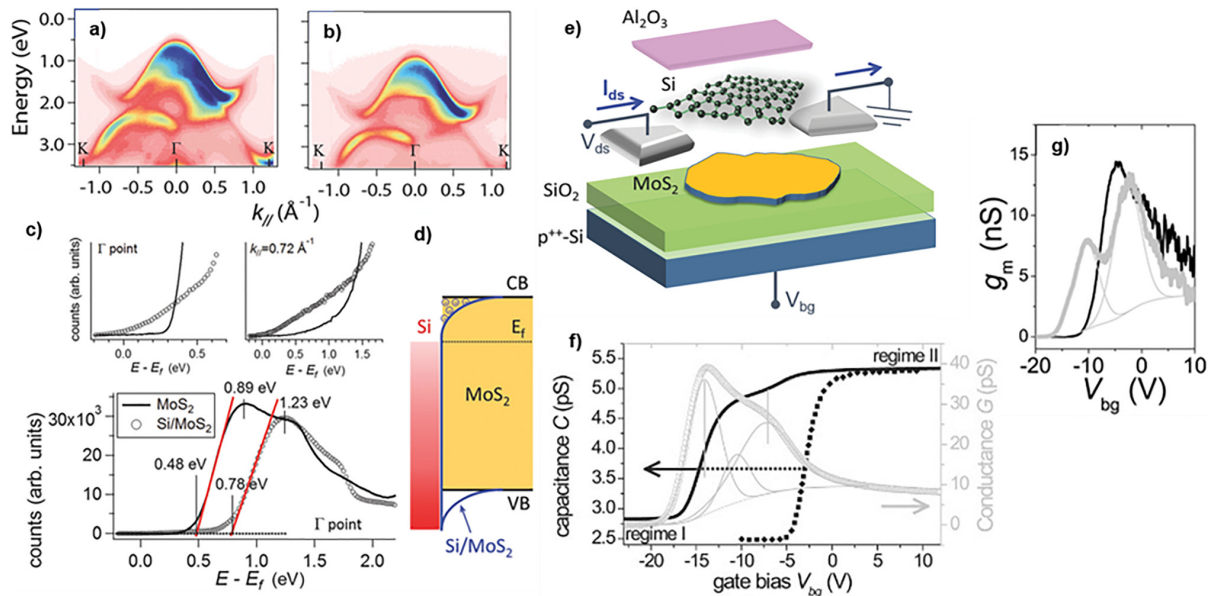


FIG. 3. Valence band structure of (a) bare MoS₂ and (b) MoS₂ after Si deposition at 200 °C collected with a photon energy $h\nu = 100$ eV along the K- Γ -K reciprocal lattice direction. (c) Bottom: Comparative line profiles of the valence band plots taken at the Γ point for bare MoS₂ (black line) and after the growth of Si nanosheets (circles). Top: Line profile in the vicinity of the Fermi level taken at the Γ point (left) and at $k_{\parallel} = 0.72 \text{ \AA}^{-1}$ (right). (d) Schematic diagram of the electronic bands at the Si/MoS₂ interface. (e) Sketch of the fabrication process of the Si/MoS₂ FET. (f) Admittance response of the Si/MoS₂ FET. The capacitance-voltage (black line) and conductance-voltage (gray circles) curves are shown. (g) Comparative transconductance g_m plot as a function of gate bias derived at a source-drain voltage of 0.2 V. Gray lines are from the Si/MoS₂ FET, while the black line from MoS₂ FET. Reproduced with permission from Molle *et al.*, Adv. Mater. Interfaces 3, 1500619 (2016). Copyright 2016 John Wiley and Sons.

MoS₂ FET the g_m curve exhibited one peak while for Si-MoS₂ FET the profile is double peaked. Thus, in agreement with the admittance response, the authors have concluded that two active channels are formed at MoS₂/SiO₂ and Si/MoS₂ interfaces. The conduction through the Si nanosheets is neglected as the transconductance peak is comparable with the MoS₂/SiO₂ channel and suggests a semiconducting behavior rather than the expected metallic one of the silicene layer. This can be due to the disconnection of different grains in the Si nanosheet surface that can compromise the overall electrical transport properties. It cannot be excluded that the Al₂O₃ capping has no influence on the mobility of the Si/MoS₂ interface, but the creation of a conductive channel at the Si/MoS₂ interface can be a direct consequence of the Si-induced band bending and suggests n-type doping due to the electron transfer in the topmost region of MoS₂ induced by the Si nanosheets. Silicene deposition has to be improved both in quality and size of layers in order to reach higher carrier mobility, but this framework is a relevant starting point for the optimization and tuning of van der Waals heterostructures for nano- and optoelectronic applications.

Interestingly, Van Bremen *et al.*⁶⁵ found experimental STM results similar to those previously reported by Chiappe *et al.*⁶¹ but the interpretations given in the two works are completely different. Indeed, the formers⁶⁵ claimed that, upon low rate deposition at room temperature, Si intercalated between MoS₂ instead of growing on top of the substrate. This interpretation relies on the fact that after deposition of silicon onto MoS₂, the surface showed hills-and-valley structures with the same lattice constant of 3.16 Å (parameter consistent

with the pristine MoS₂). The transitions from hills to valley were gradual and not step-like as it would be expected for islands epitaxially grown on top of substrates. Moreover, the spectroscopy data showed no particular differences in the I(V) over the different areas as well as a uniform work function probed via spatial maps of dI/dz. X-ray photoelectron spectroscopy (XPS) measurements were also performed on the samples. The data revealed that upon Ar sputtering of the Si/MoS₂ surface the signal from silicon increased instead of decreasing, opposite to what expected in the case of islands sitting on top of the substrate. From the experimental considerations above, van Bremen *et al.*⁶⁵ concluded that Si atoms intercalated between the MoS₂ layers rather than growing silicene islands on top of the substrate.

MoS₂ has also been experimentally investigated as a growth substrate for germanene.⁸ In this case, the deposition of Ge was performed while keeping the substrate at room temperature. Ge atoms diffuse onto the MoS₂ surface and use defects in the substrate, such as vacancies or lattice impurities,^{66,67} as nucleation points. At low coverage, the 2D Ge islands exhibit different shapes and sizes; yet they all show an interesting hexagonal shaped vacancy in their center (Fig. 4). Compared to what was observed in the case of 2D silicon nanosheets grown on MoS₂,⁶¹ here the lattice parameter of the Ge islands does not match that of the substrate, although is contracted of about 5% compared to that of free-standing germanene (3.8 Å and 3.97 Å respectively). STS data collected at room temperature on bare MoS₂ areas showed the presence of a bandgap, whereas when acquired on the islands revealed a well-defined V shape around zero bias [Fig. 4(d)], which is characteristic of 2D Dirac systems. At full monolayer

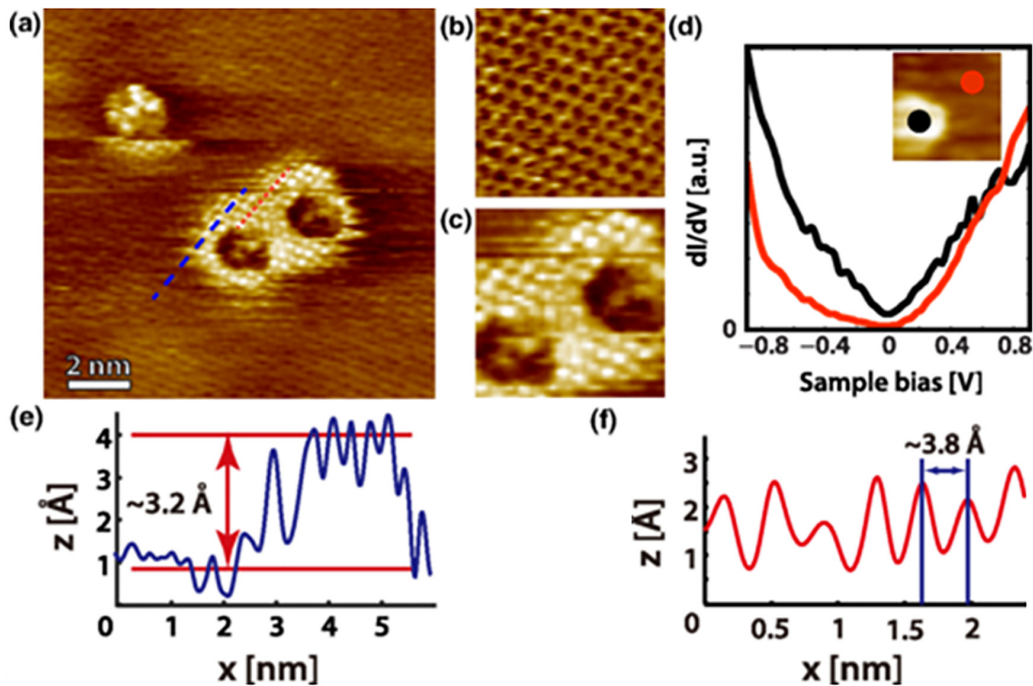


FIG. 4. (a) STM image of a germanene/MoS₂ sample ($V = 0.5$ V and $I = 0.3$ nA). (b) A zoom-in on a bare MoS₂ area. The STM image reveals a honeycomb structure with a lattice constant of 3.15 ± 0.2 Å, consistent with the MoS₂ lattice parameter ($V = 0.5$ V, $I = 0.3$ nA). (c) A zoom-in on the large germanene island of panel (a) ($V = 0.5$ V and $I = 0.3$ nA). (d) Differential conductivity recorded on a germanene island and on the MoS₂ surface, black and red curve, respectively ($V = 1$ V and $I = 0.3$ nA). (e) Line profile taken across the germanene island as indicated by the blue dashed line in (a). The apparent height of the germanene islands is ~ 3.2 Å. (f) Line profile taken on top of the germanene island indicated by the red dashed line in (a). The measured lattice constant of the germanene island corresponds to 3.8 ± 0.2 Å. Reproduced with permission from Zhang *et al.*, Phys. Rev. Lett. **116**, 256804 (2016). Copyright 2016 American Physical Society.

coverage, the lattice parameter of the Ge sheet still does not match that of the MoS₂ underneath, and the two lattices are aligned. Furthermore, DFT calculations performed on islands laterally contracted by 5% were used to support the experimental observations. The shape of both germanene and MoS₂ calculated density of states (DOS) is found to be in very good agreement with the experiments, with the only difference being the position of the Fermi energy, which is shifted in the calculated DOS of ~ 0.3 eV toward higher energy, this implying n -type doping of the system. This discrepancy could be explained by the presence of doping impurities or unsaturated defects in the sample. The DFT calculations provided further details about the band structure of the system, and revealed the presence of (i) π -bands close to the K point, and (ii) two parabolic σ bands close to Γ point. Unfortunately, the observed large buckling of germanene leads to σ - π charge transfer, which would suppress the anomalous quantum Hall effect as well as the 2D Dirac transport properties.

B. Si and Ge on Highly Oriented Pyrolytic Graphite (HOPG)

Owing to a hexagonal symmetry and a surface free of dangling bonds, highly oriented pyrolytic graphite (HOPG) is a promising candidate as a weakly interacting growth substrate for X-enes. Moreover, it is chemically inert and expected to form no alloy intermixing with

either Si or Ge.⁶⁸ In the past couple of years, the growth of silicene and germanene on HOPG has been studied intensively, and much interesting progress has very recently led to a stimulating debate.

In Ref. 69, silicon atoms were deposited on a HOPG kept at room temperature in UHV conditions. High-purity silicon was evaporated from a wafer at a nominal constant rate of 0.1 nm/min (0.04 ML/min). Atomic force microscopy (AFM) investigations showed the simultaneous presence on the sample of (i) 2D islands, (ii) areas of uncovered HOPG, and (iii) three-dimensional (3D) clusters. Atomically resolved STM data [Figs. 5(a)–5(c)] were used to provide more insights into the structure of the obtained 2D islands, and showed that these exhibit a small buckling of 0.5 Å, in good agreement with the value expected for free-standing silicene.^{5,70} Furthermore, an analysis of the Fourier transform reveals two hexagons rotated by 30° with respect to each other. The outer hexagon is relative to HOPG, corresponding to a lattice parameter of 2.4 ± 0.1 Å, while the inner one has a larger parameter, of 4.1 ± 0.2 Å, which is close to the value of 3.83 Å, theoretically predicted for free-standing silicene.⁵ The fact that the values experimentally measured for the lattice parameter and the out-of-plane buckling are so close to the ones theoretically predicted for free-standing silicene implies that silicene on HOPG is unstrained. This is indeed expected for van der Waals epitaxy,⁵⁵ and is the signature of a weak interaction between the substrate and the

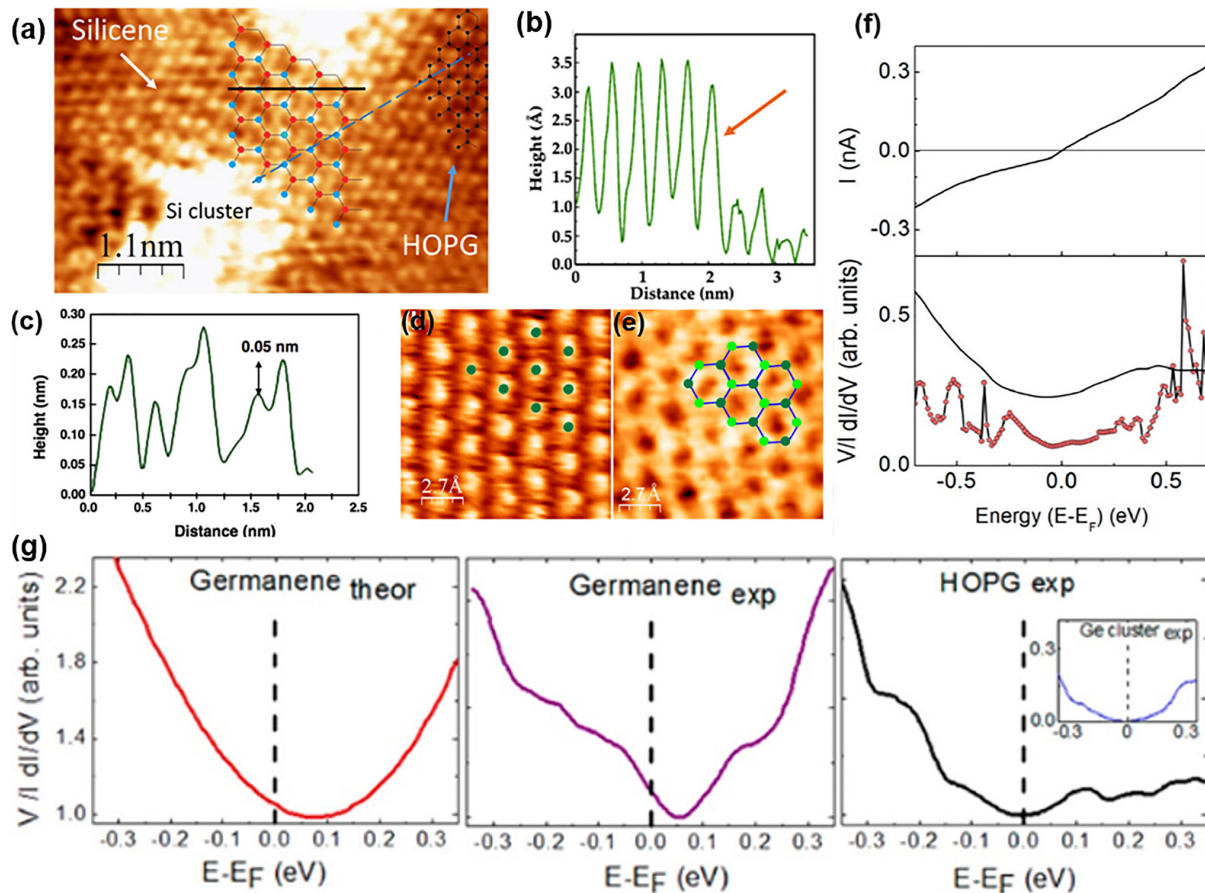


FIG. 5. (a) STM image of a HOPG substrate after deposition of 1 ML of Si. The substrate was kept at room temperature during the evaporation. The ball-and-stick models superimposed on the image represent the Si lattice (blue and red) and HOPG lattice (black). ($V = 0.3$ V, $I = 0.3$ nA). (b) Line profile recorded along the blue dashed line drawn in (a). The red arrow indicates the height of the silicene layer with respect to the HOPG surface. (c) Line profile recorded along the solid black line drawn in (a) reveals a buckling between silicon nearest neighbors of about 0.05 nm. (d) STM image of the bare graphite surface used as the substrate for germanene growth ($V = -0.106$ V, $I = 2.1$ nA). (e) STM image of the germanene island ($V = -0.860$ V, $I = 1$ nA). On the images, ball-and-stick models showing the triangular (d) and the honeycomb (e) lattices are superimposed. (f) Top, I - V curve recorded on the silicene island on HOPG. Bottom, normalized differential conductance $(V/I) dI/dV$ calculated from the curve above related to the local density of states. The red dotted line is the theoretical density of states for the system. (g) Left, calculated total DOS for germanene on graphite. Experimental $(V/I) dI/dV$ recorded at room temperature on: (middle) a germanene island, (right) the HOPG substrate and (inset) on a Ge 3D cluster. The axis labels of the inset are the same as for the main panel. Panels (a)–(c) and (f) reproduced with permission from De Crescenzi *et al.*, ACS Nano **10**, 11163 (2016). Copyright 2016 American Chemical Society. Panels (d), (e), and (g) reproduced with permission from Persichetti *et al.*, J. Phys. Chem. Lett. **7**, 3246 (2016). Copyright 2016 American Chemical Society.

ad-layer. Under this condition, silicene on HOPG is supposed to display its intrinsic electronic properties. STS performed at room temperature on silicene areas indeed shows a metallic behavior with a finite density of states at the Fermi level [Fig. 5(f)].

Similarly, in Ref. 71 the synthesis of germanene islands on HOPG at room temperature is reported. Ge was deposited using an e-beam evaporator at a rate of 0.7 ML/min. STM measurements [Figs. 5(d) and 5(e)] showed a 2D layer with lattice parameter and buckling, respectively, of 4.2 ± 0.3 Å and 0.7 Å, values that closely match those theoretically predicted for free-standing germanene, that is 3.97 Å and 0.64 Å, respectively. As in the case of silicene on HOPG, also for the case of germanene on HOPG the ad-layer seems to grow

unstrained, as expected with a substrate free of surface dangling bonds.⁵⁵ Similar to the case of silicon deposited on HOPG, also in this case three-dimensional (3D) Ge clusters can be observed, suggesting a competition between 2D and 3D growth. The structural and electronic properties of the 2D Ge on HOPG obtained by DFT calculations are consistent with the experimental findings. In particular, the islands show the Dirac cone and a distinct charge transfer with the substrate that are predicted by simulations and experimentally observed in STS spectroscopy data [Fig. 5(g)].

The conclusions of Refs. 69 and 71 regarding the formation of unstrained silicene and germanene on HOPG have been recently rejected by another research group,⁷² after reproducing the same

experimental conditions. Notably, in Ref. 72 the authors proposed a completely different interpretation of the results obtained from STM measurements. The $(\sqrt{3} \times \sqrt{3})R30^\circ$ honeycomb superstructure arising after the deposition of Si or Ge atoms was observed around step edges and Si/Ge clusters, while the majority of the atomically flat areas between clusters exhibited the triangular lattice of the HOPG surface. From the unreconstructed HOPG areas to the honeycomb superstructure areas, the change in height (i.e., the slope of the line profile taken across an area with the superstructure and one without) appeared to be smooth and continuous, and not sharp and step-like as expected for the case of silicene/germanene islands grown on top of HOPG. The observed superstructures were always confined around step edges or clusters and involved a breakdown in the lattice periodicity of graphite. Therefore, the authors in Ref. 72 proposed that the observed superstructures result from a long-range perturbation of the charge density in HOPG due to electronic interferences between surface and scattered waves from defects or clusters. Similar conditions were found after deposition of Pt particles⁷³ and creation of defects induced by Ar^+ bombardment.⁷⁴

On the other hand, shortly after the publication of Ref. 72, a new interesting analysis based on Raman spectroscopy⁷⁵ supports instead the formation of silicene on HOPG as concluded in Ref. 69. As shown in Fig. 6, *ex-situ* Raman measurements collected on uncapped silicene/HOPG samples feature a peak at 542.5 cm^{-1} .⁷⁵ Such a Raman peak is different from that of all known Si configurations and therefore recognized as an intrinsic mode of silicene. The reason why silicene's Raman features can be observed even though the sample has been exposed to air, i.e., the reason why silicene is not oxidized, might be the fact that silicene does not form on top of the graphite surface, but between its layers. Indeed, in Ref. 76 Kupchak *et al.* have recently demonstrated that Si intercalates under the topmost graphitic layer of HOPG. This was proposed after analyzing height profiles taken over bright-contrast areas in the STM images. In the case of silicene patch grown on top of the HOPG substrate, a step-like behavior of the line profile in conjunction with the silicene patch's borders is expected. Instead, the STM images reveal a smoother change in profiles, as the height gradually degrades around the highest spot in the curve. This interpretation probably resolves the doubts aroused in Ref. 72. High magnification STM images show the coexistence of Si cluster and bubbles. Theoretical calculations have shown that the presence of defects in the graphene layer lowers the energy barrier for Si penetration,⁷⁷ allowing the Si-C atom exchange mechanism also at room temperature. To better understand the nature of these bubbles, i.e., protrusions with an almost flat top, Raman measurements were performed [Fig. 6(c)]. The spectrum related to the pristine HOPG shows the characteristic D and G Raman modes.⁷⁸ After deposition of 1 ML of Si, the Raman spectrum presents a predominant feature at 517 cm^{-1} , consistent with sp^3 hybridized Si nanoclusters.⁷⁵ Additionally, a small feature arises around 538 cm^{-1} .⁷⁶ This resonance is close to the one previously reported by Castrucci *et al.*⁷⁵ at 542.5 cm^{-1} and recognized as a silicene nanosheet mode on top of HOPG. In contrast with what reported by Castrucci *et al.*,⁷⁵ dramatic changes in D and G modes of HOPG are observed in this study.⁷⁶ The D and G resonances indeed widen after the deposition of Si, as they are the result of different contributions. In particular, the G band presents components toward lower wavenumbers, while the D band intensity now dominates over that of the G band. In order to understand these

observations, Kupchak *et al.*⁷⁶ performed *ab initio* calculations. The theoretical model is in agreement with the experimental STM images and the Raman measurements, by considering the insertion of Si atoms arranged as silicene underneath the outmost graphitic layer. By modeling the tensile strain distribution of the C atoms, the percentage varies between 0 and 4% of the bond length in free-standing graphene. These strain values largely affect the vibrations of the atoms and consequently also the Raman spectrum. Indeed, the strain induces a longer lattice parameter and consequentially a shift of the G band toward lower wavenumbers.

Nevertheless, the controversy and the opposite interpretations highlight the need for more convincing results to shed light on the growth of X-enes on HOPG, and in general on layered substrates. Growing larger and more uniform silicene or germanene areas on HOPG, for instance by tuning the growth conditions (i.e., substrate temperature, evaporation rate), would be probably beneficial for resolving this debate.

C. Sn on InSb, Bi_2Te_3 , and PbTe

Very few experimental studies have been reported thus far on the growth of stanene, and mostly are on metal surfaces such as $\text{Cu}(111)$ ³⁰ and $\text{Ag}(111)$.⁴⁸ However, in the 1990s some MBE experiments might have led to the synthesis of stanene-like structures on $\text{InSb}(111)$,⁷⁹ where the authors studied the growth modes and phase transitions of α -Sn on the substrate by means of reflection high-energy electron diffraction (RHEED) and Auger electron spectroscopy. However, no atomic-scale characterization was provided at that time. Much more recently, Xu and co-authors⁸⁰ replicated that study by growing epitaxially stanene on the Sb-terminated $\text{InSb}(111)$ surface, and by carrying out RHEED and ARPES experiments. Their findings show that while monolayer stanene on $\text{InSb}(111)$ has a large bandgap of 0.44 eV, bilayer stanene is instead a semimetal, as the bandgap is filled in by InSb conduction band states. Nevertheless, the bandgap of 0.44 eV measured for single-layer stanene makes the system stanene/ $\text{InSb}(111)$ promising for quantum spin Hall applications even at room temperature, where the thermal energy $k_B T$ is 25 meV.

In Ref. 9, an interesting work reports on the growth of stanene on $\text{Bi}_2\text{Te}_3(111)$. The substrate, either bulk single crystal or thin film, was kept at RT during deposition of Sn via MBE. Figures 7(a)–7(c) display STM images and atomic model of the system. The deposition resulted in several layers of Sn with a constant spacing between layers of about $0.35 \pm 0.02 \text{ nm}$. The ARPES measurements [Figs. 7(d)–7(k)] showed that the valence band of Bi_2Te_3 shifts to higher energy with the Sn deposition, indicating electron transfer from the ad-layer to the substrate. The lattice constant for the substrate is 4.383 \AA ,⁸¹ while for free-standing stanene it is expected to be 4.62 \AA from DFT calculations.²⁴ This means that the substrate should apply a compressive strain on stanene possibly leading to an increase in the buckling from 0.85 to 1.09 Å . Theoretical models for different binding sites of stanene give similar results concerning the geometry of the system, probably due to the weak interaction with the substrate. The experimental results obtained in Ref. 9 are in agreement with theoretical calculation. Indeed, the DFT model showed that the valence band shifts upward resulting in a transition from topological insulator to metal. Thus, it can be inferred that stanene under compressive strain remains metallic.⁹ Nevertheless, it could still be possible to open a bandgap via chemical functionalization of stanene,

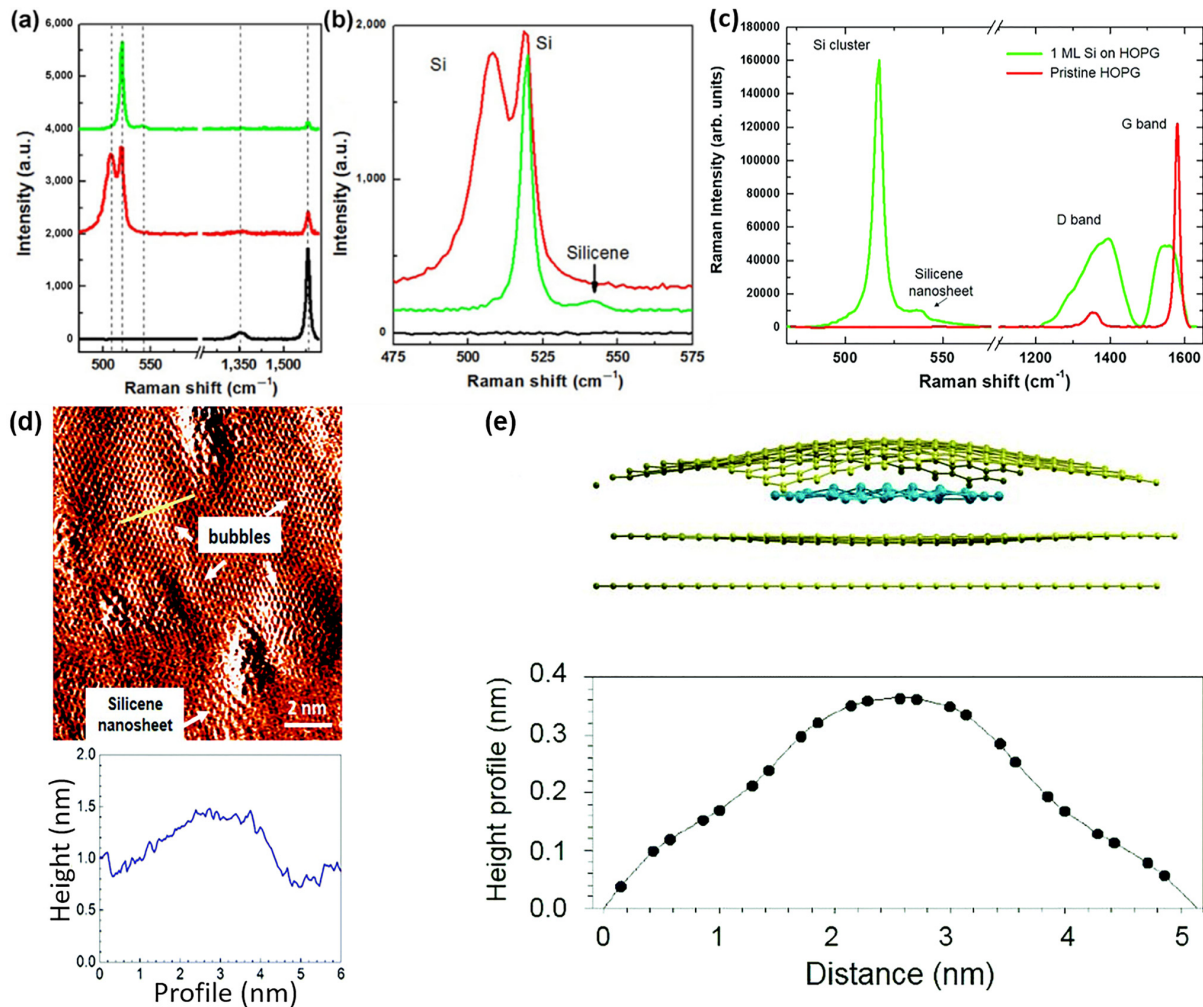


FIG. 6. (a) Raman spectroscopy of three different regions of a HOPG sample after deposition of 1 ML of Si from Ref. 81: The black line shows the standard Raman modes of bare graphite, while the red line shows the Raman modes at 510 cm^{-1} , relative to silicon nanoclusters and at 520 cm^{-1} relative to bulk silicon. The green line shows the Raman resonance at 520 cm^{-1} . (b) Blow-up around 520 cm^{-1} . The arrow shows the Raman mode at 542.5 cm^{-1} due to the silicene nanosheets on top of HOPG. (c) Raman spectra of the clean HOPG surface (red curve) and the HOPG surface after 1 ML Si deposition at room temperature (green curve) from Ref. 82. The resonance of 3D silicon is located at 517 cm^{-1} and a new peak is located at 538 cm^{-1} , which is ascribed to silicene intercalated under the first graphitic layer. The G and D bands of HOPG are different from the ones of clean HOPG due to strain experienced by the outermost graphitic layer after silicene nanosheet intercalation and the presence of graphite edges. (d) STM image of the HOPG surface after the deposition of 1 ML of Si at room temperature. Lower panel: Height profile of the bubble taken along the yellow line in the above image ($V = 0.3\text{ V}$, $I = 0.4\text{ nA}$). (e) Theoretical height of the outermost graphitic layer over the silicene nanostructure. Panels (a) and (b) reproduced with permission from Castrucci *et al.*, *Nano Res.* **11**, 5879 (2018). Copyright 2018 Springer Nature. Panel (c)–(e) reproduced with permission from Kupchak *et al.*, *Nanoscale* **11**, 6145 (2019). Copyright 2019 Royal Society of Chemistry.

which would then allow this system to host quantum spin Hall and quantum anomalous Hall states.^{82,83}

Besides the studies on InSb and Bi_2Te_3 surfaces, stanene has also been successfully fabricated on $\text{PbTe}(111)/\text{Bi}_2\text{Te}_3$ substrates via MBE.⁸⁴ The quality of the film was monitored by RHEED and confirmed via STM characterization. Very interestingly, while bulk α -tin is not superconductive, this study demonstrates that few-layer stanene is indeed a superconductor.⁸⁵ Figure 8(a) displays a sketch of the

structure of the system with trilayer Sn deposited on top of $\text{PbTe}/\text{Bi}_2\text{Te}_3/\text{Si}(111)$, with hydrogen atoms passivating the surface. Figure 8(b) shows that superconductivity emerges starting from bilayer stanene, and the sample remains a superconductor even at a thickness of 20 Sn layers (NSn). It is also evident that the critical temperature (T_c) increases with the number of Sn layers [Figs. 8(b) and 8(c)], as already found for other ultrathin film systems.^{86,87} Besides, T_c also depends strongly on the thickness of the PbTe buffer layer [Fig. 8(d)]. While it

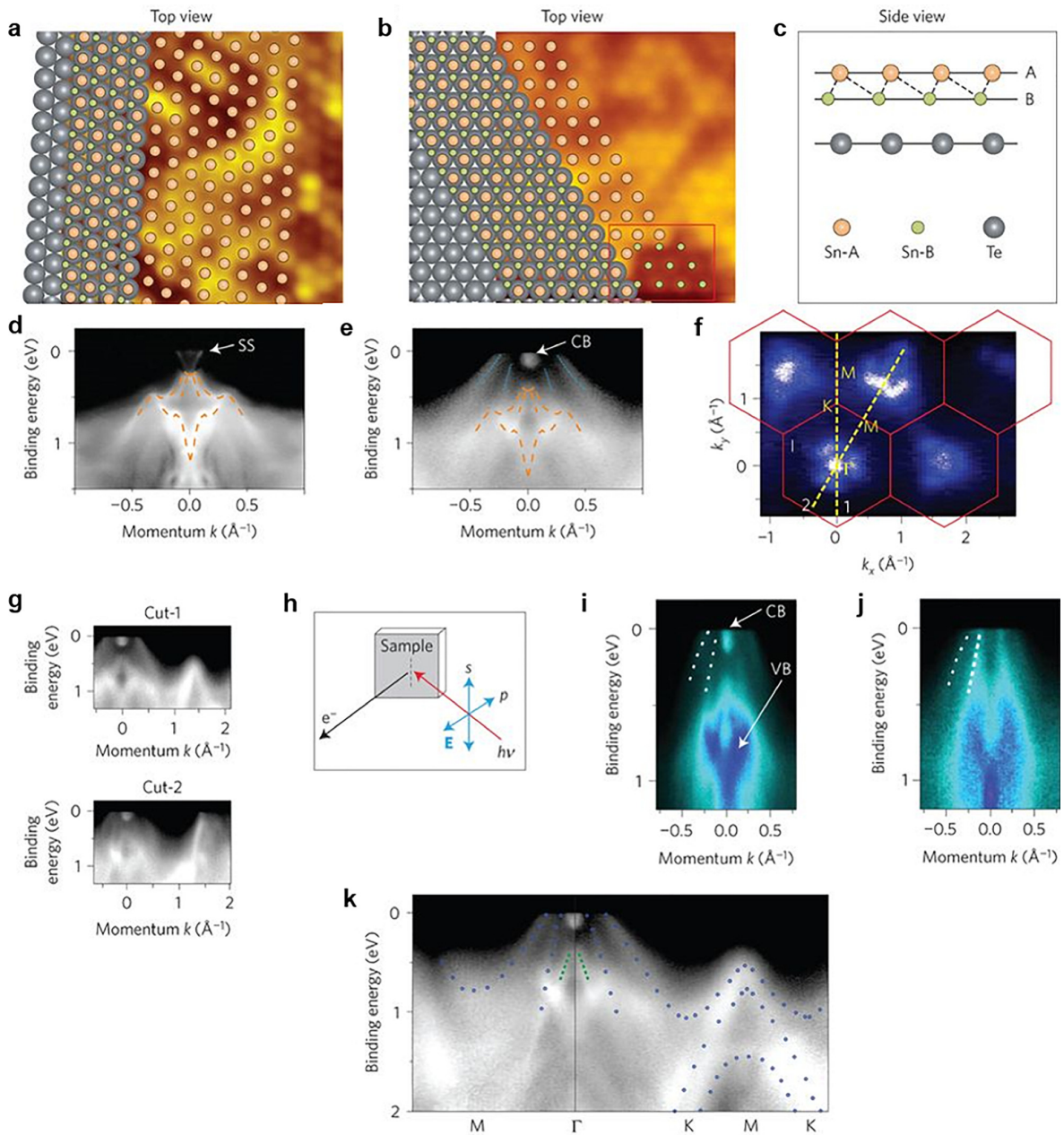


FIG. 7. (a)–(c) Model of the atomic structure of 2D stanene on the Bi_2Te_3 (111). The green and orange balls represent the bottom and top Sn atoms, respectively. The gray balls represent the surface Te atoms of the substrate. (a) Top view of the top Sn atoms. (b) Top view of both the top and bottom Sn atoms. (c) Side view. (d) and (e) ARPES spectra of Bi_2Te_3 (111) (d) and stanene on Bi_2Te_3 (e) along the $\text{K}-\Gamma-\text{K}$ direction. The orange dashed lines define the bulk band dispersions of Bi_2Te_3 . The blue dotted lines define the valence bands of stanene. “SS” marks the surface state and “CB” marks the conduction band of Bi_2Te_3 , respectively. (f) Fermi surface mapping in large momentum space. The red hexagons are the 2D Brillouin zones of stanene. (g) ARPES spectra along two momentum directions marked by yellow lines in (f). (h) Sketch of the two light polarizations used in the experiments. (i) and (j) ARPES spectra taken under p-polarization (i) and s-polarization (j). White dotted lines mark the valence bands of stanene. “VB” marks the valence band of Bi_2Te_3 . (k) ARPES spectra along the $\Gamma-\text{M}-\Gamma-\text{K}-\text{M}-\text{K}$ directions. Blue dotted lines represent the experimental electronic bands of stanene, while the green dashed lines the valence band of Bi_2Te_3 (111). Reproduced with permission from Zhu *et al.*, Nat. Mater. **14**, 1020 (2015). Copyright 2015 Springer Nature.

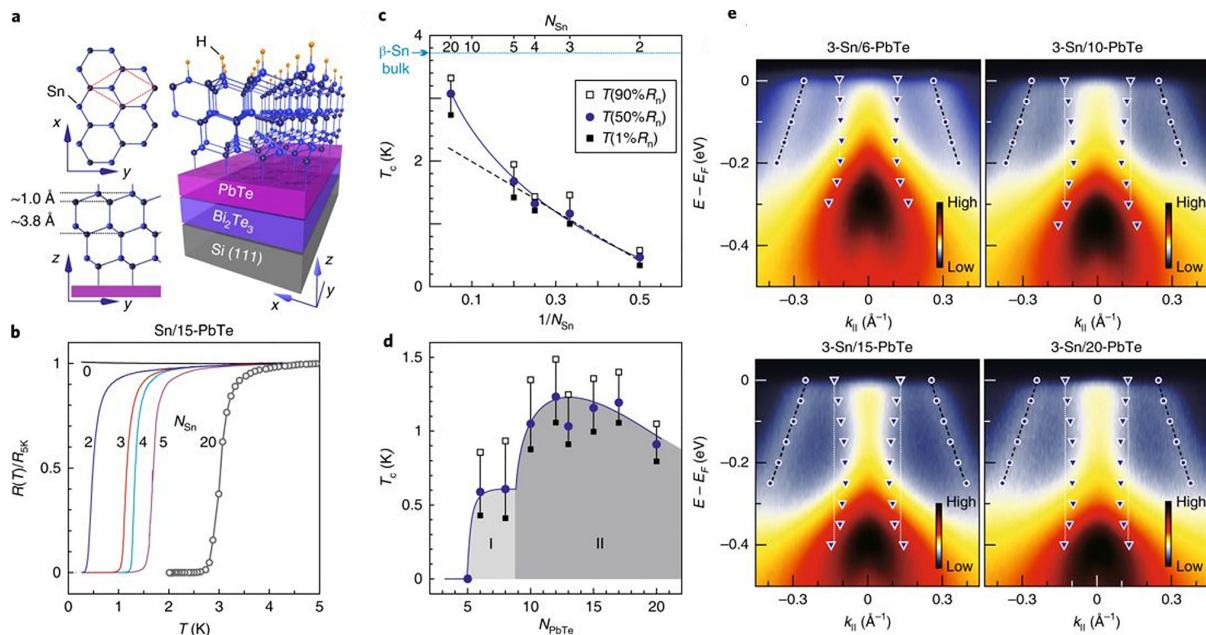


FIG. 8. (a) Sketch of the Sn/PbTe/Bi₂Te₃ structure and the stanene lattice. (b) Normalized resistance of stanene with varying the number of Sn layers grown on PbTe (15 layers). (c) T_c as a function of the number of stanene layers (N_{Sn}). (d) T_c as a function of PbTe layers (N_{PbTe}). The three data points of T_c in a row represent the temperatures where the resistance drops to 1%, 50%, and 90% of the normal resistance (R_n). The T_c in the bulk β -Sn is 3.7 K. (e) Dependence of the band structure around the Γ -point for trilayer stanene on the number of PbTe layers. Circles indicate the linearly dispersed valence band. Triangles indicate the width of the parabolic band around $k_{||}$. Reproduced with permission from Liao *et al.*, Nat. Phys. **14**, 344 (2018). Copyright 2018 Springer Nature.

seems that there is no dependence of T_c for stanene grown on less than 6 PbTe layers, T_c doubles when the number of PbTe layers is larger than 8. The authors explain this finding as due to variation in the density of states, as observed from ARPES experiments, and the release of mechanical strain caused by the lattice mismatch with the substrate.⁸⁸

Figure 8(e) indeed shows ARPES data of a trilayer stanene with increasing number of PbTe layers (N_{PbTe}), where two different valence bands can be identified. One parabolic band below the Fermi level, and one with linear dispersion with the two arms crossing the Fermi level. When N_{PbTe} increases, the two valence bands downshift due to an enhancement in the electron transfer from PbTe buffer layer, and a third band becomes visible around the Fermi level. There is therefore a transformation of the trilayer stanene from a one-band to a two-band system when it is grown on 10-layer PbTe or thicker. Theoretical calculations supported the ARPES data and even showed an s-p band inversion at Γ point resulting in a topologically nontrivial phase.^{83,89,90} This remarkable study hence opens to the possibility of integration of topological insulator and superconductor in the same material owing to the delicate dependence of T_c and N_{Sn} .

III. OTHER POTENTIAL SUBSTRATES FOR GROUP-IV X-ENES GROWTH

In addition to the layered substrates discussed above, many other possible suitable candidates for epitaxial growth of X-enes have been discussed theoretically, and preliminary experimental data are also available in some cases, but no conclusive structural characterization

of the grown 2D layer has been reported yet. Although these substrates are not yet sufficiently studied, we believe they could lead to interesting discoveries in the near future. Among those, the layered material InSe, the insulating calcium difluoride (CaF₂), the oxides LaAlO₃ and Al₂O₃ and graphene on SiC have received particular interest.

A. InSe

Similar to HOPG and MoS₂ mentioned earlier, InSe is a layered material with the consecutive layers interacting among each other through van der Waals forces; its bulk crystal is a direct bandgap semiconductor with anisotropic electronic properties and lattice constant of about 4 Å.^{91,92} The lack of dangling bonds, the hexagonal symmetry and a small lattice mismatch with silicene and germanene make it an interesting candidate as a growth substrate for 2D group-IV materials. First-principles calculations performed by Fan *et al.*⁹³ show that both silicene and germanene can be indeed stably formed on InSe, and that their intrinsic electronic properties are largely preserved. Notably, silicene (germanene) on InSe would display a Dirac-cone-like dispersion with a bandgap of 141 meV (149 meV). A more interesting finding, though, is the ultrahigh carrier mobility on the order of 10^5 cm² V⁻¹ s⁻¹ that makes them extremely appealing for the realization of novel electronic devices based on van der Waals heterostructures.

Since it has been recently reported that InSe thin films can be exfoliated from bulk crystals and deposited on substrates such as silicon oxides, glass, or mica,⁹⁴ it is reasonable to foresee that the first attempts at growing silicene or germanene on it will soon appear.

B. CaF_2

Calcium difluoride is a ceramic widely used for the production of mineral and organic fluorine-based chemicals and glass. Recently, it has also been studied for growth of epitaxial thin films such as lithium fluoride⁹⁵ and for fabrication of ionic superconducting materials.⁹⁶ Among the diverse industrial applications, CaF_2 is especially important in the production of hydrofluoric acid (HF), because fluorite, i.e., the mineral form of CaF_2 , is the most important source in this process. In the production of HF, fluorite needs to be separated from the surrounding minerals through a front-floating technique as removal of fluorite in flotation leads to the reduction of operating costs. This process is performed in an aqueous environment, and therefore, the characterization of fluorite surface in the presence of water is crucial for industries. For this reason, many surface science groups worldwide have been studying the CaF_2 surface.^{97–99} It is expected, however, that CaF_2 could also be a suitable substrate for the growth of silicene. Indeed, because of electrostatic reasons, the cleaved $\text{CaF}_2(111)$ surface terminates with a F^- layer,¹⁰⁰ with the F^- ions arranged in a triangular pattern with spacing of 3.88 Å. This provides a lattice mismatch of only 0.5% with silicene. From theoretical calculations, such little mismatch and consequent small tensile strain do not affect the Dirac cone in silicene. Moreover, the completely filled valence shell makes the $\text{CaF}_2(111)$ surface inert¹⁰¹ and a good candidate as a substrate for van der Waals epitaxy of ad-layers.⁵⁵ Kokott *et al.*,⁶³ by means of parameter-free DFT calculations, showed that when silicene is formed on the $\text{CaF}_2(111)$ surface it has a buckling of 0.43 Å, which opens up a small bandgap of 52 meV, as reported in Fig. 9. The distance between the substrate and silicene ad-layer is 2.70 Å, suggesting the presence of weak van der Waals interaction. Although it is a promising route, the experimental realization of silicene on CaF_2 is still lacking, yet highly desired. The large bandgap of the substrate would prevent the study of silicene/ CaF_2 by means of STM; hence, AFM should instead be used for the structural investigation of the system.

C. Oxides

As ideal growth substrates need to be inert in order to leave unaltered the 2D overlayer's intrinsic electronic properties, oxides are of course an attractive choice.

1. LaAlO_3

Oxide lanthanum aluminate, LaAlO_3 (LAO), is a notable example. It has a high value of dielectric constant ($\kappa = 24$), is thermodynamically stable, and hence does not intermix with, for instance, silicon.¹⁰² A promising study on epitaxial growth of Si on LAO substrates is reported in Ref. 103, where a single layer of Si is deposited via MBE onto a $\text{LAO}(111)-(2\sqrt{3} \times 2\sqrt{3})R30^\circ$ reconstructed surface. The growth experiments were performed at different substrate temperatures (i.e., 300 °C and 500 °C) and followed using the RHEED technique. The RHEED pattern reported here in Figs. 10(a)–10(f) shows both Kikuchi lines, connecting the bright spots of the pattern, and integral streaks related to $\text{LAO}(111)$ after deposition. The combination of those two elements suggests that the surface remains flat and that silicon grows as a two-dimensional layer. The complementary XPS analysis [Figs. 10(g)–10(n)] revealed no evolution in the spectra of O 1s and Al 2p peaks, suggesting that the LAO crystalline structure is not modified and does not intermix with Si, as expected due to the repulsion between Al and Si.¹⁰⁴ Therefore, it is expected that only weak interaction is present between the substrate and overlayer. Interestingly, the Si 2s core-level XPS peak shows a higher energy component at 153.2 eV and a lower one at 150.5 eV. The higher binding component is consistent with the formation of Si-O bonds and its energetic position does not shift when the substrate temperature changes, meaning that there is no formation of other silicate compounds. On the other end, the lower component is instead related to the formation of Si-Si bonds. This component increases in intensity with the growth temperature, suggesting a larger Si-Si formation on the LAO surface at 500 °C than at 300 °C. These studies on LAO hold much promise for growing 2D silicon layers on insulating surfaces. Nevertheless, further studies especially by means of scanning probe microscopy techniques that are able to probe the atomic structure of the grown ad-layer are required, since as of today the morphology of such samples is not known. If structural studies were to confirm the presence of 2D silicon sheets, it would be then extremely interesting to investigate their electronic properties, and compare them to related theoretical calculations.

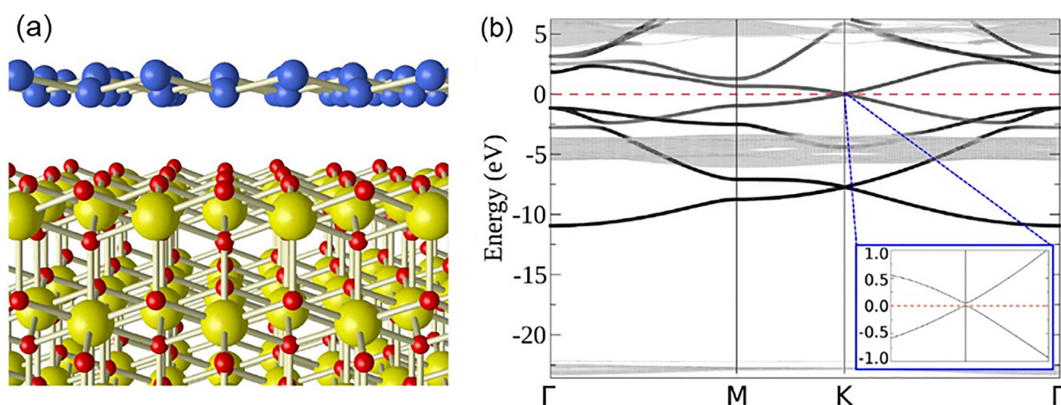


FIG. 9. (a) Sketch of silicene adsorbed on a clean $\text{CaF}_2(111)$ surface. Si, Ca, and F atoms in blue, yellow, and red, respectively. (b) Calculated band structure of silicene adsorbed on $\text{CaF}_2(111)$. The regions of the dense slab bands represent the projected bulk CaF_2 band structures. The silicene bands are indicated by black lines. The red-dashed horizontal line represents the Fermi level. Reproduced with permission from Kokott *et al.*, *J. Phys. Condens. Matter* **26**, 185002 (2014). Copyright 2014 Institute of Physics.

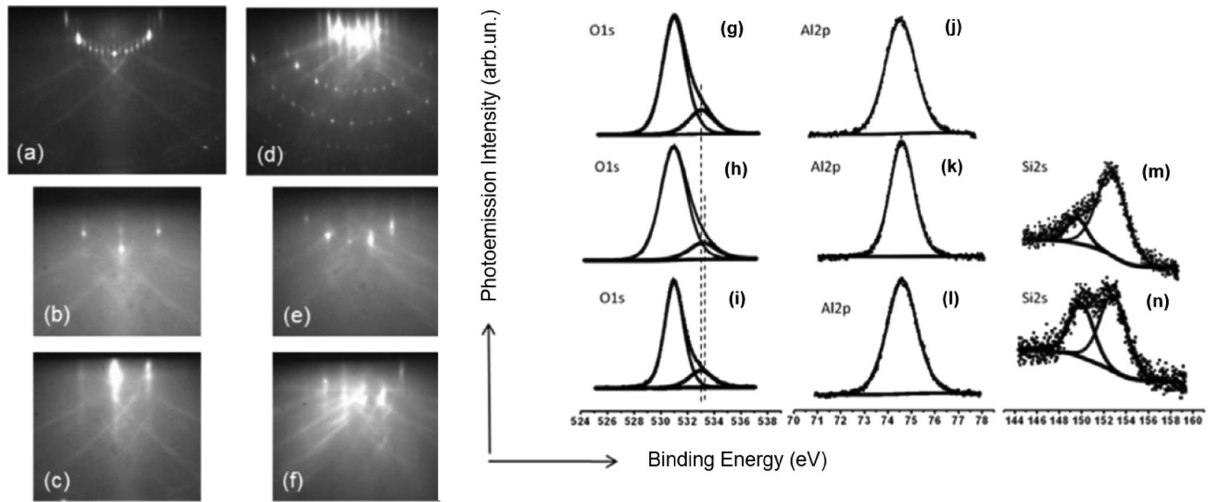


FIG. 10. RHEED pattern evolution, along the $\langle 112 \rangle$ azimuth (a)–(c) and $\langle 110 \rangle$ azimuth (d)–(f) for the clean LaAlO_3 substrate (a) and (d), after deposition of 1 ML of Si at 300 °C (b) and (e) and 500 °C (c) and (f). XPS O 1s (g)–(i), Al 2p (j)–(l) and Si 2s (m) and (n) core level peak evolution on clean LaAlO_3 (111) surface (g) and (j) after deposition of 1 ML of Si at 300 °C (h), (k), and (m) and at 500 °C (i), (l), and (n). Reproduced with permission from Ben Azzouz *et al.*, *J. Phys. Conf. Ser.* **491**, 012003 (2014). Licensed under a Creative Commons Attribution (CC-BY-3.0) license.

2. $\text{Al}_2\text{O}_3(0001)$

A very recent work reports on the optical conductivity of ultrathin Si nanosheets grown on $\text{Al}_2\text{O}_3(0001)$.¹⁰⁵ This is an interesting choice of substrate because it exhibits a wide bandgap of 8.8 eV (Ref. 106) and the Dirac point of a silicene ad-layer is predicted to lie just in the middle of this gap.¹⁰⁷ Furthermore, theoretical calculations show that silicene on $\text{Al}_2\text{O}_3(0001)$ has a low-buckled structure.¹⁰⁷ Two sets of samples were investigated. The first one had a variable thickness of the Si nanosheets ranging from 1.5 to 0.5 nm (VT), while the second one had a constant thickness of 0.5 nm (CT). The chemical status of as-grown Si nanosheets was characterized by *in situ* XPS experiments, whereas the thickness was measured by *ex-situ* AFM measurements after the samples had been capped with a 5 nm thick layer of amorphous Al_2O_3 in order to prevent air-induced oxidation [Fig. 11(a)]. By knowing the refraction index of the substrate and measuring the optical transmittance $T(\omega)$ of the samples, the authors eventually determined its optical conductivity $\sigma(\omega) = \sigma_1(\omega) + i\sigma_2(\omega)$ and observed a Dirac-like behavior in the infrared part of the conductivity spectra. Indeed, in the sample with a constant thickness of 0.5 nm (that is, a silicene monolayer) $\sigma_1(\omega)$ displays a behavior consistent with that predicted for a 2D layer of Si. The optical behavior of these samples is summarized in Figs. 11(b)–11(e). Notably, the absorption spectra show a peak at 1.4 eV in the infrared range, peak that then raises linearly around 3 eV up to the ultraviolet range. The same features are predicted by *ab initio* calculations for I and II interband transitions in free-standing silicene.^{108–110} More interestingly, the conductance is quantized and depends on the layer thickness, which is for instance a characteristic of 2D Dirac fermions in graphene and thus suggests that the deposited Si indeed grows in a 2D fashion. Although in the early times the excitement about silicene was mainly due to the possibility of realizing high-performance electrical devices, like field-effect transistors,⁵² the observation of Dirac-like optical conductivity might

trigger the interest toward a silicene-based photonics. Nonetheless, the Raman spectra of these samples feature only the mode related to 3D cubic silicon at 520.5 cm^{-1} [Fig. 11(f)].¹⁰⁵ Hence, the absence of a peak related to silicene, which should be at higher wavenumbers, around 540 cm^{-1} ,^{75,76} might in fact cast doubt on the successful synthesis of 2D silicene on $\text{Al}_2\text{O}_3(0001)$, which could be instead an ultrathin 3D silicon film. Therefore, a deeper characterization of the structural properties of the grown film, by means for instance of *in situ* “noncontact” atomic force microscopy (on uncapped samples) or a surface-sensitive diffraction technique, is highly desired.

D. Epitaxial graphene/SiC

As the passivation of SiC surfaces due to the epitaxial growth of graphene has been intensively studied,^{111–114} and the Dirac cone feature of silicene and germanene on graphene surface is predicted to be maintained,¹¹⁵ the G/SiC system may also be an adequate substrate to grow group-IV X-enes. This possibility has been theoretically studied by Matusalem and coworkers,¹¹⁶ where the slab method is used to simulate the SiC substrate covered by graphene and silicene/germanene/stanene as ad-layers. Using first-principles calculations, the authors demonstrated that C-terminated SiC (000-1) covered by graphene could be used as a substrate to epitaxially grow X-enes in general with a low-buckled structure. The interaction between the overlayer and substrate is indeed weak, leading to the maintenance of the Dirac cone feature, even if small gaps are opened (96 meV, 116 meV, and 146 meV for silicene, germanene, and stanene, respectively). The presence of Dirac cones calls for an investigation of the topological nature of the overlayers. Graphene affects the topological behavior present in the free-standing group IV X-enes. For silicene, which is the most strongly bound to graphene among the three, the interaction is strong enough to destroy the topological character of the system. For germanene, the charge transfer is really small toward

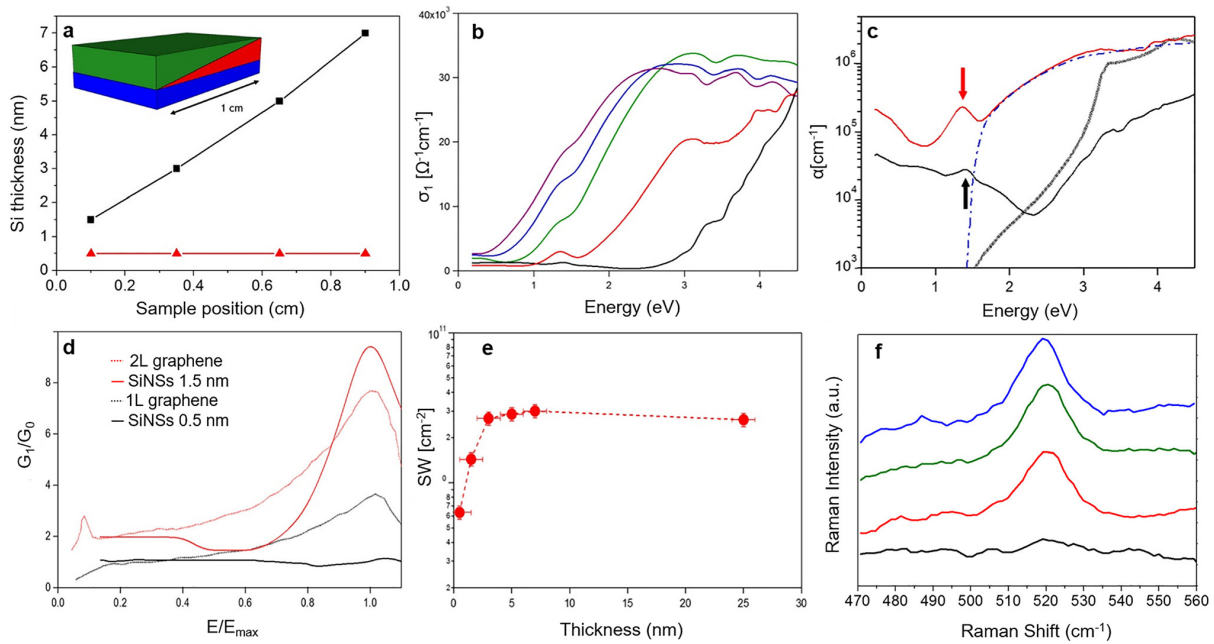


FIG. 11. (a) Si nanosheet thickness measured by AFM for the samples with variable (black dots) and constant (red triangles) nominal thickness, VT and CT, respectively. The inset displays the schematics of the Al_2O_3 -capped (green) VT sample showing the increasing silicon thickness (red) on the $\text{Al}_2\text{O}_3(0001)$ substrate (blue). (b) Real part of the optical conductivity $\sigma_1(\omega)$ for five Si thicknesses: 0.5 nm (black), 1.5 nm (red), 3 nm (green), 5 nm (blue), and 7 nm (purple). (c) The absorption coefficient $\alpha(\omega)$ for the 0.5 nm and 1.5 nm thick film (black and red curves), of the 25 nm-thick Si bulk reference (dashed-dotted blue line) and that of crystalline bulk silicon (dashed gray line). Black and red arrows point out the transition for 0.5 nm and 1.5 nm, respectively. (d) Real part of the optical conductance $G_1(\omega)$ normalized to the universal optical conductance G_0 for the 0.5 nm (black line) and 1.5 nm (red line) thickness Si nanosheets compared with single and two layers of graphene. (e) Optical spectral weight for the five thicknesses in (b) and for the 25 nm-thick sample used as reference. (f) Raman spectra collected at various positions in the VT sample, showing the Raman mode of cubic Si at around 520 cm^{-1} . Reproduced with permission from Grazianetti *et al.*, *Nano Lett.* **18**, 7124 (2018). Copyright 2018 American Chemical Society.

graphene and therefore, the topological properties are maintained. For stanene instead, contradicting features are present;^{116,117} thus, the appearance of topological behavior is still not clear.

Experimentally, however, Sone *et al.*¹¹⁸ attempted to grow 2D silicon on graphene previously deposited on 6H-SiC (0001) but could not succeed even if various substrate temperatures were employed. Instead, they found nanometer-thick flower-like dendritic islands of silicon when it was deposited with the substrate being in the temperature range 290–420 K. Higher temperatures would instead lead to formation of featureless clusters [Figs. 12(a)–12(e)].

On the other hand, it could be interesting to investigate the possibility of intercalating Si/Ge/Sn under graphene grown on a SiC substrate, as recently proposed for Si with graphene/Ru.¹¹⁹ In this way, the corresponding X-ene would be protected from oxidation upon reaction with air by the graphene top layer. Few studies go toward this direction, but it is worth considering the study reported by Visikovskiy *et al.*,¹²⁰ where interface modifications due to the successful intercalation of Si atoms between graphene and the underneath SiC substrate were indeed shown [Figs. 12(f)–12(h)]. Along the same line, Si/Ge/Sn could be intercalated under other 2D materials rather than graphene, as it was recently demonstrated for the case of Si intercalated under hexagonal boron nitride grown on ZrB_2 .¹²¹ From an electronic structure perspective, no indication of interaction between the silicene layer

and the hexagonal boron nitride coating was observed, and silicene was protected from oxidation upon exposure to air for a period of time of at least 1 h.

IV. ADDITIONAL SYNTHESIS ROUTES BEYOND EPITAXY

An alternative strategy for obtaining group-IV X-enes not necessarily deposited on metal surfaces is through modification of X-enes-based composites. Notable examples of such composites are the layered Zintl phases such as calcium disilicide (CaSi_2)¹²² and germanide (CaGe_2).⁵⁴

CaSi_2 consists of a puckered Si layer intercalated by Ca layers (Fig. 13). ARPES maps of CaSi_2 show a massless Dirac-cone at the k-point in the Brillouin zone, which is however very far from the Fermi level due to charge transfer to the Si layer from the Ca counterions.¹²² This strong effect of the external environment (i.e., the presence of the Ca layers) does not allow studying the intrinsic silicene properties, not so different from the case of silicene grown on metals. Therefore, to reduce the electrostatic interaction between Si and Ca layers, Yaokawa *et al.* intercalated F ions into the system in order to form ionic bonds between Ca and F.¹²³ Through this process, the authors obtained patches of bilayer silicene structures with a 2D

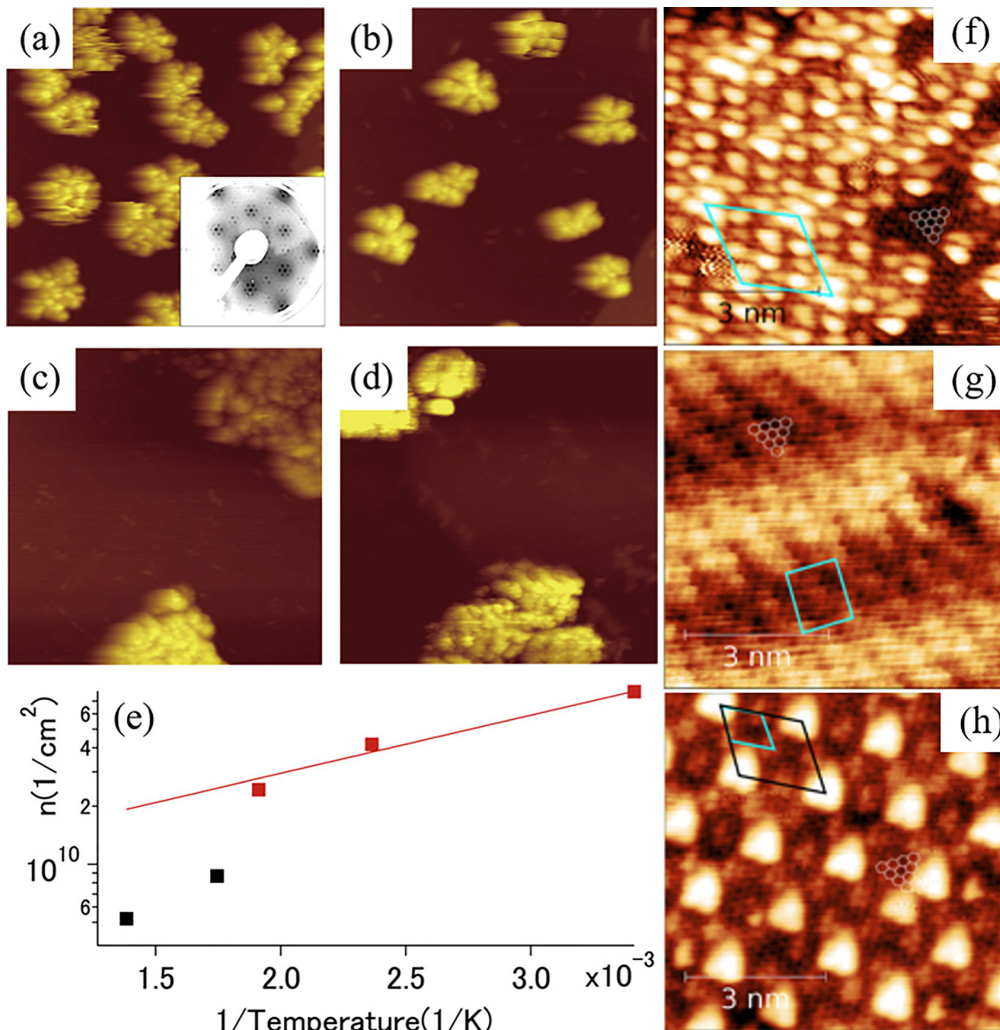


FIG. 12. STM images of the graphene surface after depositing 0.9 ML of Si at (a) 290, (b) 420, (c) 570, and (d) 720 K. The image size is $120 \times 120 \text{ nm}^2$ ($V = 2.0 \text{ V}$ and $I = 0.1 \text{ nA}$). The inset in (a) is the corresponding low energy electron diffraction pattern, taken with an incident electron energy of 140 eV. (e) Temperature dependence of the Si island density during the 0.9 ML Si deposition. The solid line is the fitting of the statistically meaningful data at 290, 420, and 520 K. (f)–(h) STM images of Si-intercalated structures under graphene on SiC(0001) interfaces: (f) hexagonal 2×2 interface, (g) rectangular $(2,3 \times 4)$ and (h) (3×3) interface. Panels (a)–(e) reproduced with permission from Sone *et al.*, Jpn. J. Appl. Phys. **55**, 035502 (2016). Copyright 2016 The Japan Society of Applied Physics. Panels (f)–(h) reproduced with permission from Visikovskiy *et al.*, Phys. Rev. B **94**, 245421 (2016). Copyright 2016 American Physical Society.

translation symmetry and a wavy morphology, where Si atoms show tetrahedral coordination.

In a different study, Chen *et al.*⁵⁴ used a two-step process to obtain germanene from CaGe_2 . First, CaGe_2 is turned into bulk germanene (i.e., hydrogenated germanene) following the topotactic deintercalation method in which H atoms replace Ca atoms, according to the chemical reaction $\text{CaGe}_2 + 2\text{HCl} \rightarrow 2\text{GeH} + \text{CaCl}_2$.¹²⁴ In the second step, germanene flakes are mechanically exfoliated onto SiO_2 slabs and then turned into germanene by thermal annealing. Interestingly, while the germanene flakes show high resistance (sheet resistance

above $10 \text{ M}\Omega$ at room temperature), the annealed germanene has a resistivity of $\sim 10^{-7} \Omega\text{m}$, which is orders of magnitude lower than any other allotrope of Ge. More interestingly, in the magneto transport measurements, the authors also observe evidence of weak antilocalization at low temperature and low magnetic fields, as the result of the strong spin–orbit coupling expected in germanene.

V. OUTLOOK AND CONCLUSIONS

Silicene, germanene, and stanene are examples of synthetic elemental 2D materials,¹²⁵ meaning that there are no bulk analogs from

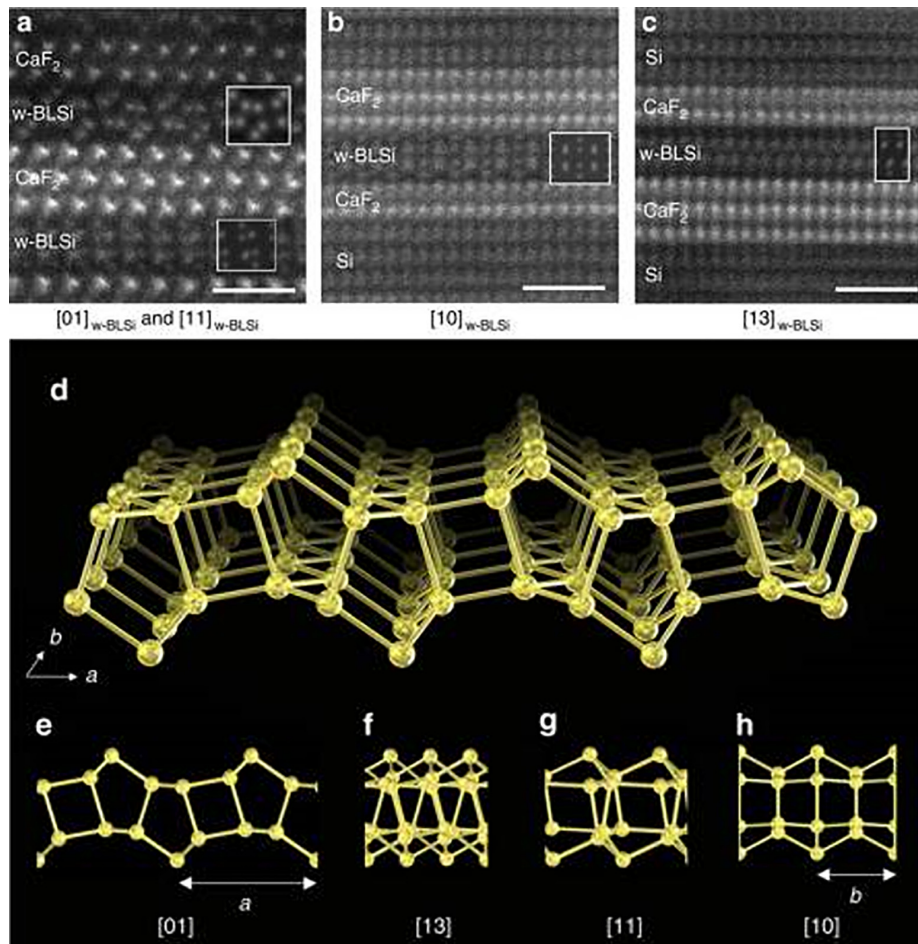


FIG. 13. (a)–(c) Experimental (main panels) and simulated (insets) high-angle annular dark field scanning transmission electron micrographs of the bilayer silicene structure, denoted as w-BLSi. (a) The $[01]_{w-BLSi}$ and $[11]_{w-BLSi}$ incident directions ($[1-10]_{CaF_2}$). (b) the $[10]_{w-BLSi}$ and $[11-2]_{Si}$ and CaF_2 directions and (c) the $[13]_{w-BLSi}$ and $[11-2]_{Si}$ and CaF_2 directions. (d) Schematic illustration of the w-BLSi atomic structure. (e)–(h) Schematic structures projected in each direction along $[01]$, $[13]$, $[11]$, and $[10]$ directions respectively in (e), (f), (g), and (h). All scale bars 1 nm. Reproduced with permission from Yaokawa, *et al.*, Nat. Commun. 7, 10657 (2016). Licensed under a Creative Commons Attribution (CC-BY_4.0) license.

which they can be derived. Instead, they need to be synthesized via physical and/or chemical processes that often require highly technical skills and costly, specialized instrumentations. As a consequence, the rate of progress in these materials is much slower than that of other 2D materials, which can be instead exfoliated from layered bulk systems, like for instance graphene (from graphite), transition metal dichalcogenides, and hexagonal boron nitride. Furthermore, the investigation of their intrinsic electronic properties, crucial for further advancing the field, is hampered by the metals that are usually used as growth substrates, since they (i) strongly interact with the 2D ad-layer, and (ii) do not allow for direct integration in electronic devices. Besides, it is not trivial to exclude formation of surface alloys between Si/Ge/Sn and a given metal substrate, which has even led to doubt the formation of silicene and germanene on metals.^{126–131}

In this context, successfully synthesizing these 2D materials on “nonmetals” would therefore represent a certain breakthrough in the field because these substrates are supposed to interact only weakly with the 2D ad-layer, hence preserving its intrinsic electronic properties. Therefore, in this review we have focused on the synthesis and characterization of silicene, germanene, and stanene on such materials.

The first class of possible nonmetal substrate candidates that we have considered is layered materials, such as MoS_2 , HOPG, Bi_2Te_3 , InSe, PbTe, and graphene because of their hexagonal symmetry and lack of dangling bonds. They are ideal substrates for van der Waals epitaxy,^{55–58} moreover, MoS_2 , Bi_2Te_3 and InSe, being semiconductors, would enable direct fabrication of electronic devices. However, we also pointed out that the layered structure of this type of substrates can in

fact be a serious problem, as the deposited Si/Ge/Sn atoms may diffuse below the topmost layer(s) of the substrate and intercalate, thus making the interpretation of the results extremely difficult. On the other hand, intercalation of Si, Ge, or Sn and possibly the consequent formation of silicene, germanene, or stanene under another layered material could actually represent an interesting opportunity worth investigating. Indeed, being formed under a coating layer, the X-enes could be effectively protected from degradation in air, as Ref. 76 reports for the case of silicene intercalated under the topmost graphitic layer of HOPG. This growth process somewhat recalls the migration-enhanced encapsulated growth technique that allowed stabilizing 2D GaN under a graphene layer.¹³²

Another insulating substrate that we have discussed is calcium difluoride. It forms with silicene an almost lattice-matched system and does not affect silicene's Dirac cone; however, no experimental study has been reported yet.

The last class of substrates that we have considered is oxides. Indeed, owing to their large band gaps, they might be ideal substrates as they would enable direct fabrication of electronic devices. As of today, however, very few studies have focused on this class of substrates and only preliminary results have been reported. Particularly fascinating is the possible observation of quantized optical conductance depending on the thickness for silicon deposited on Al₂O₃(0001). Yet, as we commented on the text, conclusive and decisive proofs of successful growth are still unavailable.

Finally, we have also presented an alternative route to epitaxy on solid surfaces. It consists instead of chemical modification of X-ene-based composites, and we have reported examples of synthesis of silicene and germanene.

In conclusion, as we show in this review, it is clear that the topic is still in a truly early stage. Some experimental studies have been reported, and although they show somewhat similar observations, the interpretation is often very different and the consequent debate is still unsettled. Therefore, more efforts need to be devoted to realizing X-enes on non-metal substrates with higher structural quality, and on a larger scale.

ACKNOWLEDGMENTS

L.C. and M.G. acknowledge funding by the Young Investigator Program of Villum Fonden, Project No. 19130. M.D.C. acknowledges the European Community for the Horizon 2020 MSC-RISE Project DisetCom (No. GA823728).

REFERENCES

- ¹K. S. Novoselov, A. K. Geim, S. V. Morozov, D. Jiang, Y. Zhang, S. V. Dubonos, I. V. Grigorieva, and A. A. Firsov, *Science* **306**, 666 (2004).
- ²A. K. Geim and K. S. Novoselov, *Nat. Mater.* **6**, 183 (2007).
- ³A. H. Castro Neto, F. Guinea, N. M. R. Peres, K. S. Novoselov, and A. K. Geim, *Rev. Mod. Phys.* **81**, 109 (2009).
- ⁴F. Schwierz, *Nat. Nanotechnol.* **5**, 487 (2010).
- ⁵S. Cahangirov, M. Topsakal, E. Aktürk, H. Şahin, and S. Ciraci, *Phys. Rev. Lett.* **102**, 236804 (2009).
- ⁶B. Feng, Z. Ding, S. Meng, Y. Yao, X. He, P. Cheng, L. Chen, and K. Wu, *Nano Lett.* **12**, 3507 (2012).
- ⁷M. E. Dávila, L. C. Lew Yan Voon, J. Zhao, and G. Le Lay, *Semicond. Semimetals* **95**, 149 (2016).
- ⁸L. Zhang, P. Bampoulis, A. N. Rudenko, Q. Yao, A. Van Houselt, B. Poelsema, M. I. Katsnelson, and H. J. W. Zandvliet, *Phys. Rev. Lett.* **116**, 256804 (2016).
- ⁹F. Zhu, W. Chen, Y. Xu, C. Gao, D. Guan, C. Liu, D. Qian, S.-C. Zhang, and J. Jia, *Nat. Mater.* **14**, 1020 (2015).
- ¹⁰P. Tang, P. Chen, W. Cao, H. Huang, S. Cahangirov, L. Xian, Y. Xu, S. C. Zhang, W. Duan, and A. Rubio, *Phys. Rev. B: Condens. Matter Mater. Phys.* **90**, 1 (2014).
- ¹¹M. E. Dávila, L. Xian, S. Cahangirov, A. Rubio, and G. Le Lay, *New J. Phys.* **16**, 095002 (2014).
- ¹²H. Oughaddou, H. Enriquez, M. R. Tchalala, H. Yildirim, A. J. Mayne, A. Bendounan, G. Dujardin, M. Ait Ali, and A. Kara, *Prog. Surf. Sci.* **90**, 46 (2015).
- ¹³C. Grazianetti, E. Cinquanta, and A. Molle, *2D Mater.* **3**, 012001 (2016).
- ¹⁴M. Chhowalla, D. Jena, and H. Zhang, *Nat. Rev. Mater.* **1**, 16052 (2016).
- ¹⁵M. Houssa, A. Dimoulas, and A. Molle, *J. Phys. Condens. Matter* **27**, 253002 (2015).
- ¹⁶A. Acun, L. Zhang, P. Bampoulis, M. Farmanbar, A. van Houselt, A. N. Rudenko, M. Lingenfelder, G. Brocks, B. Poelsema, M. I. Katsnelson, and H. J. W. Zandvliet, *J. Phys. Condens. Matter* **27**, 443002 (2015).
- ¹⁷S. Balendhran, S. Walia, H. Nili, S. Sriram, and M. Bhaskaran, *Small* **11**, 640 (2015).
- ¹⁸J. H. Chen, C. Jang, S. Xiao, M. Ishigami, and M. S. Fuhrer, *Nat. Nanotechnol.* **3**, 206 (2008).
- ¹⁹M. Sotoodeh, A. H. Khalid, and A. A. Rezazadeh, *J. Appl. Phys.* **87**, 2890 (2000).
- ²⁰D. L. Rode, *Phys. Status Solidi* **53**, 245 (1972).
- ²¹F. P. Bundy, *Physica A* **156**, 169 (1989).
- ²²A. Molle, J. Goldberger, M. Houssa, Y. Xu, S. Zhang, and D. Akinwande, *Nat. Mater.* **16**, 163 (2017).
- ²³C. C. Liu, W. Feng, and Y. Yao, *Phys. Rev. Lett.* **107**, 076802 (2011).
- ²⁴B. Van Den Broek, M. Houssa, E. Scalise, G. Pourtois, V. V. Afanas'ev, and A. Stesmans, *2D Mater.* **1**, 021004 (2014).
- ²⁵M. Ezawa, *J. Phys. Soc. Jpn.* **81**, 104713 (2012).
- ²⁶M. Tahir, A. Manchon, K. Sabeeh, and U. Schwingenschlögl, *Appl. Phys. Lett.* **102**, 162412 (2013).
- ²⁷Y. Kim, K. Choi, J. Ihm, and H. Jin, *Phys. Rev. B: Condens. Matter Mater. Phys.* **89**, 085429 (2014).
- ²⁸W. F. Tsai, C. Y. Huang, T. R. Chang, H. Lin, H. T. Jeng, and A. Bansil, *Nat. Commun.* **4**, 1500 (2013).
- ²⁹L. C. Lew Yan Voon, J. Zhu, and U. Schwingenschlögl, *Appl. Phys. Rev.* **3**, 040802 (2016).
- ³⁰J. Deng, B. Xia, X. Ma, H. Chen, H. Shan, X. Zhai, B. Li, A. Zhao, Y. Xu, W. Duan, S.-C. Zhang, B. Wang, and J. G. Hou, *Nat. Mater.* **17**, 1081 (2018).
- ³¹H. Liu, J. Gao, and J. Zhao, *J. Phys. Chem. C* **117**, 10353 (2013).
- ³²R. Quhe, R. Fei, Q. Liu, J. Zheng, H. Li, C. Xu, Z. Ni, Y. Wang, D. Yu, Z. Gao, and J. Lu, *Sci. Rep.* **2**, 853 (2012).
- ³³P. De Padova, C. Quaresima, C. Ottaviani, P. M. Sheverdyayeva, P. Moras, C. Carbone, D. Topwal, B. Olivieri, A. Kara, H. Oughaddou, B. Aufray, and G. Le Lay, *Appl. Phys. Lett.* **96**, 1 (2010).
- ³⁴S. Cahangirov, M. Topsakal, and S. Ciraci, *Phys. Rev. B: Condens. Matter Mater. Phys.* **81**, 1 (2010).
- ³⁵P. De Padova, P. Perfetti, B. Olivieri, C. Quaresima, C. Ottaviani, and G. Le Lay, *J. Phys.: Condens. Matter* **24**, 223001 (2012).
- ³⁶P. Vogt, P. De Padova, C. Quaresima, J. Avila, E. Frantzeskakis, M. C. Asensio, A. Resta, B. Ealet, and G. Le Lay, *Phys. Rev. Lett.* **108**, 155501 (2012).
- ³⁷D. Chiappe, C. Grazianetti, G. Tallarida, M. Fanciulli, and A. Molle, *Adv. Mater.* **24**, 5088 (2012).
- ³⁸H. Enriquez, S. Vizzini, A. Kara, B. Lalmi, and H. Oughaddou, *J. Phys.: Condens. Matter* **24**, 314211 (2012).
- ³⁹L. Huang, Y.-F. Zhang, Y.-Y. Zhang, W. Xu, Y. Que, E. Li, J.-B. Pan, Y.-L. Wang, Y. Liu, S.-X. Du, S. T. Pantelides, and H.-J. Gao, *Nano Lett.* **17**, 1161 (2017).
- ⁴⁰L. Meng, Y. Wang, L. Zhang, S. Du, R. Wu, L. Li, Y. Zhang, G. Li, H. Zhou, W. A. Hofer, and H.-J. Gao, *Nano Lett.* **13**, 685 (2013).
- ⁴¹A. Fleurence, R. Friedlein, T. Ozaki, H. Kawai, Y. Wang, and Y. Yamada-Takamura, *Phys. Rev. Lett.* **108**, 5501 (2012).
- ⁴²C. Lee, A. Fleurence, Y. Yamada-Takamura, T. Ozaki, and R. Friedlein, *Phys. Rev. B: Condens. Matter Mater. Phys.* **90**, 5422 (2014).
- ⁴³H. Oughaddou, S. Sawaya, J. Goniakowski, B. Aufray, G. Le Lay, G. Le Lay, J. M. Gay, G. Trégliat, J. P. Bibérian, N. Barrett, C. Guillot, A. Mayne, and G. Dujardin, *Phys. Rev. B: Condens. Matter Mater. Phys.* **62**, 16653 (2000).

- ⁴⁴M. E. Dávila, L. Xian, S. Cahangirov, A. Rubio, and G. Le Lay, *New J. Phys.* **16**, 095002 (2014).
- ⁴⁵L. Li, S. Z. Lu, J. Pan, Z. Qin, Y. Q. Wang, Y. Wang, G. Y. Cao, S. Du, and H. J. Gao, *Adv. Mater.* **26**, 4820 (2014).
- ⁴⁶M. Derivaz, D. Dentel, R. Stephan, M.-C. Hanf, A. Mehdaoui, P. Sonnet, and C. Pirri, *Nano Lett.* **15**, 2510 (2015).
- ⁴⁷J. Gou, Q. Zhong, S. Sheng, W. Li, P. Cheng, H. Li, L. Chen, and K. Wu, *2D Mater.* **3**, 045005 (2016).
- ⁴⁸J. Yuhara, Y. Fujii, K. Nishino, N. Isobe, M. Nakatake, L. Xian, A. Rubio, and G. Le Lay, *2D Mater.* **5**, 025002 (2018).
- ⁴⁹Y. Wang, J. Li, J. Xiong, Y. Pan, M. Ye, Y. Guo, H. Zhang, R. Quhe, and J. Lu, *Phys. Chem. Chem. Phys.* **18**, 19451 (2016).
- ⁵⁰P. Pflugradt, L. Matthes, and F. Bechstedt, *New J. Phys.* **16**, 075004 (2014).
- ⁵¹A. Podsiadly-Paszowska and M. Krawiec, *Phys. Chem. Chem. Phys.* **17**, 2246 (2015).
- ⁵²L. Tao, E. Cinquanta, D. Chiappe, C. Grazianetti, M. Fanciulli, M. Dubey, A. Molle, and D. Akinwande, *Nat. Nanotechnol.* **10**, 227 (2015).
- ⁵³C. Grazianetti, E. Cinquanta, L. Tao, P. De Padova, C. Quaresima, C. Ottaviani, D. Akinwande, and A. Molle, *ACS Nano* **11**, 3376 (2017).
- ⁵⁴Q. Chen, L. Liang, G. Potsi, P. Wan, J. Lu, T. Giousis, E. Thomou, D. Gournis, P. Rudolf, and J. Ye, *Nano Lett.* **19**, 1520 (2019).
- ⁵⁵A. Koma, *Thin Solid Films* **216**, 72 (1992).
- ⁵⁶L. A. Walsh and C. L. Hinkle, *Appl. Mater. Today* **9**, 504 (2017).
- ⁵⁷A. Koma, K. Sunouchi, and T. Miyajima, *Microelectron. Eng.* **2**, 129 (1984).
- ⁵⁸A. Koma, *J. Vac. Sci. Technol. B: Microelectron. Nanometer Struct.* **3**, 724 (2002).
- ⁵⁹D. Chiappe, E. Scalise, E. Cinquanta, C. Grazianetti, B. van den Broek, M. Fanciulli, M. Houssa, and A. Molle, *Adv. Mater.* **26**, 2096 (2014).
- ⁶⁰D. Jarivala, V. K. Sangwan, L. J. Lauhon, T. J. Marks, and M. C. Hersam, *ACS Nano* **8**, 1102 (2014).
- ⁶¹O. V. Yazyev and A. Kis, *Mater. Today* **18**, 20 (2015).
- ⁶²M. Houssa, G. Pourtois, V. V. Afanas'Ev, and A. Stesmans, *Appl. Phys. Lett.* **97**, 112106 (2010).
- ⁶³S. Kokott, P. Pflugradt, L. Matthes, and F. Bechstedt, *J. Phys.: Condens. Matter* **26**, 185002 (2014).
- ⁶⁴A. Molle, A. Lamperti, D. Rotta, M. Fanciulli, E. Cinquanta, and C. Grazianetti, *Adv. Mater. Interfaces* **3**, 1500619 (2016).
- ⁶⁵R. van Bremen, Q. Yao, S. Banerjee, D. Cakir, N. Oncel, and H. J. W. Zandvliet, *Beilstein J. Nanotechnol.* **8**, 1952 (2017).
- ⁶⁶R. Addou, L. Colombo, and R. M. Wallace, *ACS Appl. Mater. Interfaces* **7**, 11921 (2015).
- ⁶⁷P. Vancsó, G. Z. Magda, J. Peto, J. Y. Noh, Y. S. Kim, C. Hwang, L. P. Biró, and L. Tapasztó, *Sci. Rep.* **6**, 1 (2016).
- ⁶⁸D. H. Lee, J. Yi, J. M. Lee, S. J. Lee, Y. J. Doh, H. Y. Jeong, Z. Lee, U. Paik, J. A. Rogers, and W. Il Park, *ACS Nano* **7**, 301 (2013).
- ⁶⁹M. De Crescenzi, I. Berbezier, M. Scarselli, P. Castrucci, M. Abbarchi, A. Ronda, F. Jaldali, J. Park, and H. Vach, *ACS Nano* **10**, 11163 (2016).
- ⁷⁰Y. Ding and J. Ni, *Appl. Phys. Lett.* **95**, 083115 (2009).
- ⁷¹L. Persichetti, F. Jaldali, H. Vach, A. Sgarlata, I. Berbezier, M. De Crescenzi, and A. Balzarotti, *J. Phys. Chem. Lett.* **7**, 3246 (2016).
- ⁷²W. Peng, T. Xu, P. Diener, L. Biadala, M. Berthe, X. Pi, Y. Borensztein, A. Curcella, R. Bernard, G. Prévot, and B. Grandier, *ACS Nano* **12**, 4754 (2018).
- ⁷³T. Kondo, Y. Iwasaki, Y. Honma, Y. Takagi, S. Okada, and J. Nakamura, *Phys. Rev. B: Condens. Matter Mater. Phys.* **80**, 2 (2009).
- ⁷⁴J. C. M. López, M. C. G. Passeggi, and J. Ferrón, *Surf. Sci.* **602**, 671 (2008).
- ⁷⁵P. Castrucci, F. Fabbri, T. Delise, M. Scarselli, M. Salvato, S. Pascale, R. Francini, I. Berbezier, C. Lechner, F. Jaldali, H. Vach, and M. De Crescenzi, *Nano Res.* **11**, 5879 (2018).
- ⁷⁶I. Kupchak, F. Fabbri, M. De Crescenzi, M. Scarselli, M. Salvato, T. Delise, I. Berbezier, O. Pulci, and P. Castrucci, *Nanoscale* **11**, 6145 (2019).
- ⁷⁷G. Li, Y. Zhang, H.-J. Gao, M. Ouyang, H. Zhou, L. Huang, W. Xu, A. C. Ferrari, S. Du, and L. Pan, *J. Am. Chem. Soc.* **137**, 7099 (2015).
- ⁷⁸A. Ferrari and D. Basko, *Nat. Nanotechnol.* **8**, 235 (2013).
- ⁷⁹A. O. T. Osaka, H. Omi, and K. Yamamoto, *Phys. Rev. B* **50**, 7567 (1994).
- ⁸⁰C.-Z. Xu, Y.-H. Chan, P. Chen, X. Wang, D. Flóttotto, J. A. Hlevyack, G. Bian, S.-K. Mo, M.-Y. Chou, and T.-C. Chiang, *Phys. Rev. B* **97**, 035122 (2018).
- ⁸¹B. Y. Yavorsky, N. F. Hinsche, I. Mertig, and P. Zahn, *Phys. Rev. B: Condens. Matter Mater. Phys.* **84**, 165208 (2011).
- ⁸²S. C. Wu, G. Shan, and B. Yan, *Phys. Rev. Lett.* **113**, 1 (2014).
- ⁸³Y. Xu, B. Yan, H. J. Zhang, J. Wang, G. Xu, P. Tang, W. Duan, and S. C. Zhang, *Phys. Rev. Lett.* **111**, 1 (2013).
- ⁸⁴M. Liao, Y. Zang, Z. Guan, H. Li, Y. Gong, K. Zhu, X. P. Hu, D. Zhang, Y. Xu, Y. Y. Wang, K. He, X. C. Ma, S. C. Zhang, and Q. K. Xue, *Nat. Phys.* **14**, 344 (2018).
- ⁸⁵W. Chang, S. M. Albrecht, T. S. Jespersen, F. Kuemmeth, P. Krogstrup, J. Nygård, and C. M. Marcus, *Nat. Nanotechnol.* **10**, 232 (2015).
- ⁸⁶Y. Saito, T. Nojima, and Y. Iwasa, *Nat. Rev. Mater.* **2**, 16094 (2017).
- ⁸⁷C. Brun, T. Cren, D. Roditchev, C. Brun, T. Cren, and D. Roditchev, *Supercond. Sci. Technol.* **30**, 013003 (2017).
- ⁸⁸Y. Zang, T. Jiang, Y. Gong, Z. Guan, C. Liu, M. Liao, K. Zhu, Z. Li, L. Wang, W. Li, C. Song, D. Zhang, Y. Xu, K. He, X. Ma, S. C. Zhang, and Q. K. Xue, *Adv. Funct. Mater.* **28**, 1802723 (2018).
- ⁸⁹B. H. Chou, Z. Q. Huang, C. H. Hsu, F. C. Chuang, Y. T. Liu, H. Lin, and A. Bansil, *New J. Phys.* **16**, 115008 (2014).
- ⁹⁰Y. Xu, P. Tang, and S. C. Zhang, *Phys. Rev. B: Condens. Matter Mater. Phys.* **92**, 081112 (2015).
- ⁹¹J. Camassel, P. Merle, H. Mathieu, and A. Chevy, *Phys. Rev. B* **17**, 4718 (1978).
- ⁹²A. R. Goi, A. Cantarero, U. Schwarz, K. Syassen, and A. Chevy, *Phys. Rev. B* **45**, 4221 (1992).
- ⁹³Y. Fan, X. Liu, J. Wang, H. Ai, and M. Zhao, *Phys. Chem. Chem. Phys.* **20**, 11369 (2018).
- ⁹⁴G. W. Mudd, S. A. Svatek, T. Ren, A. Patané, O. Makarovskiy, L. Eaves, P. H. Beton, Z. D. Kovalyuk, G. V. Lashkarev, Z. R. Kudrynskiy, and A. I. Dmitriev, *Adv. Mater.* **25**, 5714 (2013).
- ⁹⁵S. Klumpp and H. Dabringhaus, *Surf. Sci.* **417**, 323 (1998).
- ⁹⁶L. N. Patro and K. Hariharan, *Solid State Ionics* **239**, 41 (2013).
- ⁹⁷Y. Foucaud, M. Badawi, L. O. Filippov, I. V. Filippova, and S. Lebègue, *J. Phys. Chem. B* **122**, 6829 (2018).
- ⁹⁸G. Jordan and W. Rammensee, *Surf. Sci.* **371**, 371 (1997).
- ⁹⁹N. H. De Leeuw, J. A. Purton, S. C. Parker, G. W. Watson, and G. Kresse, *Surf. Sci.* **452**, 9 (2000).
- ¹⁰⁰P. W. Tasker, *J. Phys. C Solid State Phys.* **12**, 4977 (1979).
- ¹⁰¹K. Ueda, A. Takano, X. Yong-nian, Z. Kai-ming, and X. Xi, *Jpn. J. Appl. Phys.* **2**, 134 (1989).
- ¹⁰²X. B. Lu, X. Zhang, R. Huang, H. B. Lu, Z. H. Chen, W. F. Xiang, M. He, B. L. Cheng, H. W. Zhou, X. P. Wang, C. Z. Wang, and B. Y. Nguyen, *Appl. Phys. Lett.* **84**, 2620 (2004).
- ¹⁰³C. Ben Azzouz, A. Akremi, M. Derivaz, J. L. Bischoff, M. Zanouni, and D. Dentel, *J. Phys. Conf. Ser.* **491**, 012003 (2014).
- ¹⁰⁴K. B. Jinesh, Y. Lamy, R. A. M. Wolters, J. H. Klootwijk, E. Tois, F. Roozeboom, and W. F. A. Besling, *Appl. Phys. Lett.* **93**, 192912 (2008).
- ¹⁰⁵C. Grazianetti, S. De Rosa, C. Martella, P. Targa, D. Codegani, P. Gori, O. Pulci, A. Molle, and S. Lupi, *Nano Lett.* **18**, 7124 (2018).
- ¹⁰⁶R. H. French, *J. Am. Ceram. Soc.* **73**, 477 (1990).
- ¹⁰⁷M. X. Chen, Z. Zhong, and M. Weinert, *Phys. Rev. B* **94**, 5409 (2016).
- ¹⁰⁸L. Matthes, O. Pulci, and F. Bechstedt, *New J. Phys.* **16**, 105007 (2014).
- ¹⁰⁹F. Bechstedt, L. Matthes, P. Gori, and O. Pulci, *Appl. Phys. Lett.* **100**, 2010 (2012).
- ¹¹⁰L. Matthes, P. Gori, O. Pulci, and F. Bechstedt, *Phys. Rev. B: Condens. Matter Mater. Phys.* **87**, 5438 (2013).
- ¹¹¹D. Mayou, T. Li, J. Hass, A. N. Marchenkov, E. H. Conrad, P. N. First, W. A. De Heer, C. Berger, X. Wu, N. Brown, C. Naud, X. Li, Z. Song, D. Mayou, T. Li, J. Hass, A. N. Marchenkov, E. H. Conrad, P. N. First, and W. A. De Heer, *Science* **312**, 1191 (2006).
- ¹¹²K. V. Emtsev, A. Bostwick, K. Horn, J. Jobst, G. L. Kellogg, L. Ley, J. L. McChesney, T. Ohta, S. A. Reshanov, J. Röhrl, E. Rotenberg, A. K. Schmid, D. Waldmann, H. B. Weber, and T. Seyller, *Nat. Mater.* **8**, 203 (2009).
- ¹¹³Y. Qi, S. H. Rhim, G. F. Sun, M. Weinert, and L. Li, *Phys. Rev. Lett.* **105**, 085502 (2010).

- ¹¹⁴J. Sforzini, L. Nemeč, T. Denig, B. Stadtmüller, T. L. Lee, C. Kumpf, S. Soubatch, U. Starke, P. Rinke, V. Blum, F. C. Bocquet, and F. S. Tautz, *Phys. Rev. Lett.* **114**, 106804 (2015).
- ¹¹⁵Y. Cai, C. P. Chuu, C. M. Wei, and M. Y. Chou, *Phys. Rev. B: Condens. Matter Mater. Phys.* **88**, 245408 (2013).
- ¹¹⁶F. Matusalem, D. S. Koda, F. Bechstedt, M. Marques, and L. K. Teles, *Sci. Rep.* **7**, 15700 (2017).
- ¹¹⁷R. Yu, X. L. Qi, A. Bernevig, Z. Fang, and X. Dai, *Phys. Rev. B: Condens. Matter Mater. Phys.* **84**, 075119 (2011).
- ¹¹⁸J. Sone, T. Yamagami, K. Nakatsuji, and H. Hirayama, *Jpn. J. Appl. Phys.* **55**, 035502 (2016).
- ¹¹⁹G. Li, L. Zhang, W. Xu, J. Pan, S. Song, Y. Zhang, H. Zhou, Y. Wang, L. Bao, Y.-Y. Zhang, S. Du, M. Ouyang, S. T. Pantelides, and H.-J. Gao, *Adv. Mater.* **30**, 1804650 (2018).
- ¹²⁰A. Visikovskiy, S. I. Kimoto, T. Kajiwara, M. Yoshimura, T. Iimori, F. Komori, and S. Tanaka, *Phys. Rev. B* **94**, 245421 (2016).
- ¹²¹F. B. Wiggers, A. Fleurence, K. Aoyagi, T. Yonezawa, Y. Yamada-Takamura, H. Feng, J. Zhuang, Y. Du, A. Y. Kovalgin, and M. P. de Jong, *2D Mater.* **6**, 035001 (2019).
- ¹²²E. Noguchi, K. Sugawara, R. Yaokawa, T. Hitosugi, H. Nakano, and T. Takahashi, *Adv. Mater.* **27**, 856 (2015).
- ¹²³R. Yaokawa, T. Ohsuna, T. Morishita, Y. Hayasaka, M. J. S. Spencer, and H. Nakano, *Nat. Commun.* **7**, 10657 (2016).
- ¹²⁴B. N. Madhushankar, A. Kaverzin, T. Giousis, G. Potsi, D. Gournis, P. Rudolf, G. R. Blake, C. H. Van Der Wal, and B. J. Van Wees, *2D Mater.* **4**, 021009 (2017).
- ¹²⁵A. J. Mannix, B. Kiraly, M. C. Hersam, and N. P. Guisinger, *Nat. Rev. Chem.* **1**, 0014 (2017).
- ¹²⁶M. Satta, P. Lacovig, N. Apostol, M. Dalmiglio, F. Orlando, L. Bignardi, H. Bana, E. Travaglia, A. Baraldi, S. Lizzit, and R. Laricprete, *Nanoscale* **10**, 7085 (2018).
- ¹²⁷G. Prévot, R. Bernard, H. Cruguel, A. Curcella, M. Lazzari, T. Leoni, L. Masson, A. Ranguis, and Y. Borenstein, *Phys. Status Solidi* **253**, 206 (2016).
- ¹²⁸T. Shirai, T. Shirasawa, T. Hirahara, N. Fukui, T. Takahashi, and S. Hasegawa, *Phys. Rev. B* **89**, 241403 (2014).
- ¹²⁹Y. Borenstein, A. Curcella, S. Royer, and G. Prévot, *Phys. Rev. B* **92**, 155407 (2015).
- ¹³⁰G. Prévot, R. Bernard, H. Cruguel, and Y. Borenstein, *Appl. Phys. Lett.* **105**, 3106 (2014).
- ¹³¹C. S. Ho, S. Banerjee, M. Batzill, D. E. Beck, and B. E. Koel, *Surf. Sci.* **603**, 1161 (2009).
- ¹³²Z. Y. Al Balushi, K. Wang, R. K. Ghosh, R. A. Vilá, S. M. Eichfeld, J. D. Caldwell, X. Qin, Y. C. Lin, P. A. Desario, G. Stone, S. Subramanian, D. F. Paul, R. M. Wallace, S. Datta, J. M. Redwing, and J. A. Robinson, *Nat. Mater.* **15**, 1166 (2016).

Paper II

M. Galbiati, L. Persichetti, P. Gori, O. Pulci, M. Bianchi,
L. Di Gaspare, J. Tersoff, C. Coletti, P. Hofmann, M. De
Seta, and L. Camilli.

**Tuning the Doping of Epitaxial Graphene on a
Conventional Semiconductor via Substrate Surface
Reconstruction.** *Journal of Physical Chemistry Letters*,

12, 1262-1267 (2021)

Tuning the Doping of Epitaxial Graphene on a Conventional Semiconductor via Substrate Surface Reconstruction

Miriam Galbiati, Luca Persichetti,* Paola Gori,* Olivia Pulci, Marco Bianchi, Luciana Di Gaspare, Jerry Tersoff, Camilla Coletti, Philip Hofmann, Monica De Seta, and Luca Camilli*



Cite This: *J. Phys. Chem. Lett.* 2021, 12, 1262–1267



Read Online

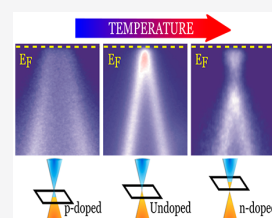
ACCESS |

Metrics & More

Article Recommendations

Supporting Information

ABSTRACT: Combining scanning tunneling microscopy and angle-resolved photoemission spectroscopy, we demonstrate how to tune the doping of epitaxial graphene from *p* to *n* by exploiting the structural changes that occur spontaneously on the Ge surface upon thermal annealing. Furthermore, using first-principle calculations, we build a model that successfully reproduces the experimental observations. Since the ability to modify graphene electronic properties is of fundamental importance when it comes to applications, our results provide an important contribution toward the integration of graphene with conventional semiconductors.



Integrating graphene into conventional semiconductor technology is expected to pave the way for the realization of novel device architectures with compelling properties.^{1–3} The first experimental demonstrations of such devices include infrared image sensor arrays,⁴ radio frequency gas sensors,⁵ and vertical transistors for ultrahigh frequency operations.⁶ However, unlocking the true potential of these novel architectures is possible only if complete control of the full integration process is achieved. To this end, it is essential to understand the structural and electronic properties of the combined graphene/semiconductor substrate system.

Among conventional semiconductors of technological relevance, germanium (Ge) is unique as a substrate for growth of monolayer graphene.⁷ It has sufficient catalytic activity with respect to the precursor gas, without a disruptive chemical affinity for carbon (in contrast to Si). Consequently, the graphene/Ge system has recently attracted a great deal of interest both in materials science^{8–11} and device physics.^{12–14} Previous work has demonstrated that the Ge(001) surface forms high-index facets upon graphene synthesis, making the system unsuitable for further processing.^{12,15,16} In contrast, such faceting does not occur for the Ge(110) surface,^{17,18} which can support growth of single-crystal graphene on wafer scale.^{7,19–22}

At present, the understanding of the graphene/Ge(110) interface is largely limited to its morphology, while too little is known of the electronic properties. It has been reported that samples grown via chemical vapor deposition (CVD) feature a hydrogen-passivated Ge surface²³ (from now on, **phase α**), and that upon annealing in vacuum above 350 °C, this surface reconstructs into a novel (6×2) phase (**phase β**) after hydrogen desorption.^{23–25} It has also been shown that further in-vacuum annealing to temperatures closer to the Ge melting point leads to additional structural modifications of the Ge

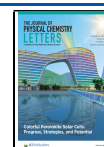
surface and possibly to the formation of stronger bonds between graphene and Ge²⁵ (hereinafter, we refer to this phase obtained by post-growth high-temperature annealing as **phase γ**). Yet, despite such morphological studies, nothing is currently known about whether and how these structural changes affect the system's electronic properties. The reported scanning tunneling spectroscopy (STS) studies have not been conclusive,²⁶ perhaps because that technique provides very local information and tends to be mostly sensitive to states at low *k*. Moreover, STS spectra appear to be largely dominated by features coming from the Ge substrate in this system. Thus, in order to obtain information on the band structure of the whole system on a larger scale, we use angle-resolved photoemission spectroscopy (ARPES), which has been previously used to characterize phase γ ²⁷ as well as for a sample where the phase was not determined.²⁸ In addition, high-temperature annealing drives in Ge the formation of defects, such as vacancies, that are known to induce significant electronic modifications in the Ge substrate.^{29–32} As a result of the complex behavior and limited information, a compelling theoretical picture has not been developed yet. Earlier attempts to build models able to reproduce the experimental results required the presence of an extraordinary high dopant segregation.²⁷

To bridge this gap, we present here a combined scanning tunneling microscopy (STM) and ARPES study of all three graphene/Ge(110) phases mentioned above. The annealing

Received: December 11, 2020

Accepted: January 20, 2021

Published: January 26, 2021



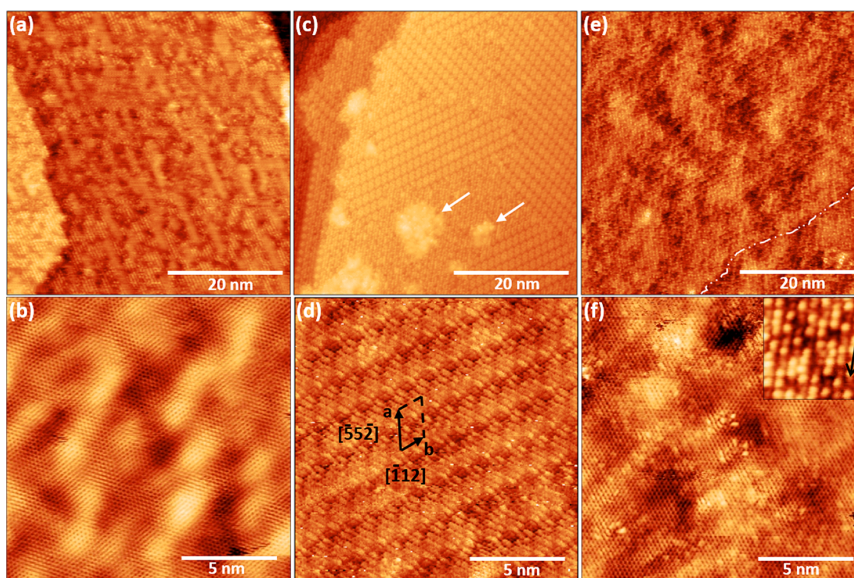


Figure 1. STM investigation of the graphene/Ge(110) interface for all the different phases. (a, b) STM images of phase α ($V = -1.0$ V and $I = 0.8$ nA in (a); $V = 0.4$ V and $I = 1.0$ nA in (b)). (c, d) STM images of phase β ($V = -1.5$ V and $I = 0.8$ nA in (c); $V = -1.5$ V and $I = 0.3$ nA in (d)). (c) Coexistence of phases α and β . (d) High magnification image of phase β . In black, a and b indicate the unit cell vectors. (e, f) STM images of phase γ ($V = -1.2$ V and $I = 0.8$ nA in (e); $V = -0.5$ V and $I = 0.8$ nA in (f)). Inset of (f): Atomic-resolution STM image showing the Ge substrate. The black arrow marks the $[-110]$ direction. Inset area is 5×5 nm² ($V = -1.2$ V and $I = 0.8$ nA). Figure S1 in the Supporting Information shows the fast fourier transform (FFT) of panel (b), (d), and (f).

processes induce structural changes in the interface, and we show that these in turn modify the interaction between graphene and Ge. In particular, these changes affect graphene doping, which is a crucial parameter for device applications. Furthermore, we build a model that, accounting for the presence of vacancies in Ge, successfully predicts the experimentally measured electronic properties of the system.

Figure 1 shows STM images of the three different phases of the graphene/Ge(110) interface, phases α , β , and γ . When the sample is in phase α , it is possible to observe the terraces and monatomic steps of the Ge substrate (Figure 1a). The graphene film appears to be rippled, but the graphene lattice can be clearly observed (Figure 1b). Upon annealing the sample above 350 °C in ultrahigh vacuum (UHV), the H–Ge bond is broken and the Ge surface reconstructs into phase β .²⁴ The size of the phase β areas depends on the duration of the annealing process. Therefore, phases α and β can coexist, as shown in the STM image reported in Figure 1c. The occasional protrusions in graphene, indicated by the arrows in Figure 1c, are nanobubbles formed by trapped hydrogen molecules that were formed upon rupture of the Ge–H bond.³³ It can be noticed that they are mainly located at the Ge step edges or at the edges between areas of different phases. The atomically resolved STM image in Figure 1d shows the unit cell of phase β and the corresponding lattice vectors ($a = 2.06$ nm and $b = 1.30$ nm). Low-energy electron diffraction (LEED), Figure S2, confirms the presence of the phase β , which gives rise to a moiré pattern around graphene's primary spots. Finally, Figures 1e and 1f report characteristic STM images of phase γ , i.e., after annealing the sample above 700 °C in UHV conditions. This surface does not show the long-range order characteristic of phase β anymore (Figure 1e). In fact, the Ge terraces appear to be rough, with the atomic steps being hardly recognizable. In Figure 1e, a step edge is highlighted by a dot-

dashed white line just to its right. The graphene lattice is still clearly visible (Figure 1f); however, when the tunneling bias is high enough, graphene becomes transparent and the Ge lattice underneath can be imaged (inset of Figure 1f and Figure S3). In particular, it is possible to observe that although the Ge atoms are overall aligned along the $[-110]$ direction (marked by black arrow in the inset), many of them appear to be displaced from their lattice site either in the in-plane or out-of-plane direction. Additionally, the presence of several defects, especially vacancies, can also be noticed.

In order to relate the above-mentioned morphological changes to the electronic structure of the graphene/Ge interface, we performed ARPES for the three different phases. The measured dispersion, shown as photoemission intensity as a function of binding energy and k , is given in Figure 2a–c, with the upper (lower) panels of the figures showing data collected perpendicular (parallel) to the Γ –K direction of the graphene Brillouin zone. The crossing point of the linearly dispersing π -band branches visible in Figure 2a–c defines the position of the Dirac point (E_D). By linear extrapolation (see Experimental Methods in the Supporting Information), E_D is found at binding energy of 0.376 ± 0.018 eV above the Fermi energy (E_F) for phase α , indicating that graphene is p-doped. Further information can be extracted from the momentum distribution curve (MDC) line width, which provides insights into the graphene integrity and its interaction with the substrate. The MDC line width (fwhm) orthogonal to the Γ –K direction and taken at 0.70 eV below the Fermi level is 0.153 ± 0.002 Å⁻¹. When phase α is annealed in vacuum above 350 °C and turns into phase β , a reduction in the doping level is observed (Figure 3b). Indeed, E_D is now very close to E_F , at a binding energy of 0.045 ± 0.005 eV. Thus, graphene is close to an undoped state, indicating little charge transfer with the substrate. Moreover, the MDC line width now measures 0.111

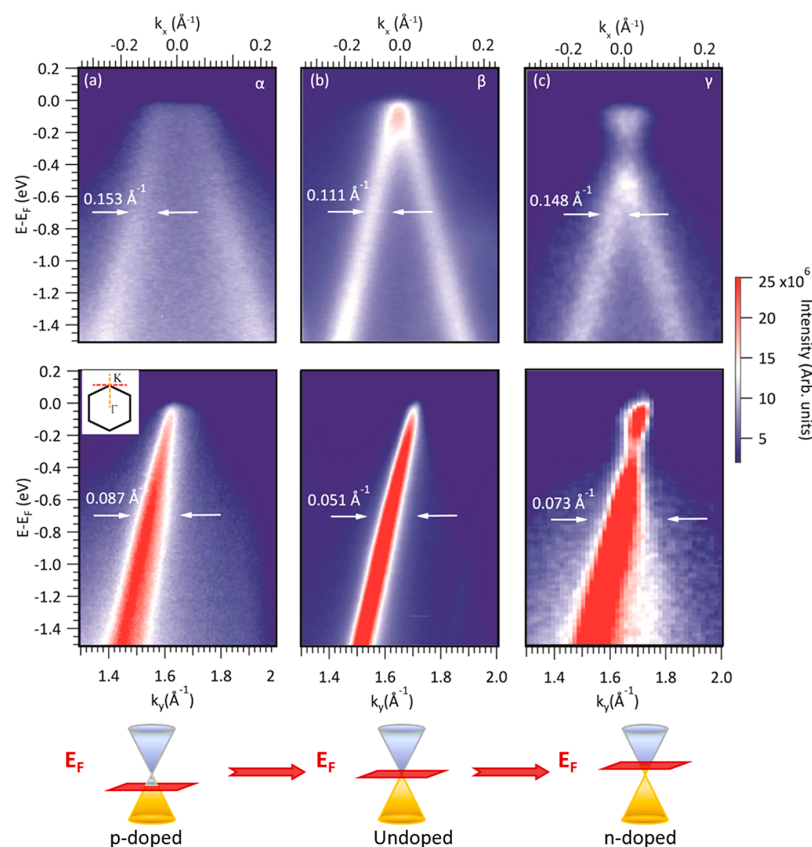


Figure 2. Photoemission intensity of the graphene/Ge(110) system in (a) phase α , (b) phase β , and (c) phase γ . The spectra were acquired along the direction orthogonal to the Γ -K direction ((a-c) upper panels) and along the Γ -K direction ((a-c) lower panels) in the Brillouin zone, as schematically shown in the inset in the middle panel in (a). Bottom row: sketch highlighting the graphene doping level in the three phases.

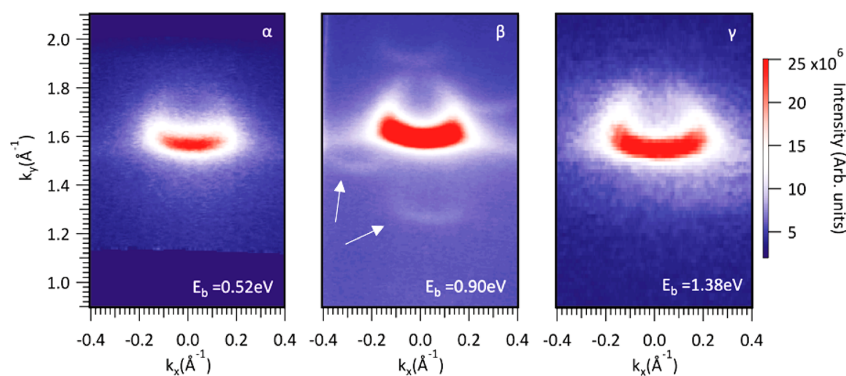


Figure 3. Constant binding energy cuts at 0.90 eV below the extrapolated Dirac point for phase α (left), phase β (middle), and phase γ (right). The white arrows in the middle panel point to the position of two out of four replicas.

\AA^{-1} , a value almost 30% smaller than that of phase α , indicating a weaker interaction between substrate and graphene in phase β . This finding is rather interesting and highlights the opportunity for controlling the graphene doping and substrate interaction by suitable processing.

An additional modification of the electronic properties is found for phase γ , i.e., after a high-temperature annealing of the sample. In this case graphene is n-doped, with E_D found at 0.478 ± 0.007 eV below E_F . This experimental finding is

similar to other reported ARPES measurements performed on graphene/Ge(110) after the sample was annealed at 800 °C in vacuum.²⁷ Previously, the best available explanation to the n-type doping was surface segregation of Sb atoms (about 1 monolayer) upon the high-temperature annealing. Sb is present as a dopant in the bulk of Ge also in our samples, and from our STM images we note the bright patches that may appear suggestive of regions of dopant segregations. However, we rule out this interpretation as similar bright patches are seen

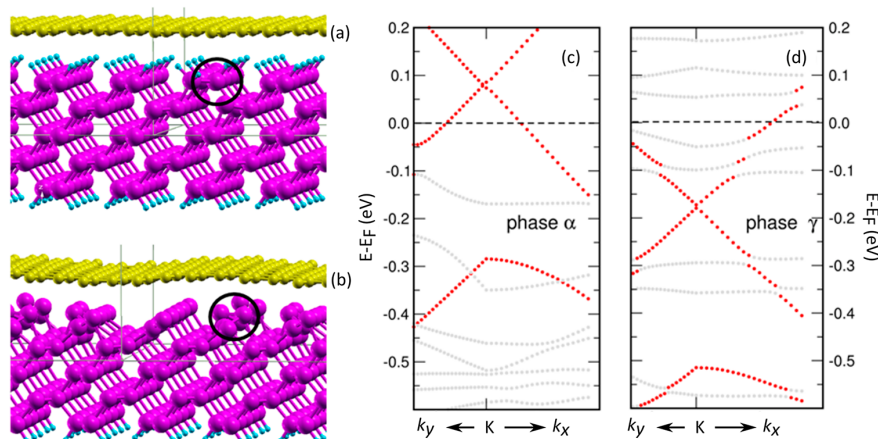


Figure 4. 3D side-view of phase α with all dangling bonds being H-terminated (a) and of phase γ (b). Cyan denotes H atoms, violet Ge atoms, and yellow C atoms. The black circles highlight the region where the vacancy has been introduced. (c, d) Corresponding calculated electronic band structures around K with a total k range of 0.07 \AA^{-1} . Red dots represent graphene-derived states, whereas gray dots represent Ge or H states.

also in the as-grown sample (compare Figure 1a and Figure 1e). For phase γ , the MDC line width is $0.148 \pm 0.002 \text{ \AA}^{-1}$, similar to that found for phase α and larger than that of phase β . Thus, we can conclude that after the high-temperature annealing, the graphene/Ge interaction is stronger than in phase β , but graphene does not degrade because a poorer structural quality would lead to a broadening in the MDC spectral line width with respect to phase α . Furthermore, we note the opening of a small band gap in graphene for phase γ [Figure 2(c) and Figure S4], induced by the stronger interaction with the substrate.²⁵

The k -dependent photoemission intensity at a constant energy of 0.90 eV below E_D is shown in Figure 3 for phases α (left), β (middle), and γ (right), respectively. For phase β , four replicas around the K point (we mark two of them by white arrows) can be observed along with the main Dirac cone. These replicas are due to the superperiodic potential imposed by the moiré of graphene and (6×2) Ge surface reconstruction. Accordingly, the pattern from the replicas is consistent with the LEED pattern of the corresponding sample reported in Figure S2. Interestingly, we do not observe any emerging minigaps at the crossing points of the replicas with the graphene main cone, in contrast to what is found for the case of, for instance, graphene/Ir(111).^{34,35} In particular, from the analysis of the MDCs taken along k_x close to the location where the replica crosses the main cone, the intensity of the spectral function does not vanish or decrease as expected in the case of a minigap (see Figure S5). Furthermore, we notice that the same constant binding energy cut shows no replicas for the other two sample phases.

To gain more insights into the system, we have built a theoretical model based on ab initio calculations to describe phase α and phase γ (see Theoretical Methods in the Supporting Information for more details), which represent the two cases showing opposite doping of graphene. We do not attempt modeling of phase β because of its large cell and complexity.

Phase α is modeled by a 5-layer Ge(110) 3×5 slab, with both surfaces saturated with H, and a graphene layer on top, with a 4×8 periodicity in the rectangular supercell. The geometry is depicted in Figure 4a. Phase γ is modeled by the same supercell but without H atoms on the top of the Ge(110)

substrate (see Figure 4b). A key feature of our models is the presence of a vacancy in the surface layer of the Ge substrate (one vacancy in the 3×5 cell). The location of the vacancy is highlighted by the black circle in Figure 4a,b (additionally, the position of the missing Ge atom is also shown in Figures S6 and S7). As known in the literature,^{14,29–32} when Ge is brought to high temperature (like the temperature used for graphene growth), a spontaneous formation of vacancies occurs, starting first at the surface and then spreading throughout the bulk. This confers to the Ge wafer a p-doping character regardless of the initial nominal doping. Indeed, by performing Hall measurements on different bare Ge substrates, which are nominally n-doped, we do measure p-type doping after they have been annealed in H_2/Ar atmosphere to the same temperature used for graphene growth (Figure S8).

The electronic band structure obtained for phase α shows that the Fermi level lies below the Dirac point, giving rise to p-doping of graphene (Figure 4c). This is qualitatively in agreement with the experiment reported in Figure 2a. To corroborate our hypothesis about the presence of vacancies in the Ge substrate, we have performed additional simulations with (i) no vacancy and with (ii) a Sb atom replacing the vacancy (Sb is the dopant nominally present in our Ge substrate). Both calculations give a Fermi level above the Dirac point, corresponding to n-doped graphene, thus at odds with the experiment (see Table S1). Therefore, we believe that thermally induced vacancies and not Sb segregation play a key role in determining the doping seen in the experiment for phase α .

Phase γ was simulated by removing the H atoms on the top Ge(110) surface. In this case, we found several local minima in energy after geometrical relaxation, in contrast to the single energy minimum observed for phase α . While the most stable structure is an ordered Ge(110) surface, the other minima correspond to slightly disordered Ge surfaces (Figure 4b), with a total energy within a few meV/(C atom) from the ordered one. The occurrence of a disordered surface is in fact supported by the STM images displayed in Figure 1e,f and Figure S3. The electronic band structure of this disordered phase is reported in Figure 4d, where we can see that the Fermi level lies above the Dirac point. Hence, graphene is n-doped, in agreement with the ARPES data (Figure 2c). Furthermore, we

stress that a similar result, that is, n-doped graphene, is achieved when another disordered configuration of phase γ is used, where the surface Ge atoms are intentionally disordered. Instead, when an ordered Ge surface is used to simulate phase γ , no agreement with the experiment is found (see Table S1). Therefore, we believe that disorder in the Ge surface and not Sb segregation plays a key role in determining the doping seen in the experiment for phase γ .

These results highlight the richness of the graphene/Ge(110) system and suggest that the experimentally observed behavior reflects not only the role of Ge–H bonds but also of Ge vacancies and disorder, all of which evolve with increasing temperature.

In conclusion, through a combination of STM and ARPES we have experimentally demonstrated that the electronic properties of the graphene/Ge(110) system are significantly modified by temperature-driven structural changes occurring at the interface. Annealing processing can indeed be used to tune the doping of graphene via modification of its interaction with the Ge substrate. Notably, graphene is p-doped after CVD growth, nearly intrinsic (undoped) upon annealing above 350 °C when the Ge surface rearranges into the 6×2 reconstruction, and then n-doped if the sample is annealed above 700 °C. Starting from the STM observations we also build a theoretical model that successfully reproduces the ARPES experimental trend. Since a comprehensive understanding of the electronic properties of graphene/semiconductor interface is critical when it comes to applications, our results provide an important contribution toward the integration of graphene with conventional semiconductors.

■ ASSOCIATED CONTENT

SI Supporting Information

The Supporting Information is available free of charge at <https://pubs.acs.org/doi/10.1021/acs.jpcllett.0c03649>.

Experimental and theoretical methods; further analysis of the STM and ARPES data; LEED micrographs of phase β ; Hall and resistivity measurements of Ge substrates; and additional simulations (PDF)

■ AUTHOR INFORMATION

Corresponding Authors

Luca Persichetti – Department of Sciences, Roma Tre University, 00146 Rome, Italy; orcid.org/0000-0001-6578-254X; Email: luca.persichetti@uniroma3.it

Luca Camilli – Department of Physics, Technical University of Denmark, 2800 Lyngby, Denmark; Department of Physics, University of Rome “Tor Vergata”, 00133 Rome, Italy; orcid.org/0000-0003-2498-0210; Email: luca.camilli@roma2.infn.it

Paola Gori – Department of Engineering, Roma Tre University, 00146 Rome, Italy; Email: paola.gori@uniroma3.it

Authors

Miriam Galbiati – Department of Physics, Technical University of Denmark, 2800 Lyngby, Denmark

Olivia Pulci – Department of Physics, University of Rome “Tor Vergata”, 00133 Rome, Italy; Istituto Nazionale di Fisica Nucleare, 00133 Rome, Italy; orcid.org/0000-0002-9725-487X

Marco Bianchi – Department of Physics and Astronomy, Aarhus University, 8000 Aarhus C, Denmark

Luciana Di Gaspare – Department of Sciences, Roma Tre University, 00146 Rome, Italy; orcid.org/0000-0003-3134-7296

Jerry Tersoff – IBM Research Division, T.J. Watson Research Center, New York 10598, United States

Camilla Coletti – Center for Nanotechnology Innovation @ NEST and Graphene Laboratories, Istituto Italiano di Tecnologia, Pisa 56127, Italy; orcid.org/0000-0002-8134-7633

Philip Hofmann – Department of Physics and Astronomy, Aarhus University, 8000 Aarhus C, Denmark; orcid.org/0000-0002-7367-5821

Monica De Seta – Department of Sciences, Roma Tre University, 00146 Rome, Italy; orcid.org/0000-0002-8920-8371

Complete contact information is available at: <https://pubs.acs.org/doi/10.1021/acs.jpcllett.0c03649>

Notes

The authors declare no competing financial interest.

■ ACKNOWLEDGMENTS

The authors are grateful to Mads Brandbyge and Fei Gao for the useful discussions. The authors thank Dr. Andrea Notargiacomo for the Hall measurements and Dr. Vaidotas Miseikis for support in growing the samples. This work is supported by the VILLUM FONDEN through the Young Investigator Program (project no. 19130) and the Centre of Excellence for Dirac Materials (grant no. 11744). L.C. acknowledges support from the Italian Ministry of Education, University and Research (MIUR) via “Programma per Giovani Ricercatori - Rita Levi Montalcini 2017”. O.P. acknowledges funding from the HORIZON 2020 E.U. MSCA-RISE project DiSeTCom (GA 823728). The computing resources and related technical support have been provided by CRESCO/ENEAGRID High Performance Computing infrastructure (ENEA, the Italian National Agency for New Technologies, Energy and Sustainable Economic Development). C.C. acknowledges the Graphene Flagship Core 3 (contract no. 881603).

■ REFERENCES

- (1) Akinwande, D.; Huyghebaert, C.; Wang, C.-H.; Serna, M. I.; Goossens, S.; Li, L.-J.; Wong, H. S. P.; Koppens, F. H. L. Graphene and two-dimensional materials for silicon technology. *Nature* **2019**, *573* (7775), 507–518.
- (2) Neumaier, D.; Pindl, S.; Lemme, M. C. Integrating graphene into semiconductor fabrication lines. *Nat. Mater.* **2019**, *18* (6), 525–529.
- (3) Tománek, D. Interfacing graphene and related 2D materials with the 3D world. *J. Phys.: Condens. Matter* **2015**, *27* (13), 133203.
- (4) Goossens, S.; Navickaite, G.; Monasterio, C.; Gupta, S.; Piqueras, J. J.; Pérez, R.; Burwell, G.; Nikitskiy, I.; Lasanta, T.; Galán, T.; Puma, E.; Centeno, A.; Pesquera, A.; Zurutuza, A.; Konstantatos, G.; Koppens, F. Broadband image sensor array based on graphene–CMOS integration. *Nat. Photonics* **2017**, *11* (6), 366–371.
- (5) Mortazavi Zanjani, S. M.; Holt, M.; Sadeghi, M. M.; Rahimi, S.; Akinwande, D. 3D integrated monolayer graphene–Si CMOS RF gas sensor platform. *npj 2D Materials and Applications* **2017**, *1* (1), 36.
- (6) Liu, C.; Ma, W.; Chen, M.; Ren, W.; Sun, D. A vertical silicon-graphene-germanium transistor. *Nat. Commun.* **2019**, *10* (1), 4873.

- (7) Lee, J.-H.; Lee, E. K.; Joo, W.-J.; Jang, Y.; Kim, B.-S.; Lim, J. Y.; Choi, S.-H.; Ahn, S. J.; Ahn, J. R.; Park, M.-H.; Yang, C.-W.; Choi, B. L.; Hwang, S.-W.; Whang, D. Wafer-Scale Growth of Single-Crystal Monolayer Graphene on Reusable Hydrogen-Terminated Germanium. *Science* **2014**, *344* (6181), 286–289.
- (8) Rojas Delgado, R.; Jacobberger, R. M.; Roy, S. S.; Mangu, V. S.; Arnold, M. S.; Cavallo, F.; Lagally, M. G. Passivation of Germanium by Graphene. *ACS Appl. Mater. Interfaces* **2017**, *9* (20), 17629–17636.
- (9) Akhtar, F.; Dabrowski, J.; Lisker, M.; Yamamoto, Y.; Mai, A.; Wenger, C.; Lukosius, M. Investigation of the Oxidation Behavior of Graphene/Ge(001) Versus Graphene/Ge(110) Systems. *ACS Appl. Mater. Interfaces* **2020**, *12* (2), 3188–3197.
- (10) Kiraly, B.; Jacobberger, R. M.; Mannix, A. J.; Campbell, G. P.; Bedzyk, M. J.; Arnold, M. S.; Hersam, M. C.; Guisinger, N. P. Electronic and Mechanical Properties of Graphene–Germanium Interfaces Grown by Chemical Vapor Deposition. *Nano Lett.* **2015**, *15* (11), 7414–7420.
- (11) Dedkov, Y.; Voloshina, E. Epitaxial graphene/Ge interfaces: a minireview. *Nanoscale* **2020**, *12* (21), 11416–11426.
- (12) Jacobberger, R. M.; Kiraly, B.; Fortin-Deschenes, M.; Levesque, P. L.; McElhinny, K. M.; Brady, G. J.; Rojas Delgado, R.; Singha Roy, S.; Mannix, A.; Lagally, M. G.; Evans, P. G.; Desjardins, P.; Martel, R.; Hersam, M. C.; Guisinger, N. P.; Arnold, M. S. Direct oriented growth of armchair graphene nanoribbons on germanium. *Nat. Commun.* **2015**, *6*, 8006.
- (13) Zeng, L.-H.; Wang, M.-Z.; Hu, H.; Nie, B.; Yu, Y.-Q.; Wu, C.-Y.; Wang, L.; Hu, J.-G.; Xie, C.; Liang, F.-X.; Luo, L.-B. Monolayer Graphene/Germanium Schottky Junction As High-Performance Self-Driven Infrared Light Photodetector. *ACS Appl. Mater. Interfaces* **2013**, *5* (19), 9362–9366.
- (14) Pea, M.; De Seta, M.; Di Gaspare, L.; Persichetti, L.; Scaparro, A. M.; Miseikis, V.; Coletti, C.; Notargiacomo, A. Submicron Size Schottky Junctions on As-Grown Monolayer Epitaxial Graphene on Ge(100): A Low-Invasive Scanned-Probe-Based Study. *ACS Appl. Mater. Interfaces* **2019**, *11* (38), 35079–35087.
- (15) Scaparro, A. M.; Miseikis, V.; Coletti, C.; Notargiacomo, A.; Pea, M.; De Seta, M.; Di Gaspare, L. Investigating the CVD Synthesis of Graphene on Ge(100): toward Layer-by-Layer Growth. *ACS Appl. Mater. Interfaces* **2016**, *8* (48), 33083–33090.
- (16) Persichetti, L.; Di Gaspare, L.; Fabbri, F.; Scaparro, A. M.; Notargiacomo, A.; Sgarlata, A.; Fanfoni, M.; Miseikis, V.; Coletti, C.; De Seta, M. Abrupt changes in the graphene on Ge(001) system at the onset of surface melting. *Carbon* **2019**, *145*, 345–351.
- (17) Rogge, P. C.; Foster, M. E.; Wofford, J. M.; McCarty, K. F.; Bartelt, N. C.; Dubon, O. D. On the rotational alignment of graphene domains grown on Ge(110) and Ge(111). *MRS Commun.* **2015**, *5* (3), 539–546.
- (18) Persichetti, L.; De Seta, M.; Scaparro, A. M.; Miseikis, V.; Notargiacomo, A.; Ruocco, A.; Sgarlata, A.; Fanfoni, M.; Fabbri, F.; Coletti, C.; Di Gaspare, L. Driving with temperature the synthesis of graphene on Ge(110). *Appl. Surf. Sci.* **2020**, *499*, 143923.
- (19) Dai, J.; Wang, D.; Zhang, M.; Niu, T.; Li, A.; Ye, M.; Qiao, S.; Ding, G.; Xie, X.; Wang, Y.; Chu, P. K.; Yuan, Q.; Di, Z.; Wang, X.; Ding, F.; Yakobson, B. I. How Graphene Islands Are Unidirectionally Aligned on the Ge(110) Surface. *Nano Lett.* **2016**, *16* (5), 3160–3165.
- (20) Becker, A.; Wenger, C.; Dabrowski, J. Influence of temperature on growth of graphene on germanium. *J. Appl. Phys.* **2020**, *128* (4), 045310.
- (21) Wang, T.; Li, P.; Hu, X.; Gao, M.; Di, Z.; Xue, Z.; Zhang, M. Wafer-scale fabrication of single-crystal graphene on Ge(110) substrate by optimized CH₄/H₂ ratio. *Appl. Surf. Sci.* **2020**, *529*, 147066.
- (22) Kim, H. W.; Jeon, I.; Ko, W.; Kim, S. H. Unidirectional growth of graphene nano-islands from carbon cluster seeds on Ge(110). *Appl. Surf. Sci.* **2021**, *536*, 147722.
- (23) Zhou, D.; Niu, Z.; Niu, T. Surface Reconstruction of Germanium: Hydrogen Intercalation and Graphene Protection. *J. Phys. Chem. C* **2018**, *122* (38), 21874–21882.
- (24) Campbell, G. P.; Kiraly, B.; Jacobberger, R. M.; Mannix, A. J.; Arnold, M. S.; Hersam, M. C.; Guisinger, N. P.; Bedzyk, M. J. Epitaxial graphene-encapsulated surface reconstruction of Ge(110). *Physical Review Materials* **2018**, *2* (4), 044004.
- (25) Kiraly, B.; Mannix, A. J.; Jacobberger, R. M.; Fisher, B. L.; Arnold, M. S.; Hersam, M. C.; Guisinger, N. P. Driving chemical interactions at graphene-germanium van der Waals interfaces via thermal annealing. *Appl. Phys. Lett.* **2018**, *113* (21), 213103.
- (26) Kim, H. W.; Ko, W.; Joo, W.-J.; Cho, Y.; Oh, Y.; Ku, J.; Jeon, I.; Park, S.; Hwang, S. W. Unraveling the Structural and Electronic Properties of Graphene/Ge(110). *J. Phys. Chem. Lett.* **2018**, *9* (24), 7059–7063.
- (27) Tesch, J.; Paschke, F.; Fonin, M.; Wietstruk, M.; Böttcher, S.; Koch, R. J.; Bostwick, A.; Jozwiak, C.; Rotenberg, E.; Makarova, A.; Paulus, B.; Voloshina, E.; Dedkov, Y. The graphene/n-Ge(110) interface: structure, doping, and electronic properties. *Nanoscale* **2018**, *10* (13), 6088–6098.
- (28) Ahn, S. J.; Kim, H. W.; Khadka, I. B.; Rai, K. B.; Ahn, J. R.; Lee, J.-H.; Kang, S. G.; Whang, D. Electronic Structure of Graphene Grown on a Hydrogen-terminated Ge (110) Wafer. *J. Korean Phys. Soc.* **2018**, *73* (5), 656–660.
- (29) Mayburg, S. Vacancies and Interstitials in Heat Treated Germanium. *Phys. Rev.* **1954**, *95* (1), 38–43.
- (30) Logan, R. A. Thermally Induced Acceptors in Germanium. *Phys. Rev.* **1956**, *101* (5), 1455–1459.
- (31) Vanhellefont, J.; Lauwaert, J.; Witecka, A.; Śpiewak, P.; Romandic, I.; Clauws, P. Experimental and theoretical study of the thermal solubility of the vacancy in germanium. *Phys. B* **2009**, *404* (23), 4529–4532.
- (32) Segers, S. H.; Lauwaert, J.; Clauws, P.; Simoen, E.; Vanhellefont, J.; Callens, F.; Vrielinck, H. Direct estimation of capture cross sections in the presence of slow capture: application to the identification of quenched-in deep-level defects in Ge. *Semicond. Sci. Technol.* **2014**, *29* (12), 125007.
- (33) Jia, P.; Chen, W.; Qiao, J.; Zhang, M.; Zheng, X.; Xue, Z.; Liang, R.; Tian, C.; He, L.; Di, Z.; Wang, X. Programmable graphene nanobubbles with three-fold symmetric pseudo-magnetic fields. *Nat. Commun.* **2019**, *10* (1), 3127.
- (34) Larciprete, R.; Ulstrup, S.; Lacovig, P.; Dalmiglio, M.; Bianchi, M.; Mazzola, F.; Hornekær, L.; Orlando, F.; Baraldi, A.; Hofmann, P.; Lizzit, S. Oxygen Switching of the Epitaxial Graphene–Metal Interaction. *ACS Nano* **2012**, *6* (11), 9551–9558.
- (35) Pletkosić, I.; Kralj, M.; Pervan, P.; Brako, R.; Coraux, J.; N'Diaye, A. T.; Busse, C.; Michely, T. Dirac Cones and Minigaps for Graphene on Ir(111). *Phys. Rev. Lett.* **2009**, *102* (5), 056808.

Paper III

M. Galbiati, M. Scarselli, F. Arciprete, M. De Crescenzi
and L. Camilli.

Scanning tunneling microscopy study of CaF₂ on Si(111): Observation of metastable reconstructions.
<https://doi.org/10.1088/1361-6463/ac378d> *Journal of*

Physics D: Applied Physics, **55**, 095304 (2021)

Scanning tunneling microscopy study of CaF₂ on Si(111): observation of metastable reconstructions

Miriam Galbiati¹, Manuela Scarselli², Fabrizio Arciprete², Maurizio De Crescenzi² and Luca Camilli^{1,2,*} 

¹ Department of Physics, Technical University of Denmark, building 311 Fysikvej, 2800 Kgs. Lyngby, Denmark

² Dipartimento di Fisica, Università degli studi di Roma Tor Vergata, via della Ricerca Scientifica 1, 00133 Roma, Italy

E-mail: luca.camilli@roma2.infn.it

Received 6 September 2021, revised 27 October 2021

Accepted for publication 8 November 2021

Published 23 November 2021



Abstract

The deposition of calcium fluoride (CaF₂) on Si(111) at temperatures above 570 °C has been studied with scanning tunneling microscopy. At such temperatures, triangular calcium fluoride islands are formed both on terraces and along the phase domain boundaries of the (7 × 7) reconstruction of the Si(111) substrate. In addition to the formation of islands, we observe that CaF₂ molecules react with the substrate inducing large areas of its surface to reconstruct into (√3 × √3) and c(2 × 4) phases. Upon annealing at 600 °C, the abovementioned areas of (√3 × √3) and c(2 × 4) turn into the stable (3 × 1) phase upon desorption of fluorine. Calcium fluoride islands are stable at this temperature. Depositions of calcium fluoride performed with Si substrate kept at higher temperature, namely at 680 °C, lead directly to the formation of (3 × 1) phase due to the complete desorption of fluorine, without passing through the formation of the metastable (√3 × √3) and c(2 × 4) phases. If CaF₂/Si(111) is brought at even higher temperatures, Ca also starts desorbing and the (7 × 7)-Si(111) reconstruction can eventually be restored.

Keywords: CaF₂, epitaxy, metastable reconstructions, scanning tunneling microscopy, Si(111)

(Some figures may appear in colour only in the online journal)

1. Introduction

The epitaxial growth of CaF₂ on Si has received a great deal of attention during the last decades [1–3]. Indeed, owing to the large CaF₂ band gap and its ability to grow homogeneously on Si, CaF₂/Si represents a promising platform for semiconductor-on-insulator devices and has been studied, for example, in the context of resonant tunneling diodes [4–6]. Moreover, it has been proposed very recently as a suitable

substrate for the growth of silicene—a two-dimensional allotrope of silicon [7, 8]. Furthermore, due to the small lattice mismatch of 0.6% at room temperature, the CaF₂/Si(111) system is also of importance when it comes to advancing our fundamental understanding of heteroepitaxial processes.

The structure and morphology of the surface formed upon deposition of CaF₂ onto Si(111) substrate changes dramatically depending on the substrate temperature during the deposition. For example, a F:Ca ratio of 2:1 has been reported when CaF₂ is deposited at RT [9]. The CaF₂ molecules dissociate on the (7 × 7)-Si(111) surface [10, 11] and below 200 °C temperature condition the (7 × 7) reconstruction is maintained

* Author to whom any correspondence should be addressed.

on the Si(111) surface. Moreover, core levels spectroscopy measurements have reported the formation of both Si-F and Si-Ca bonds [12, 13]. On the other hand, if CaF₂/Si is annealed after deposition or if CaF₂ is deposited at higher substrate temperatures, F:Ca ratio changes and becomes 1:1 for temperatures above 550 °C [9, 14–16], indicating desorption of fluorinated species. As a result, the morphology of the deposited films is modified as well [9, 15, 17–20].

Despite the numerous studies already available in the literature, this topic is not exhausted yet. For example, it is still unclear if preferential absorption sites for CaF₂ molecules exist on the (7 × 7)-Si(111) surface. In addition, another issue that is still debated is the nature of the point-like defects that are often observed with scanning tunneling microscopy (STM) on the epitaxially grown CaF₂ islands. When CaF₂ grows on (7 × 7)-Si(111) at high temperature, silicon surface below the CaF₂ film loses its reconstruction and turns into a (1 × 1) phase. Earlier studies have concluded that the excess Si atoms that are produced during this transformation remain at the CaF/Si interface and eventually form characteristic point-like defects [21, 22]. A recent study that combines STM and non-contact atomic force microscopy experiments has instead proposed a new explanation based on Si atoms leaving the surface as SiF_x, at least partially, at high temperature [13].

Furthermore, although it is known that deposition of calcium fluoride at temperatures around 600 °C leads to formation of (3 × 1) reconstruction due to desorption of F, information is scarce about what happens to the Si surface at slightly lower temperature, that is, just about at the onset of F desorption. Most of the studies have focused more on the growing CaF₂ film rather than the surrounding Si surface [9, 15, 17–20]. Some studies have reported low-energy electron diffraction (LEED) experiments performed on samples in a broad temperature range [14, 15, 23]; however, LEED only provides information on structures that are coherent over a large area and therefore is not capable of investigating structures with sub-micron size. Thus, if the surface is not homogeneous, atomic details from small areas would remain hidden. Here, we use STM to make a comparative study between (a) samples grown at 570 °C and then annealed in vacuum at higher temperatures, and (b) samples directly grown at 680 °C. From these observations we propose that just below 600 °C the etching of some of the Si atoms and the consequent strain induced to the surface lead to the formation of metastable Si reconstructions, namely ($\sqrt{3} \times \sqrt{3}$) and c(2 × 4). These reconstructions are stable when the sample is cooled down and can therefore be imaged. However, when the sample is brought at 600 °C, they will turn into a Ca-induced stable (3 × 1) reconstruction due to a significant desorption of F.

2. Method

Sample preparation and STM experiments were performed under ultra-high-vacuum conditions with a base pressure better than 10⁻¹⁰ mbar. B-doped p-type Si(111) samples were

prepared by direct current flash cycles above 1200 °C to form the (7 × 7) reconstruction after an initial radiative annealing at around 550 °C. The CaF₂ pellet (99.9% from MaTeck, Germany) was loaded into a Mo crucible and deposited using a QUAD-EV-C e-beam evaporator (Mantis LTD, UK). The depositions were performed with power in the range 12–14 W. In all the experiments, Si was heated by direct current during CaF₂ deposition; the substrate temperatures stated herein were measured using an optical pyrometer (emissivity 0.7). CaF₂ coverage was always less than 1 ML. The coverage was evaluated *a posteriori* from STM images and using the flooding function of WSxM software [24]; the deposition rates are estimated to be around 0.01 ML min⁻¹. STM and scanning tunneling spectroscopy (STS) experiments were performed using the LT-UHV Infinity System (Scienta Omicron GmbH, Taunusstein, Germany) operated at <10 K. For STM, the bias voltage is given with respect to the sample voltage. Chemically etched W tip was used for STM measurements. Data were analyzed using GWYDDION software [25]. STS measurements were acquired via lock-in technique with 10 mV modulation and frequency of 5893 Hz.

3. Results and discussion

Figure 1 shows the surface of a Si(111) sample after deposition of 0.20 ML of CaF₂ at 570 °C. The topography of the surface is rather inhomogeneous. Indeed, the sample surface exhibits three different types of regions: unreacted areas of Si(111) showing the well-studied (7 × 7) reconstruction; triangular-shaped islands of calcium fluoride; extended areas of reacted Si(111), where the (7 × 7) reconstruction has been lost. Concerning the islands, from figure 1(a) it is possible to observe how they nucleate both on terraces and along the phase boundaries (white dashed line in figure 1(a) marks one of the phase boundaries as example). Regarding the region of reacted Si(111), although it looks quite disordered, we can still pinpoint small patches showing the ($\sqrt{3} \times \sqrt{3}$) and c(2 × 4) reconstructions (figures 1(c)–(e)), which are known to be metastable phases with a high atom density [26–28]. Since the surface shows three different types of regions, it is noteworthy to highlight differences with STS measurements. Indeed, figure 2 reports STS measurements on the sample grown at 570 °C. The spectra acquired on the same type of region are consistent with each other, while among the different regions the spectra show some compelling qualitative differences. The STS spectra taken on the unreacted (7 × 7)-Si(111) are in agreement with previous work [29] that reports the opening of a considerable gap when measurements are performed at very low temperature (<10 K), as in our experiments. Both reacted and unreacted Si areas show a small feature centered at 1.5 V (marked with dashed line), already observed for (7 × 7)-Si(111) [29]. This feature is instead absent in the CaF₂ island. The reacted Si also displays a peak at 2 V, undetected in the unreacted area. Furthermore, at negative voltages both the reacted Si and the CaF₂ island exhibit a step-like rise from

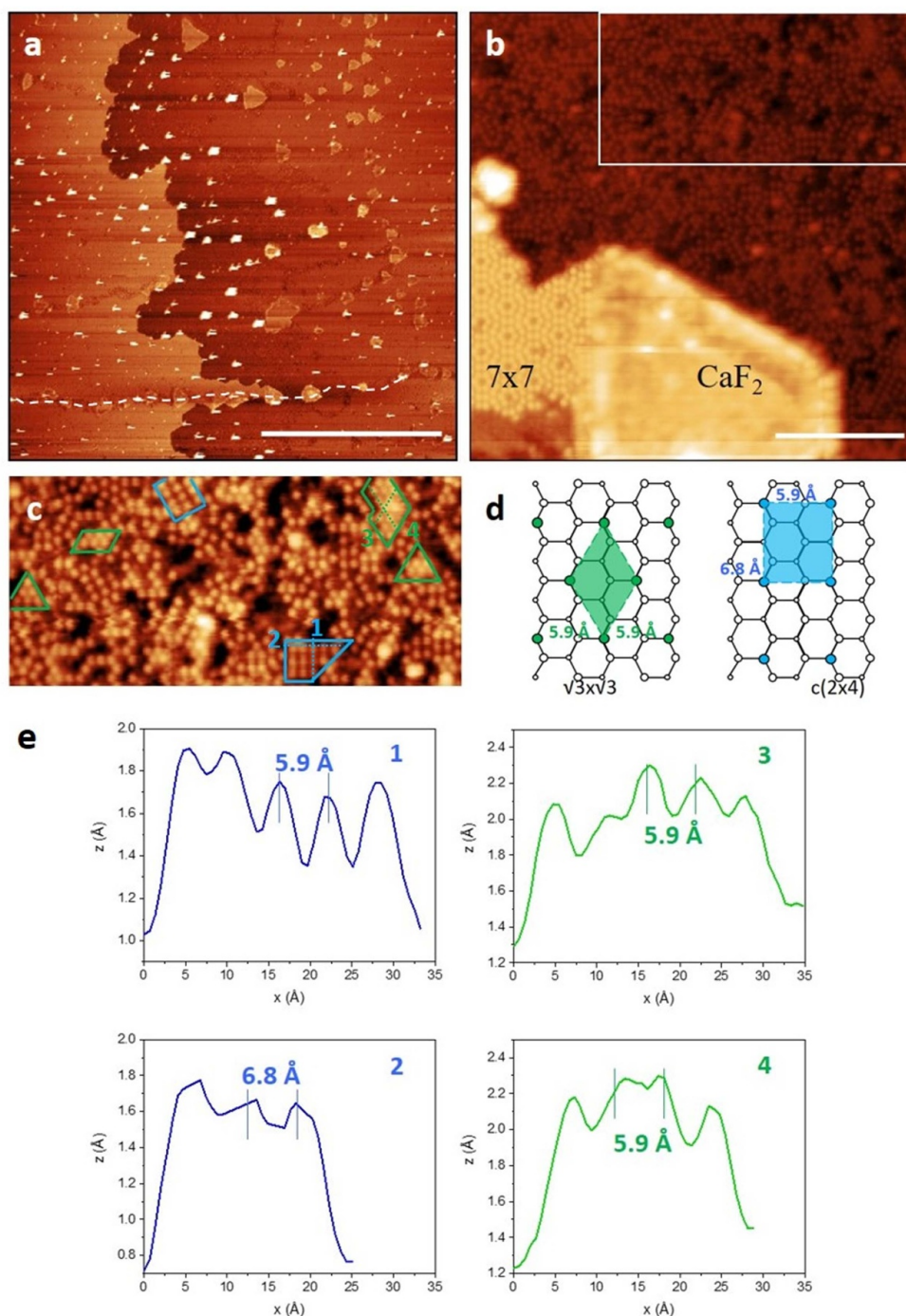


Figure 1. (a)–(c) STM images of sample after deposition of 0.20 ML of CaF_2 at $570 \text{ }^\circ\text{C}$ showing the unreacted (7×7) and reacted Si areas. The white dashed line in panel (a) marks one of the phase boundaries along which the CaF_2 islands tend to nucleate. (c) Blow-up of $25 \times 12 \text{ nm}^2$ rectangular area marked in the top-right corner in (b). The areas highlighted in light blue and green represent patches of $c(2 \times 4)$ and $(\sqrt{3} \times \sqrt{3})$ reconstructions, respectively. Scale bar 200 nm (a), 10 nm (b). (d) Schematics of $(\sqrt{3} \times \sqrt{3})$ and $c(2 \times 4)$ unit cell reconstruction. Si atoms of the unit cells of $(\sqrt{3} \times \sqrt{3})$ and $c(2 \times 4)$ phases are highlighted in green and blue, respectively. (e) Line profiles taken on the STM image as indicated in panel (c). The periodicities of first-neighbor atoms are consistent with those expected for the $c(2 \times 4)$ and $(\sqrt{3} \times \sqrt{3})$ reconstructions. (a) $V = 3.0 \text{ V}$ and $I = 0.5 \text{ nA}$. (b) and (c) $V = 3.0 \text{ V}$ and $I = 0.6 \text{ nA}$.

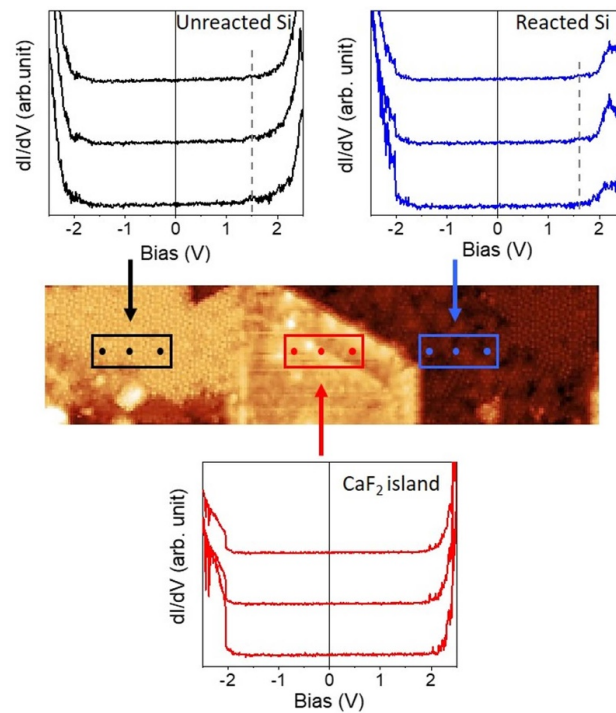


Figure 2. STS measurements recorded via lock-in technique on the three different types of regions on the sample where 0.20 ML of CaF_2 was deposited at 570°C on Si(111). Namely, the three regions are unreacted Si (black spectra), reacted Si (blue spectra) and a CaF_2 island (red spectra). Three spectra were acquired on three different spots within the same type of region, as indicated by the rectangular boxes in the STM image. These spectra are vertically shifted by an arbitrary quantity for visualization purpose.

around -2 V. The CaF_2 also features a rise at $+2$ V, in agreement with previous work [30].

It would now be interesting to observe what happens when the temperature is raised, as it is known that the higher the temperature, the higher the probability of desorption of fluorine, F, and fluorinated species, SiF_x .

As seen in figures 3(a) and (b), upon annealing at 600°C , both the triangular-shaped CaF_2 islands (marked with white arrows in figure 3(a)) and the unreacted (7×7) -Si(111) regions are apparently not affected and still clearly visible on the surface. However, the areas previously covered by $c(2 \times 4)$ and $(\sqrt{3} \times \sqrt{3})$ reconstructions have disappeared, whereas the (3×1) reconstruction is now observable. These observations suggest that the reacted Si areas showing $c(2 \times 4)$ and $(\sqrt{3} \times \sqrt{3})$ reconstructions have turned into the stable (3×1) reconstruction, which is known to form once F has desorbed [10, 23]. Indeed, (3×1) reconstruction has been observed to form also upon deposition of pure Ca atoms, and identified as a mixture of (3×2) and $c(6 \times 2)$ reconstructions [31].

We speculate that just below 600°C , F atoms starts combining with the substrate to form volatile SiF_x species that desorb from the surface [9, 13–16]. The removal of Si atoms is the key factor that leads the surface to rearrange into the $c(2 \times 4)$ and $(\sqrt{3} \times \sqrt{3})$ reconstructions. These reconstructions were also observed for example for stepped Si surfaces or in the case of Si/Ge epitaxial films [32, 33]. The appearance of the metastable phases represents the onset of radical structural changes

of the substrate that will eventually lead to the formation of the stable (3×1) reconstruction at even higher temperatures once the majority to all F atoms have desorbed.

To confirm that the (3×1) reconstruction is the stable phase at high temperature (that is, above 600°C), we report in figures 3(c) and (d) STM images of a sample where CaF_2 was deposited on Si(111) at 680°C . These experiments reveal the presence of large areas of clean (7×7) -Si(111) and large areas of (3×1) reconstruction. Interestingly, the CaF_2 islands are no longer visible. Thus, at these high temperatures, not only the F atoms that had reacted with Si have left the substrate surface, but also the F atoms within the calcium fluoride islands. Furthermore, it is worth noting here that the (3×1) areas show several point-like defects (see for example the bright spots in the STM images in figures 3(b) and (d)). In the case of epitaxial CaF_2 islands, similar bright spots were ascribed to excess Si atoms due to the mass transport associated to the transition $(7 \times 7) \rightarrow (1 \times 1)$ reconstruction [21]. Similarly, due to the low atomic density of the (3×1) reconstruction [31, 34], we hypothesize that the observed bright spots in our STM images might be due to excess Si atoms.

At even higher temperatures, namely above 700°C , even Ca starts to desorb from the surface, and the (7×7) -Si(111) surface can be eventually restored. Figure 4 indeed shows the sample in figure 1 after flash annealing at 1200°C . Only (7×7) areas can be observed on the surface.

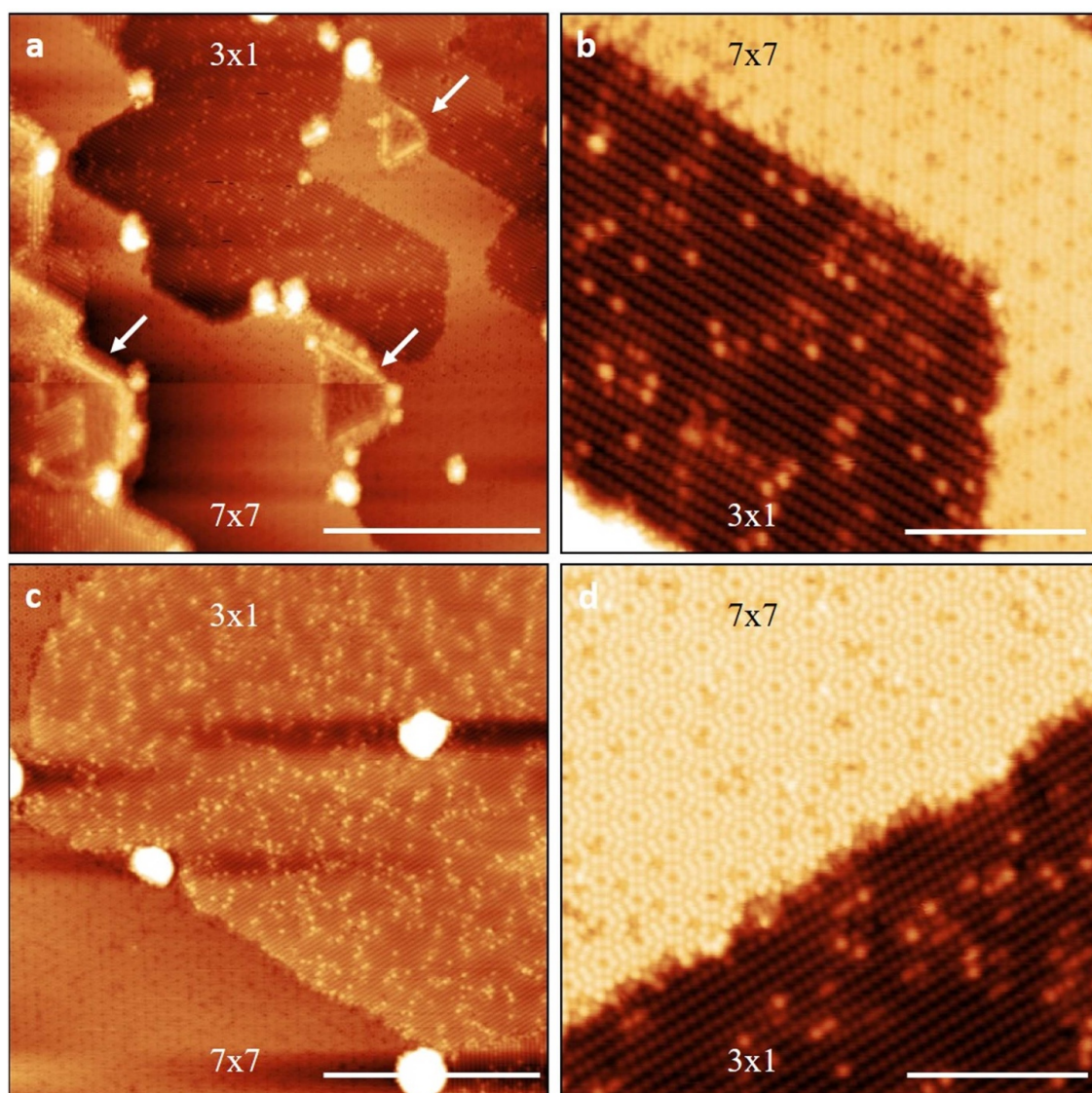


Figure 3. STM images of the samples after deposition of 0.20 ML of CaF_2 at 570°C and post-deposition annealing at 600°C (a) and (b); and after deposition of 0.60 ML of CaF_2 at 680°C (c) and (d). White arrows in panel (a) indicate the triangular shaped CaF_2 islands. Scale bars 200 nm (a), (c) and 10 nm (b), (d). $V = 3.0$ V and $I = 0.2$ nA (a), (b). (c) $V = 2.5$ V, $I = 0.6$ nA and (d) $V = 2.5$ V, $I = 0.5$ nA.

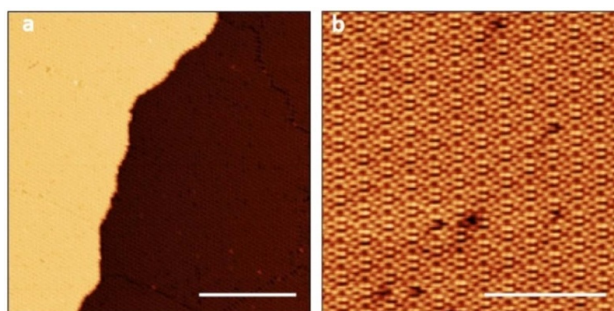


Figure 4. STM images of CaF_2/Si after flash annealing at 1200°C . The surface reveals only (7×7) areas. (a) $V = -2.5$ V and $I = 0.5$ nA. Scale bar 50 nm. (b) $V = 3.5$ V and $I = 0.15$ nA. Scale bar 10 nm.

4. Conclusions

We have reported an STM study of the CaF₂/Si(111) system. When CaF₂ is deposited at 570 °C, the surface exhibits the coexistence of unreacted areas with (7 × 7)-Si(111), triangular-shaped calcium fluoride islands and reacted areas exhibiting small patches of (√3 × √3) and c(2 × 4) reconstructions. When the sample is annealed in vacuum at higher temperatures after growth, the metastable (√3 × √3) and c(2 × 4) phases turn into the stable (3 × 1). CaF₂ islands are still observed. If CaF₂ is instead deposited on Si at 680 °C, most of F desorb from the surface and only areas of (3 × 1) or (7 × 7) can be seen, while the triangular CaF₂ islands are not stable anymore. Annealing at even higher temperature leads to desorption of Ca as well, and only (7 × 7) reconstruction is observed on the surface after flash annealing above 1200 °C.

Data availability statement

The data that support the findings of this study are available upon reasonable request from the authors.

Acknowledgments

This research is supported by the VILLUM FONDEN through the Young Investigator Program (Project No. 19130). L C acknowledges support from the Italian Ministry of Education, University and Research (MIUR) via ‘Programma per Giovani Ricercatori—Rita Levi Montalcini 2017’.

Conflict of interest

The authors declare that they have no known competing financial interests or personal relationships that could have appeared to influence the work reported in this paper.

ORCID iD

Luca Camilli  <https://orcid.org/0000-0003-2498-0210>

References

- [1] Olmstead M A 1999 Heteroepitaxy of disparate materials: from chemisorption to epitaxy in CaF₂/Si(111) *Thin Films: Heteroepitaxial Systems* ed W K Liu and M B Santos (Singapore: World Scientific) pp 211–66
- [2] Wollschläger J 2002 Resonant tunnelling devices based on epitaxial insulator-semiconductor structures: growth and characterisation of CaF₂ films on Si(111) *Recent Research Developments in Applied Physics* ed S Pandalai (Trivandrum: Transworld Research Network) pp 621–95
- [3] Wollschläger J 2002 Substrate-step-induced effects on the growth of CaF₂ on Si(111) *Appl. Phys. A: Mater. Sci. Process.* **75** 155–66
- [4] Wang C R, Müller B H and Hofmann K R 2003 CaF₂/Si/CaF₂ double-barrier resonant-tunnelling diodes on Si substrates *Nanotechnology* **14** 1192–6
- [5] Watanabe M, Suemasu T, Muratake S and Asada M 1993 Negative differential resistance of metal (CoSi₂)/insulator (CaF₂) triple-barrier resonant tunneling diode *Appl. Phys. Lett.* **62** 300–2
- [6] Wang C R, Bierkandt M, Paprotta S, Wietler T and Hofmann K R 2005 CaF₂/Si/CaF₂ resonant tunneling diodes grown by B surfactant-mediated epitaxy *Appl. Phys. Lett.* **86** 033111
- [7] Kokott S, Pflugradt P, Matthes L and Bechstedt F 2014 Nonmetallic substrates for growth of silicene: an *ab initio* prediction *J. Phys. Condens. Matter* **26** 185002
- [8] Galbiati M, Motta N, De Crescenzi M and Camilli L 2019 Group-IV 2D materials beyond graphene on nonmetal substrates: challenges, recent progress, and future perspectives *Appl. Phys. Rev.* **6** 041310
- [9] Olmstead M A and Bringans R D 1990 Initial stages of epitaxial semiconductor-insulator heterointerface formation *J. Electron Spectrosc. Relat. Phenom.* **51** 599–612
- [10] Lucas C A, Loretto D and Wong G C L 1994 Epitaxial growth mechanisms and structure of CaF₂/Si(111) *Phys. Rev. B* **50** 14340–53
- [11] Sumiya T, Miura T and Tanaka S 1996 Initial growth stage of CaF₂ on Si(111)-7 × 7 studied by high temperature UHV-STM *Surf. Sci.* **357** 896–9
- [12] Olmstead M A, Uhrberg R I G, Bringans R D and Bachrach R Z 1987 Photoemission study of bonding at the CaF₂-on-Si(111) interface *Phys. Rev. B* **35** 7526–32
- [13] Rahe P, Smith E F, Wollschläger J and Moriarty P J 2018 Formation routes and structural details of the CaF₁ layer on Si(111) from high-resolution noncontact atomic force microscopy data *Phys. Rev. B* **97** 125418
- [14] Olmstead M A 1986 Initial formation of the interface between a polar insulator and a nonpolar semiconductor: CaF₂ on Si(111) *J. Vac. Sci. Technol. B* **4** 1123
- [15] Rieger D, Himpfel F J, Karlsson U O, Mcfeely F R, Morar J F and Yarmoff J A 1986 Electronic structure of the CaF₂/Si(111) interface *Phys. Rev. B* **34** 7295–306
- [16] Karlsson U O, Himpfel F J, Morar J F, Rieger D and Yarmoff J A 1986 Electronic structure of molecular beam epitaxy grown CaF₂ on Si(111) *J. Vac. Sci. Technol. B* **4** 1117
- [17] Tromp R M and Reuter M C 1988 Structure of the Si(111)-CaF₂ interface *Phys. Rev. Lett.* **61** 1756
- [18] Wang C R, Müller B H, Bugiel E and Hofmann K R 2004 Temperature-dependent growth mechanisms of CaF₂ on Si(111) *J. Vac. Sci. Technol. A* **22** 2182–7
- [19] Harada J, Takahashi I, Itoh Y, Sokolov N S, Yakovlev N L, Shusterman Y and Alvarez J C 1996 X-ray scattering from surfaces and interfaces and its application to the characterization of CaF₂/Si(111) interfaces *J. Cryst. Growth* **163** 31–38
- [20] Sokolov N S, Alvarez J C, Gastev S V, Shusterman Y V, Takahashi I, Itoh Y, Harada J and Overney R M 1996 High quality CaF₂ layers on Si(111) with type-A epitaxial relation at the interface *J. Cryst. Growth* **169** 40–50
- [21] Nakayama T, Katayama M, Selva G and Aono M 1994 Mechanism of epitaxial growth of monolayer CaF on Si(111)-(7 × 7) *Phys. Rev. Lett.* **72** 1718–21
- [22] Nakayama T and Aono M 1998 Creation and consumption of free Si atoms at the growth front of a CaF monolayer on Si(111)7x7 *Phys. Rev. B* **57** 1855–9
- [23] Sumiya T 2000 Initial growth stages of CaF₂ on Si(111) investigated by scanning tunneling microscopy *Appl. Surf. Sci.* **156** 85–96
- [24] Horcas I, Fernández R, Gómez-Rodríguez J M, Colchero J, Gómez-Herrero J and Baro A M 2007 WSXM: a software

- for scanning probe microscopy and a tool for nanotechnology *Rev. Sci. Instrum.* **78** 013705
- [25] Nečas D and Klapetek P 2012 Gwyddion: an open-source software for SPM data analysis *Cent. Eur. J. Phys.* **10** 181–8
- [26] Becker R S, Golovchenko J A, Higashi G S and Swartzentruber B S 1986 New reconstructions on silicon (111) surfaces *Phys. Rev. Lett.* **57** 1020–3
- [27] Köhler U, Demuth J E and Hamers R J 1989 Scanning tunneling microscopy study of low-temperature epitaxial growth of silicon on Si(111)-(7 × 7) *J. Vac. Sci. Technol. A* **7** 2860–7
- [28] Yang Y-N and Williams E D 1994 High atom density in the “1×1” phase and origin of the metastable reconstructions on Si(111) *Phys. Rev. Lett.* **72** 1862–5
- [29] Mysliveček J, Strážnická A, Steffl J, Sobotník P, Ošťádal I and Voigtländer B 2006 Structure of the adatom electron band of the Si(111)-7 × 7 surface *Phys. Rev. B* **73** 161302
- [30] Klust A, Ohta T, Bostwick A A, Rotenberg E, Yu Q, Ohuchi F S and Olmstead M A 2005 Electronic structure evolution during the growth of ultrathin insulator films on semiconductors: from interface formation to bulklike Ca₂ *Phys. Rev. B* **72** 205336
- [31] Saranin A A, Lifshits V G, Ignatovich K V, Bethge H, Kayser R, Goldbach H, Klust A, Wollschläger J and Henzler M 2000 Restructuring process of the Si(111) surface upon Ca deposition *Surf. Sci.* **448** 87–92
- [32] Zhachuk R, Teys S and Coutinho J 2013 Strain-induced structure transformations on Si(111) and Ge(111) surfaces: a combined density-functional and scanning tunneling microscopy study *J. Chem. Phys.* **138** 224702
- [33] Zhachuk R, Coutinho J, Dolbak A, Cherepanov V and Voigtländer B 2017 Si(111) strained layers on Ge(111): evidence for c(2 × 4) domains *Phys. Rev. B* **96** 085401
- [34] Saranin A A, Zotov A V, Lifshits V G, Ryu J-T, Kubo O, Tani H, Harada T, Katayama M and Oura K 1998 Reexamination of the Si(111)3 × 1–Na reconstruction on the basis of Si atom density and unit cluster determination *Phys. Rev. B* **58** 3545–8

Bibliography

- [1] T. N. Theis and H. P. Wong. “The End of Moore’s Law: A New Beginning for Information Technology”. In: *Comput. Sci. Eng* 19.June 2016 (1975), pp. 41–50 (cit. on p. 1).
- [2] F. Schwierz. “Graphene transistors”. In: *Nat. Nanotechnol.* 5.July (2010), pp. 487–496 (cit. on pp. 1, 82).
- [3] R. H. Dennard, F. H. Gaensslen, H.-N. Yu, V. L. Rideout, E. Bassous, and A. R. LeBlanc. “Design of Ion-Implanted MOSFET ’ s with Very Small Physical Dimensions”. In: *Proc. IEEE International Electron Devices Meeting (IEDM)* (1974), pp. 789–792 (cit. on p. 1).
- [4] M. M. Waldrop. “More Than Moore”. In: *Nature News* 530 (2016), pp. 145–147 (cit. on p. 1).
- [5] Y. Liu, X. Duan, H.-J. Shin, S. Park, Y. Huang, and X. Duan. “Promises and prospects of two-dimensional transistors”. In: *Nature* 591.7848 (2021), pp. 43–53 (cit. on p. 1).
- [6] D. Akinwande, C. Huyghebaert, C.-H. Wang, M. I. Serna, S. Goossens, L.-J. Li, H.-S. P. Wong, and F. H. L. Koppens. “Graphene and two-dimensional materials for silicon technology”. In: *Nature* 573.7775 (2019), pp. 507–518 (cit. on pp. 1, 6).
- [7] Y. Taur, C. H. Wann, and D. J. Frank. “25 nm CMOS Design Considerations”. In: *IEEE J. Solid-State Circuits* 9, 9 (1998), pp. 789–792 (cit. on p. 2).
- [8] S. Veeraraghavan and J. Fossum. “Short-channel effects in SOI MOSFETs”. In: *IEEE Transactions on Electron Devices* 36.3 (1989), pp. 522–528 (cit. on p. 2).
- [9] D. J. Frank, Y. Taur, H.-s. P. Wong, and S. Member. “Generalized Scale Length for Two-Dimensional Effects in MOSFET ’ s”. In: *IEEE Electron Device Letters* 19.10 (1998), pp. 385–387 (cit. on p. 3).

- [10] C. D. English, G. Shine, V. E. Dorgan, K. C. Saraswat, and E. Pop. “Improved Contacts to MoS₂ Transistors by Ultra-High Vacuum Metal Deposition”. In: *Nano Letters* 16.6 (2016), pp. 3824–3830 (cit. on p. 3).
- [11] X. Zang, T. Wang, Z. Han, L. Li, and X. Wu. “Recent Advances of 2D Nanomaterials in the Electrode Materials of Lithium-Ion Batteries”. In: *Nano* 14.02 (2019), p. 1930001 (cit. on p. 4).
- [12] M. Yi and Z. Shen. “A review on mechanical exfoliation for the scalable production of graphene”. In: *Journal of Materials Chemistry A* 3.22 (2015), pp. 11700–11715 (cit. on p. 3).
- [13] N. Petrone, C. R. Dean, I. Meric, A. M. van der Zande, P. Y. Huang, L. Wang, D. Muller, K. L. Shepard, and J. Hone. “Chemical Vapor Deposition-Derived Graphene with Electrical Performance of Exfoliated Graphene”. In: *Nano Letters* 12.6 (2012), pp. 2751–2756 (cit. on p. 5).
- [14] F. Xia, D. B. Farmer, Y.-m. Lin, and P. Avouris. “Graphene Field-Effect Transistors with High On/Off Current Ratio and Large Transport Band Gap at Room Temperature”. In: *Nano Letters* 10.2 (2010), pp. 715–718 (cit. on p. 5).
- [15] M. Y. Han, B. Özyilmaz, Y. Zhang, and P. Kim. “Energy Band-Gap Engineering of Graphene Nanoribbons”. In: *Physical Review Letters* 98.20 (2007), p. 206805. arXiv: 0702511 [cond-mat] (cit. on p. 5).
- [16] J. H. Jørgensen et al. “Symmetry-Driven Band Gap Engineering in Hydrogen Functionalized Graphene”. In: *ACS Nano* 10.12 (2016), pp. 10798–10807 (cit. on p. 5).
- [17] R. Balog et al. “Bandgap opening in graphene induced by patterned hydrogen adsorption”. In: *Nature Materials* 9.4 (2010), pp. 315–319 (cit. on p. 5).
- [18] S. Y. Zhou, G.-H. Gweon, A. V. Fedorov, P. N. First, W. A. de Heer, D.-H. Lee, F. Guinea, A. H. Castro Neto, and A. Lanzara. “Substrate-induced bandgap opening in epitaxial graphene”. In: *Nature Materials* 6.10 (2007), pp. 770–775. arXiv: 0709.1706 (cit. on p. 5).
- [19] Z. H. Ni, T. Yu, Y. H. Lu, Y. Y. Wang, Y. P. Feng, and Z. X. Shen. “Uniaxial Strain on Graphene: Raman Spectroscopy Study and Band-Gap Opening”. In: *ACS Nano* 2.11 (2008), pp. 2301–2305 (cit. on p. 5).
- [20] A. H. Castro Neto, F. Guinea, N. M. R. Peres, K. S. Novoselov, and A. K. Geim. “The electronic properties of graphene”. In: *Reviews of Modern Physics* 81.1 (2009), pp. 109–162. arXiv: 0709.1163 (cit. on pp. 5, 7, 8).

- [21] K. S. Novoselov, A. K. Geim, S. V. Morozov, D. Jiang, Y. Zhang, S. V. Dubonos, I. V. Grigorieva, and A. A. Firsov. “Electric Field Effect in Atomically Thin Carbon Films”. In: *Science* 306.5696 (2004), pp. 666–669 (cit. on p. 5).
- [22] R. R. Nair, P. Blake, a. N. Grigorenko, K. S. Novoselov, T. J. Booth, T. Stauber, N. M. R. Peres, and a. K. Geim. “Fine Structure Constant Defines Visual Transparency of Graphene”. In: *Science* 320.June (2008), p. 2008. arXiv: 0803.3718v1 (cit. on p. 7).
- [23] A. A. Balandin, S. Ghosh, W. Bao, I. Calizo, D. Teweldebrhan, F. Miao, and C. N. Lau. “Superior thermal conductivity of single-layer graphene”. In: *Nano Letters* 8.3 (2008), pp. 902–907. arXiv: 0802.1367v1 (cit. on p. 7).
- [24] C. Lee, X. Wei, J. W. Kysar, and J. Hone. “Measurement of the Elastic Properties and Intrinsic Strength of Monolayer Graphene”. In: *Science* 321.July (2008), pp. 385–388 (cit. on p. 7).
- [25] P. Avouris. “Graphene: Electronic and photonic properties and devices”. In: *Nano Letters* 10.11 (2010), pp. 4285–4294 (cit. on pp. 7, 8).
- [26] D. C. Elias et al. “Dirac cones reshaped by interaction effects in suspended graphene”. In: *Nat Phys* 7.9 (2011), pp. 701–704 (cit. on p. 7).
- [27] A. K. Geim and K. S. Novoselov. “The rise of graphene”. In: *Nat Mater* 6.3 (2007), pp. 183–191 (cit. on p. 8).
- [28] S. De and J. N. Coleman. “Are there fundamental limitations on the sheet resistance and transmittance of thin graphene films?” In: *ACS Nano* 4.5 (2010), pp. 2713–2720 (cit. on p. 8).
- [29] W. Kerner and G. Schnable. “Low-Pressure Chemical Vapor Deposition for Very Large-Scale Integration Processing - A Review”. In: *IEEE Transactions on Electron Devices* 26.4 (1979), pp. 647–657 (cit. on p. 9).
- [30] A. W. Tsen, L. Brown, R. W. Havener, and J. Park. “Polycrystallinity and Stacking in CVD Graphene”. In: *Accounts of Chemical Research* 46.10 (2013), pp. 2286–2296 (cit. on p. 10).
- [31] X. Li et al. “Large-area synthesis of high-quality and uniform graphene films on copper foils.” In: *Science* 324.5932 (2009), pp. 1312–1314. arXiv: 0905.1712 (cit. on p. 10).
- [32] K. S. Kim, Y. Zhao, H. Jang, S. Y. Lee, J. M. Kim, K. S. Kim, J. H. Ahn, P. Kim, J. Y. Choi, and B. H. Hong. “Large-scale pattern growth of graphene films for stretchable transparent electrodes”. In: *Nature* 457.7230 (2009), pp. 706–710 (cit. on pp. 10, 12).

- [33] G. Lupina et al. “Residual metallic contamination of transferred chemical vapor deposited graphene”. In: *ACS Nano* 9.5 (2015), pp. 4776–4785 (cit. on p. 10).
- [34] A. Ambrosi and M. Pumera. “The CVD graphene transfer procedure introduces metallic impurities which alter the graphene electrochemical properties”. In: *Nanoscale* 6.1 (2014), pp. 472–476 (cit. on p. 10).
- [35] H. Wang and G. Yu. “Direct CVD Graphene Growth on Semiconductors and Dielectrics for Transfer-Free Device Fabrication”. In: *Advanced Materials* 28.25 (2016), pp. 4956–4975 (cit. on p. 10).
- [36] L. Tai, D. Zhu, X. Liu, T. Yang, L. Wang, R. Wang, S. Jiang, Z. Chen, Z. Xu, and X. Li. “Direct Growth of Graphene on Silicon by Metal-Free Chemical Vapor Deposition”. In: *Nano-Micro Letters* 10.2 (2018), p. 20 (cit. on p. 10).
- [37] G. Wang et al. “Direct growth of graphene film on germanium substrate”. In: *Scientific Reports* 3 (2013), pp. 1–6. arXiv: 0810.5358 (cit. on pp. 11, 12).
- [38] J.-H. Lee et al. “Wafer-Scale Growth of Single-Crystal Monolayer Graphene on Reusable Hydrogen-Terminated Germanium”. In: *Science* 344.6181 (2014), pp. 286–289 (cit. on pp. 11, 14–16, 50).
- [39] R. M. Jacobberger et al. “Direct oriented growth of armchair graphene nanoribbons on germanium”. In: *Nature Communications* 6 (2015), pp. 1–8 (cit. on pp. 11, 12).
- [40] L. H. Zeng et al. “Monolayer graphene/germanium schottky junction as high-performance self-driven infrared light photodetector”. In: *ACS Applied Materials and Interfaces* 5.19 (2013), pp. 9362–9366 (cit. on p. 11).
- [41] M. Pea, M. De Seta, L. Di Gaspare, L. Persichetti, A. M. Scaparro, V. Misikis, C. Coletti, and A. Notargiacomo. “Submicron Size Schottky Junctions on As-Grown Monolayer Epitaxial Graphene on Ge(100): A Low-Invasive Scanned-Probe-Based Study”. In: *ACS Applied Materials & Interfaces* 11.38 (2019), pp. 35079–35087 (cit. on pp. 11, 63).
- [42] R. Rojas Delgado, R. M. Jacobberger, S. S. Roy, V. S. Mangu, M. S. Arnold, F. Cavallo, and M. G. Lagally. “Passivation of Germanium by Graphene”. In: *ACS Applied Materials and Interfaces* 9.20 (2017), pp. 17629–17636 (cit. on p. 11).

- [43] F. Akhtar, J. Dabrowski, M. Lisker, Y. Yamamoto, A. Mai, C. Wenger, and M. Lukosius. “Investigation of the Oxidation Behavior of Graphene/Ge(001) Versus Graphene/Ge(110) Systems”. In: *ACS Applied Materials and Interfaces* 12.2 (2020), pp. 3188–3197 (cit. on p. 11).
- [44] B. Kiraly, R. M. Jacobberger, A. J. Mannix, G. P. Campbell, M. J. Bedzyk, M. S. Arnold, M. C. Hersam, and N. P. Guisinger. “Electronic and Mechanical Properties of Graphene-Germanium Interfaces Grown by Chemical Vapor Deposition”. In: *Nano Letters* 15.11 (2015), pp. 7414–7420 (cit. on pp. 11, 69, 70).
- [45] Y. Dedkov and E. Voloshina. “Epitaxial graphene/Ge interfaces: A minireview”. In: *Nanoscale* 12.21 (2020), pp. 11416–11426 (cit. on p. 11).
- [46] G. Lippert et al. “Graphene grown on Ge(0 0 1) from atomic source”. In: *Carbon* 75 (2014), pp. 104–112 (cit. on p. 11).
- [47] K. M. McElhinny, R. M. Jacobberger, A. J. Zaugg, M. S. Arnold, and P. G. Evans. “Graphene-induced Ge (001) surface faceting”. In: *Surface Science* 647 (2016), pp. 90–95 (cit. on pp. 11, 12).
- [48] A. M. Scaparro, V. Miseikis, C. Coletti, A. Notargiacomo, M. Pea, M. De Seta, and L. Di Gaspare. “Investigating the CVD Synthesis of Graphene on Ge(100): Toward Layer-by-Layer Growth”. In: *ACS Applied Materials and Interfaces* 8.48 (2016), pp. 33083–33090 (cit. on p. 12).
- [49] C. Mendoza, P. Caldas, F. Freire, and M. Maia da Costa. “Growth of single-layer graphene on Ge (1 0 0) by chemical vapor deposition”. In: *Applied Surface Science* 447 (2018), pp. 816–821 (cit. on p. 12).
- [50] L. Persichetti, L. Di Gaspare, F. Fabbri, A. Scaparro, A. Notargiacomo, A. Sgarlata, M. Fanfoni, V. Miseikis, C. Coletti, and M. De Seta. “Abrupt changes in the graphene on Ge(001) system at the onset of surface melting”. In: *Carbon* 145 (2019), pp. 345–351 (cit. on pp. 12, 13).
- [51] A. Laine and M. DeSeta. “Surface phase transitions of Ge(100) from temperature-dependent valence-band photoemission”. In: *Physical Review B - Condensed Matter and Materials Physics* 57.23 (1998), pp. 14654–14657 (cit. on p. 12).
- [52] U. Tartaglino, T. Zykova-Timan, F. Ercolessi, and E. Tosatti. “Melting and nonmelting of solid surfaces and nanosystems”. In: *Physics Reports* 411.5 (2005), pp. 291–321. arXiv: 0504680 [cond-mat] (cit. on p. 12).
- [53] J. M. Wofford, S. Nie, K. F. McCarty, N. C. Bartelt, and O. D. Dubon. “Graphene islands on Cu foils: The interplay between shape, orientation, and defects”. In: *Nano Letters* 10.12 (2010), pp. 4890–4896 (cit. on p. 14).

- [54] Z. J. Wang et al. “Direct observation of graphene growth and associated copper substrate dynamics by in situ scanning electron microscopy”. In: *ACS Nano* 9.2 (2015), pp. 1506–1519 (cit. on p. 14).
- [55] L. Persichetti, A. Sgarlata, M. Fanfoni, and A. Balzarotti. “Irreversible order-disorder transformation of Ge(0 0 1) probed by scanning tunnelling microscopy”. In: *Journal of Physics: Condensed Matter* 27.43 (2015), p. 435001 (cit. on p. 14).
- [56] P. Dabrowski, M. Rogala, I. Pasternak, J. Baranowski, W. Strupinski, M. Kopciuszynski, R. Zdyb, M. Jalochocki, I. Lutsyk, and Z. Klusek. “The study of the interactions between graphene and Ge(001)/Si(001)”. In: *Nano Research* 10.11 (2017), pp. 3648–3661 (cit. on p. 14).
- [57] A. C. Ferrari and D. M. Basko. “Raman spectroscopy as a versatile tool for studying the properties of graphene”. In: *Nature Nanotechnology* 8.4 (2013), pp. 235–246. arXiv: arXiv:1306.5856v1 (cit. on pp. 14, 43, 44).
- [58] T. T. Pham, N. D. Nam, and R. Sporcken. “Surface morphology, structural and electronic properties of graphene on Ge(111) via direct deposition of solid-state carbon atoms”. In: *Thin Solid Films* 639 (2017), pp. 84–90 (cit. on p. 14).
- [59] J. Dai et al. “How Graphene Islands Are Unidirectionally Aligned on the Ge(110) Surface”. In: *Nano Letters* 16.5 (2016), pp. 3160–3165 (cit. on pp. 16, 69).
- [60] A. Becker, C. Wenger, and J. Dabrowski. “Influence of temperature on growth of graphene on germanium”. In: *Journal of Applied Physics* 128.4 (2020), p. 045310 (cit. on p. 16).
- [61] T. Wang, P. Li, X. Hu, M. Gao, Z. Di, Z. Xue, and M. Zhang. “Wafer-scale fabrication of single-crystal graphene on Ge(1 1 0) substrate by optimized CH₄/H₂ ratio”. In: *Applied Surface Science* 529.June (2020), p. 147066 (cit. on p. 16).
- [62] H. W. Kim, I. Jeon, W. Ko, and S. H. Kim. “Unidirectional growth of graphene nano-islands from carbon cluster seeds on Ge(1 1 0)”. In: *Applied Surface Science* 536.September 2020 (2021), p. 147722 (cit. on p. 16).
- [63] P. C. Rogge, M. E. Foster, J. M. Wofford, K. F. McCarty, N. C. Bartelt, and O. D. Dubon. “On the rotational alignment of graphene domains grown on Ge(110) and Ge(111)”. In: *MRS Communications* 5.3 (2015), pp. 539–546 (cit. on p. 16).

- [64] L. Persichetti et al. “Driving with temperature the synthesis of graphene on Ge(110)”. In: *Applied Surface Science* 499.May 2019 (2020), p. 143923 (cit. on p. 16).
- [65] D. Zhou, Z. Niu, and T. Niu. “Surface Reconstruction of Germanium: Hydrogen Intercalation and Graphene Protection”. In: *Journal of Physical Chemistry C* 122.38 (2018), pp. 21874–21882 (cit. on pp. 17, 47, 50, 69).
- [66] G. P. Campbell, B. Kiraly, R. M. Jacobberger, A. J. Mannix, M. S. Arnold, M. C. Hersam, N. P. Guisinger, and M. J. Bedzyk. “Epitaxial graphene-encapsulated surface reconstruction of Ge(110)”. In: *Physical Review Materials* 2.4 (2018), p. 044004 (cit. on pp. 17, 47, 50, 69).
- [67] B. Kiraly, A. J. Mannix, R. M. Jacobberger, B. L. Fisher, M. S. Arnold, M. C. Hersam, and N. P. Guisinger. “Driving chemical interactions at graphene-germanium van der Waals interfaces via thermal annealing”. In: *Applied Physics Letters* 113.21 (2018), pp. 1–6 (cit. on pp. 17, 47, 50, 69, 73).
- [68] M. Galbiati et al. “Tuning the Doping of Epitaxial Graphene on a Conventional Semiconductor via Substrate Surface Reconstruction”. In: *Journal of Physical Chemistry Letters* 12.4 (2021), pp. 1262–1267 (cit. on pp. 17, 18, 48, 50–54, 57, 59, 61–65).
- [69] M. Galbiati, M. Scarselli, F. Arciprete, M. De Crescenzi, and L. Camilli. “Scanning tunneling microscopy study of CaF₂ on Si(111): Observation of metastable reconstructions”. In: *Journal of Physics D: Applied Physics* 55.9 (2021), p. 95304 (cit. on pp. 17, 18, 80, 94, 95, 97, 98).
- [70] M. Galbiati, N. Motta, M. De Crescenzi, and L. Camilli. “Group-IV 2D materials beyond graphene on nonmetal substrates: Challenges, recent progress, and future perspectives”. In: *Applied Physics Reviews* 6.4 (2019), p. 041310 (cit. on pp. 17, 18, 79).
- [71] S. Mobilio, F. Boscherini, and C. Meneghini. *Synchrotron Radiation*. Ed. by S. Mobilio, F. Boscherini, and C. Meneghini. 1st ed. Berlin, Heidelberg: Springer Berlin Heidelberg, 2015, pp. XXIV, 799 (cit. on pp. 23–25, 32, 38, 40).
- [72] J. Liouville. “Sur l’équation aux différences partielles $\{d^2 \log \lambda \over du dv\} \pm \{\lambda \over 2a^2\} = 0$.” In: *Journal de Mathématiques Pures et Appliquées* (1853), pp. 71–72 (cit. on p. 27).
- [73] G. Binnig, H. Rohrer, C. Gerber, and E. Weibel. “Tunneling through a controllable vacuum gap”. In: *Applied Physics Letters* 40.2 (1982), pp. 178–180 (cit. on p. 27).

- [74] G. Binnig, C. F. Quate, and C. Gerber. “Atomic Force Microscope”. In: *Physical Review Letters* 56.9 (1986). Ed. by R. Splinter, pp. 930–933 (cit. on p. 27).
- [75] Y. Martin and H. K. Wickramasinghe. “Magnetic imaging by “force microscopy” with 1000 Å resolution”. In: *Applied Physics Letters* 50.20 (1987), pp. 1455–1457 (cit. on p. 27).
- [76] S. Kano, T. Tada, and Y. Majima. “Nanoparticle characterization based on STM and STS”. In: *Chemical Society Reviews* 44.4 (2015), pp. 970–987 (cit. on p. 29).
- [77] J. Bardeen. “Tunnelling from a Many-Particle Point of View”. In: *Physical Review Letters* 6.2 (1961), pp. 57–59 (cit. on p. 30).
- [78] J. Tersoff and D. R. Hamann. “Theory and Application for the Scanning Tunneling Microscope”. In: *Physical Review Letters* 50.25 (1983), pp. 1998–2001 (cit. on p. 30).
- [79] J. Tersoff and D. R. Hamann. “Theory of the scanning tunneling microscope”. In: *Physical Review B* 31.2 (1985), pp. 805–813 (cit. on p. 30).
- [80] R. M. Feenstra, J. A. Stroscio, J. Tersoff, and A. P. Fein. “Atom-selective imaging of the GaAs(110) surface”. In: *Physical Review Letters* 58.12 (1987), pp. 1192–1195 (cit. on p. 31).
- [81] G. Binnig and H. Rohrer. “Scanning tunneling microscopy”. In: *Surface Science* 126.1-3 (1983), pp. 236–244 (cit. on p. 31).
- [82] H. Hertz. “Ueber einen Einfluss des ultravioletten Lichtes auf die elektrische Entladung”. In: *Annalen der Physik und Chemie* 267.8 (1887), pp. 983–1000 (cit. on p. 32).
- [83] A. Einstein. “Zur Theorie der Lichterzeugung und Lichtabsorption”. In: *Annalen der Physik* 325.6 (1906), pp. 199–206 (cit. on p. 32).
- [84] I. Chorkendorff and J. W. Niemantsverdriet. *Concept of Modern Catalysis and Kinetics*. Wiley-VCH, 2003 (cit. on pp. 37, 39).
- [85] E. Tatarova et al. “Towards large-scale in free-standing graphene and N-graphene sheets”. In: *Scientific Reports* 7.1 (2017), p. 10175 (cit. on p. 42).
- [86] A Das et al. “Monitoring dopants by Raman scattering in an electrochemically top-gated graphene transistor.” In: *Nature nanotechnology* 3.4 (2008), pp. 210–5. arXiv: 0709.1174 (cit. on pp. 43, 45, 77).

- [87] P. Y. Yu and M. Cardona. *Fundamentals of Semiconductors*. Fourth Edi. Graduate Texts in Physics. Berlin, Heidelberg: Springer Berlin Heidelberg, 2010, pp. XXII, 778 (cit. on pp. 43, 44).
- [88] A. C. Ferrari et al. “Raman spectrum of graphene and graphene layers”. In: *Physical Review Letters* 97.18 (2006), pp. 1–4 (cit. on pp. 44, 45).
- [89] R. M. Jacobberger, M. J. Dodd, M. Zamiri, A. J. Way, M. S. Arnold, and M. G. Lagally. “Passivation of Germanium by Graphene for Stable Graphene/Germanium Heterostructure Devices”. In: *ACS Applied Nano Materials* 2.7 (2019), pp. 4313–4322 (cit. on p. 47).
- [90] W. Chen, X. Wang, S. Li, C. Yan, L. He, P. Zhang, Y. Yang, D. Ma, J. Nie, and R. Dou. “Robust atomic-structure of the 6×2 reconstruction surface of Ge(110) protected by the electronically transparent graphene monolayer”. In: *Physical Chemistry Chemical Physics* 22.39 (2020), pp. 22711–22718 (cit. on p. 49).
- [91] P. Jia et al. “Programmable graphene nanobubbles with three-fold symmetric pseudo-magnetic fields”. In: *Nature Communications* 10.1 (2019), pp. 6–11 (cit. on pp. 50, 75).
- [92] H. W. Kim, W. Ko, W. J. Joo, Y. Cho, Y. Oh, J. Ku, I. Jeon, S. Park, and S. W. Hwang. “Unraveling the Structural and Electronic Properties of Graphene/Ge(110)”. In: *Journal of Physical Chemistry Letters* 9.24 (2018), pp. 7059–7063 (cit. on p. 57).
- [93] S. V. Hoffmann, C. Søndergaard, C. Schultz, Z. Li, and P. Hofmann. “An undulator-based spherical grating monochromator beamline for angle-resolved photoemission spectroscopy”. In: *Nuclear Instruments and Methods in Physics Research, Section A: Accelerators, Spectrometers, Detectors and Associated Equipment* 523.3 (2004), pp. 441–453 (cit. on p. 58).
- [94] R. Larciprete et al. “Oxygen Switching of the Epitaxial Graphene–Metal Interaction”. In: *ACS Nano* 6.11 (2012), pp. 9551–9558 (cit. on p. 61).
- [95] I. Pletikosić, M. Kralj, P. Pervan, R. Brako, J. Coraux, A. T. N’Diaye, C. Busse, and T. Michely. “Dirac Cones and Minigaps for Graphene on Ir(111)”. In: *Physical Review Letters* 102.5 (2009), p. 056808 (cit. on p. 61).
- [96] P. Giannozzi et al. “QUANTUM ESPRESSO: a modular and open-source software project for quantum simulations of materials”. In: *Journal of Physics: Condensed Matter* 21.39 (2009), p. 395502. arXiv: 0906.2569 (cit. on p. 62).

- [97] M. Dion, H. Rydberg, E. Schröder, D. C. Langreth, and B. I. Lundqvist. “Van der Waals Density Functional for General Geometries”. In: *Physical Review Letters* 92.24 (2004), p. 246401. arXiv: 0402105 [cond-mat] (cit. on p. 62).
- [98] A. Tkatchenko and M. Scheffler. “Accurate Molecular Van Der Waals Interactions from Ground-State Electron Density and Free-Atom Reference Data”. In: *Physical Review Letters* 102.7 (2009), p. 073005 (cit. on p. 62).
- [99] S. Mayburg. “Vacancies and Interstitials in Heat Treated Germanium”. In: *Physical Review* 95.1 (1954), pp. 38–43 (cit. on p. 63).
- [100] R. A. Logan. “Thermally Induced Acceptors in Germanium”. In: *Physical Review* 101.5 (1956), pp. 1455–1459 (cit. on p. 63).
- [101] J. Vanhellefont, J. Lauwaert, A. Witecka, P. Śpiwak, I. Romandic, and P. Clauws. “Experimental and theoretical study of the thermal solubility of the vacancy in germanium”. In: *Physica B: Condensed Matter* 404.23-24 (2009), pp. 4529–4532 (cit. on p. 63).
- [102] S. H. Segers, J. Lauwaert, P. Clauws, E. Simoen, J. Vanhellefont, F. Calens, and H. Vrielinck. “Direct estimation of capture cross sections in the presence of slow capture: application to the identification of quenched-in deep-level defects in Ge”. In: *Semiconductor Science and Technology* 29.12 (2014), p. 125007 (cit. on p. 63).
- [103] J. Tesch et al. “The graphene/n-Ge(110) interface: structure, doping, and electronic properties”. In: *Nanoscale* 10.13 (2018), pp. 6088–6098 (cit. on pp. 65, 69).
- [104] R. Blume, D. Rosenthal, J.-P. Tessonier, H. Li, A. Knop-Gericke, and R. Schlögl. “Characterizing Graphitic Carbon with X-ray Photoelectron Spectroscopy: A Step-by-Step Approach”. In: *ChemCatChem* 7.18 (2015), pp. 2871–2881 (cit. on p. 72).
- [105] L. G. Bulusheva, A. V. Okotrub, I. P. Asanov, A. Fonseca, and J. B. Nagy. “Comparative Study on the Electronic Structure of Arc-Discharge and Catalytic Carbon Nanotubes”. In: *The Journal of Physical Chemistry B* 105.21 (2001), pp. 4853–4859 (cit. on p. 72).
- [106] L. G. Bulusheva et al. “Creation of nanosized holes in graphene planes for improvement of rate capability of lithium-ion batteries”. In: *Nanotechnology* 29.13 (2018), p. 134001 (cit. on p. 72).

- [107] L. G. Bulusheva, V. E. Arkhipov, K. M. Popov, V. I. Sysoev, A. A. Makarova, and A. V. Okotrub. “Electronic Structure of Nitrogen- and Phosphorus-Doped Graphenes Grown by Chemical Vapor Deposition Method”. In: *Materials* 13.5 (2020), p. 1173 (cit. on pp. 72, 77).
- [108] R. Balog et al. “Hydrogen interaction with graphene on Ir(1 1 1): a combined intercalation and functionalization study”. In: *Journal of Physics: Condensed Matter* 31.8 (2019), p. 085001 (cit. on pp. 72, 77).
- [109] E. Grånäs, T. Gerber, U. A. Schröder, K. Schulte, J. N. Andersen, T. Michely, and J. Knudsen. “Hydrogen intercalation under graphene on Ir(111)”. In: *Surface Science* 651 (2016), pp. 57–61 (cit. on p. 72).
- [110] U. A. Schröder et al. “Core level shifts of intercalated graphene”. In: *2D Materials* 4.1 (2016), p. 015013 (cit. on p. 72).
- [111] K. Hatano, Y. Asano, Y. Kameda, A. Koshio, and F. Kokai. “Formation of Germanium-Carbon Core-Shell Nanowires by Laser Vaporization in High-Pressure Ar Gas without the Addition of Other Metal Catalysts”. In: *Materials Sciences and Applications* 08.12 (2017), pp. 838–847 (cit. on pp. 72, 73).
- [112] K. Prabhakaran and T. Ogino. “Oxidation of Ge(100) and Ge(111) surfaces: an UPS and XPS study”. In: *Surface Science* 325.3 (1995), pp. 263–271 (cit. on p. 73).
- [113] P. E. Eriksson and R. I. Uhrberg. “Surface core-level shifts on clean Si(001) and Ge(001) studied with photoelectron spectroscopy and density functional theory calculations”. In: *Physical Review B - Condensed Matter and Materials Physics* 81.12 (2010), pp. 1–6 (cit. on p. 73).
- [114] A. Goldoni, S. Modesti, and V. Dhanak. “Evidence for three surface components in the 3d core-level photoemission spectra of Ge(100)-(2×1) surface”. In: *Physical Review B - Condensed Matter and Materials Physics* 54.16 (1996), pp. 11340–11345 (cit. on p. 73).
- [115] T. W. Pi, J. F. Wen, C. P. Ouyang, and R. T. Wu. “Surface core-level shifts of Ge(100) - 2 × 1”. In: *Physical Review B - Condensed Matter and Materials Physics* 63.15 (2001), pp. 2–4 (cit. on p. 73).
- [116] K. Prabhakaran, F. Maeda, Y. Watanabe, and T. Ogino. “Distinctly different thermal decomposition pathways of ultrathin oxide layer on Ge and Si surfaces”. In: *Applied Physics Letters* 76.16 (2000), pp. 2244–2246 (cit. on p. 73).

- [117] J. Oh and J. C. Campbell. “Thermal desorption of Ge native oxides and loss of Ge from the surface”. In: *Materials Science in Semiconductor Processing* 13.3 (2010), pp. 185–188 (cit. on p. 73).
- [118] D. A. Fischer, R. M. Wentzcovitch, R. G. Carr, A. Continenza, and A. J. Freeman. “Graphitic interlayer states: A carbon K near-edge x-ray-absorption fine-structure study”. In: *Physical Review B* 44.3 (1991), pp. 1427–1429 (cit. on p. 74).
- [119] D. Pacilé, M. Papagno, A. F. Rodríguez, M. Grioni, L. Papagno, Ç. Ö. Girit, J. C. Meyer, G. E. Begtrup, and A. Zettl. “Near-Edge X-Ray Absorption Fine-Structure Investigation of Graphene”. In: *Physical Review Letters* 101.6 (2008), p. 066806 (cit. on pp. 74, 77).
- [120] W. Hua, B. Gao, S. Li, H. Ågren, and Y. Luo. “X-ray absorption spectra of graphene from first-principles simulations”. In: *Physical Review B* 82.15 (2010), p. 155433 (cit. on pp. 74, 77).
- [121] R. Balog, M. Andersen, B. Jørgensen, Z. Sljivancanin, B. Hammer, A. Baraldi, R. Larciprete, P. Hofmann, L. Hornekær, and S. Lizzit. “Controlling Hydrogenation of Graphene on Ir(111)”. In: *ACS Nano* 7.5 (2013), pp. 3823–3832 (cit. on p. 77).
- [122] J. E. Lee, G. Ahn, J. Shim, Y. S. Lee, and S. Ryu. “Optical separation of mechanical strain from charge doping in graphene”. In: *Nature Communications* 3.1 (2012), p. 1024 (cit. on p. 77).
- [123] S. Cahangirov, M. Topsakal, E. Aktürk, H. Şahin, and S. Ciraci. “Two- and One-Dimensional Honeycomb Structures of Silicon and Germanium”. In: *Physical Review Letters* 102.23 (2009), p. 236804 (cit. on pp. 80, 85).
- [124] B. Feng, Z. Ding, S. Meng, Y. Yao, X. He, P. Cheng, L. Chen, and K. Wu. “Evidence of Silicene in Honeycomb Structures of Silicon on Ag(111)”. In: *Nano Letters* 12.7 (2012), pp. 3507–3511 (cit. on pp. 80, 82).
- [125] M. Dávila, L. Lew Yan Voon, J. Zhao, and G. Le Lay. “Elemental Group IV Two-Dimensional Materials Beyond Graphene”. In: *Semiconductors and Semimetals*. Vol. 95. 2016, pp. 149–188 (cit. on p. 80).
- [126] L. Zhang, P. Bampoulis, A. N. Rudenko, Q. Yao, A. van Houselt, B. Poelsema, M. I. Katsnelson, and H. J. W. Zandvliet. “Structural and Electronic Properties of Germanene on MoS₂”. In: *Physical Review Letters* 116.25 (2016), p. 256804. arXiv: 1706.00680 (cit. on p. 80).

- [127] F.-f. Zhu, W.-j. Chen, Y. Xu, C.-l. Gao, D.-d. Guan, C.-h. Liu, D. Qian, S.-C. Zhang, and J.-f. Jia. “Epitaxial growth of two-dimensional stanene”. In: *Nature Materials* 14.10 (2015), pp. 1020–1025 (cit. on p. 80).
- [128] P. Tang, P. Chen, W. Cao, H. Huang, S. Cahangirov, L. Xian, Y. Xu, S.-C. Zhang, W. Duan, and A. Rubio. “Stable two-dimensional dumbbell stanene: A quantum spin Hall insulator”. In: *Physical Review B* 90.12 (2014), p. 121408. arXiv: 1407.1929 (cit. on p. 80).
- [129] M. E. Dávila, L. Xian, S. Cahangirov, A. Rubio, and G. Le Lay. “Germanene: A novel two-dimensional germanium allotrope akin to graphene and silicene”. In: *New Journal of Physics* 16.111 (2014). arXiv: 1309.2242 (cit. on pp. 80, 82).
- [130] H. Oughaddou, H. Enriquez, M. R. Tchalala, H. Yildirim, A. J. Mayne, A. Bendounan, G. Dujardin, M. Ait Ali, and A. Kara. “Silicene, a promising new 2D material”. In: *Progress in Surface Science* 90.1 (2015), pp. 46–83 (cit. on p. 80).
- [131] C. Grazianetti, E. Cinquanta, and A. Molle. “Two-dimensional silicon: the advent of silicene”. In: *2D Materials* 3.1 (2016), p. 012001 (cit. on p. 80).
- [132] M. Chhowalla, D. Jena, and H. Zhang. “Two-Dimensional Semiconductors for Transistors”. In: *Nature Reviews Materials* 1 (2016), p. 16052 (cit. on p. 80).
- [133] M Houssa, A Dimoulas, and A Molle. “Silicene: a review of recent experimental and theoretical investigations”. In: *Journal of Physics: Condensed Matter* 27.25 (2015), p. 253002 (cit. on p. 80).
- [134] A Acun et al. “Germanene: the germanium analogue of graphene”. In: *Journal of Physics: Condensed Matter* 27.44 (2015), p. 443002 (cit. on p. 80).
- [135] S. Balendhran, S. Walia, H. Nili, S. Sriram, and M. Bhaskaran. “Elemental Analogues of Graphene: Silicene, Germanene, Stanene, and Phosphorene”. In: *Small* 11.6 (2015), pp. 640–652 (cit. on p. 80).
- [136] Z. Xiong, L. Zhong, H. Wang, and X. Li. “Structural Defects, Mechanical Behaviors, and Properties of Two-Dimensional Materials”. In: *Materials* 14.5 (2021), p. 1192 (cit. on p. 81).
- [137] A. Molle, J. Goldberger, M. Houssa, Y. Xu, S.-c. Zhang, and D. Akinwande. “Buckled two-dimensional Xene sheets”. In: *Nature Materials* 16.2 (2017), pp. 163–169 (cit. on p. 80).

- [138] C.-C. Liu, W. Feng, and Y. Yao. “Quantum Spin Hall Effect in Silicene and Two-Dimensional Germanium”. In: *Physical Review Letters* 107.7 (2011), p. 076802 (cit. on p. 81).
- [139] B Van Den Broek, M. Houssa, E. Scalise, G. Pourtois, V. V. Afanas’ev, and A. Stesmans. “Two-dimensional hexagonal tin: ab initio geometry, stability, electronic structure and functionalization”. In: *2D Materials* 1.2 (2014), p. 021004 (cit. on p. 81).
- [140] M. Ezawa. “Quasi-Topological Insulator and Trigonal Warping in Gated Bilayer Silicene”. In: *Journal of the Physical Society of Japan* 81.10 (2012), p. 104713 (cit. on p. 81).
- [141] M. Tahir, A. Manchon, K. Sabeeh, and U. Schwingenschlögl. “Quantum spin/valley Hall effect and topological insulator phase transitions in silicene”. In: *Applied Physics Letters* 102.16 (2013), p. 162412 (cit. on p. 81).
- [142] Y. Kim, K. Choi, J. Ihm, and H. Jin. “Topological domain walls and quantum valley Hall effects in silicene”. In: *Physical Review B* 89.8 (2014), p. 085429 (cit. on p. 81).
- [143] L. C. Lew Yan Voon, J. Zhu, and U. Schwingenschlögl. “Silicene: Recent theoretical advances”. In: *Applied Physics Reviews* 3.4 (2016), p. 040802 (cit. on p. 82).
- [144] J. Deng et al. “Epitaxial growth of ultraflat stanene with topological band inversion”. In: *Nature Materials* 17.12 (2018), pp. 1081–1086 (cit. on p. 82).
- [145] H. Liu, J. Gao, and J. Zhao. “Silicene on Substrates: A Way To Preserve or Tune Its Electronic Properties”. In: *The Journal of Physical Chemistry C* 117.20 (2013), pp. 10353–10359 (cit. on p. 82).
- [146] R. Quhe et al. “Tunable and sizable band gap in silicene by surface adsorption”. In: *Scientific Reports* 2.1 (2012), p. 853 (cit. on p. 82).
- [147] P. De Padova et al. “Evidence of graphene-like electronic signature in silicene nanoribbons”. In: *Applied Physics Letters* 96.26 (2010), p. 261905 (cit. on p. 82).
- [148] S. Cahangirov, M. Topsakal, and S. Ciraci. “Armchair nanoribbons of silicon and germanium honeycomb structures”. In: *Physical Review B* 81.19 (2010), p. 195120. arXiv: 1001.1601 (cit. on p. 82).
- [149] P. De Padova, P. Perfetti, B. Olivieri, C. Quaresima, C. Ottaviani, and G. Le Lay. “1D graphene-like silicon systems: silicene nano-ribbons”. In: *Journal of Physics: Condensed Matter* 24.22 (2012), p. 223001 (cit. on p. 82).

- [150] P. Vogt, P. De Padova, C. Quaresima, J. Avila, E. Frantzeskakis, M. C. Asensio, A. Resta, B. Ealet, and G. Le Lay. “Silicene: Compelling Experimental Evidence for Graphenelike Two-Dimensional Silicon”. In: *Physical Review Letters* 108.15 (2012), p. 155501 (cit. on p. 82).
- [151] D. Chiappe, C. Grazianetti, G. Tallarida, M. Fanciulli, and A. Molle. “Local Electronic Properties of Corrugated Silicene Phases”. In: *Advanced Materials* 24.37 (2012), pp. 5088–5093. arXiv: 0811.4412 (cit. on p. 82).
- [152] H. Enriquez, S. Vizzini, A. Kara, B. Lalmi, and H. Oughaddou. “Silicene structures on silver surfaces”. In: *Journal of Physics: Condensed Matter* 24.31 (2012), p. 314211. arXiv: 1206.6246 (cit. on p. 82).
- [153] X. Huang, J. Guan, Z. Lin, B. Liu, S. Xing, W. Wang, and J. Guo. “Epitaxial Growth and Band Structure of Te Film on Graphene”. In: *Nano Letters* 17.8 (2017), pp. 4619–4623 (cit. on p. 82).
- [154] L. Meng et al. “Buckled Silicene Formation on Ir(111)”. In: *Nano Letters* 13.2 (2013), pp. 685–690 (cit. on p. 82).
- [155] A. Fleurence, R. Friedlein, T. Ozaki, H. Kawai, Y. Wang, and Y. Yamada-Takamura. “Experimental Evidence for Epitaxial Silicene on Diboride Thin Films”. In: *Physical Review Letters* 108.24 (2012), p. 245501 (cit. on p. 82).
- [156] C.-C. Lee, A. Fleurence, Y. Yamada-Takamura, T. Ozaki, and R. Friedlein. “Band structure of silicene on zirconium diboride (0001) thin-film surface: Convergence of experiment and calculations in the one-Si-atom Brillouin zone”. In: *Physical Review B* 90.7 (2014), p. 075422. arXiv: 1407.2698 (cit. on p. 82).
- [157] L. Li, S.-z. Lu, J. Pan, Z. Qin, Y.-q. Wang, Y. Wang, G.-y. Cao, S. Du, and H.-J. Gao. “Buckled Germanene Formation on Pt(111)”. In: *Advanced Materials* 26.28 (2014), pp. 4820–4824 (cit. on pp. 82, 83).
- [158] M. Derivaz, D. Dentel, R. Stephan, M.-C. Hanf, A. Mehdaoui, P. Sonnet, and C. Pirri. “Continuous Germanene Layer on Al(111)”. In: *Nano Letters* 15.4 (2015), pp. 2510–2516 (cit. on pp. 82, 83).
- [159] J. Gou, Q. Zhong, S. Sheng, W. Li, P. Cheng, H. Li, L. Chen, and K. Wu. “Strained monolayer germanene with 1×1 lattice on Sb(111)”. In: *2D Materials* 3.4 (2016), p. 045005 (cit. on pp. 82, 83).
- [160] J. Yuhara, Y. Fujii, K. Nishino, N. Isobe, M. Nakatake, L. Xian, A. Rubio, and G. L. Lay. “Large area planar stanene epitaxially grown on Ag(111)”. In: *2D Materials* 5.2 (2018), p. 025002 (cit. on pp. 82, 83).

- [161] Y. Wang, J. Li, J. Xiong, Y. Pan, M. Ye, Y. Guo, H. Zhang, R. Quhe, and J. Lu. “Does the Dirac cone of germanene exist on metal substrates?” In: *Physical Chemistry Chemical Physics* 18.28 (2016), pp. 19451–19456 (cit. on p. 83).
- [162] P. Pflugradt, L. Matthes, and F. Bechstedt. “Silicene on metal and metalized surfaces: ab initio studies”. In: *New Journal of Physics* 16.7 (2014), p. 075004 (cit. on p. 83).
- [163] A. Podsiadły-Paszowska and M. Krawiec. “Dirac fermions in silicene on Pb(111) surface”. In: *Physical Chemistry Chemical Physics* 17.3 (2015), pp. 2246–2251 (cit. on p. 83).
- [164] L. Tao, E. Cinquanta, D. Chiappe, C. Grazianetti, M. Fanciulli, M. Dubey, A. Molle, and D. Akinwande. “Silicene field-effect transistors operating at room temperature”. In: *Nature Nanotechnology* 10.3 (2015), pp. 227–231 (cit. on p. 83).
- [165] C. Grazianetti, E. Cinquanta, L. Tao, P. De Padova, C. Quaresima, C. Ottaviani, D. Akinwande, and A. Molle. “Silicon Nanosheets: Crossover between Multilayer Silicene and Diamond-like Growth Regime”. In: *ACS Nano* 11.3 (2017), pp. 3376–3382 (cit. on pp. 83, 84).
- [166] Y. Borensztein, A. Curcella, S. Royer, and G. Prévot. “Silicene multilayers on Ag(111) display a cubic diamondlike structure and a 3×3 reconstruction induced by surfactant Ag atoms”. In: *Physical Review B* 92.15 (2015), p. 155407 (cit. on pp. 83, 87).
- [167] G. Prévot, R. Bernard, H. Cruguel, and Y. Borensztein. “Monitoring Si growth on Ag(111) with scanning tunneling microscopy reveals that silicene structure involves silver atoms”. In: *Applied Physics Letters* 105.21 (2014), p. 213106 (cit. on p. 83).
- [168] C.-S. Ho, S. Banerjee, M. Batzill, D. E. Beck, and B. E. Koel. “Formation and structure of a $(19 \times 19)R23.4^\circ$ -Ge/Pt(111) surface alloy”. In: *Surface Science* 603.9 (2009), pp. 1161–1167 (cit. on p. 83).
- [169] Q. Chen, L. Liang, G. Potsi, P. Wan, J. Lu, T. Giousis, E. Thomou, D. Gournis, P. Rudolf, and J. Ye. “Highly Conductive Metallic State and Strong Spin–Orbit Interaction in Annealed Germanane”. In: *Nano Letters* 19.3 (2019), pp. 1520–1526 (cit. on p. 84).
- [170] A. Koma. “Van der Waals epitaxy—a new epitaxial growth method for a highly lattice-mismatched system”. In: *Thin Solid Films* 216.1 (1992), pp. 72–76 (cit. on p. 84).

- [171] L. A. Walsh and C. L. Hinkle. “van der Waals epitaxy: 2D materials and topological insulators”. In: *Applied Materials Today* 9 (2017), pp. 504–515 (cit. on p. 84).
- [172] A. Koma, K. Sunouchi, and T. Miyajima. “Fabrication and characterization of heterostructures with subnanometer thickness”. In: *Microelectronic Engineering* 2.1-3 (1984), pp. 129–136 (cit. on pp. 84, 87).
- [173] D. Chiappe, E. Scalise, E. Cinquanta, C. Grazianetti, B. van den Broek, M. Fanciulli, M. Houssa, and A. Molle. “Two-Dimensional Si Nanosheets with Local Hexagonal Structure on a MoS₂ Surface”. In: *Advanced Materials* 26.13 (2014), pp. 2096–2101 (cit. on pp. 84, 85).
- [174] A. Molle, A. Lamperti, D. Rotta, M. Fanciulli, E. Cinquanta, and C. Grazianetti. “Electron Confinement at the Si/MoS₂ Heterosheet Interface”. In: *Advanced Materials Interfaces* 3.10 (2016), p. 1500619 (cit. on p. 85).
- [175] M. De Crescenzi, I. Berbezier, M. Scarselli, P. Castrucci, M. Abbarchi, A. Ronda, F. Jardali, J. Park, and H. Vach. “Formation of Silicene Nanosheets on Graphite”. In: *ACS Nano* 10.12 (2016), pp. 11163–11171 (cit. on pp. 85, 86).
- [176] I Kupchak, F Fabbri, M. D. Crescenzi, M Scarselli, M Salvato, T Delise, I Berbezier, O Pulci, and P Castrucci. “Scanning Tunneling microscopy and Raman evidence of silicene nanosheets intercalated into graphite surfaces at room temperature”. In: *Nanoscale* 11.13 (2019), p. 6145 (cit. on p. 85).
- [177] W. Peng et al. “Resolving the Controversial Existence of Silicene and Germanene Nanosheets Grown on Graphite”. In: *ACS Nano* 12.5 (2018), pp. 4754–4760 (cit. on p. 86).
- [178] G. W. Mudd et al. “Tuning the Bandgap of Exfoliated InSe Nanosheets by Quantum Confinement”. In: *Advanced Materials* 25.40 (2013), pp. 5714–5718 (cit. on p. 87).
- [179] K. Saiki, Y. Sato, and A. Koma. “Adsorption of Oxygen on Electron-Bombarded CaF₂ (111) Surfaces”. In: *Japanese Journal of Applied Physics* 28.Part 2, No. 1 (1989), pp. L134–L137 (cit. on p. 87).
- [180] S. Kokott, P. Pflugradt, L. Matthes, and F. Bechstedt. “Nonmetallic substrates for growth of silicene: an ab initio prediction”. In: *Journal of Physics: Condensed Matter* 26.18 (2014), p. 185002 (cit. on p. 87).

- [181] M. A. Olmstead. “Heteroepitaxy of disparate materials: From chemisorption to epitaxy in CaF₂/Si(111)”. In: *Thin Films: Heteroepitaxial Systems*. Ed. by W. K. Liu and M. B. Santos. Singapore: World Scientific, 1999. Chap. 15 sec.5 (cit. on p. 87).
- [182] J Wollschläger. “Resonant tunnelling devices based on epitaxial insulator-semiconductor structures: Growth and characterisation of CaF₂ films on Si(111)”. In: *Recent Research Developments in Applied Physics*. Ed. by S. Pandalai. Trivandrum: Transworld Research Network, 2002. Chap. 5_II, pp. 621–695 (cit. on p. 87).
- [183] J. Wollschläger. “Substrate-step-induced effects on the growth of CaF₂ on Si(111)”. In: *Applied Physics A: Materials Science & Processing* 75.1 (2002), pp. 155–166 (cit. on pp. 87, 91, 92).
- [184] C. R. Wang, B. H. Müller, and K. R. Hofmann. “CaF₂/Si/CaF₂ double-barrier resonant-tunnelling diodes on Si substrates”. In: *Nanotechnology* 14.11 (2003), pp. 1192–1196 (cit. on p. 87).
- [185] M. A. M. Watanabe, T. Suemasu, S. Muratake. “Negative differential resistance of metal resonant tunneling diode”. In: *Applied Physics Letters* 62.3 (2010), p. 300 (cit. on p. 87).
- [186] C. R. Wang, M. Bierkandt, S. Paprotta, T. Wietler, and K. R. Hofmann. “CaF₂SiCaF₂ resonant tunneling diodes grown by B surfactant-mediated epitaxy”. In: *Applied Physics Letters* 86.3 (2005), p. 033111 (cit. on p. 87).
- [187] T. Nakayama, M. Katayama, G. Selva, and M. Aono. “Mechanism of epitaxial growth of monolayer CaF on Si(111)-(7×7)”. In: *Physical Review Letters* 72.11 (1994), pp. 1718–1721 (cit. on pp. 88, 96).
- [188] T Nakayama and M Aono. “Creation and consumption of free Si atoms at the growth front of a CaF monolayer on Si(111)-(7×7)”. In: *Physical Review B* 57.3 (1998), p. 1855 (cit. on p. 88).
- [189] P. Rahe, E. F. Smith, J. Wollschläger, and P. J. Moriarty. “Formation routes and structural details of the CaF₁ layer on Si(111) from high-resolution non-contact atomic force microscopy data”. In: *Physical Review B* 97.12 (2018), p. 125418 (cit. on pp. 88, 91, 93, 96).
- [190] T. Sumiya, T. Miura, and S.-i. Tanaka. “Initial growth stage of CaF₂ on Si(111)-(7×7) studied by high temperature UHV-STM”. In: *Surface Science* 357 (1996), p. 896 (cit. on pp. 88, 89).

- [191] R. M. Tromp and M. C. Reuter. “Structure of the Si(111)-CaF₂ Interface The growth conditions of CaF₂ on Si(111) were optimized by monitoring the interface formation in situ with x-ray photoelectron spectroscopy, ultraviolet photoelectron spectroscopy, and medium-energy ion scattering”. In: *Physical Review Letters* 61.15 (1988), p. 1756 (cit. on pp. 88, 92).
- [192] C. R. Wang, B. H. Müller, E. Bugiel, and K. R. Hofmann. “Temperature-dependent growth mechanisms of CaF₂ on Si(111)”. In: *Journal of Vacuum Science & Technology A: Vacuum, Surfaces, and Films* 22.5 (2004), pp. 2182–2187 (cit. on pp. 88, 92).
- [193] J. Wollschläger and A. Meier. “Film and interface morphology of CaF₂ grown on Si(111) at low temperature”. In: *Journal of Applied Physics* 79.9 (1996), pp. 7373–7375 (cit. on p. 88).
- [194] A. I. Lucas, D. Loretto, and G. C. L. Wong. “Epitaxial growth mechanisms and structure of CaF₂/Si(111)”. In: *Physical Review B* 50.19 (1994), p. 14340 (cit. on p. 89).
- [195] K. Takayanagi, Y. Tanishiro, M. Takahashi, and S. Takahashi. “Structural analysis of Si(111)-7×7 by UHV-transmission electron diffraction and microscopy”. In: *Journal of Vacuum Science & Technology A: Vacuum, Surfaces, and Films* 3.3 (1985), pp. 1502–1506 (cit. on pp. 89, 90).
- [196] J. Wang, L. Jin, H. Zhou, H. Fu, C. Song, S. Meng, and J. Zhang. “Direct imaging of surface states hidden in the third layer of Si (111)-7 × 7 surface by p z -wave tip”. In: *Applied Physics Letters* 113.3 (2018), p. 031604 (cit. on p. 89).
- [197] R. Wolkow and P. Avouris. “Atom-resolved surface chemistry using scanning tunneling microscopy”. In: *Physical Review Letters* 60.11 (1988), pp. 1049–1052 (cit. on pp. 90, 91).
- [198] P. Avouris and R. Wolkow. “Atom-resolved surface chemistry studied by scanning tunneling microscopy and spectroscopy”. In: *Physical Review B* 39.8 (1989), pp. 5091–5100 (cit. on p. 90).
- [199] R. J. Hamers, R. M. Tromp, and J. E. Demuth. “Surface Electronic Structure of Si (111)-(7×7) Resolved in Real Space”. In: *Physical Review Letters* 56.18 (1986), pp. 1972–1975 (cit. on pp. 90, 93).
- [200] P. Avouris and In-Whan Lyo. “Probing and inducing surface chemistry with the STM: the reactions of Si(111)-7 × 7 with H₂O and O₂”. In: *Surface Science* 242.1-3 (1991), pp. 1–11 (cit. on pp. 90, 91).

- [201] H.-J. Liu, Z.-X. Xie, H. Watanabe, J. Qu, and K.-i. Tanaka. “Site-selective adsorption of C₂H₅OH and NO depending on the local structure or local electron density on the Si(111)-7×7 surface”. In: *Physical Review B* 73.16 (2006), p. 165421 (cit. on pp. 90, 91).
- [202] M. N. Piancastelli, N. Motta, A. Sgarlata, A. Balzarotti, and M. De Crescenzi. “Topographic and spectroscopic analysis of ethylene adsorption on Si(111)7×7 by STM and STS”. In: *Physical Review B* 48.24 (1993), pp. 17892–17896 (cit. on pp. 90, 91).
- [203] M. A. Olmstead, R. I. G. Uhrberg, R. D. Bringans, and R. Z. Bachrach. “Photoemission study of bonding at the CaF₂-on-Si(111) interface”. In: *Physical Review B* 35.14 (1987), pp. 7526–7532 (cit. on pp. 91, 96).
- [204] M. Olmstead and R. Bringans. “Initial stages of epitaxial semiconductor-insulator heterointerface formation”. In: *Journal of Electron Spectroscopy and Related Phenomena* 51 (1990), pp. 599–612 (cit. on pp. 92, 93).
- [205] D Rieger, F. J. Himpsel, U. O. Karlsson, F. R. Mcfeely, J. F. Morar, and J. A. Yarmoff. “Electronic structure of the CaF₂/Si(111) interface”. In: *Physical Review B* 34.10 (1986), p. 7295 (cit. on pp. 92, 93).
- [206] J. Harada, I. Takahashi, Y. Itoh, N. Sokolov, N. Yakovlev, Y. Shusterman, and J. Alvarez. “X-ray scattering from surfaces and interfaces and its application to the characterization of CaF₂/Si(111) interfaces”. In: *Journal of Crystal Growth* 163.1-2 (1996), pp. 31–38 (cit. on p. 92).
- [207] N. Sokolov, J. Alvarez, S. Gastev, Y. Shusterman, I. Takahashi, Y. Itoh, J. Harada, and R. Overney. “High quality CaF₂ layers on Si(111) with type-A epitaxial relation at the interface”. In: *Journal of Crystal Growth* 169.1 (1996), pp. 40–50 (cit. on p. 92).
- [208] M. A. Olmstead. “Initial formation of the interface between a polar insulator and a nonpolar semiconductor: CaF₂ on Si(111)”. In: *Journal of Vacuum Science & Technology B: Microelectronics and Nanometer Structures* 4.4 (1986), p. 1123 (cit. on pp. 92, 93, 96).
- [209] R. S. Becker, J. A. Golovchenko, G. S. Higashi, and B. S. Swartzentruber. “New Reconstructions on Silicon (111) Surfaces”. In: *Physical Review Letters* 57.8 (1986), pp. 1020–1023 (cit. on p. 93).
- [210] U. Köhler, J. E. Demuth, and R. J. Hamers. “Scanning tunneling microscopy study of low-temperature epitaxial growth of silicon on Si(111)-(7×7)”. In: *Journal of Vacuum Science & Technology A: Vacuum, Surfaces, and Films* 7.4 (1989), pp. 2860–2867 (cit. on p. 93).

- [211] Y.-N. Yang and E. D. Williams. “High atom density in the “ 1×1 ” phase and origin of the metastable reconstructions on Si(111)”. In: *Physical Review Letters* 72.12 (1994), pp. 1862–1865 (cit. on p. 93).
- [212] R. Feenstra and A. Slavin. “Scanning tunneling microscopy and spectroscopy of cleaved and annealed Ge(111) surfaces”. In: *Surface Science* 251-252.C (1991), pp. 401–407 (cit. on p. 93).
- [213] R. S. Becker, J. A. Golovchenko, D. Hamann, and B. S. Swartzentruber. “Real-Space Observation of Surface States on Si(111) 7×7 with the Tunneling Microscope”. In: *Phys. Rev. Lett.* 55.19 (1985), pp. 2032–2035 (cit. on p. 93).
- [214] J. Mysliveček, A. Stróżecka, J. Steffl, P. Sobotík, I. Ošt’ádal, and B. Voigtländer. “Structure of the adatom electron band of the Si(111) 7×7 surface”. In: *Physical Review B* 73.16 (2006), p. 161302 (cit. on p. 93).
- [215] A. Klust, T. Ohta, A. A. Bostwick, E. Rotenberg, Q. Yu, F. S. Ohuchi, and M. A. Olmstead. “Electronic structure evolution during the growth of ultrathin insulator films on semiconductors: From interface formation to bulklike CaF₂”. In: *Physical Review B* 72.20 (2005), p. 205336 (cit. on p. 93).
- [216] U. O. Karlsson, F. J. Himpsel, J. F. Morar, D. Rieger, and J. A. Yarmoff. “Electronic structure of molecular beam epitaxy grown CaF₂ on Si(111)”. In: *Journal of Vacuum Science & Technology B: Microelectronics and Nanometer Structures* 4.4 (1986), p. 1117 (cit. on p. 93).
- [217] R. Zhachuk, S. Teys, and J. Coutinho. “Strain-induced structure transformations on Si(111) and Ge(111) surfaces: A combined density-functional and scanning tunneling microscopy study”. In: *Journal of Chemical Physics* 138.22 (2013), p. 224702. arXiv: 1302.1050 (cit. on p. 96).
- [218] R. Zhachuk, J. Coutinho, A. Dolbak, V. Cherepanov, and B. Voigtländer. “Si(111) strained layers on Ge(111): Evidence for $c(2\times 4)$ domains”. In: *Physical Review B* 96.8 (2017), pp. 1–7 (cit. on p. 96).
- [219] T. Sumiya. “Initial growth stages of CaF₂ on Si(111) investigated by scanning tunneling microscopy”. In: *Applied Surface Science* 156.1-4 (2000), pp. 85–96 (cit. on p. 96).

